1223

Bridge Design and Performance and Composite Materials

Foreword

Of the 14 papers in this Record, 10 are concerned with design of bridge elements, one is about service life prediction of bridges, one examines mechanical anchors in concrete, one reports tests on fiber reinforced plastic structural members, and one discusses the concept of fiber reinforced plastic and concrete highway tunnels.

Dusel reports on cyclic and sustained tension tests of mechanical anchors used for attaching signs, inspection ladders, brackets, and other items to concrete. Abendroth and Greimann present two design alternatives, based on one-tenth scale laboratory tests, full-scale field tests, and finite element investigations, for piles used integrally at abutments. Mozingo describes tests of a 1:12 scale model of a 46-ft. span timber bridge with steel strips stressing a double layer of square wood elements. The double layer was used to accommodate today's smaller timber sizes, and stressing increased structural rigidity by a factor of 2.25.

Burke reports on the history of a 150-year-old bridge whose innovative design used a local foundry's ability to make tubular iron castings. The 80-ft. span continues to carry full legal loads. Van Lund et al. describe a bridge substructure replacement that permitted widening of the Interstate below to eight lanes. Peer review of eight designs for the project resulted in the selection of a two-hinge steel arch, partly because this design permitted erection with the least traffic interruption and public hazard.

Wipf et al. use a finite element program with three-dimensional elements to examine the effect of transverse and longitudinal stiffening of steel stringer bridges. The authors found that stiffening could increase the live-load ratings of simple span bridges by 30 percent and that stiffening of continuous stringer bridges could be detrimental because the stress at unstiffened locations could be increased. Wiley et al. determined the effect of four different post-tensioning configurations by measurements on a one-third scale continuous three-span composite bridge model. The post tensioning helped strengthen negative moment regions.

Hiremath et al., in tests of two Washington State DOT series 14 girders joined to form a continuous member, concluded that the joined series 14 girders without endblocks will perform effectively as continuous girders as long as they are placed normal to the support and a specified sequence of construction is followed. Hwang and Nowak report on a study to develop a prediction method for the dynamic load effect on a girder bridge. Bakht and Pinjarkar's review indicates inconsistencies in a wide variety of methods for interpreting dynamic test data and proposed a preferred method of calculating dynamic factors.

Yen and Lai report on time-strain measurements due to truck loads on two steel girder bridges, including vibration frequencies, modes, and damping. They found that the bridge vibrated mainly in one fundamental mode, analogous to the static deflection shape assumed in design. Jiang and Sinha describe a process for using present condition, age, and probability of deterioration rates to predict the service life of bridges.

Bank reports on laboratory bending and shear tests on high narrow flange and wide flange pultruded fiber-reinforced plastic (FRP) beam sections, as well as an analysis of a FRP rigid frame. Kaempen describes the conceptual use of fiber-reinforced plastic and concrete as underwater highway tunnel sections.

Transportation Research Record 1223

Contents

Evaluation of Mechanical Expansion Anchors

JOHN P. DUSEL, JR.

Results of research conducted on mechanical expansion anchors for the purpose of revising an existing acceptance specification used by the California Department of Transportation are presented in this paper. The main objective of the research was to refine a portion of the standard specification dealing with mechanical expansion anchors, whose key requirement is to limit the amount of displacement that a mechanical expansion anchor can exhibit while being subjected to moderate sustained tensile loading. The scope of the work included (a) classifying mechanical expansion anchors from 14 manufacturers into five main categories and then further segregating them into types within each category, (b) conducting 465 ultimate tensile load tests on ¼-, ½-, and ¾-in.-diameter zinc-electroplated mechanical expansion anchors to determine the point at which slip or yield occurs and their mean ultimate strength, (c) performing a total of 394 sustained tensile load creep tests at two different concrete strengths, (d) determining physical properties and chemical composition of suitable anchors, and (e) refining the standard specification and preparing a standard test method, California Test 681. The main alteration in the anchor specification included lowering the magnitudes of some sustained tension test loads for the required creep test and reducing the permitted displacement (0.050 to 0.035 in.) and time period (100 to 48 hrs) during which creep is monitored. The two anchor types found to be the best in each of their respective categories— shell and stud—are (a) the shell nondrilling internal plug and (b) the stud wedge.

The California Department of Transportation (Caltrans) has an ongoing need to attach various fabricated products, including signs, inspection ladders, hand rail, glare screen posts, crash cushion bases, and various brackets, to surfaces of existing concrete structures. In many instances, both designers and maintenance personnel require a relatively inexpensive, yet reliable, anchorage device—the mechanical expansion anchor—where more substantial or permanent anchoring methods are deemed unnecessary.

In recent years, many new types of mechanical expansion anchors have been developed. One of the newer types—the stud wedge—has become popular with many contractors. Reasons for its popularity are as follows:

- All required studs, nuts, and washers are furnished with the anchor;
- A multihole base plate can be used as a drill template, minimizing misaligned holes;
- The costs of drill bits and hole preparation are lower because the drill hole diameters required are smaller than those needed for shell-type anchors; and
- By minimizing drill hole diameters, the chance of encountering rebar is reduced.

California Department of Transportation, Transportation Laboratory, 5900 Folsom Boulevard, Sacramento, Calif. 95819.

A new improved style of shell anchor is a type having an internal tapered plug and is often referred to as "drop-in."

Until recent research was undertaken (1), only two older kinds of mechanical anchors—the flush-mounted shell external plug and stud external plug—had been tested and approved by Caltrans. In order for a mechanical expansion anchor to be approved for use in Caltrans contracts, requirements of the Caltrans *Standard Specifications* (Jan. 1988, Section 75-1.03) must be met.

Caltrans is the only known organization that considers the amount of creep of concrete anchorage devices during sustained tension loading to be the most meaningful measure of an anchor's ability to perform well under severe field conditions. Since 1973, Caltrans has included a creep evaluation as one of the key points in its specification. Before July 1984, acceptable anchors could not exhibit more than 0.050 in. of movement while subjected to a specified sustained tensile test load for a period of 100 hr. Unfortunately, no known manufacturer currently provides creep data, either short or long term, for mechanical expansion anchors. Almost all, however, offer ultimate shear and tension test data, which can be obtained relatively quickly and cheaply. Design engineers are concerned more with the "yield point" of an anchorage system, the amount of creep that may occur during long-term sustained loading, the performance of an anchor during dynamic loading, and the ability of an anchor to maintain a high tensile load after anchor movement has begun.

Before this research project (1) was completed, very little creep test data for mechanical expansion anchors were available (2), and there was no uniform test procedure established to determine creep. Some of the sustained tension test load values shown in earlier Caltrans standard specifications that were required to evaluate anchor creep were thought to be unrealistically high. Many of these test load values had been obtained by either interpolation or extrapolation from a few known sustained tension load values that had been determined for popular anchor sizes from a limited number of manufacturers.

Furthermore, there were no uniform requirements established for important physical properties of concrete test specimens in which mechanical expansion anchors were evaluated. Such important properties include compressive strength, modulus of elasticity, and cure time. Testing equipment and procedures used to collect the limited creep data also varied.

Because of the lack of demand for creep data by general users, manufacturers have been reluctant to spend the funds necessary to obtain comprehensive creep data for their mechanical anchors. Creep data are costly and time-consuming to develop and generally there has been little demand for such data by most users. Therefore, manufacturers have been

unwilling to provide creep data and unable to recommend realistic reductions in their published ultimate loads for conditions where either sustained tensile, dynamic, or impact loading govern.

A literature search was conducted and no published information concerning creep of mechanical expansion anchors was found. However, some interesting research papers dealing with both the static and dynamic behavior of mechanical expansion anchors were discovered (3–5).

The main objective of this research was to revise the existing Caltrans specification for mechanical expansion anchors as necessary, so that the sustained tensile test load values and the magnitude of displacement used to evaluate creep would be realistic numbers. To accomplish this objective, the scope of the research work included

- Classifying the variety of mechanical expansion anchors available;
- Conducting short-term direct tension tests and sustained tensile load (creep) tests;
- Determining physical properties, chemical composition, and corrosion resistance of suitable anchors;
- Developing a precise test method; and
- Revising the standard specification.

DESCRIPTION OF TEST PROGRAM

Test Program Phases

To satisfy the project objective, the testing program was divided into five phases:

- Phase 1: Classifying various mechanical expansion anchors into distinct categories and determining anchor properties such as chemical composition, hardness, and corrosion resistance; performing chemical analysis on mechanical expansion anchors to determine percentage of key elements in the anchor metal.
- Phase 2: Conducting short-term direct tension tests to determine approximate system yield points and maximum pullout strengths for each anchor type.
- Phase 3: Conducting sustained tensile load tests to determine appropriate sustained load levels and typical magnitudes of creep for anchors in each major category and type; developing a comprehensive test method to evaluate creep of mechanical expansion anchors was done concurrently.
- Phase 4: Conducting additional sustained tensile load tests while varying the compressive strength of concrete in the test slabs to evaluate the effect of lower compressive strengths on the ability of anchors to resist sustained loads.
- Phase 5: Revising Section 75-1.03 of the July 1984 Caltrans *Standard Specifications* to reflect research results.

Classification of Mechanical Expansion Anchors

Through a literature search performed early in the project, a listing of 14 mechanical expansion anchor companies in the United States—Ackerman Johnson (formerly Illinois), CEB Corporation (formerly Chicago), Cunningham, Hilti, Liebig, Molly, Phillips, Ramset, Rawlplug, Star, U.S.E. Diamond, Universal, Wej-it, and Williams—was compiled.

A preliminary evaluation of more than 80 different mechanical expansion anchors was made. Anchors were grouped into one of five categories shown in Table 1. Classifications were made based on appearance, dimensions, method of functioning, and unique physical characteristics.

Test Specimens

Mechanical Expansion Anchors

All mechanical expansion anchors used for testing had a standard zinc-electroplated coating. Anchor lengths tested were generally the shortest available.

Phase 1: Samples of ½- and ¾-in.-diameter mechanical expansion anchors from six major manufacturers were chosen for evaluation to determine hardness of anchor parts, chemical composition, and potential for corrosion in a salt spray environment. These manufacturers were Hilti, Molly, Phillips, Ramset, Rawlplug, and Star.

Phase 2: A total of 465 mechanical expansion anchors from 14 manufacturers were tested for ultimate tensile strength. Anchor sizes evaluated were ¼-, ½-, and ¾-in.-diameter in the shell and stud categories and additional sizes in the miscellaneous category.

Phase 3: A total of 322 mechanical expansion anchors were tested for periods up to 100 hr to determine creep behavior under a sustained tensile load. Sizes and types of anchors tested are shown in Table 2. Tests were performed in unreinforced concrete slabs having nominal compressive strengths of 5,000 psi. Anchor categories evaluated included the shell and stud. Sizes tested included the ¼-, ½-, and ¾-in.-diameter anchors. Manufacturers of anchors evaluated included Hilti, Molly, Phillips, Ramset, Rawlplug, and Star.

Phase 4: A total of 72 mechanical expansion anchors, which appeared to be acceptable from the results of Phase 3 testing, were evaluated in concrete of a lower compressive strength (4,000 psi) to determine its effects on creep. Anchor sizes tested (shown in Table 3) include ¼-, ½-, and ¾-in. diameters. Anchors from the same manufacturers evaluated in Phase 3 were used here.

Concrete Slabs

Ready-mix concrete was used to construct test slabs, which were unreinforced. The aggregate used conformed to the 1-in. maximum grading in Caltrans *Standard Specifications* (CSS) (Jan. 1988, Section 90-3.04). For testing in Phases 2 and 3, a Class A concrete (CSS, Jan. 1988), containing 564 pounds of Type II modified portland cement per cubic yard (six-sack mix) was used. The average slump attained was 3 in. The average compressive strength of each test slab was determined by averaging compressive strengths of three 6- x 12-in. concrete cylinders made and cured with the slabs. The average compressive strength of concrete used in Phase 2 test slabs was 4,000 psi. The average compressive strength of concrete in all Phase 3 test slabs at the time of testing was between 4,800 and 5,200 psi. For Phase 4 testing, a lower strength Class B concrete (CSS, Jan. 1988) was used, which contained 470 pounds of Type II modified portland cement per cubic yard (five-sack mix). The average slump attained was 4 in.

TABLE 1 GROUPINGS OF MECHANICAL EXPANSION ANCHORS

CATEGORY/TYPE	GENERAL CHARACTERISTICS
1. SHELL a. Non-drilling External Plug b. Non-drilling Internal Plug c. Self-drilling External Plug	Thick-walled steel sleeves have internal threads in the top half, and are slotted near the base of the sleeve. The slotted base is expanded with either an external or internal tapered plug. The mounting stud or bolt is separate from the shell body and is not furnished with anchor.
2. STUD a. External Plug b. Wedge c. Sleeve	A special steel rod is threaded at the top end and develops grip by either spreading the base of the stud with a hard tapered plug or wedging a thin steel collar between a cone-shaped base and the hole sides.
3. EXPANSION SHIELD a. Single b. Double	A two-piece die-cast zinc shell is expanded with an internally threaded cone. The shield is set by applying torque to the mounting bolt.
4. CAULKING a. Single b. Multiple	This two-piece anchor is comprised of a lead sleeve and die-cast zinc threaded cone. The anchor is set by driving the lead sleeve around the cone.
5. MISCELLANEOUS	Special mechanical expansion anchors with unique or hybrid features.

The average compressive strength of concrete used in all low-strength test slabs at the time of testing was between 3,800 and 4,200 psi.

Test slabs for evaluating ¼- and ½-in.-diameter anchors were approximately 5½ in. deep. Test slabs for evaluating ¾-in.-diameter anchors were approximately 7½ in. deep.

Installation of Anchors

Anchorage devices were installed according to the manufacturer's specific instructions when supplied. Manufacturers normally provided most of the following information:

● Nominal drill bit diameter required (although the diameter tolerance of the carbide tip was not typically specified by the manufacturer);
● Minimum hole depth;
● Required use of a special installation tool; and
● For stud anchors, specified turn-of-nut or torque value to be applied to set anchors.

A rotary impact hammer with carbide-tipped bits was used to drill all holes in the hardened concrete slabs. The diameters of the drill bit tips were measured frequently to ensure conformance to limits prescribed in ANSI Standard B94.12-1977.

TABLE 2 SUMMARY OF SUSTAINED LOAD TESTING CONDUCTED IN PHASE 3

Sustained tensile test loads (pounds)/number tested

Size	Shell		Stud		Total
	Int. Plug	Ext. Plug	Ext. Plug	Wedge	Tested
1/4 *	1250/9 1500/11 1800/3	1000/5 1500/7 1800/6	1000/13 1500/7 1800/8	1000/11 1500/9 1800/6	95
1/2 *	3400/3 3500/2 4000/7 4300/2 4500/14 5000/10	3400/9	3400/9	3400/15 3600/10 3800/8 4000/2 4200/3	94
3/4 *	5000/9 6000/24 7000/5 8000/7	5000/6 6000/9	5000/14 6000/8	5000/25 5500/9 6000/17	133
Total Tests/ Type	106	42	59	115	322

* Size in inches

TABLE 3 SUMMARY OF SUSTAINED LOAD TESTING CONDUCTED IN PHASE 4

Type	Stud		Shell		Test	Total Number of
					Load,	Tests/
Size	Wedge	Ext. Plug	Int. Plug	Ext. Plug	lbs.	Size
1/2	9	9	9	9	3400	36
3/4	9	9	9	9	5000	36
Total No. of Tests per Type	18	18	18	18		72

Uniform hole depths were intentionally chosen for each different anchor type and diameter evaluated, with the exception of shell anchors. The depth selected for a particular anchor type was the largest minimum depth specified by any of the manufacturers whose anchors were being tested. All minimum hole depths specified for shell anchors, however, were increased ½ in. This current Caltrans requirement (6) ensures that anchors are securely seated. All installation holes drilled in concrete slabs were thoroughly cleaned after drilling by blowing out dust and debris with compressed air and a nozzle.

One installation torque value was selected for all anchors tested in each anchor classification, type, and size. A single value was determined for a particular anchor type so that the torque would be within ranges recommended by other manufacturers of similar anchors being tested. Researchers felt this procedure would ensure consistency in installation so that

results could be compared directly. Values of other parameters, including hole depth, tip diameter of drill bits, setting procedures used, and installation torque versus turn-of-nut values, were measured and recorded for each test.

Test Equipment and Procedures

All anchors evaluated in this research were tested under conditions similar to those encountered in Caltrans' contracts. Installation and testing were performed according to requirements and procedures in California Test 681 (7), a standard test method developed in this research project for evaluating creep of mechanical expansion anchors.

Short-Term Direct Tension Pullout Tests (Phase 2)

A minimum of three replicate tests was performed on anchors from each manufacturer tested. Minimum edge distance for all anchors tested in Phase 2 and subsequent phases was 5 hole diameters, and minimum spacing between all anchors was 10 hole diameters. If dispersion of pullout data was large and the results from any one test deviated more than 15 percent from the mean, then two additional pullout tests were performed.

A special movable loading frame, shown in Figure 1, supported the hydraulic ram and load cell. A set of interchangeable base rings with different diameters was made and a ring was chosen that would avoid any reaction on the concrete
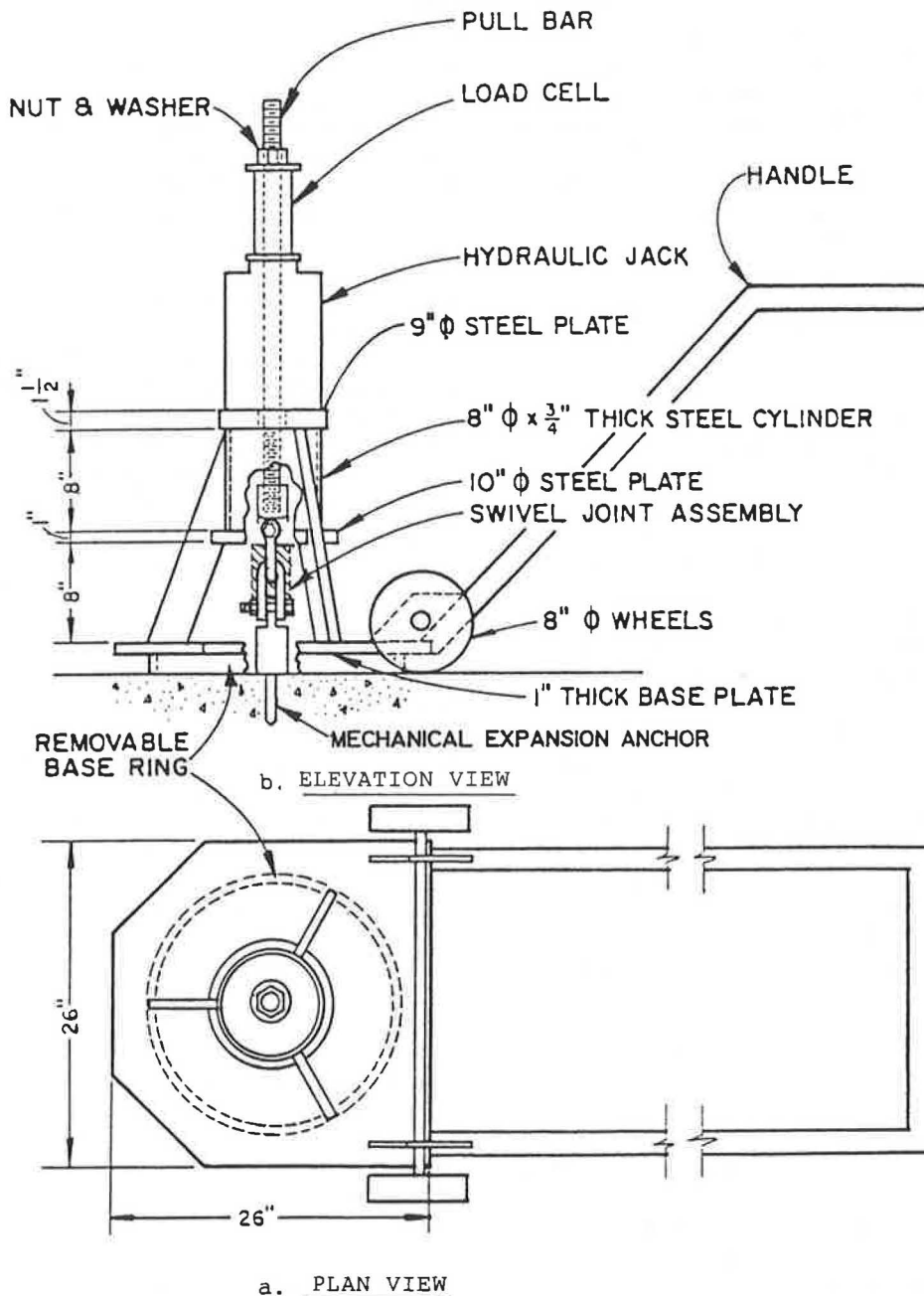

FIGURE 1   Portable testing apparatus ror conducting short-term ultimate tension load tests.

slab close to the mechanical expansion anchor. The external tensile load was applied to installed expansion anchors through a load collar, which simulated a base plate. The load collar was held firmly against the concrete surface by preload in the anchor stud, which was required when installing all anchors. Two interlocked chain shackles eliminated bending moments and linked the load collar to the pull rod. The pull rod extended through a hydraulic ram and load cell.

A stiff steel arm was used to support two linear potentiometers whose readings were averaged to determine mean displacement. The arm was securely attached to the load collar by a threaded cap.

In all tests performed, graphs of axial tensile load versus time and anchor displacement versus time were plotted simultaneously by an XYY recorder.

At the beginning of each pullout test, a small external tensile load was applied to the pull rod to seat parts of the testing apparatus. External loads were applied so that the time required to reach the ultimate load was between 60 and 90 sec. For ¼-in.-diameter anchors, loading rates ranged from 1 to 3 kips per minute. Loading rates for the ½-in.-diameter anchors were 5.6 to 8 kips per minute. The ¾-in.-diameter anchors were loaded at rates ranging from 12 to 20 kips per minute. Tests were continued until anchor displacement exceeded 0.5 in.

Creep Tests on Anchors in 5,000 psi Concrete (Phase 3)

Both stud- and shell-type anchors were tested by applying a sustained axial load for periods of up to 100 hr to determine the amount of displacement. Concrete having a compressive strength of 5,000 psi was used for all tests in Phase 3.

A constant sustained external load was maintained on each mechanical anchor by forces from stiff, compressed railroad car springs, bearing plates, and a pull rod. A sketch of the test apparatus is shown in Figure 2. Tensile loads were initially applied by a 120-kip single acting ram. The appropriate tensile load could be locked off using a nut that was on the pull rod, just below the load cell. As in short-term pullout testing, external loads were transferred to the installed expansion anchor through the base of a load collar. Studs of all mechanical expansion anchors were preloaded during installation with a specific torque to firmly press the base of the load collar against the surface of the concrete slab.

In this paper, the term *creep* is defined as the total movement of the bottom surface of the anchor nut, relative to the surface of the concrete slab, that occurs from the time after the anchor has been installed and the installation torque has been applied until the 48-hr test period—during which the anchor is subjected to the full sustained test load—has elapsed. This movement or displacement includes initial slip and elastic stretch of the stud, as well as any creep occurring in the test period.

The sustained tension test loads were applied at a constant rate not greater than 1,000 lb/min. until the desired load was reached. Sustained loads were maintained to within ±5 percent of the initial settings for the duration of each test. As the test program progressed, magnitudes of the sustained tensile test loads were adjusted downward below slip points (the level at which major anchor movement or displacement first occurs) as necessary until acceptable anchor creep was achieved.

Magnitudes of sustained test loads were finally deemed acceptable when anchors from at least 50 percent of the manufacturers tested passed. In the earlier 1981 Caltrans *Standard Specifications* (Section 75-1.03), anchors were deemed acceptable when they could maintain the specified tension test load for 100 hr without displacing more than 0.050 in. Test loads were maintained for 100 hr in all creep tests performed on ¼- and ¾-in.-diameter anchors. From the analysis of creep data from ¼- and ¾-in.-diameter anchors in this research, it was determined that the test duration could be reduced to 48 hr. For all tests conducted on ½-in.-diameter anchors, test loads were maintained only for a 48-hr period.

Hardness, Chemical Analysis, and Corrosion Tests (Phase 1)

To minimize the number of samples evaluated, Phase 1 testing was performed after completing work on Phases 2 and 3. At least three hardness readings were taken on each specimen. The type of metal used in anchor parts was determined using various types of elemental chemical evaluations.

Salt spray corrosion testing was conducted to determine the relative protection provided by the thin coating of electroplated zinc typically found on most mechanical expansion anchors, when subjected to a moderate or severely corrosive environment.

Three anchors from each of the six major manufacturers were installed in concrete test blocks and exposed to salt spray testing (ASTM B117-73) for varying lengths of time. Galvanized steel base plates were secured to concrete test blocks with mechanical expansion anchors using typical installation procedures to simulate real field conditions. Different specimens were removed from the salt spray chamber after various lengths of exposure up to 48 days (1,152 hr), then were disassembled, broken open and inspected for corrosion.

Creep Tests on Anchors in 4,000 psi Concrete (Phase 4)

Both ½- and ¾-in.-diameter stud- and shell-type anchors were tested in a lower-strength concrete having a compressive strength ranging from 3,800 to 4,200 psi, using similar procedures as in Phase 3. External sustained load levels used in Phase 4 testing were the maximum levels determined in Phase 3 testing, where over 50 percent of the manufacturers tested were capable of maintaining the applied load with less than 0.050-in. total displacement. Test loads were maintained for periods of 48 hr.

DISCUSSION OF TEST RESULTS

Phase 1:

Material Hardness and Chemical Analysis

Through preliminary chemical analysis, some of the anchor types were eliminated from consideration because they were fabricated from metals other than steel or stainless steel. No significant findings resulted from hardness tests.
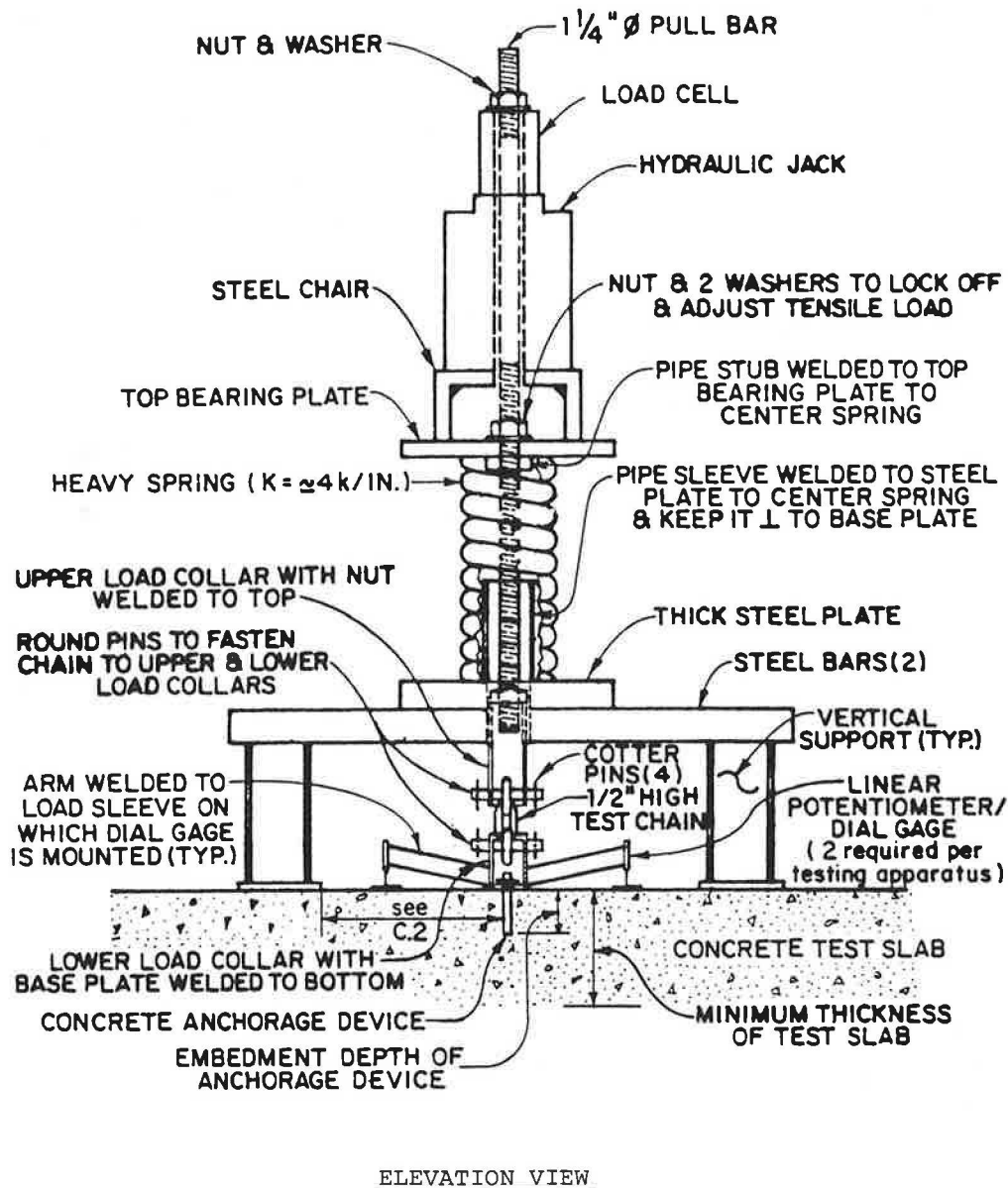
ELEVATION VIEW

FIGURE 2 Sustained tension load testing apparatus used to evaluate creep (elevation view).

Corrosion Resistance

In salt spray testing representing a severely corrosive atmosphere, moderate corrosion of mechanical anchor parts that were electroplated with zinc (nut, stud tip, and washer) and located above the concrete surface was typical in a relatively short time period. Below the surface of the concrete, however, the amount of sacrificial zinc corrosion of the mechanical anchor bodies observed was relatively minor and only a small amount of corrosion of the lower anchor body steel occurred.

Phase 2: Short-Term Direct Tension Pullout Tests

Ultimate tensile loads obtained for mechanical expansion anchors tested in short-term pullout are listed in Table 4. With few exceptions, test results of individual anchors found in this research were below manufacturer's published data for the ultimate tensile loads.

Large variations in mean ultimate strengths were noted between the different types of anchors tested. In addition, variations in ultimate tensile strengths of individual anchor tests for a given anchor type were from −5 percent to +50 percent from the mean strength.

In general, both shell-type anchors tested performed well relative to stud-type anchors. Although mean ultimate pullout strengths for some stud-type anchors tested exceeded those of some shell anchor types, displacements at design loads were small.

Stud sleeve-type anchors exhibited the lowest overall average ultimate tensile load value in the ¼- and ¾-in.-diameter sizes.

The main objective of this project—developing a reasonable specification—was accomplished without thoroughly testing

TABLE 4 MEAN ULTIMATE TENSILE PULLOUT LOADS FROM SHORT-TERM TENSILE TESTS CONDUCTED IN PHASE 2

MEAN ULTIMATE TENSILE PULLOUT LOADS, KIPS

CATEGORY	TYPE	STUD SIZE	CHICAGO	CUNNINGHAM	HILTI	ILLINOIS	LIEBIG	MOLLY	PHILLIPS	RAMSET	RAWLPLUG	STAR	UNIVERSAL	USE DIAMOND	WEJ-IT	WILLIAMS	AVERAGE	NO. OF TESTS
SHELL	Non-Drilling External Plug	1/4	4.27	—	—	—	—	—	3.42	—	4.09	1.88	—	—	—	—	3.42	18
		1/2	4.43	—	—	—	—	—	7.02	—	7.35	5.97	—	—	—	—	6.08	21
		3/4	9.3	—	—	—	—	—	11.78	—	13.8	8.3	—	—	—	—	10.8	14
	Non-Drilling Internal Plug	1/4	2.52	—	2.38	—	—	2.90	2.48	3.25	2.17	—	2.14	2.06	—	—	2.49	29
		1/2	6.49	—	7.38	—	—	7.63	6.99	7.58	6.63	—	3.96	7.78	—	—	6.81	40
		3/4	10.5	—	10.8	—	—	6.3	8.7	8.9	9.27	—	4.9	10.3	—	—	8.71	40
STUD	External Plug	1/4	1.72	—	—	—	—	—	2.00	—	1.71	2.07	—	—	—	—	1.88	16
		1/2	5.93	—	—	—	—	—	5.80	—	4.84	6.14	—	—	—	—	5.68	18
		3/4	—	—	—	—	—	—	10.0	—	10.5	10.9	—	—	—	—	10.5	11
	Wedge	1/4	—	2.39	1.66	—	—	2.00	1.82	1.98	2.00	2.39	1.72	1.95	—	—	1.99	41
		1/2	—	4.39	4.42	—	—	5.92	4.78	5.11	4.35	5.81	5.80	5.00	—	—	5.06	42
		3/4	—	9.6	9.2	—	—	10.5	7.6	9.3	10.3	11.0	11.0	8.2	—	—	9.6	31
	Sleeve	1/4	—	—	—	—	—	—	0.38	0.44	0.90	1.5	—	1.44	—	—	0.93	23
		1/2	—	—	—	—	—	—	5.15	4.77	3.35	4.19	—	3.06	—	—	4.1	24
		3/4	—	—	—	—	—	—	6.65	5.7	5.6	5.7	—	5.3	—	—	5.8	17
MISCELLANEOUS		1/4	—	—	—	—	3.59	—	—	—	—	—	2.31	—	—	1.05	2.32	15
		5/16	—	—	6.91	—	—	—	—	—	—	—	—	—	—	—	6.91	3
		1/2	—	8.57	17.35	6.5	11.63	—	—	—	—	—	8.48	—	2.70	6.12	8.76	33
		5/8	—	—	28.95	—	—	—	—	—	—	—	—	—	—	—	28.95	5
		3/4	—	14.18	—	7.0	16.2	—	—	—	—	—	11.48	—	—	6.12	11.0	24
TOTAL NUMBER TESTED			32	21	36	10	16	26	67	39	66	51	39	42	15	5		465

the many specialized anchors belonging to the miscellaneous category.

Phase 3: Creep Tests on Anchors in 5,000 psi Concrete

Results of creep tests conducted on the various types of mechanical expansion anchors tested are summarized in Tables 5 and 6. It was concluded from the observations made from results of these tests, that short-term creep behavior of an anchor could be predicted just as well after 48 hr of testing as after 100 hr of testing were performed.

In general, the amount of anchor displacement measured during creep testing varied considerably, even between replicate tests within the same anchor type. Sufficient initial preloading of mechanical expansion anchors during installation is important in minimizing total creep and, hence, keeping the fixture from working loose.

The best expansion anchor type was found to be the shell internal plug. The performance of this type of anchor was characterized by its ability to carry higher sustained loads with low displacements and good reliability.

Displacements noted with the ¼-in.-diameter anchors were so inconsistent that their test results were not used to form conclusions in this report. This variability can be explained by the heterogenous nature of concrete having more influence on small anchors with limited grip area.

Sustained tensile loads that could be maintained by ½-in.-diameter mechanical expansion anchors ranged from 3,400 to 5,000 lb, and those that could be maintained by ¾-in.-diameter anchors ranged from 5,000 to 8,000 lb.

In conjunction with performing creep tests in Phase 3, a standard test method, California Test 681, was developed and printed in March 1985 (7).

Phase 4: Creep Tests on Anchors in 4,000 psi Concrete

Although only a limited amount of creep testing was conducted using Class B concrete (CSS, Jan. 1988) with a compressive strength of between 3,800 and 4,200 psi, results show that for both the ½- and ¾-in. mechanical expansion anchors tested, anchor displacement usually increases as concrete strength decreases. The small number of tests performed prevented a detailed evaluation of the effects of low concrete strength.

Phase 5: Revisions to Caltrans Standard Specification 75-1.03

As a result of the research conducted (1), appropriate revisions to the Caltrans standard specification that addresses mechanical expansion anchors was successfully revised.

CONCLUSIONS AND RECOMMENDATIONS

More than 850 ultimate pullout and creep tests were performed in this study. Based on the results of the research, a number of conclusions were drawn and recommendations made, as described in the following subsections.

Revised Standard Specification and New Test Method

Section 75-1.03 of the January 1988 edition of the Caltrans *Standard Specifications* is suitable for evaluating mechanical expansion anchors, ¾ in. and smaller. The key points of the

TABLE 5   CREEP TEST RESULTS OF SHELL MECHANICAL EXPANSION ANCHORS

Manufacturer	Sustained Load Test Performance	Shell Anchor Types and Sizes					
		INTERNAL PLUG			EXTERNAL PLUG		
		1/4-Inch @ 1250 lbs.	1/2-Inch Varies	3/4-Inch Varies	1/4-Inch @ 1000 lbs.	1/2-Inch @ 3400 lbs.	3/4-Inch Varies
HILTI	Passed	N/A			N/A	N/A	N/A
	Did Not Pass*		HDI* 5490024 @ 4000 lbs.	HDI 5490040 @ 5000 lbs.			
MOLLY	Passed	Drop-In MDI-14	Drop-In MDI-12 @ 4500 lbs.	Drop-In MDI-34 @ 5000 lbs.	N/A	N/A	N/A
	Did Not Pass*						
PHILLIPS	Passed	Multi-Set MS-14	Milti-Set RM-12 @ 3400 lbs.		Non-drilling J-14	Non-drilling J-12	
	Did Not Pass*			Multi-SetII RM-34 @ 500 lbs.			Non-drilling J-34 @ 5000 lbs.
RAMSET	Passed			Dynaset Drop-In DS-34 @ 6000 lbs.	N/A	N/A	N/A
	Did Not Pass*	Dynaset Drop-In DS-14	Dynaset* Drop-In DS-12 @ 3500 lbs.				
RAWLPLUG	Passed	N/A	Steel Drop-In 6308 @ 4000 lbs.	Steel Drop-In 6312 @ 6000 lbs.		Steel Drop-In 6465	Steel Drop-In 6468 @ 6000 lbs.
	Did Not Pass*				**Steel Drop-In 6460		
STAR	Passed	N/A	N/A	N/A	N/A		
	Did Not Pass*					Steel* Anchor 3435-00800	Steel Anchor 3455-00800 @ 3000 lbs.

*   Many of the anchors were tested at sustained loads that were higher than those recommended in the revised specification. If retested at the lower recommended test loads, anchors may pass.

**   Only two tests run; both passed.

*** N. A. – Anchor type not available.

revised specification include (a) requiring all anchor metal to be steel with a corrosion resistant coating or stainless steel, (b) limiting mechanical expansion anchor displacements to 0.035 in. while being subjected to regulated sustained external tensile loads for 48 hr, and (c) applying specified installation torque values to all mechanical expansion anchors during installation.

The standard test method for determining creep, California Test 681, provides a satisfactory method for determining short-term creep (7).

General Conclusions

There was a wide variation in performance of the mechanical expansion anchors tested in this research and often inconsistent and erratic behavior was noted, even under the best conditions.

It is evident, after doing considerable static testing, that performance of mechanical expansion anchors cannot be determined easily without considering many different variables. The most important include soundness, age, and compressive strength of concrete, proper diameter of drilled holes, thorough cleaning of holes and use of proper installation techniques, and edge distance and spacing of anchors.

This research has demonstrated that minor differences in anchor dimensions and design can significantly affect anchor performance. It was found that just because one particular size of a certain anchor type and brand may pass a creep test, there is no assurance that similar anchors of the same type but a different size will perform satisfactorily.

The use of mechanical expansion anchors should be limited to minor, noncritical applications. Where long-term structural strength or dynamic loading of a cyclic nature are involved or where nonredundant anchor failure would probably lead to injuries, it is recommended that a more positive bonding system, such as resin capsule anchors, magnesium phosphate concrete, or other suitable noncorrosive grout systems, be considered. Also, it would seem prudent to maintain the current practice of limiting the size of mechanical expansion anchors

TABLE 6 CREEP TEST RESULTS OF STUD MECHANICAL EXPANSION ANCHORS

Manufacturer	Sustained Load Test Performance	Stud Anchor Types and Sizes					
		WEDGE			EXTERNAL PLUG		
		1/4-Inch Varies	1/2-Inch Varies	3/4-Inch @ 5000 lbs.	1/4-Inch @ 1000 lbs.	1/2-Inch @ 3400 lbs.	3/4-Inch @ 5000 lbs.
HILTI	Passed				N/A	N/A	N/A
	Did Not Pass*	Kwik-Bolt 5500004 @ 1000 lbs.	Kwik-Bolt 5500052* @ 3400 lbs.	Kwik-Bolt 5500096			
MOLLY	Passed		Parabolt PB 12-234 @ 3600 lbs.		N/A	N/A	N/A
	Did Not Pass*	Parabolt PB 14-134 @ 1500		Parabolt PB 34-434			
PHILLIPS	Passed	N/A				Stud JS-12C	
	Did Not Pass*		Wedge* WS 1226 @ 3400 lbs	Wedge WS 3446	Stud JS-14C		Stud JS-34C
RAMSET	Passed	N/A		Trubolt T34434	N/A	N/A	N/A
	Did Not Pass*		Trubolt* T12234 @ 3400 lbs.				
RAWLPLUG	Passed	Rawlstud 7400 @ 1000 lbs.		Rawlstud 7440	N/A	Set-Bolt 7145	Set-Bolt 7189
	Did Not Pass*		Rawlstud* 7420 @ 3400 lbs.				
STAR	Passed		Stud Bolt 3535-26000 @ 3400 lbs.	Stud Bolt 3555-42000		Star Stud 3835-26000	
	Did Not Pass*	Stud Bolt 3515-15000 @ 1000 lbs.			Star Stud 3815-16000		Star Stud 3855-42000

*   Many of the anchors were tested at sustained loads that were higher than those recommended in the revised specification. If retested at the lower recommended test loads, anchors may pass.

** Only two tests run; both passed.

*** N. A. - Anchor type not available.

to a maximum of ¾ in. as specified in Caltrans Bridge Construction Memo 135-5.0 (6), and using redundant anchor patterns if possible.

Self-drilling mechanical expansion anchors are not recommended for use. This recommendation is based on previous research observations in which damage to the drill teeth after installation (2) and cracking in hardened skirts in installed anchors after fatigue loading (5) were observed.

Further testing is recommended to determine whether allowable design loads typically used by Caltrans designers (not greater than 50 percent of the sustained tension test loads for static load conditions) are too conservative and whether long-term creep, which results at working load levels, will be acceptable.

Best Types of Mechanical Expansion Anchors

Of the various categories and types of mechanical expansion anchors tested, the two found to perform the best were the shell nondrilling internal plug and the stud wedge anchors.

A list of anchors that were tested under a sustained tensile load during this project and found to meet creep requirements of the revised specification is included in Tables 5 and 6. Some

of the ½-in.-diameter anchors tested did not meet a trial 3,400-lb test load used in this research. If retested at the lower 3,200-lb test load in the current specification, they may be found to be acceptable.

Corrosion Resistance

Standard mechanical expansion anchor parts, which are typically electroplated with zinc, are satisfactory for rust protection of steel only in mildly corrosive environments.

Sealing the drilled hole with a high-quality silicone sealant, after installing the mechanical expansion anchor, is an effective way to help protect the lower gripping portion of the anchor from corrosion.

It is recommended that when a corrosive environment is present and a design life of over 15 yr is desired, mechanical expansion anchors be made from a suitable grade of stainless steel. It may be necessary, however, to reduce the allowable design loads when such anchors are specified, because, in limited creep testing performed outside the scope of this project, it was found that the creep of certain galvanized and stainless steel mechanical expansion anchors was higher than that found with standard electroplated zinc fasteners. Further

work with special corrosion resistant anchor finishes and types was outside the scope of this project. It is recommended that special corrosion resistant anchors be tested before use and design loads adjusted accordingly.

Recommended Installation Techniques

It was concluded that the following installation rules are important:

• Use rotary impact drilling equipment with sharp carbide-tipped bits whose tip diameters meet dimensional tolerances in ANSI Specification B94.12-1977 or bit tolerances required by manufacturers. Drill equipment in good condition is required to produce round straight holes with minimal effort. Proper hole diameter ensures adequate, but not excessive, expansion of the heads on mechanical expansion anchors.

• Clean drilled holes thoroughly. Use oil-free compressed air or a vacuum cleaner to remove loose drill dust. For optimum results, brush hole sides to loosen drill dust and increase friction.

• Follow proper anchor setting techniques specified by manufacturer; this includes use of setting tools recommended by manufacturer. Set shell-type anchors, normally flush mounted, from ½ to 1 in. below the concrete surface to help determine if properly set (6).

• Use installation torque values specified by the manufacturer, if available, or those listed in the revised Section 75-1.03 of the January 1988 Caltrans *Standard Specifications*. Adequate installation torque (preload) was deemed to be important in removing short-term slip and reducing creep, especially in stud wedge-type anchors.

Shell external plug-type anchors can be inconvenient to install because during installation the external expander plug occasionally falls out of the hole in the bottom of the body while the anchors are being tapped into the drilled holes.

Few problems were experienced when installing stud anchors (wedge or external plug). One exception is with stud external plug anchors having bodies less than ½ in. in diameter. These can be easily bent if the top of the stud is hit too hard or at a slight angle while setting. Top threads of the stud can be damaged during setting by glancing or off-centered hammer blows if not protected by a nut.

REFERENCES

1. J. P. Dusel, Jr. and C. N. Harrington. *The Evaluation of Mechanical Expansion Anchors*. Report FHWA/CA/TL-86/09. Vol. I and II. California Department of Transportation, Office of Transportation Laboratory, Sacramento, July 1986.
2. W. H. Ames, E. F. Nordlin, and E. R. Post. *Evaluation of Concrete Anchor Bolts*. Research Report 19601-762500-36390. California Department of Public Works, Division of Highways, Materials and Research Department, Sacramento, June 1968.
3. G. L. Clark. *Installation of Concrete Expansion Anchors at the Fast Flux Test Facility*. Westinghouse Hanford Company, Richland, Wash., 1981.
4. K. A. Beede and C. B. Scott. *Static and Dynamic Loading of ⅝-Inch Concrete Anchors*. Report 7745.10-72. Pacific Gas and Electric Company, Department of Engineering Research, San Francisco, Calif., Aug. 10, 1972.
5. M. S. Lin. *Drilled-In Expansion Bolts Under Static and Alternating Load*. Report BR-5853-C-4. Bechtel Power Corp., San Francisco, Calif., Jan. 1975.
6. *Mechanical Anchorage Devices: Bridge Construction Memo 135-5.0*. California Department of Transportation, Office of Transportation Laboratory, Sacramento, Feb. 8, 1982.
7. *Method for Testing Creep Performance of Concrete Anchorage Devices: California Test 681*. California Department of Transportation, Office of Transportation Laboratory, Sacramento, March 1985.

Rational Design Approach for Integral Abutment Bridge Piles

ROBERT E. ABENDROTH AND LOWELL F. GREIMANN

The piles for an integral abutment bridge are subjected to horizontal movements caused by the expansion and contraction of the bridge superstructure. To design the abutment piles properly, a rational design approach was developed to simplify the complex behavior associated with pile and soil interaction. Fundamental principles for two pile design alternatives that were formulated in a recently completed research study involving experimental and analytical investigations are presented. Alternative 1 was based on elastic behavior and is recommended for piles with limited ductility, such as timber, concrete, and steel sections having insufficient moment-rotation capacity. Alternative 2 was based on inelastic behavior involving plastic redistribution of internal forces caused by the lateral displacement of the pile head and is recommended for piles with adequate moment-rotation capacity at plastic hinge locations. Steel piles do not have to be classified as compact sections to meet the moment-rotation requirement. A ductility criterion, expressed in terms of lateral pile head displacement, is given to evaluate whether the moment-rotation capacity of an HP-shaped pile exceeds the moment rotation demand. To illustrate both design alternatives, a design example for a steel, HP-shaped, friction pile is presented. For the specific example, Alternative 2 is shown to permit the safe design of integral abutment bridges that are substantially longer than those designed according to Alternative 1.

Jointless bridges do not contain traditional expansion joints between the abutments and the bridge superstructure. Instead, the bridge girders and the abutments are connected together forming rigid joints. The piles of the integral abutment are subjected to horizontal movement as the bridge superstructure expands and contracts as a result of seasonal temperature changes. The induced axial and bending stresses in the abutment piles limit the total bridge length. These bridge length limitations vary considerably from state to state because a consistent pile design philosophy has not been established by the state departments of transportation or AASHTO. Recently conducted surveys (1–4) have shown that integral abutment bridges have been designed with a variety of specialized details. To establish rational pile design criteria, an experimental and analytical study (5) was recently completed. This research involved one-tenth scale laboratory pile tests, full-scale field tests of piles, and finite element investigations using a previously developed analytical model (2, 6) that accounts for nonlinearity of both the soil and pile behavior. The design method summarized in this paper represents a refinement of a method, previously published by Greimann and Wolde-Tinsae (7), that incorporates the AASHTO Specification on beam-column design. Equivalent cantilevers replace the actual pile

Bridge Engineering Center, Town Engineering Building, Iowa State University, Ames, Iowa 50011.

for design purposes. The problem of pile ductility (inelastic hinge rotation capacity) associated with lateral pile head displacements was also not addressed in the Greimann and Wolde-Tinsae paper (7).

Two pile design alternatives are presented that address the following three AASHTO Specification design criteria:

- Capacity of the pile as a structural member (Case A);
- Capacity of the pile to transfer the load to the ground (Case B); and
- Capacity of the ground to support the load (Case C).

Alternative 1 is a conventional elastic design approach, whereas Alternative 2 is an inelastic design approach that recognizes redistribution principles, when adequate pile ductility exists. An example is presented for the design of an HP-shaped friction pile to illustrate both design alternatives.

PILES DESIGNED AS BEAM-COLUMNS (AASHTO CASE A)

Equivalent Cantilevers

A pile embedded in soil can be analytically modeled as an equivalent beam-column without transverse loads between the member ends and with a base fixed at a specific soil depth. Either a fixed head or pinned head for the beam-column approximates the actual rotational restraint at the pile head. Figure 1 shows an idealized fixed-headed pile for both an "actual" system and the corresponding equivalent cantilever system. The total length, L, of the equivalent cantilever equals the sum of the length, l_u, above the ground and the length, l_e, from the soil surface to the fixed base of the equivalent cantilever. The three equivalent cantilever lengths (8) considered in the development of the design alternatives were the horizontal stiffness of the soil and pile system, the maximum moment in the pile, and the elastic buckling load of the pile. The pile lengths l_e and l_u can be nondimensionalized by the length, l_c, that defines whether the pile behaves as a rigid or flexible pile (9). The length l_c is given as

$$l_c = 4\sqrt[4]{EI/k_h} \tag{1}$$

where E is the modulus of elasticity for the pile material, I is the moment of inertia of the pile with respect to the plane of bending, and k_h is the horizontal stiffness of the soil. Greimann, et al. (5) developed a nondimensionalized relationship between l_u and l_e for a fixed-headed pile (Figure 2) and for a pinned-headed pile in a uniform soil.
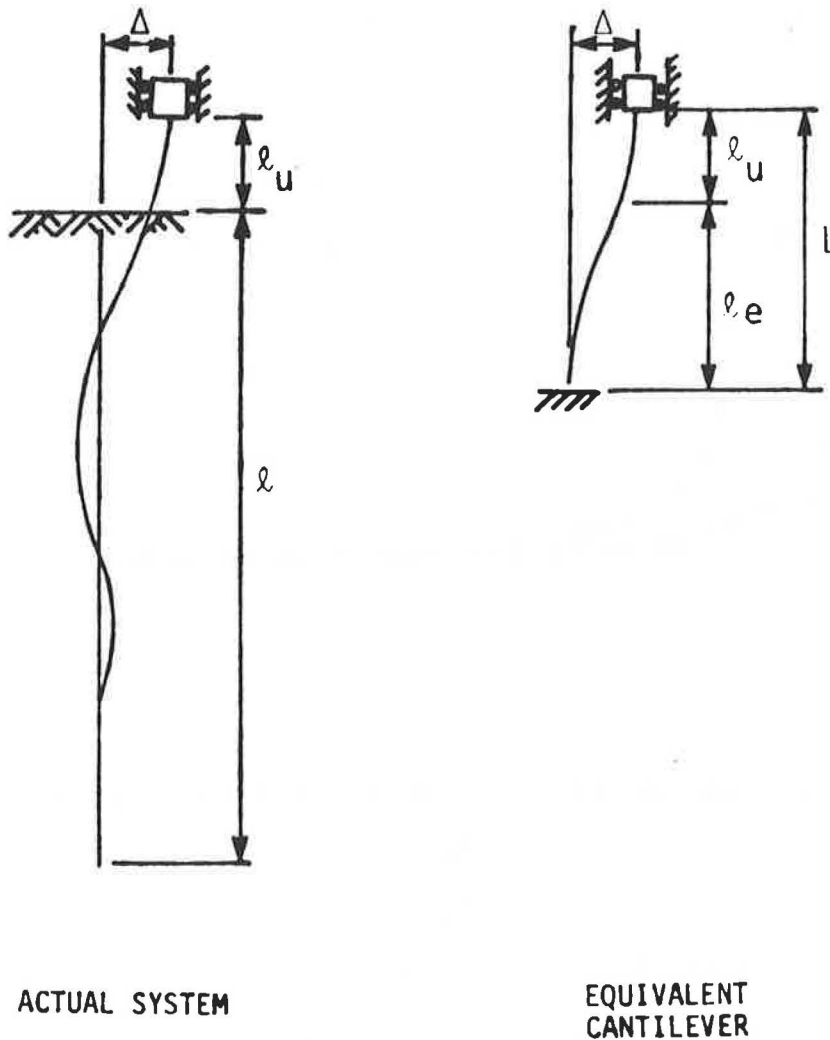
FIGURE 1   Cantilever idealization of a fixed-headed pile.

For nonuniform soil conditions, an equivalent uniform lateral soil stiffness parameter, k_e, is needed to evaluate the length l_c. Figure 3a shows the lateral stiffness, k_h, profile for a soil consisting of a sand overlaying a clay layer. The parameter k_{h1} represents the lateral stiffness of the sand at the depth l_1, whereas k_{h2} is the lateral stiffness of the clay soil. To establish k_e, the work done by the actual soil resistance (Figure 3a) in moving through the lateral soil displacement (Figure 3c) will be equated to the work done by the equivalent soil resistance (Figure 3b) in moving through the same soil displacement. Equating the external work expressions for both systems,

$$\int_o^{l_o} \frac{k_h(x)y^2}{2} \, dx = \int_o^{l_o} \frac{k_e \, y^2}{2} \, dx \tag{2}$$

where the length l_o, given by Equation 3, is the active length of the pile in bending, which is taken as one-quarter of the deflected wave shape.

$$l_o = l_c/2 \tag{3}$$

The displaced shape can be approximated by the straight line shown in Figure 3c, for which

$$y = \Delta_g \left(1 - \frac{x_1}{l_o}\right) \tag{4}$$

where Δ_g is the lateral displacement of the pile at the bottom of the abutment and x_1 is the depth below the abutment. Substituting Equation 4 into Equation 2 gives

$$k_e = \frac{3}{l_o^3} \int_o^{l_o} k_h(x) \, (l_o - x_1)^2 \, dx \tag{5}$$

The integral expression in Equation 5 is the second moment of the area of the $k_h(x)$ diagram (Figure 3a) taken about a line at the depth l_o. Because the length l_o is a function of k_e, an iterative procedure is needed to calculate k_e.

Design Alternatives 1 and 2

Design Alternative 1 is based on elastic pile behavior and neglects the potential reserve strength associated with plastic
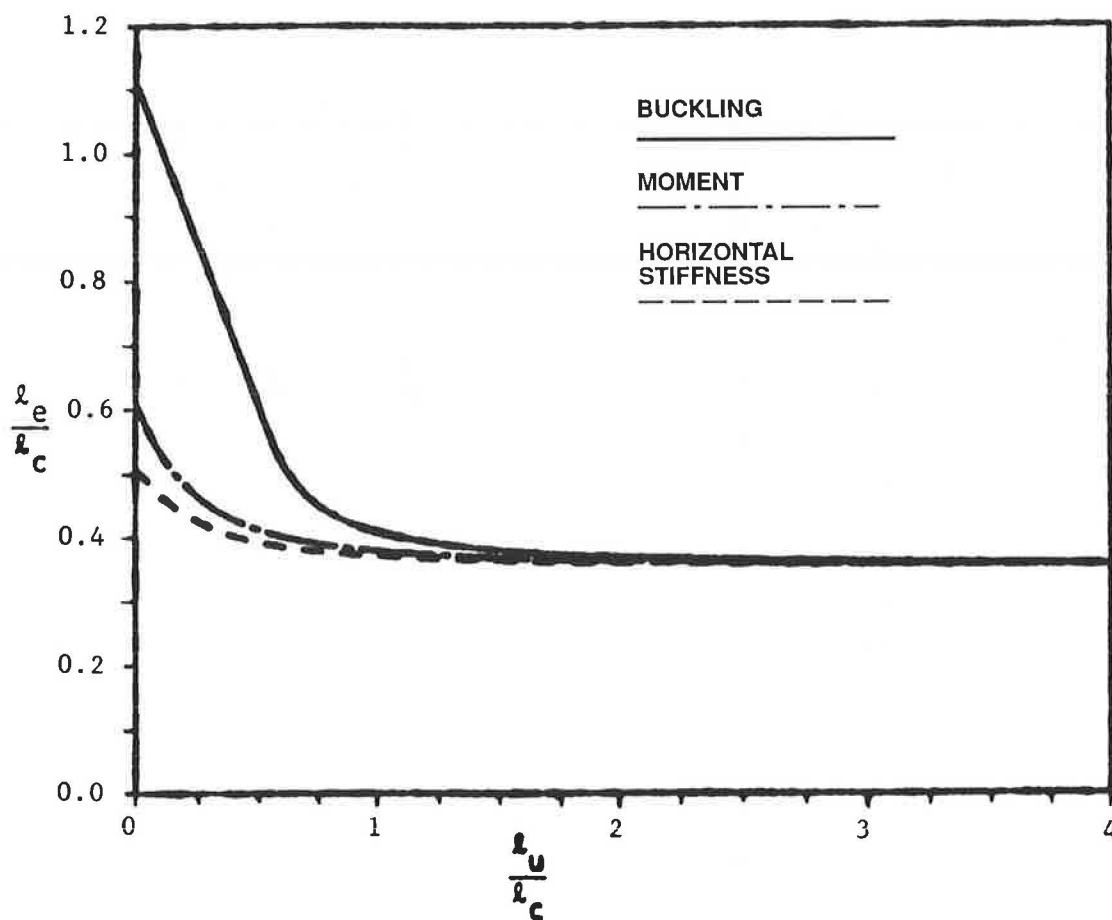
FIGURE 2 Equivalent cantilever for fixed-headed pile in a uniform soil.

hinge formations. Therefore, redistribution of internal forces is not permitted to occur for ultimate strength. This design method is a conventional elastic design procedure for the equivalent cantilever (beam-column) that considers all stresses developed in the pile. The lateral displacement, Δ, at the pile head, caused by expansion and contraction of the bridge superstructure, induces a first-order elastic end moment, M, given by

$$M = \frac{D_1 EI\Delta}{L^2} \tag{6}$$

where the bending moment coefficient D_1 equals 6 or 3 for fixed-headed or pinned-headed piles, respectively. This moment can be anticipated to dramatically affect the pile capacity.

Design Alternative 2 accounts for the redistribution of forces associated with plastic hinge formations in the pile as a result of lateral displacement of the pile head. The stresses induced by the horizontal pile head movement are considered not to significantly affect the pile ultimate strength, as long as the corresponding strains can be accommodated through adequate pile ductility. Neglecting these thermally induced pile stresses is justified by first-order plastic theory involving small displacements. According to this theory, the plastic collapse load is not affected by residual stresses, thermal stresses, imperfect fit, or, in this case, support movement (10,11), as long as local and lateral buckling are prevented.

For Alternative 2, the axial pile load, P, produces a second-order bending moment as a result of the lateral displacement at the pile head. A conservative upper bound on this induced end moment is

$$M = D_2 P\Delta \tag{7}$$

where the bending moment coefficient D_2 equals one-half or unity for fixed-headed or pinned-headed piles, respectively.

During the development of the design alternatives, comparisons were made of ultimate strength predicted by both alternatives and the experimentally verified finite element solution (5). Local and lateral buckling were not considered, because the finite element analysis did not model this type of behavior. For an HP 10 x 42 pile, the results showed that both design alternatives were conservative, considering practical ranges of sand density, clay stiffness, and column slenderness. Alternative 1 was excessively conservative for small slenderness ratios where yielding controls over stability. The design alternatives and the finite element model predicted a decrease in the ultimate pile capacity with increasing horizontal head movement.

Ductility Conditions

Both design alternatives must satisfy local buckling criteria that are not as stringent as those given in Article 10.48.1 of
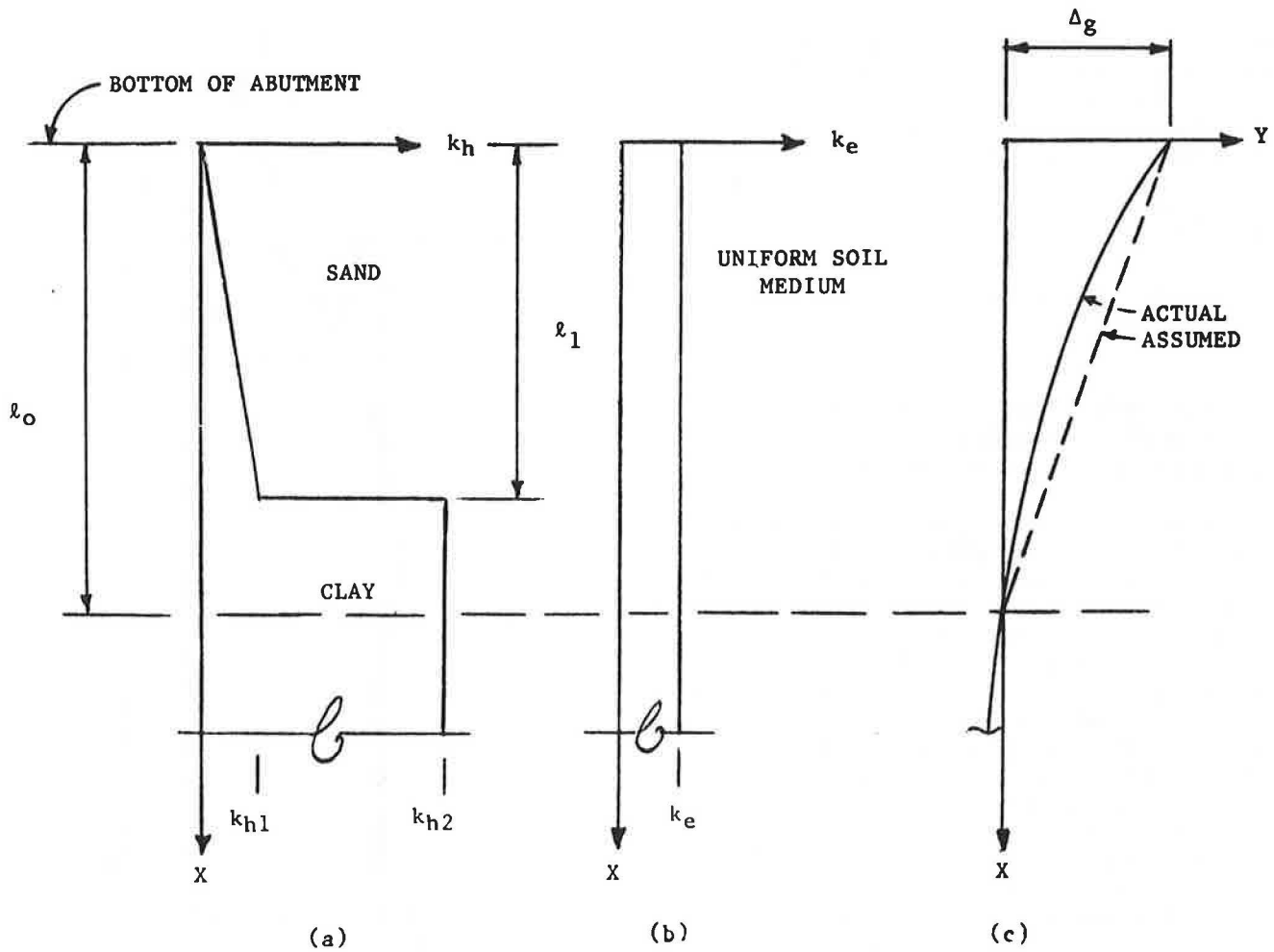
FIGURE 3 Horizontal soil stiffness and displacement: (*a*) actual soil, (*b*) equivalent soil, and (*c*) displaced shape.

the AASHTO Specification. For Alternative 1, the width-to-thickness ratios of the cross-sectional elements must be limited to prevent local buckling before the yield moment is obtained. Applying Article 1.9 of the American Institute of Steel Construction (AISC) Specification (*12*), the standard rolled HP shapes satisfy these width-thickness criteria; therefore, local buckling will not govern the pile capacity for this design alternative.

Alternative 2 requires additional ductility beyond that needed for Alternative 1 in order to develop the inelastic rotation capacity associated with plastic hinge formations. To provide the necessary inelastic rotation capacity, the flange width-to-thickness ratio must be limited to prevent local buckling for the total range of horizontal pile head movement. Based on studies of moment-rotation relationships for strong-axis bending of I-shapes (*13–16*) Greimann et al. (*5*) developed the following ductility criterion that requires that the moment-rotation demand does not exceed the moment-rotation capacity.

$$2\left[\frac{\Delta}{L} - \frac{M_p L}{6EI}\right] + \theta_w \leq \frac{3 C_i M_p L}{4EI} \tag{8}$$

where M_p is the plastic moment capacity of the pile, θ_w is the

pile head rotation caused by the bridge girder end rotation induced by gravity loads applied after the girder and abutment become monolithic, and C_i is an inelastic rotation capacity reduction factor, based on the flange width-to-thickness ratio. The expression for C_i is

$$C_i = \frac{19}{6} - \frac{b_f \sqrt{F_y}}{60 \, t_f} \tag{9}$$

where b_f and t_f are the flange width and thickness, respectively, and F_y is the yield strength. An upper bound of unity for C_i applies when $b_f/2t_f \leq 65/\sqrt{F_y}$, and a lower bound of zero governs when $b_f/2t_f \geq 95/\sqrt{F_y}$. These limits correspond to an inelastic rotation capacity of 3 and 0 (*17*), respectively. Incorporating a factor of safety equal to F_y/F_b, the ductility criterion (Equation 8), rewritten in terms of the lateral displacement of the pile head, is

$$\Delta \leq \Delta_i \tag{10}$$

with

$$\Delta_i = \Delta_b \, (D_3 + 2.25 \, C_i) \tag{11}$$

where Δ_i is the allowable displacement capacity of the pile head, D_3 is a ductility coefficient equal to 0.6 or 1.0 for fixed-headed or pinned-headed piles, respectively, and Δ_b is the horizontal movement of the pile head when the actual extreme fiber bending stress equals the allowable bending stress, F_b. The displacement Δ_b is given as

$$\Delta_b = \frac{F_b S L^2}{D_1 E I} \tag{12}$$

where S is the section modulus of the pile with respect to the plane of bending.

LATERAL DISPLACEMENT EFFECTS ON VERTICAL LOAD TRANSFER AND SOIL STRENGTH (AASHTO CASES B AND C)

Lateral displacement of the pile, shown in Figure 4, can affect the capacity of the pile to transfer load to the ground (Case B) through vertical friction along the embedment length, l, but should not affect the end bearing resistance of flexible piles ($l \geq l_c$), nor the capacity of the ground to support the load (Case C). Fleming, et al. (18) have suggested that the displacement y_{max}, representing the maximum lateral displacement below which the frictional resistance is assumed to be unaffected by the movement, be established as 2 percent of the pile diameter. The lengths l_n and l' are the lengths along the pile for which the vertical frictional resistance is assumed to be nonexistent and fully effective, respectively. The effect of the pile length, l_u, above the ground on the length l_n is shown in the nondimensionalized graph of Figure 5 for fixed-headed piles embedded in a uniform soil (or equivalent uniform soil medium). A similar figure has been developed for pinned-headed piles (5).

FRICTION PILE DESIGN EXAMPLE

To illustrate the design procedure for both Alternatives 1 and 2, a friction pile will be designed to support a vertical load, P_w, equal to 50 kips, involving dead plus live plus impact loads ($D + L + I$), for the conditions shown in Figure 6. The pile is an HP 10 × 42 with a yield strength, F_y, of 36 ksi. The abutment is supported by eight piles, as shown in Figure 7. The piles were driven in an 8-ft-deep, 2-ft-diameter, predrilled hole that is filled with loose sand. The existing soil consists of an initial 12 ft of stiff clay underlain by very stiff clay. The integral abutment bridge has seven lines of AASHTO Type III bridge girders and five spans having a total length of 360 ft. The end spans are 60 ft long.

SOLUTION

Preliminary Design

The estimated allowable frictional resistance for each steel pile will be taken as 0.8 tons per ft and 1.2 tons per ft for the stiff and very stiff clay, respectively. These values correspond to "firm silty clay" and "firm-very firm glacial clay" in the Iowa Department of Transportation (Iowa DOT) Foundation Soil Information Chart, revised June 1976. Assuming that the
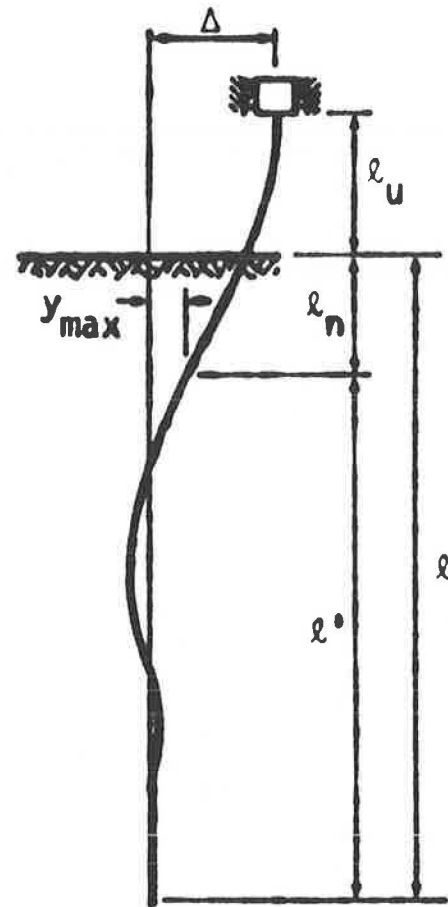
FIGURE 4 Soil-pile system for determining the friction capacity of the pile.

capacity of the pile to transfer the load to the ground (Case B) and AASHTO Group I loading controls and neglecting the sand in the predrilled hole, the length of the embedment, l_2, into the very stiff clay is

$$l_2 = \frac{(0.5)(50) - (0.8)(8)}{1.2} = 16 \text{ ft} \tag{13}$$

Equivalent Uniform Soil Stiffness

The lateral soil stiffness, k_h, for the soil in the predrilled hole is not as flexible as a loose sand because the predrilled hole has only a 2-ft diameter and the zone of influence of the pile is approximately six pile diameters or about 5 ft. Therefore, the stiffness will be assumed to correspond to that for loose-to-medium-dense sand. For loose-and-medium-dense sands, the values of k_h, obtained from Table 1 (5, excerpt from Table 2.5), are $8.0x$ and $27.0x$ ksf, respectively, where x is the depth in feet at which k_h is evaluated. For a loose-to-medium sand, k_h will be assumed to be equal to $17.5x$ ksf. The lateral stiffness of the soil below the predrilled hole corresponds to that for a stiff clay, for which k_h equals the smaller value of 580 or $(190 + 41x)$ ksf, obtained from Table 1 (5, excerpt from Table 2.4). For the sand in the predrilled hole and the stiff clay layer, Figure 3a shows the variation in k_h with depth, when
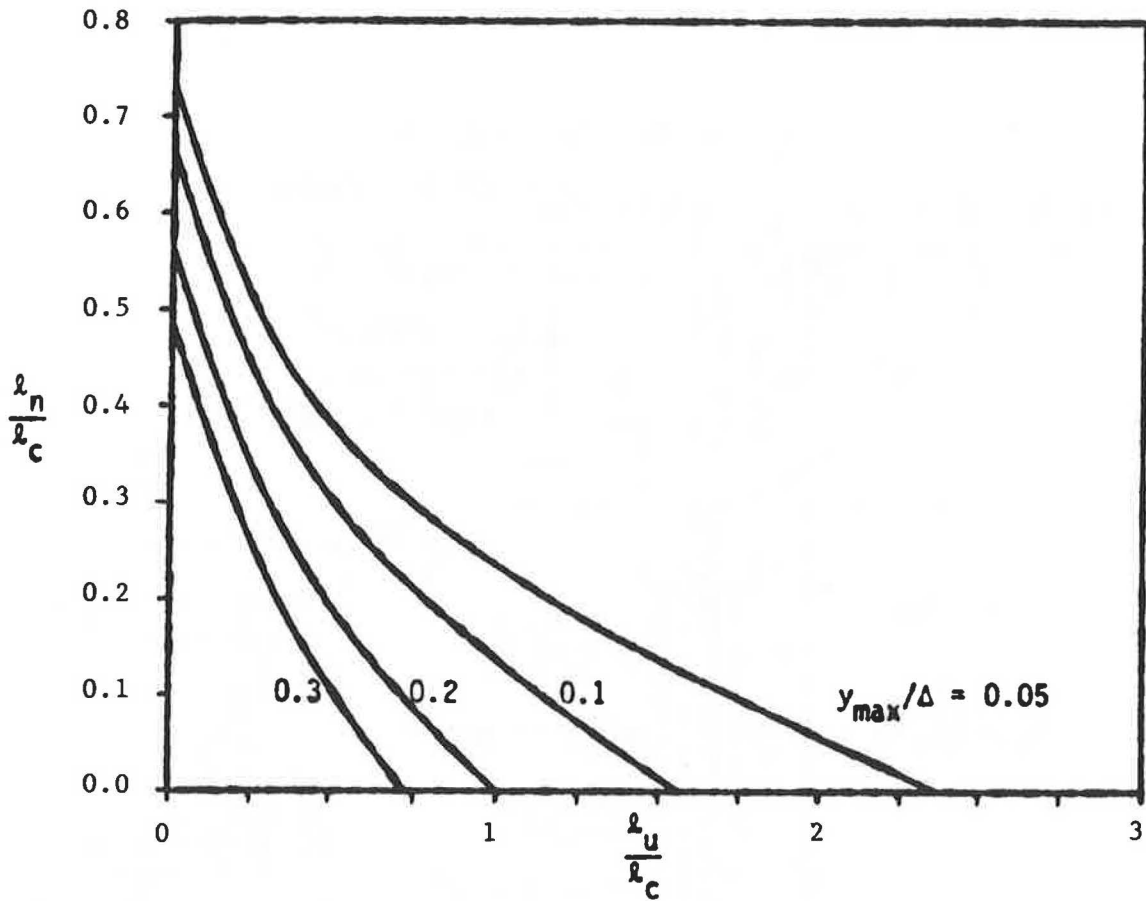
FIGURE 5 Displacement for a fixed-headed pile embedded in a uniform soil.

k_{h1} and k_{h2} equal 140 and 580 ksf, respectively, and l_1 equals 8 ft. The solution for the equivalent uniform soil stiffness, k_e, (Figure 3b) converged to 38.8 ksf after two iterations involving Equations 1 through 5. Using k_e as the lateral soil stiffness, k_h, in Equation 1, the length parameter l_c is

$$l_c = 4\sqrt[4]{\frac{2.08 \times 10^6}{(38.8)\,(144)}} = 17.6 \text{ ft} \qquad (14)$$

Equivalent Cantilever Lengths

Assuming the pile head is fixed against rotation (verified later) and taking l_u/l_c equal to 0, the equivalent embedment lengths, l_e, for stiffness, moment, and buckling, obtained from Figure 2, are

$$l_e = 0.5\, l_c = 0.5\ (17.6)$$
$$= 8.8 \text{ ft} \quad \text{stiffness}$$
$$l_e = 0.6\, l_c = 0.6\ (17.6) \qquad (15)$$
$$= 10.6 \text{ ft} \quad \text{moment}$$
$$l_e = 1.1\, l_c = 1.1\ (17.6)$$
$$= 19.4 \text{ ft} \quad \text{buckling}$$

Because l_u equals 0, the total equivalent cantilever length, L, equals l_e. Now, if the loose sand in the predrilled hole is completely neglected, the critical length, l_c, is 8.9 ft, based on the soil stiffness in the stiff clay of 580 ksf. From Figure 2, with l_u/l_c equal to 8 ft/8.9 ft or 0.9, the equivalent embedded length, l_e, of 3.6 ft is about the same for stiffness, moment, and buckling. The total equivalent cantilever length, L (equal to l_u plus l_e), would become 11.6 ft. The equivalent cantilever for the pile in loose sand should not be reasonably longer than this value. Therefore, the following total equivalent lengths will be used for design:

$$L = 8.8 \text{ ft or } 106 \text{ in.} \quad \text{stiffness}$$
$$L = 10.6 \text{ ft or } 127 \text{ in.} \quad \text{moment} \qquad (16)$$
$$L = 11.6 \text{ ft or } 139 \text{ in.} \quad \text{buckling}$$

Structural Analysis of Bridge Pile Soil System for Gravity Loads

For simplicity, an approximate structural analysis will be presented to obtain the gravity load moment in the pile for this example. An idealized structural model is shown in Figure 8. Because the composite bending stiffness of the seven girders is at least 100 times the bending stiffness of the eight piles and because the girder continuity at the first pier can be

TEMPORARY PAVING BLOCK

TOP OF ROADWAY SLAB

GRANULAR BACKFILL

$\mathfrak{C}$ ABUT.

A

AASHTO TYPE III
PRESTRESSED BEAM

$I_c = 125390$ in^4

$f'_c = 5000$ psi

$E = 150^{1.5} \times 33\sqrt{5000} = 4290$ ksi

A

8± 4"

BERM

82.5"

7.5

BERM FILL

4'

PREDRILLED
OVERSIZE HOLE
FILLED WITH LOOSE SAND

EXISTING
GROUND LINE

SECTION A-A
COMPOSITE SECTION
I = 352932 in 4

$EI = 1.51 \times 10^9$ k-in^2

4'

STIFF CLAY

STEEL PILE
HP10x42

8'

$I_y = 71.7$ in^4

$S_y = 14.2$ in^3

$r_y = 2.41$ in

$A = 12.4$ in^2

$t_f = 0.42$ in

$b_f = 10.075$ in

B   B $t_w = 0.415$ in

SECTION B-B

$d = 9.70$ in

$k = 1.06$ in

$EI = 2.08 \times 10^6$ k-in^2

ℓ_2
16'

VERY STIFF CLAY

FIGURE 6   Section through abutment and soil profile.
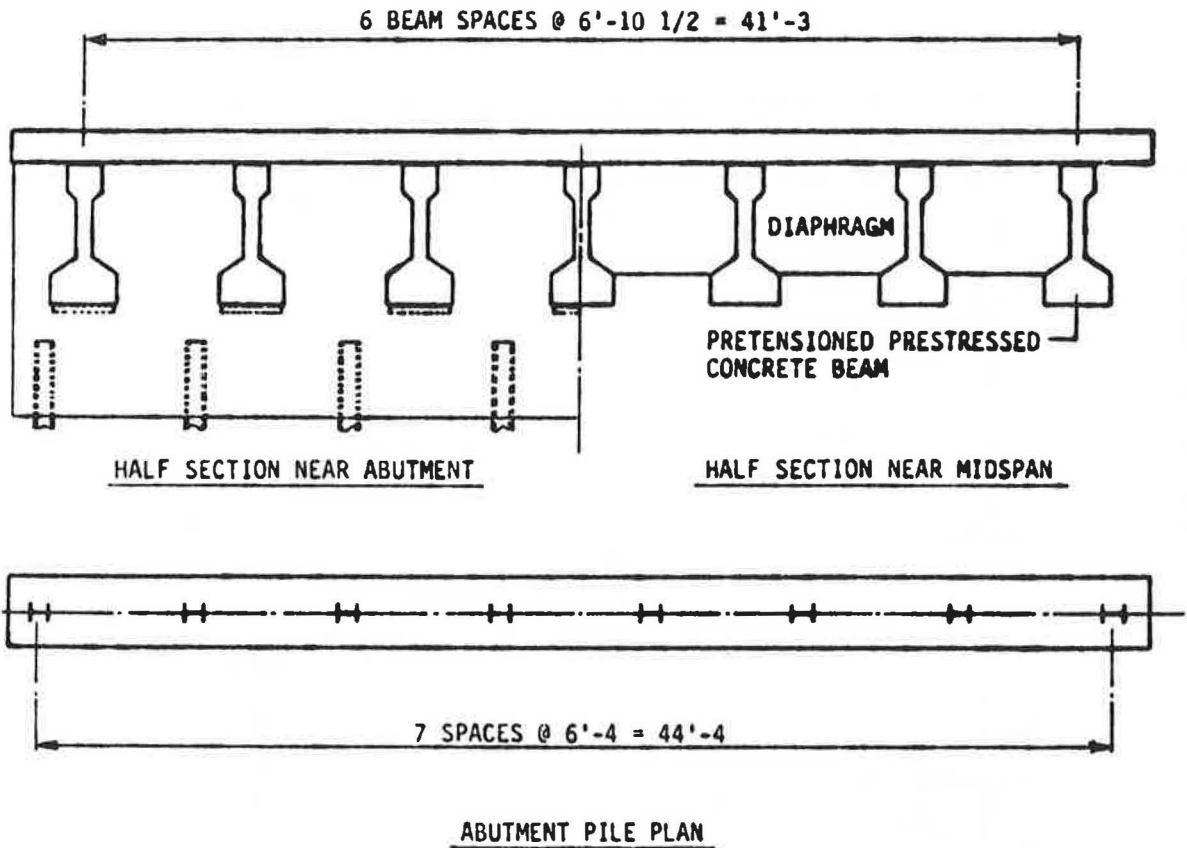
FIGURE 7 Transverse section through bridge and abutment plan.

TABLE 1 LATERAL SOIL STIFFNESS PARAMETER k_h

	k_h (ksf)
Sand	
Loose	$8x$
Medium	$27x$
Dense	$72x$
Clay	
Soft	$(24 + 5.8x) \leq 72$
Stiff	$(190 + 41x) \leq 580$
Very stiff	$(750 + 610x) \leq 2,200$

conservatively neglected when the joint rotation at the abutment is being considered, the totals of the uniformly distributed girder load, W, and the corresponding end rotation, θ_w, for the 50-kip pile load $(D + L + I)$ are

$$W = \frac{8 \, (50)2}{7} = 114 \text{ kips} \qquad (17)$$

$$\theta_w = \frac{WL_g^2}{24 \, E_g I_g} = \frac{(114)(60)^2(12)^2}{24(4290)(352,932)} = 0.00163 \text{ rad} \qquad (18)$$

where L_g, E_g, and I_g represent the length, modulus of elasticity, and moment of inertia, respectively, for an end span bridge girder. Since the top of the pile is rigidly connected to the integral abutment, the pile head will rotate by θ_w. This amount of rotation is an upper bound because the girder and

abutment are not monolithic for the total load. Therefore, an upper bound on the induced elastic moment, M_w, in the equivalent cantilever as a result of vertical load is

$$M_w = \left[\frac{4 \, EI}{L}\right] \theta_w$$

$$= \left[\frac{4(29000)(71.7)}{(10.6) \, (12)}\right] (0.00163) = 107 \text{ k-in.} \qquad (19)$$

where the equivalent cantilever length, L, for moment (Equation 16) was used.

Structural Analysis for Thermal Expansion

Again, an approximate analysis will be presented for simplicity. The horizontal displacement, Δ, at each abutment, neglecting lateral pier stiffnesses and passive soil pressure against the abutment backwalls, is given by

$$\Delta = 1/2 \; \alpha \; \Delta T_{\text{ave}} \; L_b \qquad (20)$$

where the bridge length, L_b, equals 360 ft and the coefficient of thermal expansion, α, for the concrete superstructure equals 0.000006/°F. Assuming that the bridge is constructed in the middle of an 80°F temperature range, the horizontal displacement at each abutment evaluated from Equation 20 is

$$\Delta = 1/2 \; (0.000006)(40)(360)(12) = 0.52 \text{ in.} \qquad (21)$$
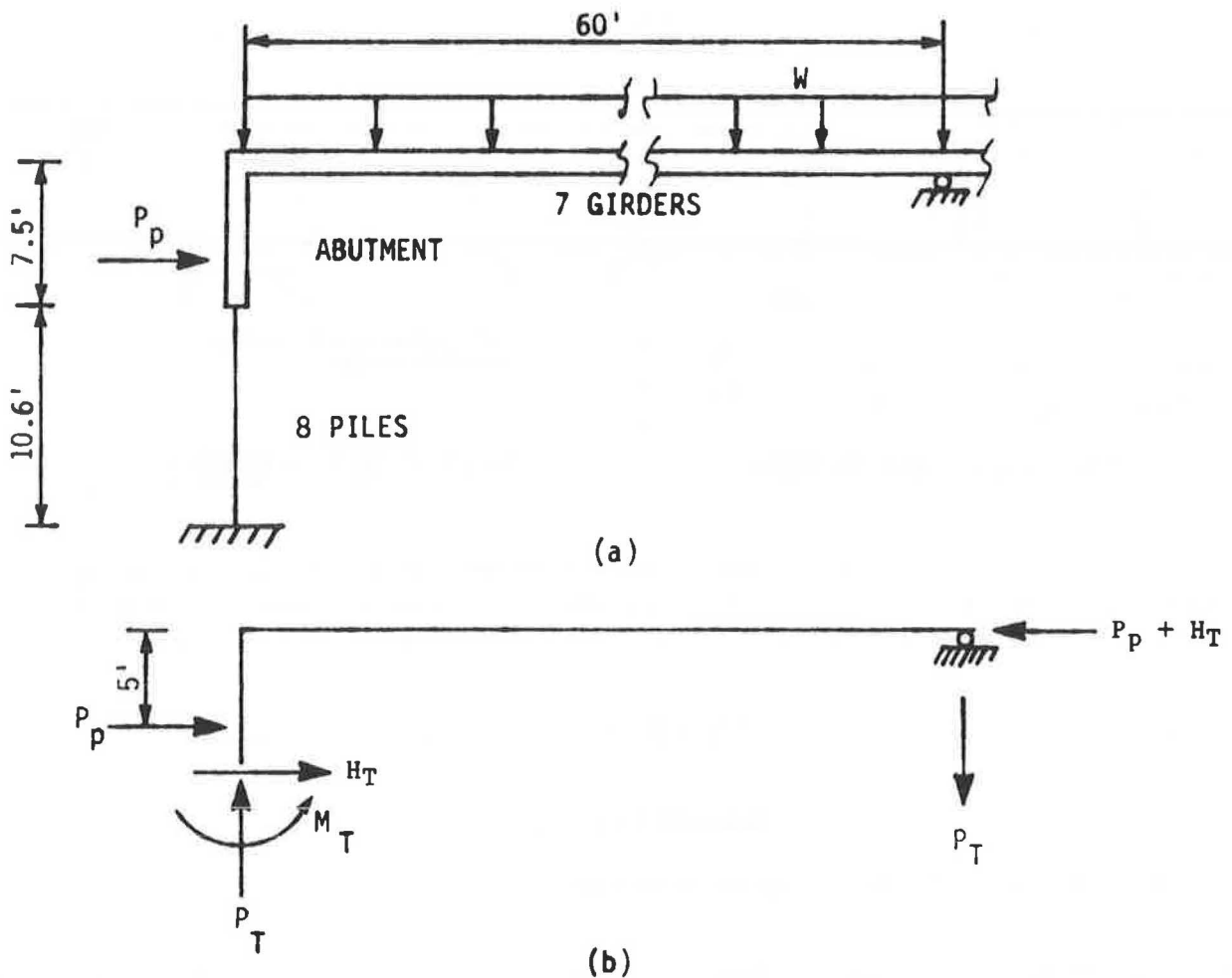
FIGURE 8   Idealized abutment foundation and girder end span: (a) structural model and (b) free body diagram.

The pile moment, M_T, (Equation 6) and corresponding horizontal force, H_T, induced by this lateral displacement are

$$M_T = \frac{6EI\Delta}{L^2} = \frac{6(29000)(71.7)(0.52)}{(127)^2} = 402 \text{ k-in.} \quad (22)$$

$$H_T = \frac{12EI\Delta}{L^3} = \frac{12(29000)(71.7)(0.52)}{(106)^3} = 10.9 \text{ kips} \quad (23)$$

where the respective equivalent cantilever lengths for the moment and the horizontal stiffness (Equation 16) have been used. (Note that M_T cannot exceed 785 k-in., which is the plastic moment capacity of the pile, and H_T cannot exceed 14.8 kips, which is the shear force associated with a plastic mechanism when L equals 106 in.)

A horizontal force on the back side of the abutment occurs as the bridge expands. This force can be estimated conservatively as the passive resistance of the soil behind the abutment, P_p. Using an elementary soil model for a granular backfill material (19),

$$P_p = \frac{1}{2} \gamma h^2 \left[\frac{1 + \sin \phi}{1 - \sin \phi} \right] \quad (24)$$

where γ is the unit soil weight, h is the abutment height, and

ϕ is the soil friction angle. Assuming that the granular backfill weighs 130 pcf and has an angle of internal friction equal to 35 degrees, the passive soil pressure along an abutment length equal to the pile spacing of 6.33 ft is

$$P_p = \frac{1}{2} (130)(7.5)^2 \left[\frac{1 + \sin 35°}{1 - \sin 35°} \right] (6.33)$$
$$= 85.4 \text{ kips} \quad (25)$$

Considering equilibrium of a simply supported girder end span shown in Figure 8b, thermal expansion of the superstructure induces an axial force in the pile, P_T, given by

$$P_T = \frac{P_P(5.0) + H_T(7.5) + M_T}{60} \quad (26)$$

Substituting values for M_T, H_T, and P_P from Equations 22, 23, and 25, respectively, into Equation 26, the thermally induced axial compression force in the pile is 9.04 kips.

Allowable Axial Stresses

Even though horizontal movement at the top of the abutment pile was caused by the expansion or contraction of the bridge

superstructure, further lateral displacement at the pile head induced by gravity loads is prevented. Therefore, the top of the equivalent cantilever is considered braced against the sidesway. At the head of the equivalent cantilever, the ratio, G, of the flexural stiffness ($4EI/L$) for the eight piles to the flexural stiffness ($3E_g I_g/L_g$) for the seven bridge girders is

$$G = \frac{4[(2.08 \times 10^6)/127](8)}{3[(1.51 \times 10^9)/720](7)} = 0.012 \qquad (27)$$

where the length of the equivalent cantilever length, L, for moment (Equation 16) was used. Because the base of the equivalent cantilever is theoretically fixed by definition ($G = 0$), the equivalent cantilever is essentially fixed at both ends, resulting in an effective length factor, K, equal to 0.5. The value of K is increased to 0.65 for design (AASHTO Specification, Table C-1). (Note that the assumption of a fixed-headed pile used in determining l_e and used in the approximate structural analyses was valid.)

The allowable axial stress, F_a, is based on the following governing slenderness ratio:

$$\frac{KL}{r_y} = \frac{(0.65)(139)}{2.41} = 37.5 \qquad (28)$$

where the equivalent cantilever length, L, for buckling (Equation 16) was used. Now, following AASHTO Specification, Table 10.32.1A, C_c, the slenderness ratio at the transition point between inelastic and elastic buckling, equals 126.1, which is greater than the governing slenderness ratio of 37.5; therefore, the allowable axial stress is

$$F_a = \frac{36}{2.12} \left[1 - \frac{(37.5)^2(36)}{4\pi^2(29000)} \right] 1.25 = 20.3 \text{ ksi} \qquad (29)$$

where the 1.25 factor represents the allowable stress increase for AASHTO Group IV loading obtained from the AASHTO Specification, Table 3.22.1A. The elastic buckling stress, $F_{e'}$, with respect to the plane of bending, including a factor of safety (AASHTO Specification, Equation 10-43) and an allowable stress increase for Group IV loading, is

$$F_{e'} = \frac{\pi^2(29000)(1.25)}{(37.5)^2(2.12)} = 120.0 \text{ ksi} \qquad (30)$$

Allowable Bending Stress

Table 10.32.1A of the AASHTO Specification lists an allowable bending stress of $0.55 F_y$. No mention is made specifically of weak axis bending or local buckling of the flange. Applying the flange width-to-thickness design criteria in the AISC Allowable Stress Design Specification (12), Article 1.5.1.4.1, modified by the ratio of the maximum permissible strong-axis bending stresses in the AASHTO and AISC Specifications ($0.55 F_y/0.66 F_y$), the following allowable weak-axis bending stresses, F_b, were developed:

$$F_b = \left[\frac{0.55}{0.66} \right] (0.75 F_y) = 0.625 F_y \qquad (31)$$

where

$$\frac{b_f}{2t_f} \le \frac{65}{\sqrt{F_y}}$$

and, by AISC Specification, Equation 1.5–5b,

$$F_b = F_y \left[0.896 - 0.0042 \frac{b_f}{2t_f} \sqrt{F_y} \right] \qquad (32)$$

where

$$\frac{65}{\sqrt{F_y}} \le \frac{b_f}{2t_f} \le \frac{95}{\sqrt{F_y}}$$

(Note that rather than using Equation 31 for the allowable bending stress, a conservative interpretation of the AASHTO Specification would be to use F_b equal to $0.55 F_y$ for both strong- and weak-axis bending. However, when local buckling governs the allowable bending stress, using $0.55 F_y$ for F_b instead of Equation 32 can be unconservative, depending on the magnitude of the width-thickness ratio.) Comparing the flange width-to-thickness proportions for an HP 10 × 42 pile ($F_y = 36$ ksi) with the two limits,

$$\frac{65}{\sqrt{F_y}} = 10.83 < \frac{b_f}{2t_f} = \frac{10.075}{2(0.420)}$$

$$= 12.0 < \frac{95}{\sqrt{F_y}} = 15.8 \qquad (33)$$

reveals that the HP 10 × 42 shape is "partially compact" with respect to the flange (12). Applying Equation 32 and including the allowable stress increase permitted for AASHTO Group IV loading, the allowable bending stress is

$$F_b = 36 [0.896 - 0.0042(12.0)\sqrt{36}](1.25)$$

$$= 26.7 \text{ ksi} \qquad (34)$$

(Note that lateral bracing is not required, because bending occurs about the weak axis (12), Commentary Article 1.5.1.4).

Applied Axial Stress

The axial stress, f_a, at the pile head for both Alternatives 1 and 2, resulting from the axial forces from the vertical load and thermal expansion (Equation 26), is

$$f_a = \frac{P_w + P_T}{A} = \frac{50 + 9.04}{12.4} = 4.76 \text{ ksi} \qquad (35)$$

Alternative 1 Applied Bending Stress

The extreme fiber flexural stress, f_b, at the pile head for Alternative 1, resulting from the moments due to vertical load (Equation 19) and thermal expansion (Equation 22), is

$$f_b = \frac{M_w + M_T}{S} = \frac{107 + 402}{14.2}$$

$$= 35.8 \text{ ksi} < F_y = 36 \text{ ksi} \qquad (36)$$

Alternative 1 Stability and Strength Interaction Criteria

For the equivalent fixed-ended beam-column, the moment gradient factor, C_m, equals 0.40. However, because the real pile is subjected to transverse loads (soil pressures), C_m can be conservatively taken as 0.85 (12, Commentary Article 1.6.1). Substituting the appropriate terms into AASHTO Equations 10-41 and 10-42, including the 25 percent allowable axial stress increase for Group IV loading,

$$\frac{4.76}{20.3} + \frac{0.85(35.8)}{[1 - (4.76/120.0)](26.7)} = 1.42 > 1 \tag{37}$$

$$\frac{4.76}{0.472(36)(1.25)} + \frac{35.8}{26.7} = 1.546 > 1 \tag{38}$$

As expected, stability and strength are not adequate, because f_b is greater than F_b. Therefore, according to Alternative 1, HP 10 × 42 piles cannot be used to support the integral abutment for this bridge example.

Alternative 2 Applied Bending Stress

The moment at the pile head for Alternative 2 is due to vertical load only (Equation 19 plus Equation 7), because Alternative 2 allows for redistribution of forces through inelastic rotation. Therefore, the stresses induced in the pile by the horizontal motion of the pile head are neglected. The moment, M, and corresponding extreme fiber flexural stress, f_b, at the pile head are

$$M = M_w + \frac{P\Delta}{2} = 107 + \frac{(59)(0.52)}{2} = 122 \text{ k-in.} \tag{39}$$

$$f_b = \frac{M}{S} = \frac{122}{14.2} = 8.59 \text{ ksi} \tag{40}$$

Alternative 2 Stability and Strength Interaction Criteria

The stability and strength conditions (AASHTO Equations 10-41 and 10-42) for Alternative 2 are

$$\frac{4.76}{20.3} + \frac{0.85(8.59)}{[1 - (4.76/120.0)](26.7)} = 0.52 < 1 \tag{41}$$

$$\frac{4.76}{0.472(36)(1.25)} + \frac{8.59}{26.7} = 0.55 < 1 \tag{42}$$

Therefore, both stability and strength are adequate for this design alternative.

Alternative 2 Ductility Criterion

Alternative 2 requires sufficient plastic hinge rotation capacity of the pile. For the HP 10 × 42 equivalent cantilever in this example, the inelastic rotation capacity reduction factor given by Equation 9 and the lateral displacement Δ_b, corresponding

to the allowable bending stress (Equation 12), are

$$C_i = \frac{19}{6} - \frac{10.075\sqrt{36}}{60(0.420)} = 0.77 \tag{43}$$

$$\Delta_b = \frac{(26.7)(14.2)^3(127)^2}{6(2.08 \times 10^6)} = 0.49 \text{ in.} \tag{44}$$

Substituting the values for C_i and Δ_b into Equation 11, the allowable horizontal displacement capacity, Δ_i, of the pile head is

$$\Delta_i = 0.49 [0.6 + 2.25 (0.77)] = 1.14 \text{ in.} \tag{45}$$

Because the lateral displacement demand, Δ, of the pile head resulting from thermal expansion (Equation 21) is only 0.52 in., the HP 10 × 42 pile has more than sufficient ductility for this example.

Induced Girder Forces

The lateral displacement of the fixed-headed abutment piling will induce an additional axial force, P_g, shear force, V_g, and bending moment, M_g, into the bridge girders (Figure 8b). These forces are reversible, based on the direction of lateral displacement, and must be considered in the girder design and in the design of the connection between each girder and the abutment. For the simplified example presented, the forces P_g, V_g, and M_g, obtained from Equations 19, 22, 23, 25, and 26, are equal to 110 kips, 10.3 kips, and 582 k-in., respectively, for both Alternatives 1 and 2.

Case B Capacity

The effect of the horizontal displacement on the capacity of the pile to transfer the load to the ground (Case B) must be checked. For the HP 10 × 42 pile, the maximum lateral displacement, y_{max}, below which the frictional capacity is unaffected, is approximately 0.2 in. (2 percent of the 10-in. pile dimension in the direction of the applied load). Therefore, the ratio of y_{max} to Δ is

$$\frac{y_{max}}{\Delta} = \frac{0.2}{0.52} = 0.38 \tag{46}$$

From Figure 5 with l_u/l_c equal to 0, the length of frictional resistance to deduct is about

$$l_n = 0.45 \, l_c = 0.45(17.6) = 7.9 \text{ ft} \tag{47}$$

Because 8 ft of frictional resistance within the predrilled hole has already been neglected, an additional deduction is not necessary, resulting in an allowable vertical capacity, P, of the pile for Load Group IV of

$$P = [(0.8)(8) + (1.2)(16)]1.25 = 32 \text{ tons} \tag{48}$$

which is greater than the applied load of 59 kips. Therefore, the pile length established from the preliminary design (Equation 13) is adequate for Case B. [Note that Case B was not con-

trolled by the thermal movement of the abutment (Load Group IV) but was controlled by the gravity load (Load Group I)].

Case C Capacity

The horizontal displacement of the pile head does not affect the capacity of the soil to support the load (Case C). Because the spacing of the piles (6 ft-4 in. center-to-center) is greater than three times the pile dimension, Case C capacity is adequate.

SUMMARY AND CONCLUSIONS

Pile ductility affects the ultimate strength and behavior of piles subjected to combined lateral displacement and vertical load. Based on the moment-rotation capacity of a pile, two approaches to determine the capacity of the pile as a structural member (Case A) were presented. Alternative 1 is an elastic design approach that should be applied for piles with limited ductility such as timber, concrete, and steel piles without inelastic rotation capabilities. For this alternative, all stresses induced by the lateral displacement of the pile head and gravity loads are considered in the design. When sufficient pile ductility exists, Alternative 2 is a design approach that can be applied to recognize redistribution of internal forces caused by plastic hinge rotation. For this alternative, the first-order stresses, but not the strains, caused by thermally induced lateral displacement of the pile head are neglected. These displacement-induced bending stresses do not affect the ultimate strength of the pile when the moment-rotation capacity exceeds the moment-rotation demand. The pile strains are investigated indirectly by a ductility criterion that was presented in terms of the pile head displacement.

To illustrate the two design alternatives, a pile design example for an integral abutment was presented. The design for a fixed-headed, HP-shaped, friction pile was simplified by the use of nondimensional graphs for equivalent cantilever lengths and effective friction length loss. The example showed that according to Alternative 1, the pile had insufficient capacity. However, according to Alternative 2, the pile had sufficient ductility, even though the pile was not a compact section and had adequate strength. For the example presented, Case B requirements, involving AASHTO Group I loading, controlled the pile design when Alternative 2 was applied for Case A conditions. The integral abutment lateral displacement, caused by a thermal expansion and contraction of 0.52 in. for the 360-ft bridge, did not detract from the strength of the pile. In fact, the lateral displacement of the pile head could have been as large as 1.14 in. before the integral abutment design would have detracted from the allowable pile load, indicating that this bridge could have been about twice as long. By recognizing the ductility characteristics of piles, Alternative 2 will permit the safe design of integral abutment bridges that can be significantly longer than those designed according to Alternative 1.

ACKNOWLEDGMENTS

REFERENCES

1. W. Zuk. *Jointless Bridges*, Report VHTRC-81-R48; FHWA/VA-81/48. Virginia Highway and Transportation Research Council, Springfield; FHWA, U.S. Department of Transportation, June 1981.
2. A. M. Wolde-Tinsae, L. F. Greimann, and P.-S. Yang. *Nonlinear Pile Behavior in Integral Abutment Bridges*. Project HR-227, ISU-ERI-Ames 82123. Iowa Department of Transportation, Des Moines, Feb. 1982.
3. A. M. Wolde-Tinsae, J. E. Klinger, M. Mafi, P. Albrecht, J. White, and N. Buresli. *Performance and Design of Jointless Bridges*. Contract DTFH61-85-C-00092, Final Report. Department of Civil Engineering, University of Maryland; FHWA, U.S. Department of Transportation, June 1987.
4. D. L. Allen. *A Survey of the States on Problems Related to Bridge Approaches*. Final Report UKTRP-85-25. Transportation Research Program, College of Engineering, University of Kentucky, Lexington; FHWA, U.S. Department of Transportation, Oct. 1985.
5. L. F. Greimann, R. E. Abendroth, D. E. Johnson, and P. E. Ebner. *Pile Design and Tests for Integral Abutment Bridges*. Project HR-273, ISU-ERI-Ames 88060, Final Report. Iowa Department of Transportation, Des Moines, Dec. 1987.
6. L. F. Greimann, P.-S. Yang, and A. M. Wolde-Tinsae. Nonlinear Analysis of Integral Abutment Bridges. *Journal of Structural Engineering*, ASCE, Vol. 112, No. 10, Oct. 1986, pp. 2263–2280.
7. L. F. Greimann and A. M. Wolde-Tinsae. Design Models for Piles in Jointless Bridges. *Journal of Structural Engineering*, ASCE, Vol. 114, No. 6, June 1988, pp. 1354–1371.
8. M. T. Davisson and K. E. Robinson. Bending and Buckling of Partially Embedded Piles. *Proc., 6th International Conference on Soil Mechanics and Foundation Engineering*, Montreal, Canada, Vol. 2, 1965, pp. 243–246.
9. H. G. Poulos and E. H. Davis. *Pile Foundation Analysis and Design*. John Wiley & Sons, Inc., New York, 1980.
10. B. G. Neal. *The Plastic Methods of Structural Analysis*. 2nd ed. John Wiley & Sons, Inc., New York, 1963.
11. M. R. Horn. *Plastic Theory of Structures*. Massachusetts Institute of Technology Press, Cambridge, 1971.
12. *Manual of Steel Construction*, 8th ed. American Institute of Steel Construction, Chicago, Ill., 1980.
13. T. V. Galambos and M. G. Lay. Studies of the Ductility of Steel Structures. *Journal of Structural Engineering*, ASCE, Vol. 91, No. 8, Aug. 1965. pp. 125–151.
14. M. G. Lay. Flange Local Buckling in Wide-Flange Shapes. *Journal of Structural Engineering*, ASCE, Vol. 91, No. 12, Dec. 1965, pp. 95–116.
15. M. G. Lay and T. V. Galambos. Inelastic Beams Under Moment Gradient. *Journal of Structural Engineering*, ASCE, Vol. 93, No. 2, Feb. 1967, pp. 381–399.
16. A. F. Lukey and P. F. Adams. Rotation Capacity of Beams Under Moment Gradient. *Journal of Structural Engineering*, ASCE, Vol. 95, No. 6, June 1969, pp. 1173–1188.
17. *Manual of Steel Construction: LRFD*, 1st ed., American Institute of Steel Construction, Chicago, Ill., 1986.
18. W. G. Fleming, A. J. Weltman, M. F. Randolph, and W. K. Elson. *Piling Engineering*. Halsted Press, New York, 1985.
19. M. G. Spangler. *Soil Engineering*, 2nd ed., International Textbook Company, 1960.

Bridge Service Life Prediction Model Using the Markov Chain

Yi Jiang and Kumares C. Sinha

This paper describes the application of Markov chain technique in estimating bridge service life. The change of bridge conditions is a stochastic process and, therefore, the service life of bridges is related to the probabilities of condition transitions. A bridge service life prediction model, using the Markov chain, was developed to reflect the stochastic nature of bridge condition and service life. The paper includes a discussion on the concept of Markov chain, the development and application of the service life prediction model using the Markov chain, and the comparison of service life predictions by statistical and Markov chain approaches.

The service life of a bridge is one of the most important factors for bridge managers to estimate or predict. This paper presents a bridge service life prediction model using Markov chain. The model was developed as a continuation of the earlier work on bridge performance analysis (1). The earlier paper involved the use of Markov chain in developing bridge performance curves. The present paper deals with prediction of bridge service life on the basis of performance analysis.

Bridge service life can be predicted by a regression analysis of bridge age versus bridge condition. However, the prediction is restricted to average or mean service life of a number of bridges. The Markov chain model provides a tool for predicting not only the average service life, but also the service life of any individual bridge.

This paper describes the bridge service life prediction model using the Markov chain. The Markov chain concept is introduced and the development and application of the model are discussed. The comparison is made between the approaches of statistical regression and Markov chain.

BRIDGE SERVICE LIFE

All federally supported bridges in Indiana have been inspected every 2 years beginning in 1978. The inspection includes rating of individual components such as deck, superstructure and substructure, as well as of the overall bridge condition. According to the FHWA bridge rating system, bridge inspectors use a range from 0 to 9, with 9 being the maximum rating number for a new condition (2). When the rating reaches a value of 3, a bridge has to be repaired or replaced, otherwise it should be closed. Therefore, the time span between a bridge being built and its condition reaching the rating of 3 was defined as the service life of the bridge. Two approaches of estimating bridge service life—statistical and Markov chain—are discussed.

School of Civil Engineering, Purdue University, West Lafayette, Ind. 47907.

STATISTICAL APPROACH

The performance curves of bridge components, such as deck, superstructure, and substructure, were developed separately for concrete and steel bridges on both Interstate and non-Interstate highways. Two of these curves, the performance curves of substructures of concrete and steel bridges on non-Interstate highways, are discussed to demonstrate the prediction methods.

The objective of developing performance curves was to find the relationship between condition rating and bridge age. A third-order polynomial model was used to obtain the regression function of the relationship. The polynomial model is expressed by the following formula (3):

$$Y_i(t) = \beta_0 + \beta_1 t_i + \beta_2 t_i^2 + \beta_3 t_i^3 + \varepsilon_i \tag{1}$$

where $Y_i(t)$ is the condition rating of a bridge at age t, t_i is the bridge age, and ε_i is the error term. This equation indicates that the condition rating of a bridge, $Y_i(t)$, depends on the bridge age of the bridge, t_i.

For a new bridge (age 0), the recorded condition rating was found always to be 9; therefore β_0 was specified as 9 to make the intercept of the regression line an integer and meaningful in practice.

When a regression model is selected for an application, it is usually not possible to make certain in advance that the model is appropriate for that application. Therefore, two regression assumptions, the constancy and normality of residual distribution, should be tested (3).

The Statistical Analysis System (SAS) statistical package was used for the test of aptness of polynomial model and for regression analysis (4). Residual plots were obtained to check the constancy of variance and the Kolomogorov-Smirnov test was used to test the normality of residual distribution. It was found that the polynomial regression function on raw data of concrete bridges met the two aptness requirements, the constancy and normality of residual distribution. However, the regression function on raw data of steel bridges did not meet the requirements. A transformation of $y' = \sqrt{y}$ on the raw data of steel bridges satisfied the necessary normality and constancy requirements.

The complete data base included about 5,700 state-owned bridges in Indiana. To evaluate the effects of the climate, traffic volume, highway system, and bridge type on bridge performance, bridges were divided into groups such as steel and concrete bridges; bridges with high, medium, or low average daily traffic; bridges in northern and southern regions; and bridges on Interstate and non-Interstate highways. Because

the factors of traffic volume and climatic region were found not statistically significant, the final factors considered in the regression analysis were highway class (Interstate and non-Interstate) and bridge type (steel and concrete). For example, to develop the performance curves of bridge substructures on non-Interstate highways, 90 concrete bridges and 90 steel bridges on non-Interstate highways were randomly selected from the complete data base. The recorded data of condition ratings and corresponding ages of these bridges from 1978 to 1986 were used to perform the regression analysis. The resulting regression function for substructure of concrete bridges was

$$Y_i(t) = 9.0 - 0.28877329t_i + 0.0093685t_i^2$$

$$- 0.00008877t_i^3 \qquad (2)$$

The regression function for substructure of steel bridges was

$$Y_i(t) = \left(\sqrt{Y_i(t)}\right)^2$$
$$= (3.0 - 0.051696t_i + 0.001715t_i^2 - 0.000021t_i^3)^2 \qquad (3)$$

Equation 3 was obtained using the transformed data and so it had different form from Equation 1.

The regression function can be used to predict service life; that is, the value of t_i corresponding to $Y_i(t) = 3$ is nothing but the estimated bridge substructure service life. Figures 1 and 2 show the curves of the regression functions and the estimated service lives obtained by solving the functions. The predicted service lives of concrete and steel bridge substructures are both 54 years, as shown in Figures 1 and 2, where *SL* represents service life and the subscripts *c* and *s* denote concrete and steel bridges.

In reality, service life varies from bridge to bridge. However, by the definition of regression analysis (3), $Y(t)$ is the average condition rating at bridge age t, that is, $\bar{r} = Y(t)$, so the service life obtained from the performance function is actually the mean or average service life of bridge substructures on non-Interstate highways, that is, $\bar{T} = SL$. As shown in Figure 3, A and B are two steel bridges with the same
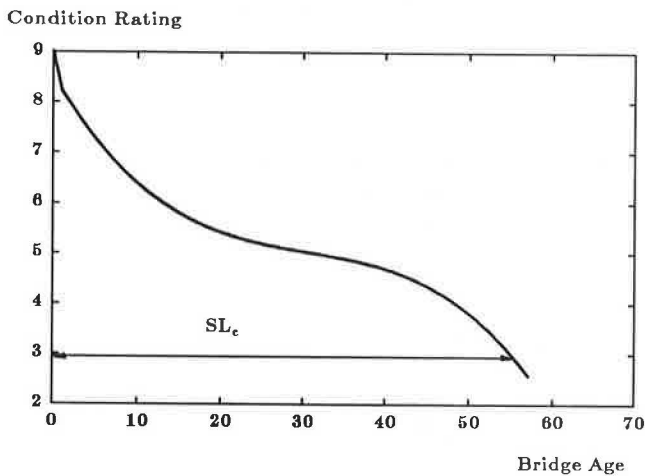
FIGURE 1 Performance curve of substructure condition of concrete bridges.
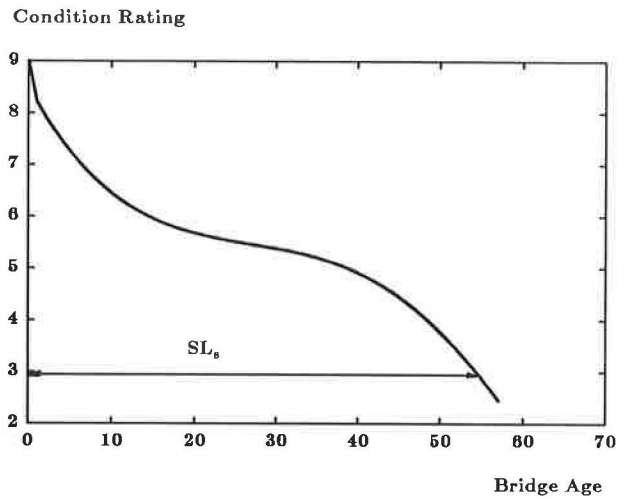
FIGURE 2 Performance curve of substructure condition of steel bridges.

bridge ages but different substructure condition ratings. The condition ratings are r_a and r_b for bridges A and B, respectively. Substructure service life of Bridge A may be predicted by the performance function because Point A is on the performance curve. Thus, it may be expected that substructure service life of bridge A equals to $\bar{T}$, the average service life of the substructures, that is, $t_1 + t_{2a} = \bar{T}$; where t_1 is the bridge age and t_{2a} is the remaining substructure service life of Bridge A. The remaining substructure service life of Bridge B, t_{2b}, cannot be estimated from the performance function because Point B is not on the performance curve. It can be guessed, however, that t_{2b} would be less than t_{2a}. It is necessary for a bridge manager to estimate t_{2b} as well as t_{2a}. Therefore, the Markov chain technique was applied to fulfill the task.

MARKOV CHAIN APPROACH

Introduction to Markov Chain

The Markov chain as applied to bridge service life prediction is based on the concept of defining states in terms of bridge condition ratings and obtaining the probabilities of bridge condition transiting from one state to another. These probabilities are represented in a matrix form that is called the transition probability matrix or simply, transition matrix, of the Markov chain. If the present state of bridge conditions or the initial state is known, the future condition and the time needed to change condition from one rating to another can be predicted through multiplications of initial state vector and the transition matrix.

Seven bridge condition ratings are defined as seven states with each condition rating corresponding to one of the states. For example, Condition 9 is defined as State 1, Rating 8 as State 2, and so on. Without repair or rehabilitation, the bridge condition rating decreases as the bridge age increases. Therefore, there is a probability of condition transiting from one state, say i, to another state, j, during a 1-year period, which is denoted by $p_{i,j}$. Table 1 shows the correspondence of condition ratings, states, and transition probabilities. Because the

Condition Rating

FIGURE 3 Example of service life predictions.

TABLE 1 CORRESPONDENCE OF CONDITION RATINGS, STATES, AND TRANSITION PROBABILITIES

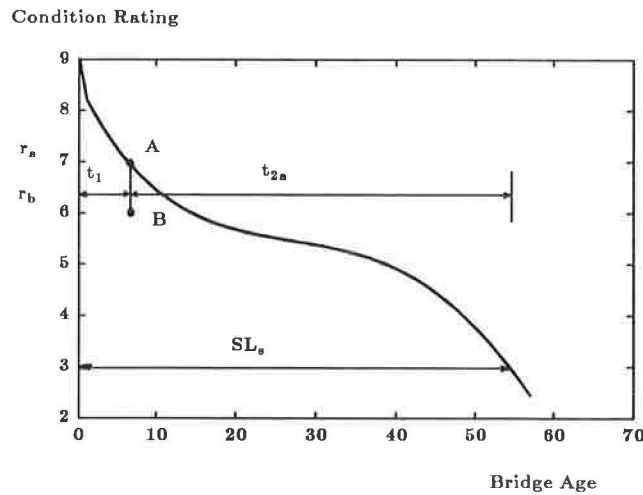|		R=9	R=8	R=7	R=6	R=5	R=4	R=3
		S=1	S=2	S=3	S=4	S=5	S=6	S=7
R=9	S=1	$p_{1,1}$	$p_{1,2}$	$p_{1,3}$	$p_{1,4}$	$p_{1,5}$	$p_{1,6}$	$p_{1,7}$
R=8	S=2	$p_{2,1}$	$p_{2,2}$	$p_{2,3}$	$p_{2,4}$	$p_{2,5}$	$p_{2,6}$	$p_{2,7}$
R=7	S=3	$p_{3,1}$	$p_{3,2}$	$p_{3,3}$	$p_{3,4}$	$p_{3,5}$	$p_{3,6}$	$p_{3,7}$
R=6	S=4	$p_{4,1}$	$p_{4,2}$	$p_{4,3}$	$p_{4,4}$	$p_{4,5}$	$p_{4,6}$	$p_{4,7}$
R=5	S=5	$p_{5,1}$	$p_{5,2}$	$p_{5,3}$	$p_{5,4}$	$p_{5,5}$	$p_{5,6}$	$p_{5,7}$
R=4	S=6	$p_{0,1}$	$p_{0,2}$	$p_{0,3}$	$p_{0,4}$	$p_{0,5}$	$p_{0,6}$	$p_{0,7}$
R=3	S=7	$p_{7,1}$	$p_{7,2}$	$p_{7,3}$	$p_{7,4}$	$p_{7,5}$	$p_{7,6}$	$p_{7,7}$

Note: R = Condition Rating

S = State

$p_{i,j}$ = Transition Probability from State i to State j

lowest recorded rating number in the data base was 3, indicating that the bridges are usually repaired or replaced at rating not less than 3, condition ratings less than 3 were not included in the transition matrix.

As a bridge age increases, the deteriorating rate of bridge conditions changes. That is, the process of condition transition is not homogeneous with respect to bridge age. To meet the homogeneity requirement of Markov chain, bridge age was divided into groups, and within each group the Markov chain was assumed to be homogeneous. Age groups consisting of 6 years were used and each group had its own transition matrix that was different from those of remaining groups.

An assumption was made that the bridge condition rating would not drop more than 1 in a single year. Thus, the bridge condition would either stay in its current rating or transit to the next lower rating in 1 year. The transition matrix has, therefore, the form

$$P = \begin{vmatrix} p(1) & q(1) & 0 & 0 & 0 & 0 & 0 \\ 0 & p(2) & q(2) & 0 & 0 & 0 & 0 \\ 0 & 0 & p(3) & q(3) & 0 & 0 & 0 \\ 0 & 0 & 0 & p(4) & q(4) & 0 & 0 \\ 0 & 0 & 0 & 0 & p(5) & q(5) & 0 \\ 0 & 0 & 0 & 0 & 0 & p(6) & q(6) \\ 0 & 0 & 0 & 0 & 0 & 0 & 1 \end{vmatrix} \quad (4)$$

where $q(i) = 1 - p(i) \cdot p(i)$ corresponds to $p_{i,i}$ and $q(i)$ to $p_{i,i+1}$ in Table 1. Therefore, $p(1)$ is the transition probability from Rating 9 (State 1) to Rating 9, and $q(1)$, from Rating 9 to Rating 8, and so on.

It should be noted that the lowest rating number before a bridge is repaired or replaced is 3. Consequently, the corresponding transition probability $p(7)$ equals 1.

Development of Transition Matrix

To estimate the transition probabilities for each age group, the following nonlinear programming objective function was formulated:

$$\min \sum_{t=1}^{N} | Y(t) - E(t, P) | \quad (5)$$

subject to

$$0 \le p(i) \le 1 \qquad i = 1, 2, \ldots, I$$

where

$N = 6$, the number of years in one age group,
$I = 6$, the number of unknown probabilities,
$P = $ a vector of length I equal to $[p(1), p(2), \ldots, p(I)]$,
$Y(t) = $ the average of condition ratings at time t, estimated by regression function, and
$E(t,P) = $ estimated value of condition rating by Markov chain at time t.

By Markov chain, the state vector for any time t, $Q_{(t)}$, can be obtained by the multiplication of initial state vector $Q_{(0)}$ and the transition probability matrix P raising the power to t (5):

$$Q_{(t)} = Q_{(0)} * P^t \quad (6)$$

Let R be a vector of condition ratings, $R = [9\ 8\ 7\ 6\ 5\ 4\ 3]$, and R' be the transform of R, then the estimated condition rating by Markov chain is,

$$E(t, P) = Q_{(t)} * R' \quad (7)$$

The objective function was to minimize the absolute distance between the average bridge condition rating at a certain age and the predicted bridge condition rating for the corresponding age generated by the Markov chain with the probabilities obtained by the nonlinear programming. The values of the regression function were taken as the average conditions, $Y(t)$, to solve the nonlinear programming or Equation 5.

A new bridge is almost always given a condition rating of

9 for all of its components, deck, superstructure, and substructure. In other words, a bridge at age 0 has a condition rating 9 for its components with unit probability. Thus, the initial state vector $Q_{(0)}$ for deck, superstructure, and substructure of a new bridge is always $[1\ 0\ 0\ .\ .\ .\ 0]$, where the numbers are the probabilities of having a condition rating of 9, 8, 7, . . ., and 3 at age 0, respectively. That is, the initial state vector of the first age group is known. Therefore, Equation 5 can be solved for Age Group 1. Age Group 2 takes the last state vector of Age Group 1 as its initial state vector, Equation 5 can also be solved for Age Group 2. In the same manner, the transition probabilities for all the age groups were obtained, as shown in Tables 2 and 3. For example, $p(1) = 0.717$ in Group 1 (Age 6 years or less) of Table 3 represents the transition probability from State 1 to State 1 in a 1-year period for substructure of steel bridges with age less or equal to 6 years, and the transition probability from State 1 to State 2 in a 1-year period is, therefore, $q(1) = 1 - 0.717 = 0.283$. The solution to this function was obtained by the Quasi-Newton method (6).

Application of Markov Chain Model

Once the transition matrices are obtained, the prediction of bridge service life can be conducted using Equations 6 and 7. By this approach, the service life prediction is not restricted to the average service life of bridges. Instead, the prediction can be made for any individual bridge or bridge component at a given bridge age with any condition rating. For the two bridges in Figure 3, the Markov chain model can be used to predict service life for both Bridge A and Bridge B.

For demonstration purpose, we assume Bridges A and B are both 9-year-old steel bridges. The substructure condition rating is 7 for Bridge A and 6 for Bridge B. From Table 3,

TABLE 2 TRANSITION PROBABILITIES FOR SUBSTRUCTURE CONDITION—CONCRETE BRIDGES, NON-INTERSTATE

Bridge Age	p(1)	p(2)	p(3)	p(4)	p(5)	p(6)
0 - 6	0.705	0.818	0.810	0.802	0.801	0.800
7 - 12	0.980	0.709	0.771	0.980	0.980	0.856
13 - 18	0.638	0.639	0.748	0.980	0.980	0.980
19 - 24	0.798	0.791	0.788	0.980	0.870	0.824
25 - 30	0.794	0.810	0.773	0.980	0.980	0.980
31 - 36	0.815	0.794	0.787	0.980	0.980	0.737
37 - 42	0.800	0.798	0.815	0.980	0.850	0.980
43 - 48	0.800	0.800	0.309	0.938	0.980	0.050
49 - 54	0.800	0.800	0.800	0.711	0.707	0.768
55 - 60	0.800	0.800	0.800	0.050	0.050	0.050

TABLE 3 TRANSITION PROBABILITIES FOR SUBSTRUCTURE CONDITIONS—STEEL BRIDGES, NON-INTERSTATE

Bridge Age	p(1)	p(2)	p(3)	p(4)	p(5)	p(6)
0 - 6	0.717	0.727	0.950	0.664	0.692	0.700
7 - 12	0.366	0.715	0.970	0.814	0.574	0.359
13 - 18	0.700	0.507	0.950	0.653	0.950	0.766
19 - 24	0.700	0.707	0.950	0.950	0.950	0.950
25 - 30	0.700	0.700	0.950	0.950	0.950	0.950
31 - 36	0.200	0.200	0.200	0.950	0.696	0.447
37 - 42	0.200	0.200	0.200	0.950	0.950	0.950
43 - 48	0.200	0.200	0.200	0.950	0.790	0.722
49 - 54	0.200	0.200	0.200	0.916	0.050	0.050
55 - 60	0.200	0.200	0.200	0.050	0.050	0.050

the corresponding transition matrix for Age 9 (in Age Group 2) is:

$$
P = \begin{vmatrix}
0.366 & 0.634 & 0 & 0 & 0 & 0 & 0 \\
0 & 0.715 & 0 & 0 & 0 & 0 & 0 \\
0 & 0 & 0.285 & 0.030 & 0 & 0 & 0 \\
0 & 0 & 0.970 & 0.814 & 0.186 & 0 & 0 \\
0 & 0 & 0 & 0 & 0.574 & 0.426 & 0 \\
0 & 0 & 0 & 0 & 0 & 0.359 & 0.641 \\
0 & 0 & 0 & 0 & 0 & 0 & 1.000
\end{vmatrix}
$$

(8)

The initial state vector of Bridge A is $Q_{(0)} = [0\ 0\ 1\ 0\ .\ .\ .\ 0]$, with the unit probability corresponding to Rating 7 ($r_a = 7$). Therefore, the state vector of Bridge A in the future can be predicted by Equation 6. The state vectors and corresponding condition ratings are as follows:

$$R = [9\ 8\ 7\ 6\ 5\ 4\ 3]$$

$$Q_{(0)} = [0\ 0\ 1\ 0\ 0\ 0\ 0]$$

$$E(0, P) = Q_{(0)} * R' = 7$$

$$Q_{(1)} = Q_{(0)} * P = [0.00\ 0.00\ 0.97\ 0.03\ 0.00\ 0.00\ 0.00]$$

$$E(1, P) = Q_{(1)} * R' = 6.97 \approx 7$$

$$Q_{(2)} = Q_{(0)} * P^2 = [0.00\ 0.00\ 0.94\ 0.05\ 0.01\ 0.00\ 0.00]$$

$$E(2, P) = Q_{(2)} * R' = 6.94 \approx 7$$

$$Q_{(3)} = Q_{(0)} * P_3 = [0.00\ 0.00\ 0.89\ 0.08\ 0.03\ 0.00\ 0.00]$$

$$E(3, P) = Q_{(3)} * R' = 6.87 \approx 7$$

Then, $Q_{(3)}$ obtained above is taken as the initial state vector of Age Group 3 (from Age 13 to Age 18) and the transition matrix for Age Group 3 is used to continue the procedure.

In general, Group n takes the last state vector of Group $n - 1$ as its initial state vector.

By this procedure, $E(45, P) = 3$ is obtained, therefore t_{2a} in Figure 1 is estimated to be 45 years. The service life of Bridge A, T_A, is predicted:

$$T_A = t_1 + t_{2a} = 9 + 45 = 54 \text{ years}$$

As expected, the value of T_A is the same as the one obtained by regression function, $SL_s = 54$, because Point A is on the performance curve.

Applying the Markov chain technique to Bridge B, $E(23, P) = 3$ is obtained. That is, t_{2b} is 23 and the service life of Bridge B is

$$T_B = t_1 + t_{2b} = 9 + 23 = 32 \text{ years}$$

As we expected, T_B is less than T_A. Similarly, for any possible value of Condition Rating r at any time, the service life can be predicted by the Markov chain. However, these predictions cannot be made by the regression function for condition ratings other than $r = 7$.

Test of Accuracy

The accuracy of the service life prediction depends on the closeness of the values of condition ratings predicted by the Markov chain and by the regression function. The chi-square goodness of fit test (7) is used to measure the closeness of the predicted values of condition ratings. The computed chi-square is given by:

$$\chi^2 = \sum_{i=1}^{k} \frac{(F_i - Y_i)^2}{E_i} \tag{8}$$

where

$\chi^2 = $ has a chi-square distribution with $k - 1$ degrees of freedom,

$E_i = $ value of condition rating in Year i predicted by the Markov chain,

$Y_i = $ value of condition rating in Year i predicted by the regression function, and

$k = $ the number of years predicted.

As an example, the results of the chi-square test for Bridge A are presented. The chi-square test was performed by using the values of $E(t, P)$ and $Y(t)$ from $t = 10$ to $t = 54$ ($k = t_{2a} = 45$) and the results indicated that the difference between the values of the Markov chain and regression function was not significant at $\alpha = 0.05$, as shown here:

$$\chi^2 = \sum_{i=1}^{45} \frac{(E_i - Y_i)^2}{E_i} = 3.111$$

$$\text{CHI}_{44}^2 \ (\chi^2 \geq 3.111) > 0.995 > \alpha = 0.05$$

Therefore, the values of condition ratings predicted by the two approaches, Markov chain and regression function, were very close.

TABLE 4 PREDICTED SUBSTRUCTURE SERVICE LIVES OF CONCRETE BRIDGES FOR DIFFERENT CONDITION RATINGS

Age	$\bar{r}_i$	r_i	Δr_i	Predicted SL	Overestimation of SL
0	9	9	0	54	0
		9	1	54	0
		8	0	54	0
4	8	7	-1	54	0
		6	-2	54	0
		5	-3	35	19
		8	1	54	0
		7	0	54	0
9	7	6	-1	54	0
		5	-2	40	14
		4	-3	19	35
		8	2	54	0
		7	1	54	0
18	6	6	0	54	0
		5	-1	42	12
		4	-2	22	32
		7	2	55	-1
42	5	6	1	54	0
		5	0	54	0
		4	-1	43	11
		6	2	56	-2
52	4	5	1	55	-1
		4	0	54	0

Note: $\bar{r}_i = $ Average Condition Rating

$r_i = $ Actual Condition Rating

$\Delta r = r_i - \bar{r}_i$

$SL = $ Service Life

(Average Service Life $= 54$ Years)

TABLE 5 PREDICTED SUBSTRUCTURE SERVICE LIVES OF STEEL BRIDGES FOR DIFFERENT CONDITION RATINGS

Age	$\bar{r}_i$	r_i	Δr_i	Predicted SL	Overestimation of SL
0	9	9	0	54	0
		9	1	54	0
		8	0	54	0
4	8	7	-1	53	1
		6	-2	25	29
		5	-3	8	46
		8	1	54	0
		7	0	54	0
9	7	6	-1	32	22
		5	-2	24	30
		4	-3	10	44
		8	2	55	-1
		7	1	55	-1
25	6	6	0	54	0
		5	-1	34	20
		4	-2	30	24
		7	2	56	-2
44	5	6	1	56	-2
		5	0	54	0
		4	-1	47	7
		6	2	56	-2
52	4	5	1	54	0
		4	0	54	0

Note: $\bar{r}_i = $ Average Condition Rating

$r_i = $ Actual Condition Rating

$\Delta r = r_i - \bar{r}_i$

$SL = $ Service Life

(Average Service Life $= 54$ Years)

COMPARISON OF SERVICE LIFE PREDICTIONS USING PERFORMANCE CURVE AND MARKOV CHAIN

The difference between the average service life of bridges, $\overline{T}$, and the predicted service life of a bridge, T_i, are defined as the overestimation of the bridge's service life by the performance curve developed through statistical regression, ΔT_i, that is, $\Delta T_i = \overline{T} - T_i$. Thus, the overestimation of service life of Bridge A and that of Bridge B in Figure 3 are:

$$\Delta T_A = \overline{T} - T_A = 54 - 54 = 0 \text{ years}$$

$$\Delta T_B = \overline{T} - T_B = 54 - 32 = 22 \text{ years}$$

where $\overline{T} = SL_s$.

When the results are examined, it can be found that the overestimation of a bridge's service life is related to the difference of the actual condition rating and the average condition rating. The r_a is equal to 7, which is the same as the value of the regression function, or average condition rating, corresponding to the bridge age of 9. Thus, the difference of r_a and the average condition rating, $\overline{r} = Y(9)$, is

$$\Delta r_a = r_a - \overline{r} = 7 - 7 = 0$$

which causes no overestimation of the bridge's service life, that is, $\Delta T_A = 0$.

However, r_b is equal to 6 and the condition rating difference is,

$$\Delta r_b = r_b - \overline{r} = 6 - 7 = -1$$

Therefore, $\Delta T_B = 22$ can be considered as the overestimation of service life by performance curve resulting from overestimating condition rating by one unit. The effect of Δr_i on ΔT_i is explained by the fact that $Q_{(0)}$ is determined by the actual condition rating of a bridge and the Markov chain equation (Equation 6). Once the transition matrix, P, is known, the state vector, $Q_{(t)}$, is determined by the initial state vector, $Q_{(0)}$.

In order to analyze this effect, the service lives of bridge substructures were obtained by the Markov chain model for various possible condition ratings. Tables 4 and 5 show the results and the corresponding values of Δr and ΔT. Comparing values of the two tables, it can be found that the values of service life overestimations for substructures of concrete and steel bridges are different. For example, for $\overline{r}_i = 7$ and $\Delta r_i = 1$, the overestimation of service life is 0 for concrete bridge substructures and 22 for steel bridge substructures.

The values of bridge substructure service life overestimations for all possible combinations of $\overline{r}_i$ and Δr_i are presented in Table 6. The paired data in Table 6 are the overestimations of service lives for steel and concrete bridge substructures. For example, for $\overline{r}_i = 6$ and $\Delta r_i = -1$, the corresponding data (20, 12) represent that the overestimation of substructure service life is 20 for a steel bridge and 12 for a concrete bridge, or $\Delta T_{si} = 20$ and $\Delta T_{ci} = 12$. The differences of the values in the table were used to perform the paired-t statistical test (3):

$$x_i = \Delta T_{si} - \Delta T_{ci}$$

where ΔT_{si} and ΔT_{ci} are the overestimations of service lives

TABLE 6 PREDICTIONS OF OVERESTIMATION OF SERVICE LIVES FOR SUBSTRUCTURES OF STEEL AND CONCRETE BRIDGES

		Actual Rating - Average Rating					
		2	1	0	-1	-2	-3
Average Rating	9	-	-	(0,0)*	-	-	-
	8	-	(0,0)	(0,0)	(1,0)	(29,0)	(46,19)
	7	-	(0,0)	(0,0)	(22,0)	(30,14)	(44,35)
	6	(-1,0)	(-1,0)	(0,0)	(20,12)	(24,32)	(36,36)
	5	(-2,-1)	(-2,0)	(0,0)	(7,11)	(10,12)	-
	4	(-2,-2)	(0,-1)	(0,0)	(2,2)	-	-

*: (a, b) -- a is the overestimation of service life of steel bridge

b is the overestimation of service life of concrete bridge
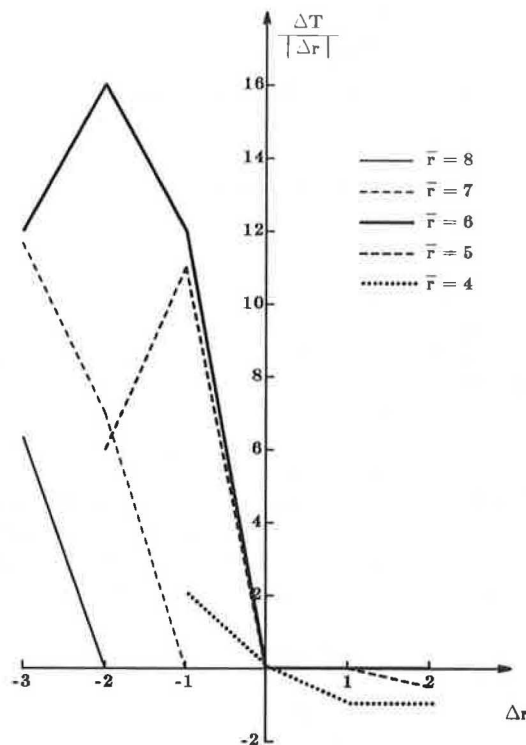
FIGURE 4 Service life sensitivity analysis for substructure of concrete bridges.

of steel and concrete bridge substructures by the performance function. Because $t^* = 2.03 > t(0.95,25) = 1.708$, the mean difference in overestimation of steel and concrete substructure service lives is significant at $\alpha = 0.05$. That is, the overestimation of service life of steel bridge substructure is more sensitive to overestimation of condition rating with respect to actual condition rating.

As can be seen, the service life of a bridge is affected by bridge type and the difference of actual condition rating and average condition rating. The average condition rating is
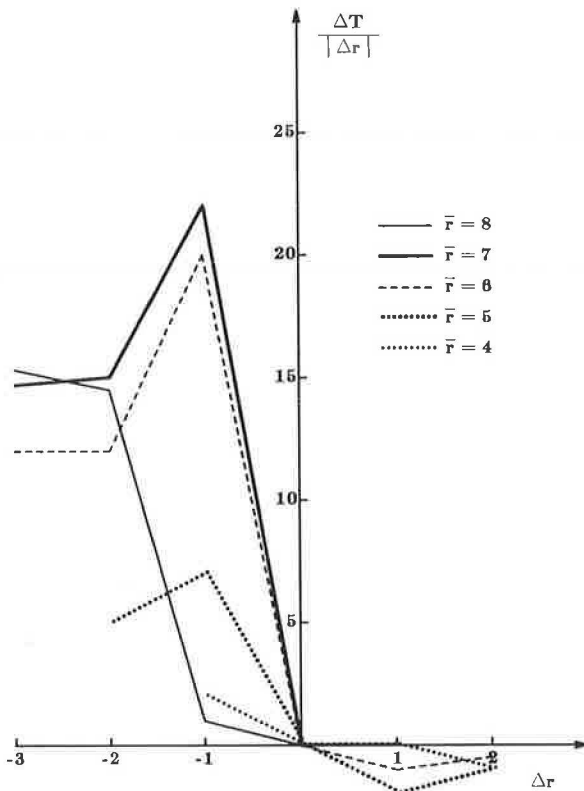
FIGURE 5 Service life sensitivity analysis for substructure of steel bridges.

CONCLUSIONS

The application of the Markov chain provides bridge managers a powerful and convenient tool for estimating bridge service life. Service life prediction by Markov chain has the advantage over the statistical regression approach in that it can be used not only to estimate the average service life of a number of bridges, but also the service life of any individual bridge. Furthermore, the Markov chain prediction is based on the current condition and age of bridges, therefore, it is simple and can be updated by new information of condition rating and bridge age. However, it should be noted that this study was based on statistical analysis of condition ratings. Condition ratings are subjective judgments, which may in themselves be biased, and therefore may affect the results of service life predictions. To reduce the bias of human judgments, a bridge condition evaluation model has been developed using the theory of fuzzy sets (8); the reliability and accuracy of service life predictions could be greatly enhanced by applying the condition evaluation model in the process of bridge condition inspection.

The theory of the Markov chain is well developed and based on simple multiplications of matrices. As compared with the regression method, the Markov chain model, a probability-based method, reflects better the stochastic nature of bridge service life. The model provides a mathematical tool for predicting bridge service life. The comparison of service life predictions of the two models enables bridge managers to study the effects of bridge types, condition ratings, and bridge ages on service lives of bridges.

ACKNOWLEDGMENT

obtained by regression function, which is the relationship between bridge age and condition rating. Therefore, the sensitivity of overestimation of bridge service life to bridge age can be studied by analyzing the sensitivity of overestimation of bridge service life to average condition rating.

Figures 4 and 5 present the curves of Δr versus $\Delta T / |\Delta r|$ for substructures of concrete and steel bridges, where $\Delta T / |\Delta r|$ represents the overestimation of service life per unit change of condition rating from average condition rating. Figure 4 shows that the curve for the average condition rating $\bar{r}_i = 6$, for substructure of concrete bridges, has the highest value of $\Delta T / \Delta r$. The average age of concrete bridge substructures corresponding to the rating of 6 is 25. Therefore, the rating given at this age can be considered to be most sensitive with respect to service life estimation. From Figure 4, it can be seen that when the average performance curve for concrete bridge substructures reaches a condition rating of 6 (Age 25), if a lower-than-average condition rating is given, the service life of the bridge would be overestimated by as much as 16 years for every unit of lower-than-average condition rating. It means that, for concrete bridge substructures, the expected overestimation of service life per unit of lower-than-average condition rating is the highest when the performance curve reaches the condition rating of 6. From Figure 5, the corresponding most critical level for steel bridge substructures is when the performance curve reaches the condition rating of 7 (Age 9). The expected overestimation in this case is 22 years. The implications of these results are that average performance functions can only be used for making macroscopic decisions at network level. However, for making decisions at a project level, Markov chain is a better tool.

REFERENCES

1. Y. Jiang, M. Saito and K. C. Sinha, Bridge Performance Prediction Model Using the Markov Chain, In *Transportation Research Record 1180*, TRB, National Research Council, Washington, D.C., Jan. 1988, pp. 31–39.
2. *Recording and Coding Guide for the Structure Inventory and Appraisal of the Nation's Bridges*. Report FHWA-ED-89-044. FHWA, U.S. Department of Transportation, Dec. 1988.
3. J. Neter and W. Wasserman. *Applied Linear Statistical Models: Regression, Analysis of Variance and Experimental Designs*. Richard D. Irwin, Inc., Homewood, Ill., 1974.
4. *SAS User's Guide: Statistics, Version 5 Edition*. SAS Institute Inc., Cary, N. C., 1985.
5. U. N. Bhat. *Elements of Applied Stochastic Processes*. John Wiley & Sons, Inc., New York, 1972.
6. D. G. Luenberger. *Linear and Nonlinear Programming*. Addison-Wesley Publishing Co., Inc., Reading Mass., 1985.
7. E. D. Rothman and W. A. Ericson. *Statistics: Methods and Applications*. Kendall/Hunt Publishing Co., Dubuque, Iowa, 1983.
8. A. B. Tee, M. D. Bowman, and K. C. Sinha, A Fuzzy Mathematical Approach for Bridge Condition Evaluation. *Civil Engineering Systems*. Vol. 5, March 17, 1988, pp. 17–24.

Bilayer Reinforced Stressed Timber Deck Bridges

Ralph R. Mozingo

Research efforts to improve the ability of timber to satisfy deflection criteria and to be economical for longer spans are leading to composite timber-steel deck bridges with transverse prestressing. The use of small size and length timbers is imperative because, quite simply, small-to-medium size trees are much more plentiful than large trees. A bilayer timber bridge model that employs both timber and steel is shown here to perform quite well. Results show that despite numerous butt joints and reliance on steel for horizontal shear, loads in excess of required magnitudes may be taken safely without undue deflections or stresses.

The use of timber for highway bridges is increasing. Some states have an abundance of wood, especially hardwood, which has not been used in bridge building. The notion that timber is unsuitable or less durable than other materials is false. In the Northeast, for example, deicing salts limit the average life of concrete bridge decks to about 15 years. Properly treated timber, on the other hand, is immune to the effects of such salts and will give useful service several times that long. An excellent paper concerning the long life and proper preservative treatment of timber bridges has been written by Muchmore (*1*).

Timber trusses of past years were vulnerable in the joints unless they were covered. The popular stressed laminated deck has no truss joints to deteriorate. Consequently, this type of timber structure, pioneered by Taylor and Csagoly (*2*) in Canada, provides a unique design for short spans wherein friction between longitudinal timber laminates is produced by tensioning of transverse prestressing rods.

Tests conducted at the University of Wisconsin (*3*) have established deflections as the governing design criterion in place of flexural or shear stresses for this type of timber deck. Resulting timber stresses are usually well within allowable values. In addition to bridges of this type built in Canada, several demonstration bridges have been built in the United States. The Trout Road Bridge, built near Houserville, Pennsylvania, in May of 1987, has been successfully monitored for 1 year (*4*). Dead and live load deflections, losses in bar forces, and moisture content of the creosoted timber deck were observed and analyzed.

Results indicate a well-behaved and esthetically pleasing bridge type for short spans. The span of 46 ft must obviously have timbers butted together at intervals. The usual procedure has been to limit butt joints no closer than every fourth member at any given bridge cross section. Large Douglas Fir timbers (4 x 16 in.) with a maximum length of 20 ft were used. Such large dimensions are scarcely procurable in most sections

of the country. Ways have been sought to form composite stressed timber decks to fully use available timber and to increase practical span lengths.

The design of an innovative stressed timber deck with laminated veneer lumber (LVL) stringers was built as a demonstration bridge of 78 ft for the Regional Timber Bridge Conference at Charleston, West Virginia, in May 1988. Composite action between LVL stringers and longitudinal oak decking was confirmed. Details of this unique design are contained in a paper titled *Design of Stressed Timber T-Beams for Highway Bridges* (unpublished) by Barry Dickson and Hota V. S. Ganga Rao of West Virginia University.

Composite action between timber and steel is also being explored. In another presentation at the conference mentioned in the previous paragraph, the writer described in the *Effects of Steel Plates Inside of Prestressed Timber Deck Bridges* (unpublished) a method, based on model studies, whereby shorter timber lengths can be effectively used when steel plates are sandwiched between timber laminates before rod stressing. Bridge stiffness was shown to more than double when about 7 percent of steel was used. Moreover, timber lengths could be reduced from 20 to 12 ft—a more practical length.

Because of the high modulus of elasticity of steel compared with timber, longer spans, smaller timber depths, better control of creep, and better orthotropic behavior are all possible when steel plates are included. Full-scale testing of such composite behavior will begin in fall 1988 in the structural laboratory at The Pennsylvania State University.

The next logical step in the development of composite timber-steel bridge decks is to consider ways of using square or nearly square timber cross sections of modest sizes—these being most prevalent from medium-to-small trees. The bilayer reinforced stressed timber deck bridge has been recently investigated as a model by the writer and forms the main focus of this paper.

It should be noted specifically that this paper reports results of model tests that have not yet been verified by prototype studies. Economic studies, because of a lack of data, will therefore have to await the construction of prototype and demonstration bridges.

BRIDGE MODEL

A 1-to-12 scale model was built to simulate the behavior of an actual structure with a span of 46 ft. Figures 1a and 1b show dimensions and loads used for the model. To maintain load symmetry about mid-span, concrete blocks were added in pairs. After each pair was added, dial gauge readings at mid-span front and rear positions were taken and averaged

212 Sackett Building, Department of Civil Engineering, The Pennsylvania State University, University Park, Pa. 16802.
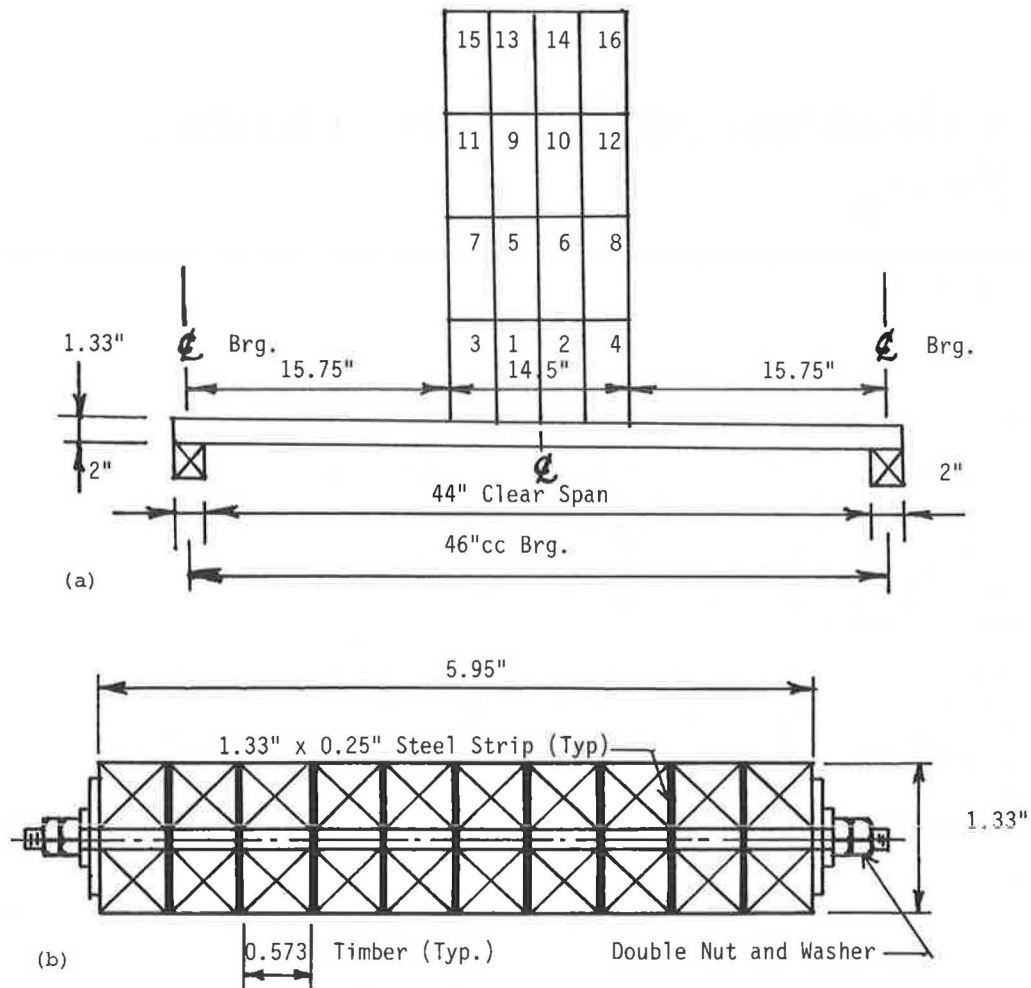
FIGURE 1   (a) bilayer model bridge with 16 concrete blocks; (b) bilayer model bridge cross section with 20 timbers and nine steel strips.

to give the displacement in inches. Each time the bridge model was reassembled (with nuts tightened), a shakedown load of 320 lb was applied and removed before any data were taken. Also, the full load remained on each assembly for 24 hr, after which unloading data were taken with concrete blocks removed in pairs. Thus the effects of creep became apparent.

Dimensions and loads for both model and prototype are listed in Table 1. The maximum load of 320 lb on the model is corrected upward by the square of the scale factor to 46,080 lb on the prototype. Moreover, if a more realistic bridge width of 26 ft is envisioned, then the equivalent total maximum load would be $26 \times 46,080/5.8 = 206,566$ lb, which exceeds two HS25-20 truck loads $(2 \times 90,000 = 180,000$ lb). The maximum model load of 320 lb thus represents more than sufficient loading for today's highway bridges.

Figure 2 shows an end cross section of the bilayer model bridge resting on a 2-in.-wide timber sill. Each layer is 10 timbers wide with nine 24-gauge sheet metal strips sandwiched between timbers. Double nuts were used to discourage stripping of the threads of the soft steel rods. The grain direction for timber cross sections was chosen randomly and the average modulus of elasticity found to be 1,405 ksi. The red oak used is well-seasoned wood taken from an old church pew. The

TABLE 1   DIMENSIONS AND LOADS

Variable	Model	Prototype
Scale	1:12	1
Span	46 in. cc brg.	46 ft cc brg.
Timber size	0.580×0.580 in.	6.96×6.96 in.
Plate size	$0.25 \times 4/3$ in.	0.30×16 in.
Number of timbers	10 each layer	10 each layer
Deck width	5.80 in.	5 ft 9.6 in.
Rod size	3/16 in.	1 in.
Rod spacing	4 in. cc	4 ft cc
Loads	16 20-lb blocks	—
Maximum load	$16 \times 20 = 320$ lb	$320 \times 12^2 = 46,080$ lb

NOTE: cc brg. = center-to-center bearings.

average moisture content was 9.7 percent, and the average modulus of rupture was 11,815 psi based on failure testing of eight specimens. Figure 3 shows the partially assembled model with stressing rods and steel strips visible. The numbering shown was necessary to ensure that timbers and steel would be in the same relative positions each time the structure was reassembled.
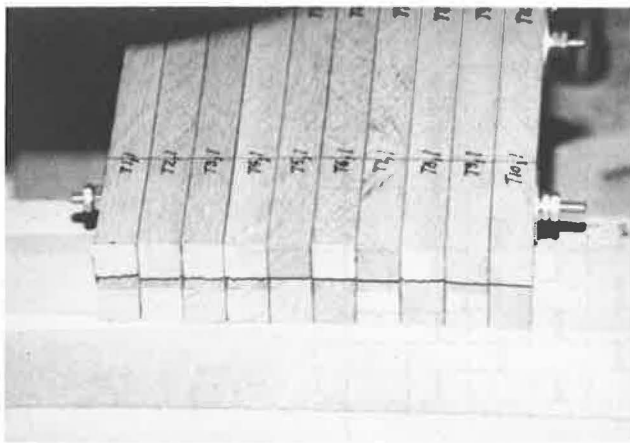
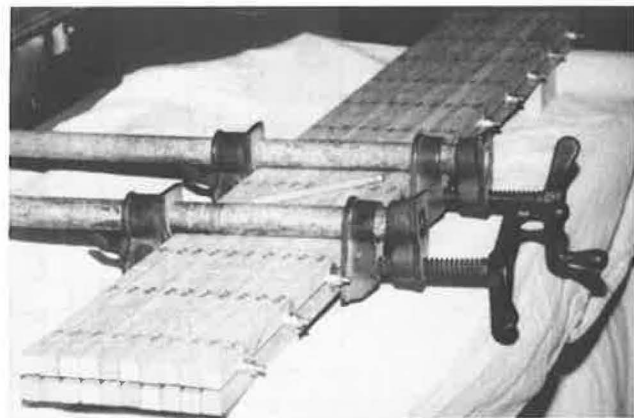FIGURE 2   End view of bilayer model bridge resting on sill.

FIGURE 4   Clamping technique used before bolt tightening of the bilayer model bridge.
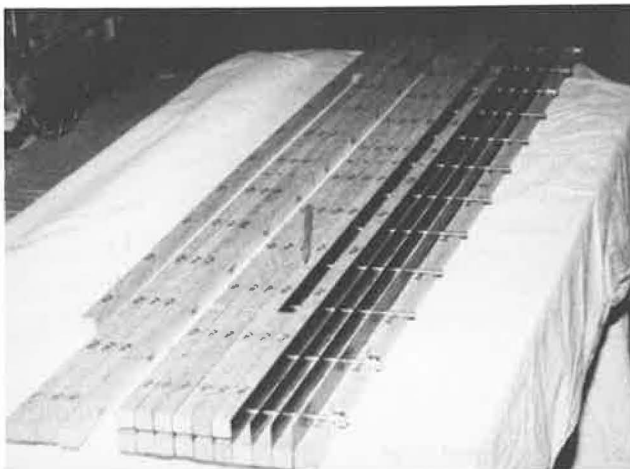

FIGURE 3   Partially assembled bilayer model bridge with steel strips and stressing rods.
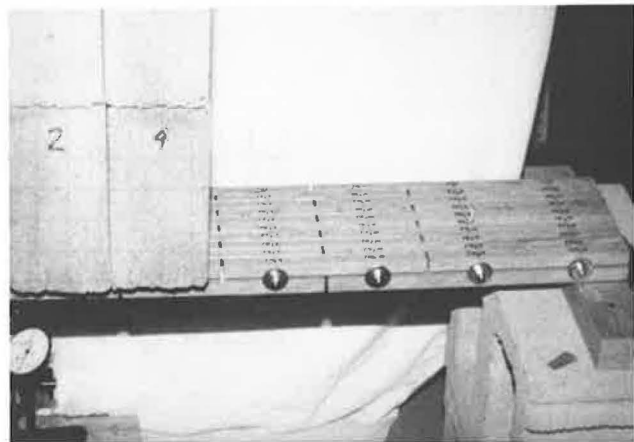

FIGURE 5   Right half of bilayer model bridge under load and showing butt joints.

Tightening of the rods was realized by first tightening clamps near the rods as shown in Figure 4. The fact that the timbers are held in place and transfer stresses to the steel strips by friction alone may seem a bit peculiar, but no slippage was observed at any time—even when an overload was on the structure. In an actual bridge deck, smaller rods could be employed in pairs to pass through top and bottom layer timbers or in a staggered pattern, although this is not necessary for structural purposes. Note also that timbers used for the model required no drilling and were simply placed. Several trials are necessary for rod tightening because the tightening of one rod tends to ease the pressure on adjacent rods. Excessive tightening however leads to shear failure of the threaded rod.

Figure 5 shows a closeup view of about one-half of the loaded beam resting on a timber sill at the right end and loaded with concrete blocks. Butt joints can be seen in both the top and side. These gaps are about 0.10 in. so that no contact between butted timber lengths will occur during the load tests. Butt joints were introduced first near beam ends then progressively toward the mid-span until a total of 80 butt joints and 100 timber lengths made up the model. At this point all

timber lengths were either 8 or 12 in. Observe that every second member is butted for top and bottom layers, which means that one-half of the timber cross section has been cut at any section of butt joints. Later results will show surprising strength of this type of composite structure despite weakening by butt joints just mentioned.

Figure 6 shows a plan view of the butt joints for the top layer. The pattern for the lower layer is simply obtained as the mirror image. Butt joints were cut first near the ends and then progressively toward mid-span until a total of 80 butt joints (100 timber segments) were present.

After completion of load tests using nine steel strips and up to 80 butt joints, further tests were run with 80 butt joints and up to 18 steel strips. The strips were added in a symmetrical fashion as depicted in Figure 7. Friction between steel strips, as well as friction between wood and steel, was found to be adequate with no apparent slippage.

TEST RESULTS

Consider the structural behavior of the model bridge. The steel strips must resist all horizontal shear at mid-depth and
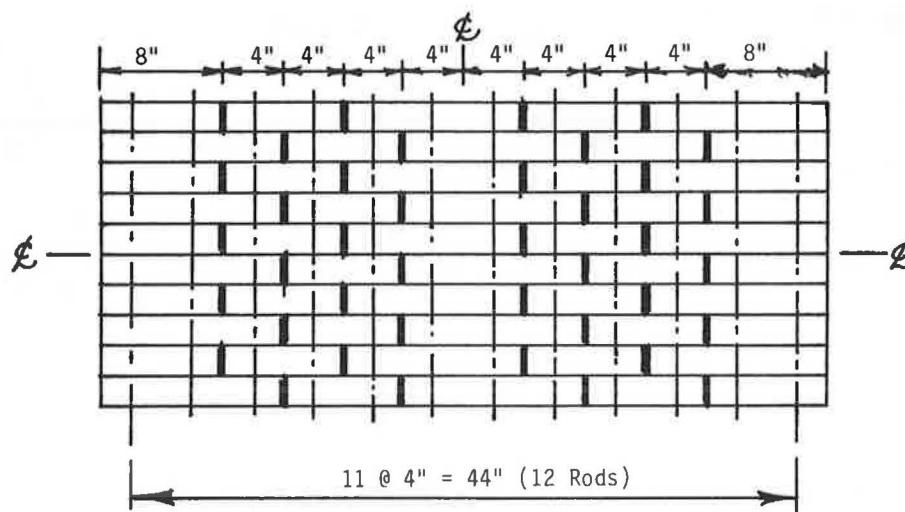
FIGURE 6 Plan view of butt joint pattern for top layer; bottom layer is mirror image.
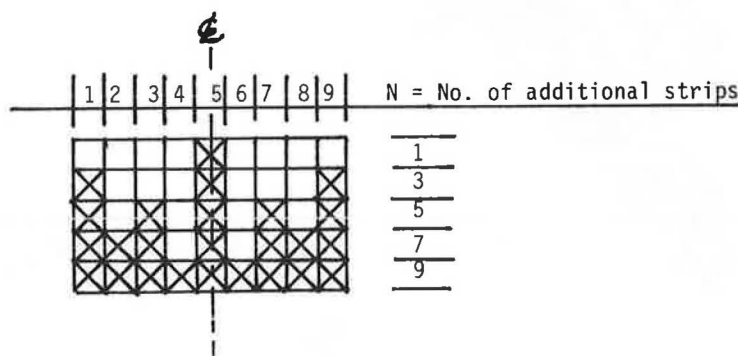

FIGURE 7 Sequence for addition of second set of nine steel strips.

transfer part of it to timbers placed away from the neutral axis. Both steel and timber resist flexural stresses and contribute to the flexural rigidity necessary to resist large displacements. The number and placement of butt joints together with the number of steel strips used become important for the structural action involved. In what follows, stresses in steel and timber are computed to show their variations. Equivalent truck loads are also shown for several conditions.

Figure 8 shows a linear relationship between applied loads and average centerline displacements except when all butt joints are present under the maximum load of 320 lb. With only 20 butt joints present near end supports, the displacement curve lies close and nearly parallel to the curve for no butt joints, indicating that although half of two timber cross sections have been cut away, the structure's flexural rigidity has been affected very little. As more butt joints are employed, the curves are seen to be spaced farther apart, indicating the increasingly detrimental effects of added joints placed closer to the region of high flexure.

It is not surprising that the curve for 80 butt joints lies farthest to the right and diverges from a straight line if it is recalled that 100 pieces of timber and nine steel strips, held together by friction, are being used to resist the maximum loading. The vertical line representing a displacement-span ratio of 1/200 indicates that fewer than 20 butt joints would

be permitted for full load. Intersection of this line with the curve for all 80 butt joints suggests that about 280 lb would be permitted if such a displacement-span stipulation were in effect. As seen later, this 320-lb load will be more than adequate.

Figure 9 illustrates an increased drop in timber modulus of elasticity (MOE) from 1,230 ksi to 865 ksi as the number of butt joints is increased toward 80. Not shown, however, is the drop from the actual modulus of solid wood of 1,405 ksi to 1,230 ksi caused by the use of the composite section in place of solid wood. The modular ratio, defined as the ratio of steel MOE/timber MOE, follows from Figure 9. These values are plotted in Figure 10. The large magnitudes between 24 and 34 shown for the modular ratio suggest the increasingly important contribution to strength made by the steel strips as the number of butt joints increases.

The modulus of elasticity of all steels lies between 29 and 30 million psi. Therefore, high-strength steels provide no better defense against large deflections than low-strength steels. They do, however, have higher allowable stresses.

Maximum timber and steel stresses under full (320 lb) loading are seen in Figures 11 and 12 to be well within usual allowable design stresses. First, for steel with a yield stress of 50 ksi, about two-thirds (33.3 ksi) would be a reasonable allowable design stress where plate buckling is precluded. For
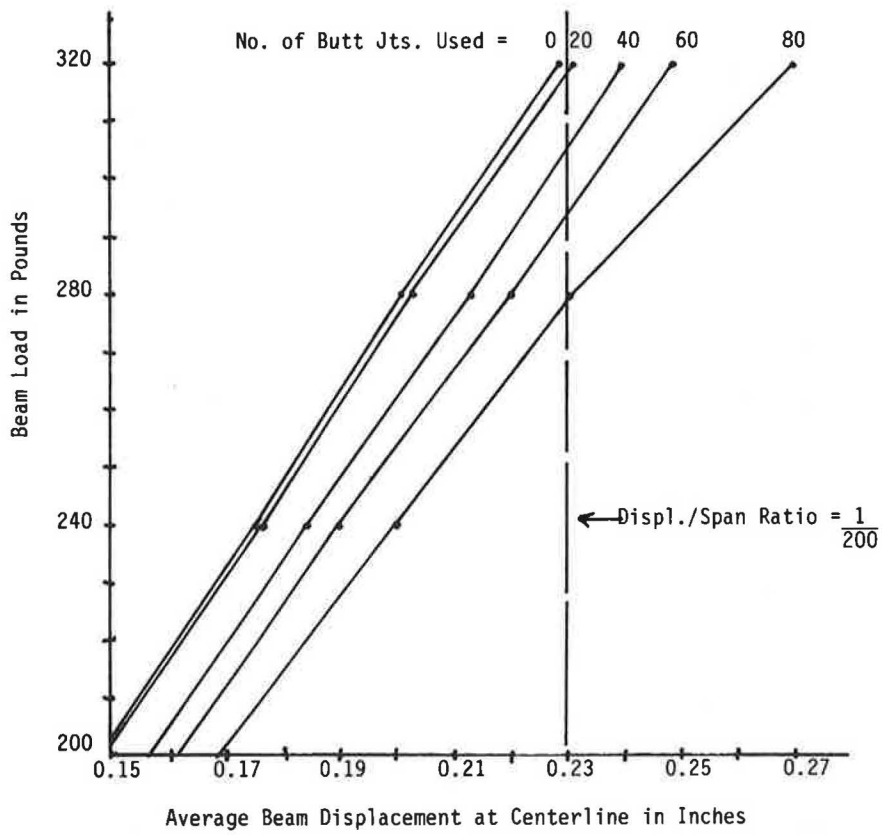
FIGURE 8 Beam load versus centerline deflection for various butt joints (nine steel strips used throughout).
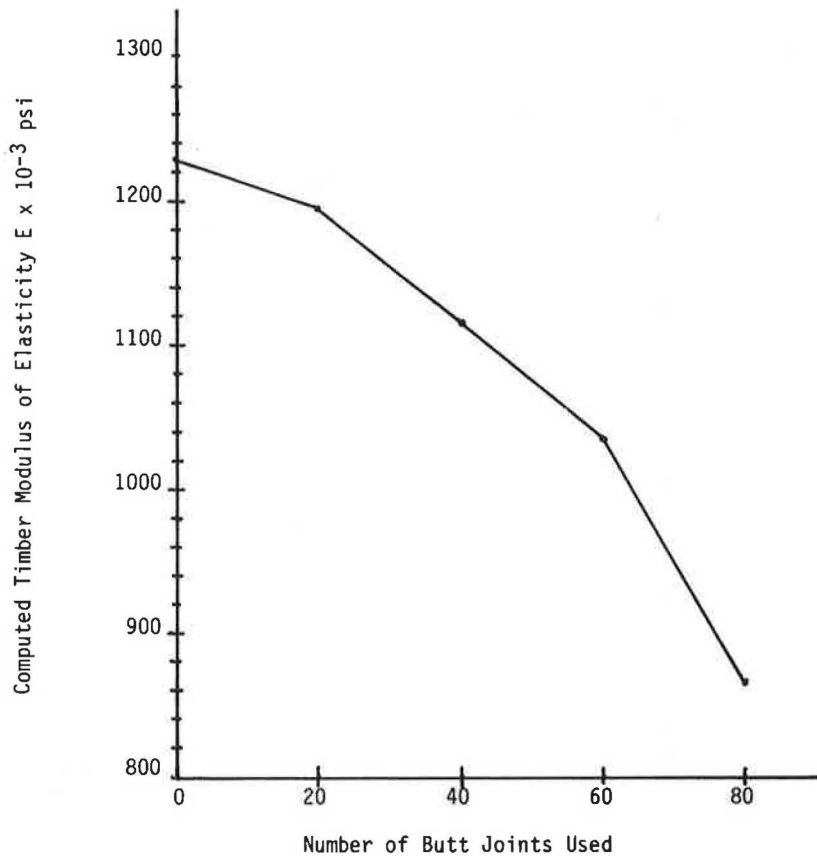

FIGURE 9 Timber modulus of elasticity versus number of butt joints used (nine steel strips used throughout).
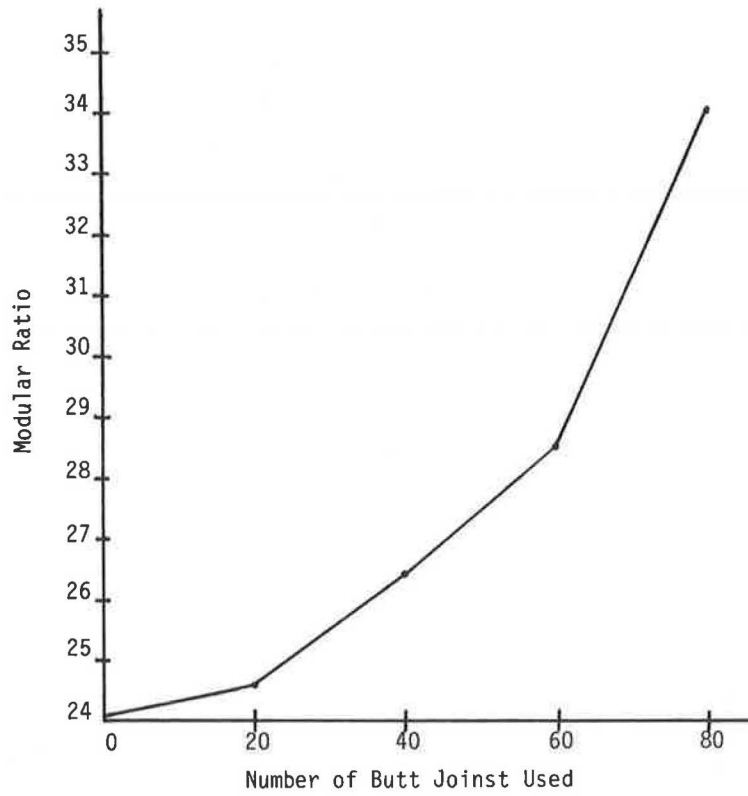
FIGURE 10 Modular ratio versus number of butt joints used (nine steel strips and 320 lbs used throughout).
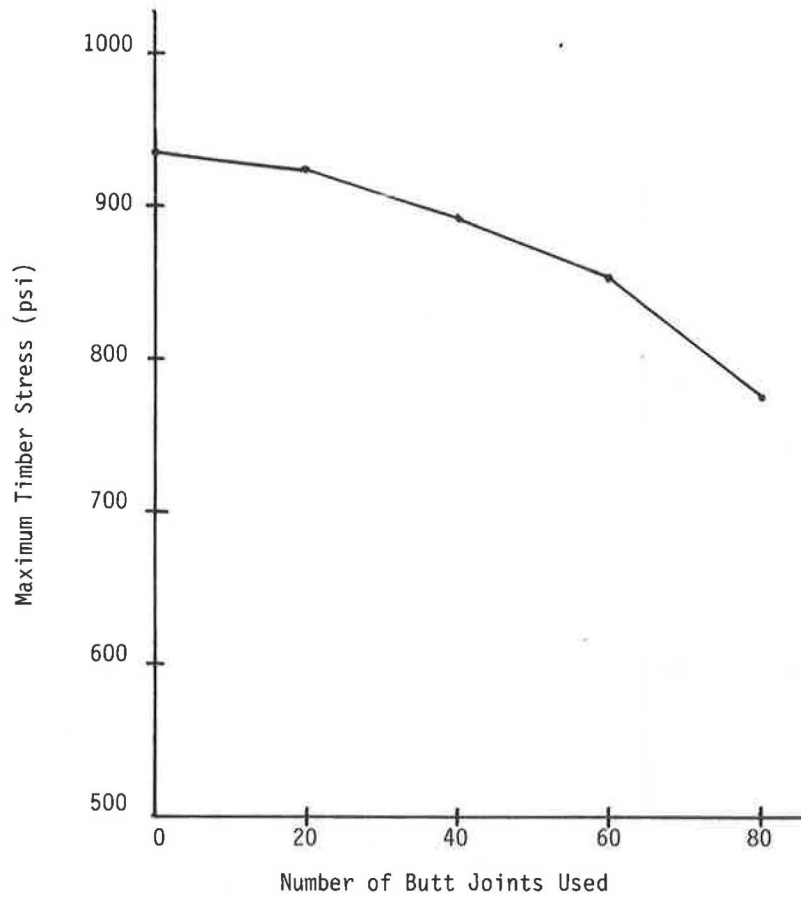

FIGURE 11 Maximum timber stress versus number of butt joints used (nine steel strips and 320 lbs used throughout).
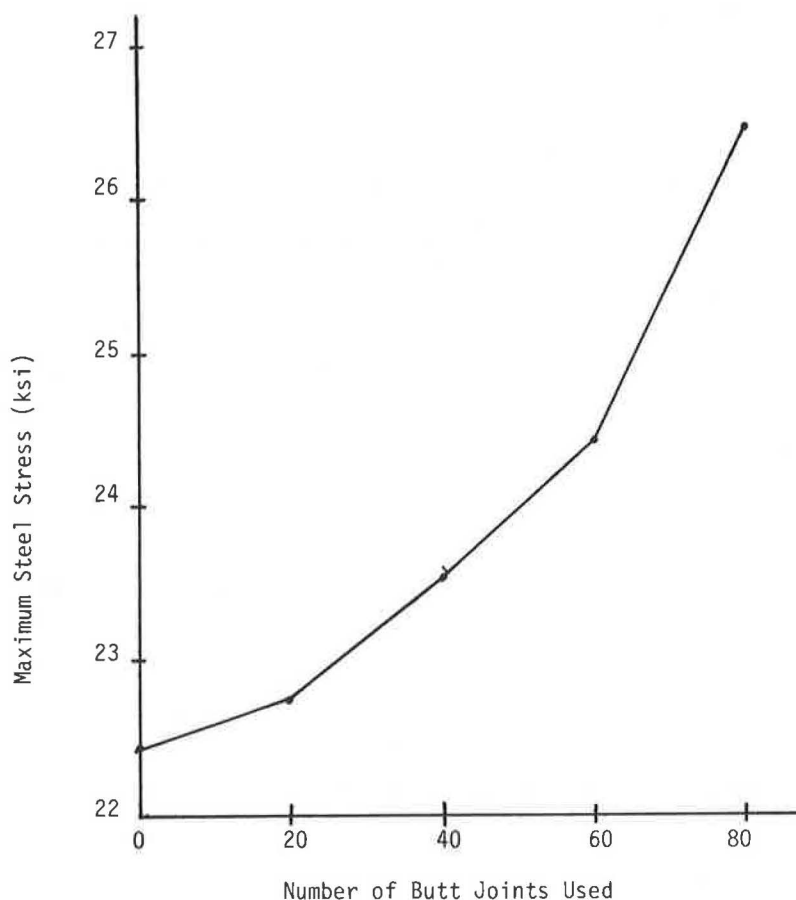
FIGURE 12 Maximum steel stress versus number of butt joints used (nine steel strips and 320 lbs used throughout).

northern red oak, used at a maximum moisture content of 19 percent, the Northeastern Lumber Manufacturing Association lists 1,600 psi as the allowable design stress for select structural beams and stringers. Note the increase in the steel stress curve to compensate for the decrease in the timber stress curve as the number of butt joints increases.

Creep effects were obtained by leaving the full load in place for 24 hr before removing it. Displacements that occurred during that 1-day period are the differences between the broken and solid curves of Figure 13. The two curves converge gradually left to right, indicating better control of creep as the amount of steel used is increased. The horizontal line representing the displacement/span ratio of 1/200 suggests that about 12 steel strips are required to meet such a deflection requirement. Plotted also for 18 steel strips are centerline displacements obtained for closed butt joints. This closing of all butt joints allowed bearing stresses to be transferred between timber ends resulting in a 5.2 percent reduction in deflections.

Flexural rigidity (EI) is a measure of the internal stiffness of a cross section. It is affected by the number and placement of butt joints, by layering of timbers as opposed to solid full-depth timbers, by the amount and arrangement of steel used, and, to some degree, by the lateral compressive stress caused by the stressing rods. As a base, a solid timber deck 5.8 in. wide and 4/3 in. deep, with no butt joints, is used. Together with $E = 1,450$ ksi for the timber, the resulting base EI is 1,609.28 k-in.^{2}. Other values of EI are taken relative to this

base EI. Define a flexural rigidity ratio (FRR) as $FRR = EI/$ base EI.

The variation in this FRR is depicted in Figure 14 as both the number of butt joints and the number of steel strips are varied. The initial value of 1.687 suggests that the composite beam with no butt joints and nine steel strips has 68.7 percent greater flexural rigidity than the beam with a base cross section. As butt joints are added, the FRR is seen to drop to a value of 1.43 for 80 butt joints and nine steel strips. The vertical line shows large FRR increases caused by the addition of more steel strips such that when 80 butt joints and 18 steel strips (9 percent) are employed, the FRR = 2.245. So, despite the decrease as a result of added butt joints, added steel raises the flexural rigidity considerably to 2.245 times the base value for a solid timber cross section of the same depth. These values bear cogitation. This increase in flexural rigidity is shown to be linear in Figure 15.

To gain a better appreciation of load effects, the equivalent truck loading, with three axles spaced at 14 in. apart on the model, was computed as 170 + 170 + 42 = 382 lb versus 320 lb actually applied. Obviously, the concrete blocks were concentrated nearer the centerline but gave the same deflection as the envisioned total truck load of 382 lb. This effect occurs independently of the number of butt joints present.

The study can be carried further by again considering the actual bridge with a 26-ft roadway width and the previously discussed displacement/span ratio of 1/200. Here, axle spac-

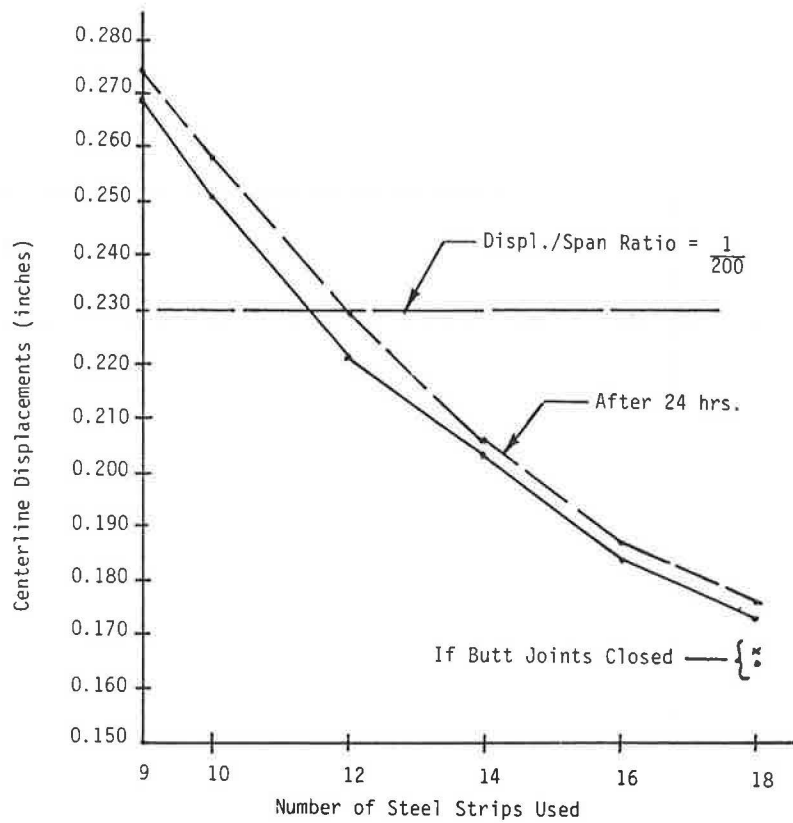**FIGURE 13** Centerline displacements for 320 lb versus number of steel strips used (80 butt joints used throughout).
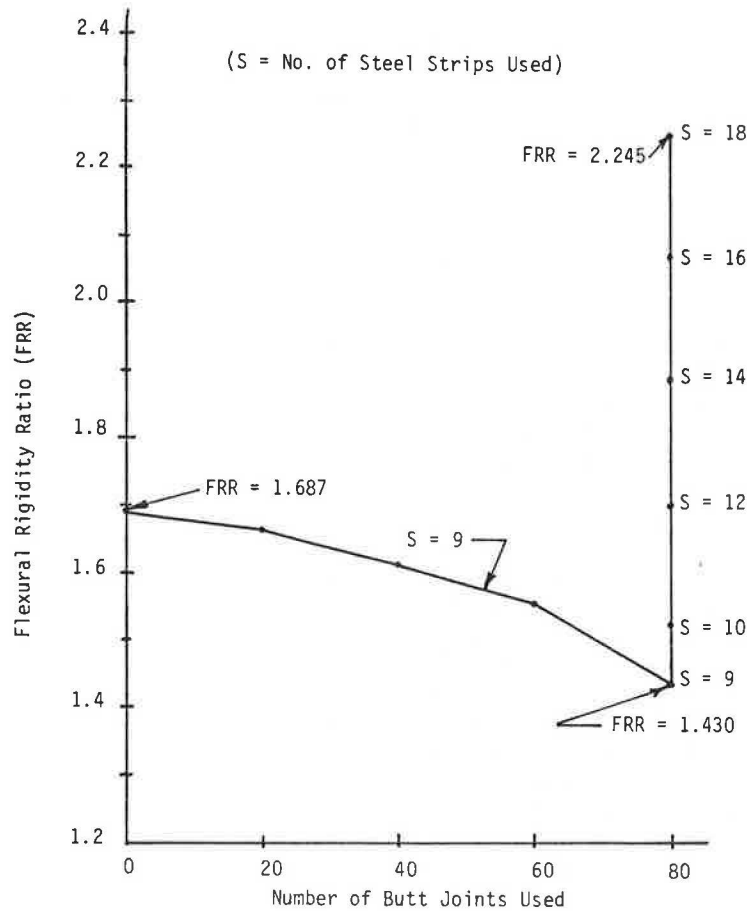

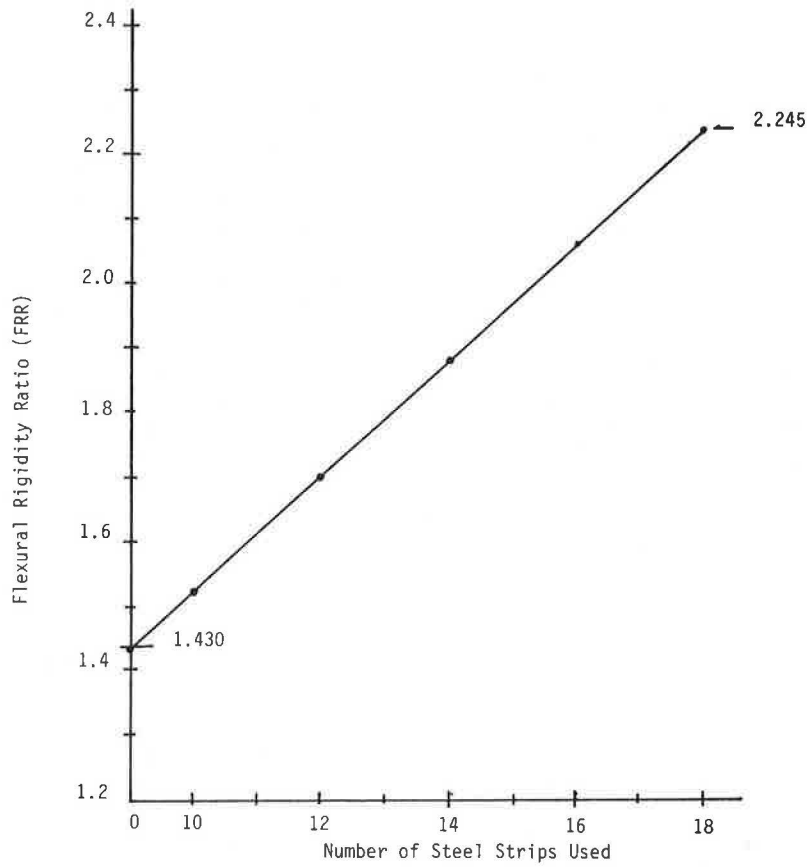**FIGURE 14** Flexural rigidity ratio versus number of butt joints and steel strips used.

FIGURE 15 Flexural rigidity ratio versus number of steel strips used (80 butt joints used throughout).
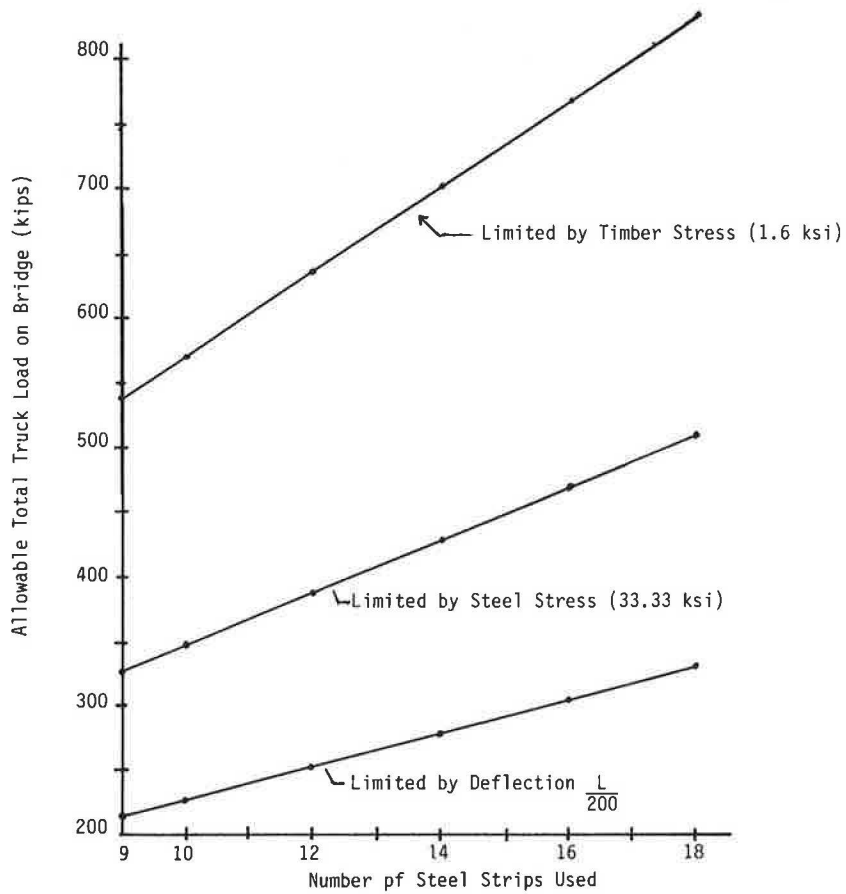

FIGURE 16 Allowable total truck load versus number of steel strips used.

ings of 14 ft and a 4-to-1 axle load ratio are assumed, similar to standard truck loadings of AASHTO specifications. Values of the allowable total truck loads, corresponding to the number of steel strips used for the model bridge, are shown as the lower straight line of Figure 16. The minimum allowable total truck (or trucks) load for the two-lane bridge is 211 kips to limit deflections and with only nine steel strips. Recall that for two HS25-20 trucks, the total load would be $2 \times 90 = 180$ kips.

What about the solid cross section? What allowable truck would it permit? Division of 211 kips by the previously given FRR = 1.43 indicates that $147 < 180$ kips would be allowed. Needless to say, the composite timber-steel deck is quite effective despite the many butt joints. Shown in Figure 16 also are lines representing the allowable truck loads with respect to steel and timber stresses. All curves vary linearly with the amount of steel used. The upper curve represents very high allowable loads based on the allowable timber stress. In other words, excessive timber stress is not the weak link in the design of such composite bilayer bridge decks.

SUMMARY

The composite model bridge deck, with two layers of timbers and with steel strips sandwiched between them, successfully carried larger loads than would normally be expected. Up to 80 butt joints (100 individual timber lengths) caused considerable reduction in the effective timber modulus of elasticity resulting in computed modular ratios between 24 and 34. These high values point to the importance of the nine steel strips used to effectively limit displacements. With 18 steel strips (9 percent of steel) and 80 butt joints, the model was found to have 2.25 times the flexural rigidity of a structure

with the same cross-section dimensions but with solid timbers of the same species and no steel strips.

Results of the one-twelfth scale model were projected to an actual structure. Allowable total truck loads were computed with respect to deflections, steel stresses, and timber stresses. The smallest allowable truck loads were caused by the imposed deflection limitation. The minimum allowable truck load of 211 kips exceeds the 180 kips that would be caused by two standard HS25-20 trucks. Allowable truck loads, based on allowable timber stress for the red oak used, were much greater than needed. An important part of the economical design of such a structure lies in the selection of the proper depth and the correct amount of steel. It is hoped that full-scale testing of the bilayer reinforced stressed timber deck bridge proposed in this paper will commence in the not-too-distant future.

REFERENCES

1. F. W. Muchmore. Designing Timber Bridges for Long Life. In *Transportation Research Record 1053*, TRB, National Research Council, Washington, D.C., 1986, pp. 12–17.
2. R. J. Taylor and P. F. Csagoly. *Transverse Post-Tensioning of Longitudinally Laminated Timber Bridge Decks*. RR220. Ministry of Transportation and Communications, Downsview, Canada, 1979.
3. M. G. Oliva and A. G. Dimakis. *Behavior of Stressed-Wood Deck Bridges*. Report 86-4. College of Engineering, University of Wisconsin, Madison, Oct. 1986.
4. R. R. Mozingo and G. DiCarlantonio. *Trout Road Bridge Project*. Final Report. Department of Civil Engineering, The Pennsylvania State University, University Park, June 1988.

Dunlap's Creek Bridge: Enduring Symbol of American Endeavor

Martin P. Burke, Jr.

The Dunlap's Creek Bridge of Brownsville, Pennsylvania, was the first all metal bridge constructed in the United States. It is located about 25 mi south of Pittsburgh near the Route 40 crossing of the Monongahela River. Designed by Captain Richard Delafield of the Corps of Engineers, it was constructed by ironmaster and steam engine builder John Snowden. Unobtrusively, this unstrengthened bridge continues to carry daily traffic and full legal loads. Although obscure and generally unheralded, it stands today after 150 years of service, an enduring symbol of American endeavor.

John Snowden was probably elated and a little apprehensive that day in 1836 when he learned he had been chosen to cast and erect the new Dunlap's Creek Bridge, the first cast iron bridge to be constructed in America (Figure 1).

THE IRONMASTER

Snowden, the 40-year-old proprietor of the Vulcan Iron and Machine Works of Brownsville, Pennsylvania, emigrated to this country as a young blacksmith from Scarborough, England. With his wife, Mary, and two small daughters, Ann and Elizabeth, he came to western Pennsylvania in 1818 looking for work. After working a short time for wages, he was able to open his own small blacksmith shop. Thereafter, a continuing demand for tools, appliances, and mechanical devices enabled him to build a foundry and machine shop. In 1836, at age 40, he was proprietor of one of the most successful iron manufacturing plants in the region.

When young Snowden first arrived in Brownsville, he found a thriving transportation center. Being a long-established inland port town located at the headwaters of the Monongahela River, it was a major western terminus for the Cumberland Road (National Road). Through it passed immigrant traffic moving west and merchant traffic moving both east and west. As one man observing traffic on the road remarked, "It looked as if the whole earth was on the road, wagons, stages, horses, cattle, hogs, sheep, and turkeys being there without number" (1, p. 253).

At Brownsville, flatboats, keelboats, and other types of river craft were built and made available to settlers bound for the western wilderness by way of the Monongahela and Ohio rivers. When Snowden arrived there in 1818, he found this town, with a widespread reputation for constructing outstanding river boats, pioneering the development of western river steamboats. Within 18 years, Snowden's own Vulcan Iron and Machine Works was successfully competing with nearby Pitts-

burg (Pittsburgh) steam engine manufacturers for local steamboat contracts. So when Snowden was informed that he and his plant had been selected by Captain Richard Delafield of the Corps of Engineers to build the first cast iron bridge in America, he must have realized that this huge contract would be a significant challenge on top of an already challenging career.

The Corps of Engineers was in charge of the repair and reconstruction of the National Road. This early wilderness road was originally opened and periodically improved to encourage immigration of settlers to the West. The road originated at the headwaters of the Potomac River (Cumberland, Maryland) and climbed westward through the Appalachian Mountains. After reaching the western plateau, the road passed through Brownsville, across the Dunlap's Creek Bridge near the Monongahela River and then westward across the Monongahela River toward Wheeling, Virginia (West Virginia).

The old Dunlap's Creek Bridge was located only a few blocks south of Snowden's iron works. It was a multiple span timber structure supported on stone piers and abutments. Built in 1821 by Samuel Story, just 3 years after Snowden arrived in Brownsville, it was the third recorded structure to span the mouth of Dunlap's Creek. The constant and heavy traffic on the road past Snowden's plant and across the bridge had deteriorated the bridge to such an extent that just 11 years after its construction, Lieutenant J. K. R. Mansfield of the Corps of Engineers wrote that "the bridge would not stand a twelve-month" (2, p. 164). Its replacement by Snowden would be the last federal contract for the reconstruction of the eastern section of the road—the most historic section of this nation's most historic road.

THE ENGINEERS

Captain Richard Delafield, superintendent in charge of this reconstruction, and his assistant, Lieutenant George W. Cass, were both graduates of the U.S. Military Academy at West Point. Delafield was a 20-year-old graduate in 1818 and Cass a 22-year-old graduate in 1832. The Academy, founded in 1802, was initially an apprentice school for military engineers, and in effect, was the first school of engineering in the United States. Consequently, both Delafield and Cass and the other members of the Corps who assisted them were probably the most highly qualified group of engineers in the United States at that time.

When Captain Delafield was considering the replacement of the dilapidated bridge, he explained to his superiors why he was proposing to use cast iron for the structure. In a Sep-

Burgess & Niple, Limited, Engineers and Architects, 5085 Reed Road, Columbus, Ohio 43220.

FIGURE 1 The Dunlap's Creek Bridge of Brownsville, Pennsylvania, the first cast iron bridge built in the United States. Photo courtesy of the Prince Maccus Publishing Company.

tember 30, 1833, letter to the chief engineer (3, p. 2), he wrote:

> In the estimates of services of the year I have asked for an appropriation for a cast-iron bridge for Dunlap's Creek, induced so to do from the circumstances of finding no durable stone that will resist the thrust of the arch required to span the creek . . . preferring it to a wooden structure perishable from the decay of timber, and exposed to fire, a risk more hazardous than with the many excellent structures of the kind throughout the country, from the circumstances of there being no guard or toll keeper to prevent travelers carrying fire through it and upon it.

That Captain Delafield was fully aware of the uniqueness of his proposal is revealed in another of his letters to the chief engineer dated March 21, 1836 (3, p. 1).

> In some one of my communications of last fall I intimated that I had matured in my mind the plan of the Cast Iron Bridge to be constructed over Dunlap's Creek—differing in its principles of construction from any of which I could find a notice by either English or French Engineers.
>
> . . . Presuming you would be pleased to see the plans before I can have it in my power to file copies of them in your Department, and that the Secretary of War might wish to see plans of the first Iron Bridge to be constructed in the country,—I have directed Lieut. McKee to pass thru: Washington on his way to Brownsville.

Both Captain Delafield and John Snowden appeared to be fully aware of the difficulty of casting and erecting a cast iron bridge. This is revealed in their agreement to build the structure under a cost-plus contract. This contract would protect Snowden from the uncertainties involved in building such an unusual structure. It would also afford Delafield the oppor-

tunity to exercise more direct control over the purchase of iron, casting, and machining the pieces, and controlling and approving the assembly and erection. Delafield's comments about the unusual aspect of this contract are recorded in his March 21, 1836, letter to the Chief Engineer (4, p. 1). He wrote:

> I propose having the castings made by a foundry at [Brownsville], purchasing all the material myself, paying the mechanics and laborers for the time actually employed, and as a rent for the foundry, use of the Lathes, Engines, workshops, Tools, and skill and service of the proprietor and foreman, give a percentage upon the wages of the people employed—By this course, I secure a choice of metal; and can control the mode of casting in any way it may be found desirable. Lieut. Cass has been ordered to go to the furnaces [at Portsmouth, Ohio] and purchase the pig metal of a quality similar to that used at Pittsburg for Gun metal.

Delafield's reference to the foundry's proprietor and foreman referred to John Snowden and John Herbertson, respectively. Herbertson, like Snowden, came to America as a young craftsman. He was born in Glasgow, Scotland, on September 16, 1805. After being apprenticed to a joiner and cabinetmaker, he emigrated aboard the ship *Commerce*, arriving here in 1822. He settled first in Pittsburgh and worked in one of the many steam engine manufacturing plants there. He then moved to Brownsville about 1827 to work on the steamboat *Highlander* and to become foreman in John Snowden's machine shop.

John Snowden had previous contracts with the Corps of Engineers. One of the largest was a contract to furnish the cast iron mile markers for the portion of the National Road between Brownsville and Wheeling. However, the contract

to cast and erect the new Dunlap's Creek Bridge could well be the most difficult project that he; his foreman, John Herbertson; and the rest of his employees had undertaken.

THE BRIDGE

Details of Delafield's design are illustrated on Figure 2, a copy of Sheet 2 of record drawings for the bridge, drawings that are signed by Captain Delafield. On the left, the assembled structure is shown with lower elliptical arch segments (voussoirs) supporting lattice-type triangulated spandrel members, roadway retainer plates, and a wrought iron sidewalk railing. The structure is described in an original memoir dated September 27, 1837, and signed by both Delafield and Cass (5, p. 206).

The Abutments and Wing Walls of this bridge are Built of sandstone. The abutments are 25' across the front, 14' thick and an average height of 42'.

The span of the arch is 80' and the rise 8'.

The arch is composed of 5 ribs 5'.77 distant from centre to centre;. . . .

The massive, or lower part of each rib is composed of nine pieces, or segments, of equal lengths called voussoirs. The voussoirs composing the same rib are not in immediate contact: transversal, or cross plates traversing at right angles all the ribs.

The voussoirs are hollow; a section gives two concentric ellipses . . . the transversal and conjugate axis of the outer ellipses are 2'-6" and 10 ¾" . . . , the thickness of the voussoirs being 1.37".

To prevent lateral motion, cross plates traverse at right angles all the ribs, and are as many in number as there are joints between the voussoirs of each rib. The cross plates are 24'-8" from out-to-out, 2'-6" wide and 2½" thick . . . .

As illustrated and described, the casting, machining, and assembly of the parts of this structure would be a challenge even for today's bridge fabricators. For Snowden, Herbertson, and the other iron workers, the number and size of castings required for this structure must have appeared intimidating, considering the relatively crude equipment available to them in 1836. For example, there were to be a total of 250 castings. The curved tubular arch rib segments each weighed 1½ tons. The immense 24-ft-8-in.-(7.52-m) long transverse brace plates weighed 2½ tons apiece. The work was further complicated because the various parts of the structure—arch segments, transverse brace plates, spandrel supporters, and curved floor plates—had to be cast and finished to tolerances close enough to assure a suitable structural fit.

When Delafield chose ironmaster John Snowden to furnish all of the iron work for the Dunlap's Creek Bridge, he apparently had full confidence in both Snowden and Herbertson. This confidence was probably based on his own inspection of Snowden's forge, foundry, and machine shops where he could observe pattern and mold making and the casting and machining of steam engine parts and other mechanical equipment. Because the first steamboat built in Brownsville, the *Comet*, was launched in 1813, by 1833 local labor and skilled craftsmen had up to 20 years of iron working experience building steamboat engines of greater and greater size.

It may not be entirely coincidental that the tubular segments chosen by Delafield for the arch ribs of the Dunlap's Creek Bridge appear similar to the cylinders being made at that time for steamboat engines (Figure 3). In fact, the work of the engine builders may have been the inspiration for Delafield when he first contemplated using cast iron for the Dunlap's Creek Bridge.

BRIDGE CONSTRUCTION

To supplement his own facilities at the Vulcan Iron and Machine Works, Snowden rented the vacant William Cock Foundry to cast the huge pieces for the bridge. This foundry was located at the corner of Water and Bridge streets, immediately southwest of the bridge site.
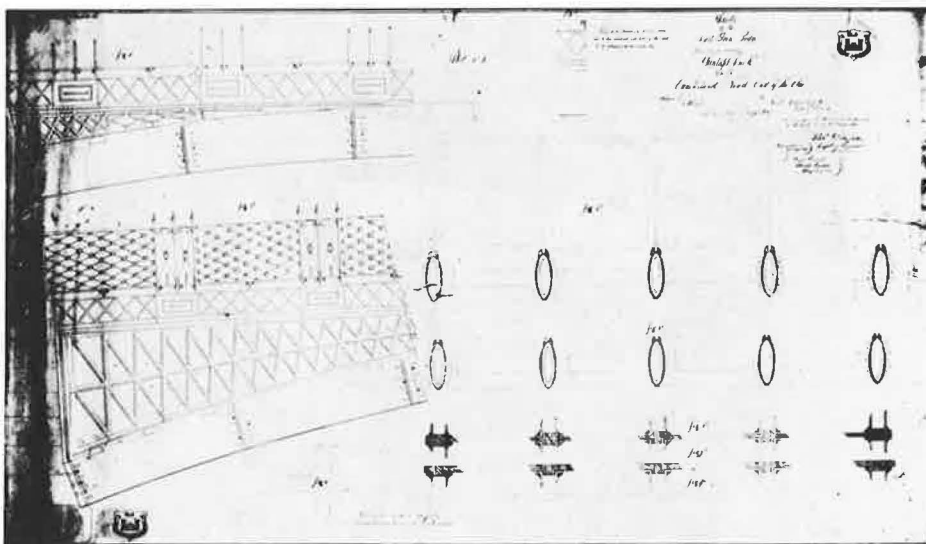

FIGURE 2   Record plan of the Dunlap's Creek Bridge signed by the designer, Captain Richard Delafield. Photo courtesy of the Museum of American History.

Construction of the extensive masonry abutments and wing-walls began late in 1836 under a separate contract with Messrs. Keys and Searight. They finished their contract in September 1837. Construction of the structure was not uneventful. In a November 1837 report, George Cass summarized his experiences as follows (*3*, p. 5):

> Everything seems to have gone wrong since the commencement of this work and I do hope that I may never have such another job in my life again. It has from the beginning to this time given me more trouble and uneasiness than a work of 10 times the magnitude ought to have done—and the only consolation that I have is that I have tried to do the best for the government and believe that I have done as well as would have been done by anyone else although perhaps not as well as could have been done.

Erection of the cast iron tubular arch segments, transversal plates, spandrel supporters, curved 1-in.-thick floor plates, and roadway retainer plates were probably assembled under John Herbertson's direction. Erection of the superstructure advanced to the extent that the structure was opened to traffic in July 1838 just 1 year before its completion and dedication.

Problems with superstructure erection appear to be revealed in a final report containing a summary of relative costs for various portions of the structure. The masonry abutments accounted for 50 percent of the total cost of the structure. Purchasing pig metal and making 250 castings accounted for 24 percent. Fitting castings accounted for 12 percent of the total cost, or one-third the cost of the superstructure. Although fitting castings probably included the cost of machining and grinding, this high cost for assembly suggests problems of geometric stability and dimensional control made more difficult by the immense size of some of the pieces that had to be cast, manipulated, and machined.

After erecting the superstructure, the cast iron surfaces were covered with a coat of "gas tar" and three coats of white lead paint (*4*, p. 4). It was officially dedicated on Independence Day, July 4, 1839.

Observing the structure 5 years later, the historian Sherman Day was inspired to write, "It [the Dunlap's Creek Bridge] is the only one of its kind, and probably the most splendid piece of bridge architecture in the United States" (*6*, p. 149) (Figure 1).

FIGURE 3 Tubular arch segments of the Dunlap's Creek Bridge. Photo courtesy of the Museum of American History, Washington, D.C.

EPILOGUE

The designers and builders of the Dunlap's Creek Bridge were more successful than they could have imagined. Its two immediate predecessors survived less than 24 years. Judge James Finley's chain link suspension bridge collapsed after only 9 years, and Samuel Story's multiple span timber structure rapidly deteriorated to a "dilapidated condition" in less than 15. In contrast, the Delafield/Snowden cast iron arch structure has now been serving traffic for 150 years.

A number of circumstances contributed to the bridge's survival. Obviously, it was well designed, well built, and constructed of durable materials. Development of the canal systems and railroads diverted much of the early heavy traffic away from the National Road and the bridge. Finally and fortunately, relocation of Route 40 (National Road) at Brownsville relieved the structure of the heavy traffic characteristic of a mainline highway.

After constructing the Dunlap's Creek Bridge, its designers and builders continued to lead eventful lives in service to their neighbors and their nation. Richard Delafield served as superintendent of the U.S. Military Academy at West Point, Chief of Engineers of the U.S. Army, and Head of the Corps of Engineers. George W. Cass, who was in charge of all aspects of the bridge's construction, had an eventful career in the field of transportation. He organized the first steamboat line on the Monongahela, established an express company, and became president of a number of railroad companies. He was twice the Democratic candidate for governor of Pennsylvania. John Snowden continued building steam engines and steamboats. During the Civil War, he once again expanded his plants to build the revolutionary steam-powered river monitors, *Manayunk* and *Umpqua* for the Union Navy. Family tradition says that John Herbertson drew the plans for the bridge (probably the shop drawings), made the patterns, and supervised the casting. He took over the rented William Cock Foundry where the bridge castings were made and it became known by his name. He and his sons continued there to build steam engines and other mechanical equipment for the boat building industry.

Today, the Dunlap's Creek Bridge can be found on a quiet street in Brownsville, Pennsylvania. Its once glistening white paint has long since been lost to dull gray; its once graceful arches are now shadowed and partly hidden by structural brackets and protruding sidewalk slabs. Vacant and decrepit buildings that line the street and crowd the creek are its silent companions. The immigrant traffic has long ago disappeared into dusty histories; the clatter and rattle of horse-drawn wagons and the reverberating echos of steamboat whistles have faded from memories; and the quiet steps of an occasional stroller have replaced the scurry of anxious pedestrians. Occasionally,

the blast of a trucker's trumpet horn shatters the stillness and raises to consciousness the steady swish and whine of high-speed highway traffic as it passes by overhead. Solitude now reigns where once tumult was king.

Amidst decay and neglect the bridge still stands, an obscure monument marking the end of the long wilderness road from Cumberland to Brownsville, the first port of embarkation for the voyage to the "land of promise." For those who know and care to remember, the silent presence of this first iron bridge evokes thoughts and visions not only of the immigrant traffic that the road and bridge made possible, but also of engineers Captain Richard Delafield and George W. Cass who designed the bridge and supervised its construction, engine builders John Snowden and John Herbertson who built the bridge, and all of the other individuals who helped to open the road and rivers for the great migration to the West. The Dunlap's Creek Bridge has become a lasting testament to their ambitions, efforts, hardships, and accomplishments. Although obscure and generally unheralded, it stands today after 150 years of service, an enduring symbol of American endeavor.

ACKNOWLEDGMENTS

REFERENCES

1. W. O'Meara. *Guns at the Forks*. Prentice-Hall, Englewood Cliffs, N.J., 1965.
2. T. B. Searight and R. Bruce. *The Old Pike: And The National Road*, Reprint. Prince Maccus Publishers, Berryville, Va., 1983.
3. Anonymous manuscript (possibly prepared by L. N. Edwards for *A Record of the History and Evolution of Early American Bridges* but not included in it). HAER Collection, Library of Congress, Washington, D.C.
4. *Notes Concerning the Construction of the Dunlap's Creek Bridge Between Brownsville and Bridgeport, Pennsylvania*. Office, Chief of Engineers, U.S. Army, Washington, D.C., 1922.
5. J. F. Bell. The First Iron Bridge in America. *The Military Engineer*, Vol. XVI, No. 87, 1924.
6. R. S. Kirby and P. G. Laurson. *The Early Years of Civil Engineering*. Yale University Press, New Haven, Conn., 1932.

Steel Arches Used in Bridge Reconstruction Over I-5

John A. Van Lund, Robert L. Chen, Yesh A. Mhatre,
and Umesh C. Vasishth

This article reviews the design and reconstruction of the Capitol Boulevard Bridge over I-5 in Olympia, Washington. The existing superstructure was retained, and a new arch supporting system was designed to replace the existing concrete piers as part of a $130,000,000 Interstate widening project. The paper describes the structure types studied, the external peer review comparing the constructibility of the concrete and steel alternatives, and the influence of aesthetics on the selection of the final structure type, two steel arches. The design of the tieback wall system, spread footing, elliptical twin-cell box arches, and load transfer by jacking is also described. The cost of the reconstruction was $3,900,000, including $1,600,000 for the tieback retaining wall system.

A decade-long project to widen 7 mi (11.3 km) of I-5 through Olympia, Washington, is scheduled for completion in 1992 and will cost $130,000,000. Of the 18 bridges spanning I-5, the Capitol Boulevard undercrossing (Figure 1) posed the most interesting engineering challenge. At this location, I-5 is 70 ft (21.4 m) below the Capitol Boulevard Bridge and is confined by embankments on each side. As originally constructed, I-5 had two lanes in each direction separated by a median. Together with shoulders, the overall width was 80 ft (24.4 m); the widening increased the number of lanes to four in each direction and increased the overall width to 146 ft (44.5 m).

The Capitol Boulevard undercrossing was built in 1957 to span the proposed location of I-5, which was to be carved out of a steep natural hillside. This continuous steel plate girder bridge has three spans of 84, 110, and 84 ft (25.6, 33.5, and 25.6 m) with girders spaced at 14.25 ft (4.34 m). The roadway width is 56 ft (17.1 m) curb to curb with two 6-ft (1.83 m) sidewalks. The existing reinforced concrete piers are 75 ft (22.9 m) high, and I-5 below is confined to the 110-ft (33.5 m) middle span between piers. The angle between the centerline of the bridge and that of I-5 is 81 degrees. This angle together with the restrictions caused by the existing piers limited further widening of I-5 to three lanes in each direction with little or no room for inside shoulders.

SITE AND TRAFFIC CONSIDERATIONS

The problem was clearly defined: how to squeeze additional lanes for I-5 under the existing bridge. Several factors made saving the existing bridge superstructure economical. Structurally the deck and girder system were in sound condition.

The steel used in the girders was 50 ksi (344 MPa) high-strength steel, which was not as widely used as ASTM A7 36 ksi (248 MPa) steel in 1957. The concrete in the deck was not cracked, spalled, or deteriorated. There were telephone cables, a gas line, and a recently relocated water line on the bridge. The existing alignment could not be improved without drastically filling and regrading the site. Therefore, building a new bridge adjacent to the existing bridge would be expensive.

I-5 is the only major north-south Interstate highway between the port cities of Portland, Oregon, and Seattle, Washington. It is the primary commercial artery from San Diego, California, to Vancouver, British Columbia. Therefore, a fundamental design consideration, in addition to saving the existing bridge superstructure, was that traffic on the bridge as well as on I-5 below could not be halted or interrupted. However, traffic could be shifted from side to side during construction.

STRUCTURE TYPE

Eight structure types (Figure 2) were considered as replacements for the existing piers. Preliminary sketches were prepared and submitted for architectural review. The concrete sloped-leg portal frame (Figure 3) and steel arch (Figure 4) were selected for further study. Models were built that allowed the aesthetics of the alternatives to be compared, indicated how each blended with the natural environment, and permitted critical evaluation from different perspectives. Specific factors considered in selecting the final structure type were function, form, proportion, color, character, economy, con-
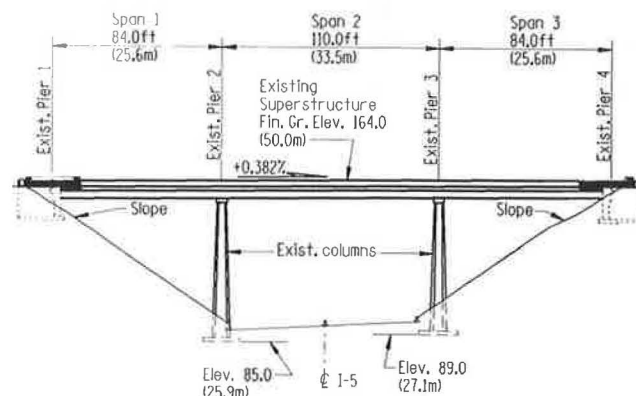

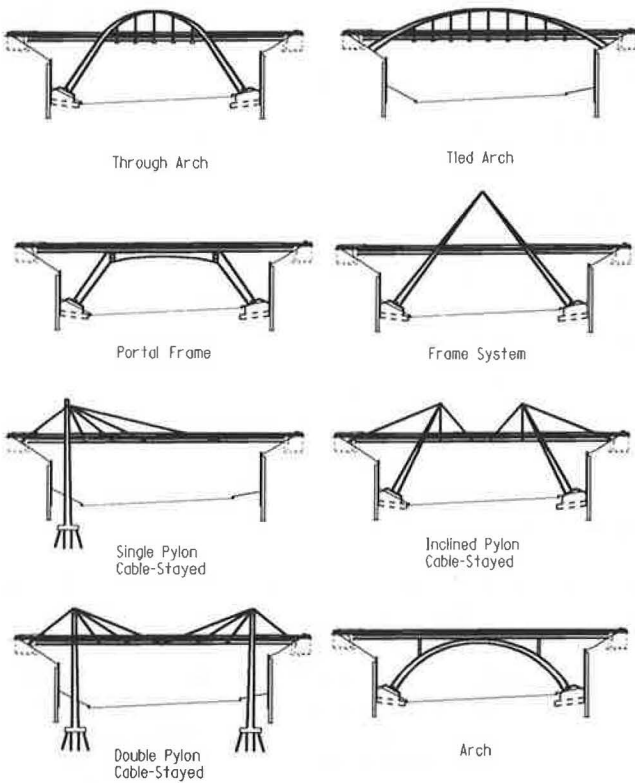**FIGURE 1 Existing structure before rehabilitation.**

FIGURE 2 Replacement structure types.

FIGURE 3 Concrete portal frame alternative
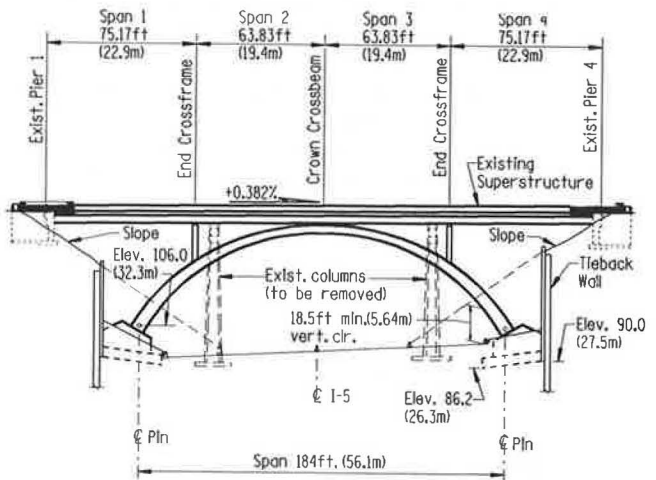
FIGURE 4 Steel arch alternative.

structibility, and most important, potential hazard to the highway users.

EXTERNAL PEER REVIEW

The external peer review of the cost estimates and constructibility of the concrete sloped-leg frame and steel arches was prepared by Andersen Bjornstad Kane Jacobs, Inc., Consulting Engineers, Seattle, Washington. It was determined that the concrete sloped-leg frame would be 43 percent less expensive to construct than the steel arch, not including the cost of the tieback walls.

To construct a cast-in-place sloped-leg concrete frame would require falsework on and over I-5 and would necessitate shifting traffic for a period of 5 to 7 weeks. This time frame would allow for constructing falsework, placing forms and concrete, curing of concrete, and form and falsework removal. The outside lanes of I-5 would be closed and a wider median constructed to accommodate a center falsework bent. The construction required for this option would cause traffic interruptions and potential hazard to the highway users.

Precast elements could be used in the sloped-leg concrete frame, which would reduce the traffic hazard period to 3 or 4 weeks. However, erection of two center struts weighing approximately 70 tons (63.5 metric tons) would require closing I-5 if they were cast full-length and erected without a center falsework bent. Halting traffic on I-5 for any period was unacceptable. If the center span struts were cast in two pieces, a

center falsework bent would be required and would pose construction problems similar to those of the cast-in-place frame.

The steel arch alternative would require no falsework. The steel elements could be supported by the existing Capitol Boulevard Bridge girders. It would be necessary to restrict traffic to the two center lanes on the Capitol Boulevard Bridge, without load restriction, until the arch was self-supporting. Traffic on I-5 below would have to be shifted from side to side during delivery and erection of the center crown crossbeam, two end crossframes, and four arch halves. One week would be required to erect and connect all elements of the steel arch assuming that all components of the arch were properly fabricated.

The external peer review concluded that the steel arches would cause the minimum traffic interruption and hazard to the public.

AESTHETICS

An aesthetically correct structure causes the observer to experience a positive emotional experience as a result of his or

her visual perception of the simplicity, strength, and purpose of a structure. According to F. Leonhardt (1):

> The arch is the strongest embodiment of a bridge, its shape expresses obviously its ability to carry the loads across a river, valley, or gorge. Therefore, arch bridges are considered beautiful by their evidently suitable shape. This is valid for small and large arch bridges alike.

From the standpoint of aesthetics, the curved lines of the steel arch are more pleasing than the straight lines of the concrete sloped-leg frame.

Three major factors favored the selection of the steel arch: ease of construction, minimal hazard to the highway users, and beauty.

PERMANENT SHORING WALLS

Before constructing the arch foundation, excavation of the steep slopes was necessary. To provide space for constructing the arch foundation and to prevent sliding of the existing end abutments of the Capitol Boulevard Bridge, a permanent retaining wall system with a maximum height of 54 ft (16.5 m) was needed. Site conditions, such as the close proximity of the proposed arch abutments, the limited vertical clearance under the bridge, and the close proximity of the existing end abutment footings, limited the type of wall that could be constructed.

Four wall types were studied: a conventional tieback retaining wall, an element wall, general proprietary wall systems, and a hand-dug reinforced concrete soldier pile wall. The tieback retaining wall with soldier piles placed through holes in the bridge deck was chosen as the most feasible option.

Soil Conditions

All the soils at the site are glacially consolidated with near horizontal bedding planes. In general, the soils consist of loose-to-medium-dense silty fine sand or sandy silt above elevation 90 (27.5 m), and medium-dense-to-dense silty sand below elevation 90 (27.5 m). A 10- to 15-ft-(3.0- to 4.6-m)-thick layer of wet silt was encountered between elevation 95 to 108 (29.0 to 32.9 m). No static groundwater was found in the four test holes drilled at the site.

Earth Pressure Coefficients

The tieback wall was designed to resist static and earthquake-induced earth pressure. For a wall with another structure within a lateral distance equal to twice the wall height the average static pressure coefficient, $\overline{K}$, is determined from the following equation (2, p. 40):

$$\overline{K} = K_o - (x/2H)(K_o - K_a) \tag{1}$$

where

x = lateral distance from adjacent structure to wall,
H = wall height,
K_o = coefficient of at-rest earth pressure, and
K_a = Coulomb's active earth pressure coefficient.

The pressure diagrams for $\overline{K}$, the lateral pressure resulting from the soil overburden, and weight of the existing bridge abutment are shown in Figures 5a, 5b, and 5c.

The lateral earthquake earth pressure coefficient was determined from a Mononobe-Okabe pseudo-static analysis. The additional dynamic earth pressure coefficient, ΔK_{ae}, was assumed to be uniformly distributed along the wall and computed as follows:

$$\Delta K_{ae} = K_{ae} - K_a \tag{2}$$

where

K_{ae} = the coefficient of lateral earthquake earth pressure, and
K_a = Coulomb's active earth pressure coefficient.

Soldier Piles

Soldier piles were spaced from 6.0 to 7.5 ft (1.8 to 2.3 m) apart and were fabricated from two HP 12- × 84-pile sections that were butt-welded at the flanges (Figure 6). As many as eight tieback anchors were required for each soldier pile because the maximum depth of excavation was 54 ft (16.5 m). These tieback anchors were drilled at an angle of 15 degrees to the horizontal. Large vertical forces from the vertical component of the tieback anchor forces were resisted by an allowable skin friction value of 1 kip per square foot (47.9 kN/m²) and an allowable end bearing value of 5 ksf (239.4 kN/m²) at the bottom of the soldier pile.

Anchors

The high-strength steel prestressing strands were designed for anchor loads ranging from a low of 60 kips (267 kN) to a high of 125 kips (556 kN). The capacity of each anchor is dependent on the type of anchor installed, drilling equipment used, experience of the contractor, and quality of workmanship. Four anchors on each wall were verified by performance tests. In addition, each anchor was prooftested before acceptance. To ensure long-term stability of the tieback wall, the free stressing length or no-load zone was extended beyond the critical failure plane, but not less than 17 ft (5.2 m) into the soil in order to avoid unacceptable prestress losses resulting from creep in the anchor or soil. The tieback wall and anchor configuration are shown in Figure 7.

The complete encapsulation of the anchor was accomplished by installing the anchor in a corrugated high density polyethylene tube and pressure grouting inside and outside the tube. In the no-load zone nearest the wall, the strands were individually greased, sheathed, placed in the polyvinyl chloride (PVC) or high-density polyethylene tube and pressure grouted inside the tube. They were not grouted on the outside, but were surrounded by a nonstructural filler such as a weak soil-cement mixture.

Timber Lagging

Treated timber lagging was 4 × 12 in. (10.2 × 30.5 cm) for soldier pile spacing 7.0 ft (2.13 m) or less, and 6 × 12 in.
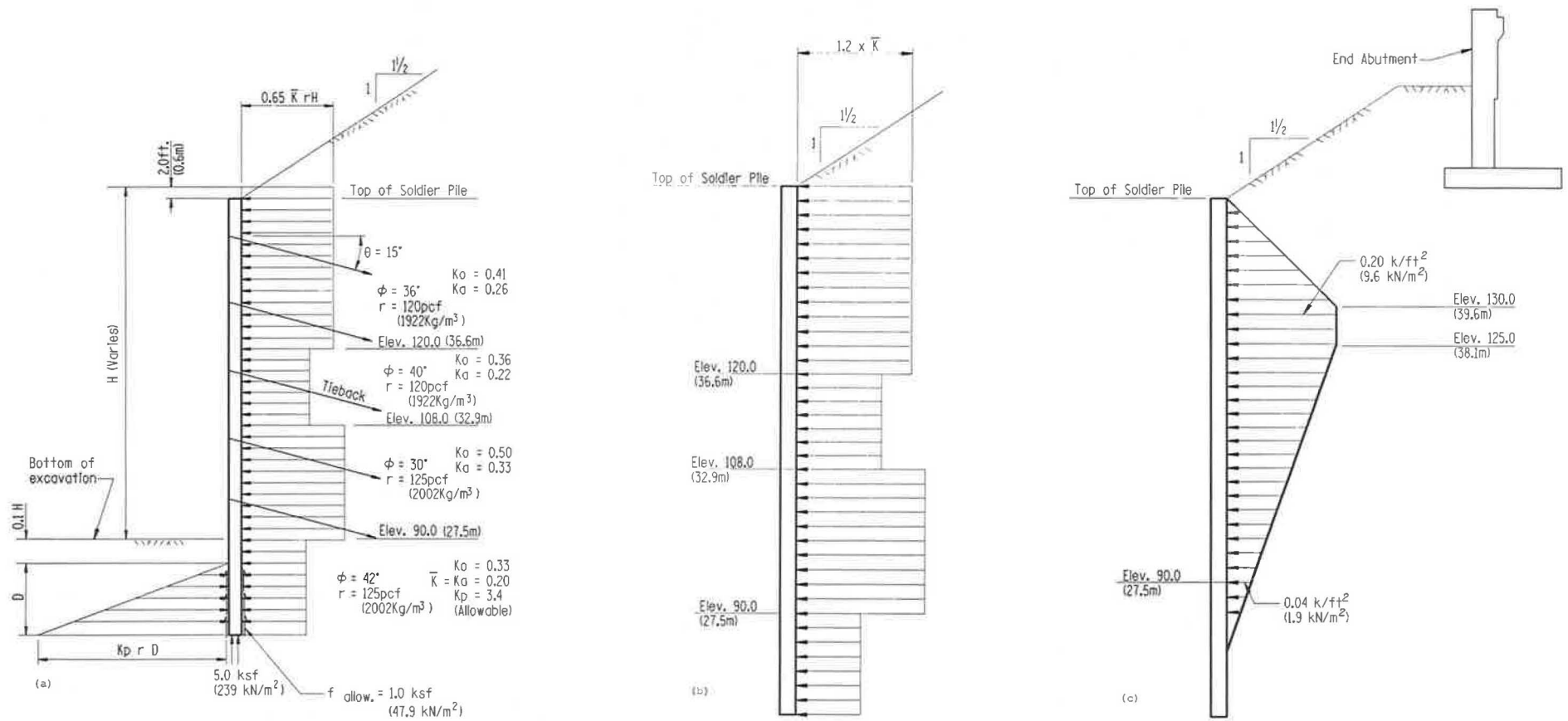
FIGURE 5 (a) Static soil pressure coefficient, $\overline{K}$, on tieback wall. (b) lateral pressure resulting from soil overburden on tieback wall. (c) lateral pressure resulting from weight from existing end abutment on tieback wall.
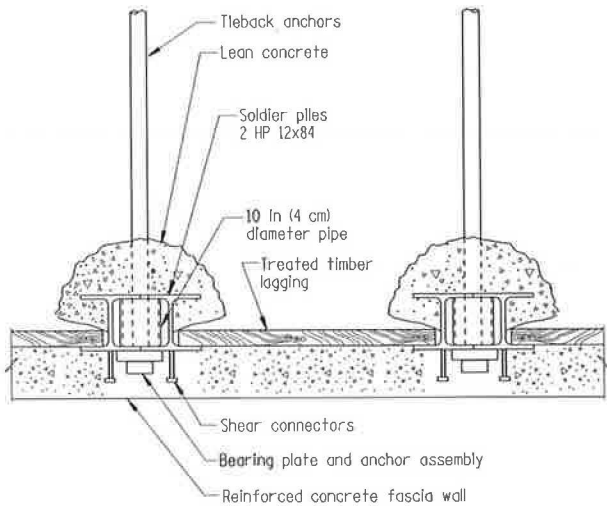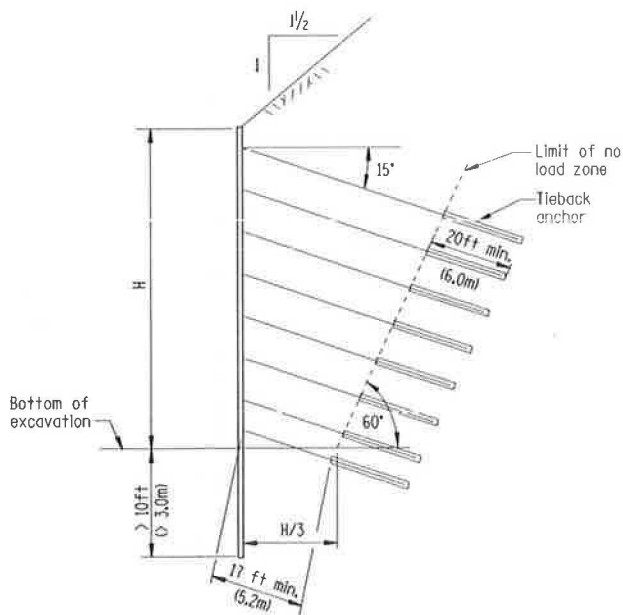
FIGURE 6 Tieback wall cross section.

FIGURE 7 Tieback wall anchor configuration.

(15.3 × 30.5 cm) for soldier pile spacing greater than 7.0 ft (2.13 m).

The lagging was designed for a uniformly distributed pressure equal to 50 percent of the lateral earth pressure and was assumed to be simply supported between the soldier piles. The 50 percent reduction was a result of the soil arching effect behind the wall. The uniform pressure distribution approximating the actual parabolic distribution was derived from Terzaghi's experiments (*3*, p. 267).

Fascia Wall

The reinforced concrete fascia wall has a minimum thickness of 12 in. (30.5 cm). The concrete strength had a compressive strength of 3,000 psi (20.7 MPa) and was anchored to the soldier piles by two rows of concrete shear connectors spaced 12 in. (30.5 cm) on center. The exterior of the fascia wall had a fractured fin finish.

ARCH FOUNDATION

Arch bridges are normally founded on rock. Any movement of the support, particularly for fixed-end arches, will produce additional stress on the arch and, if not corrected, lead to a sag at the crown. Rock stratum does not exist at this site; therefore, the arch would have to be supported on either a spread footing or a pile-supported footing.

When compared to pile-supported foundations, spread footings are relatively inexpensive. Driving and splicing piles under the existing Capitol Boulevard Bridge would be expensive because of the limited vertical clearance and would conflict with the adjacent tieback retaining wall. The reinforced concrete arch abutment and spread footing (Figure 8) were more economical to construct than a pile-supported foundation. The bottom of the footing was located at the top of the medium-dense-to-dense silty sand layer to avoid a layer of compressible sandy silt. The total weight for each arch abutment, including the 31.5- × 37.5- × 5-ft-thick (9.6- × 11.5- × 1.5-m)-thick footing, was 825 tons (748 metric tons). The settlement for total dead and live load, which produced a maximum foundation pressure of 3 tons per square foot (287.3 kN/m²), was estimated to be 2.7 in. (6.9 cm).

Space under the arch pin bearings was provided for six 100-ton (90.7 metric ton) jacks so that the arch could be restored to its original position (if unanticipated and excessive foundation settlement should occur). All settlement was expected to occur within 2 weeks after load transfer from the existing piers to the arches. Footing settlement was monitored continuously during construction.
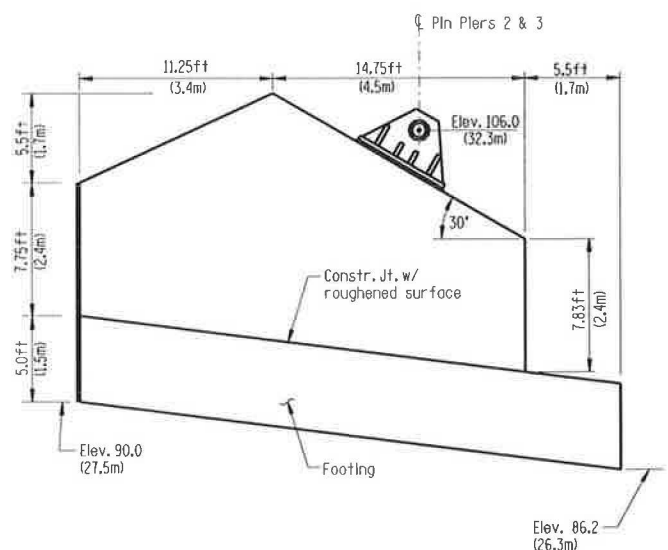

FIGURE 8 Reinforced concrete abutment and footing.

ARCHES

Unique Elliptical Arch Shape

A two-hinged arch was chosen because of potential support settlement, which in a fixed arch would produce large moments. The hinges or pins are located at each abutment. For a two-hinged arch with a rise-to-span ratio greater than 0.2, the ideal arch shape for a uniform dead load over the entire span is a parabola (*4*, p. 121). Modern steel arch bridges have such a shape (*5*, p. 281–303; *6*, p. 626; *7*, p. 124).

Three major geometrical constraints dictated the arch shape: minimum span and rise, maximum vertical clearance for traffic on the inside lane and shoulder of I-5 below the arch, and adequate vertical clearance beneath the existing pier crossarms to permit existing pier demolition. Clearances for parabolic and elliptical shaped arcs were compared. The parabolic arc provided more clearance beneath the pier crossarms, but the elliptical arc provided greater vertical clearance for traffic beneath the arch, which was a major factor favoring the choice of a symmetrical elliptical arc (Figure 9) for the arch shape.

The equation of an ellipse is

$$x^2/a^2 + y^2/b^2 = 1 \qquad (3)$$

The parametric coordinates that satisfy this equation are (*8*, p. 2)

$$x = a \cos \phi \text{ and } y = b \sin \phi \qquad (4)$$

Differentiating, the slope at any point on the elliptical arc is (*8*, p. 2)

$$dy/dx = -(b/a) \cot \phi \qquad (5)$$

From the crown of the arch, offsets to any point on the arch, for fabrication purposes, can be determined from

$$Y = b(1 - \sqrt{1 - x^2/a^2}) \qquad (6)$$

where *a* is the major axis and *b* is the minor axis of the ellipse.
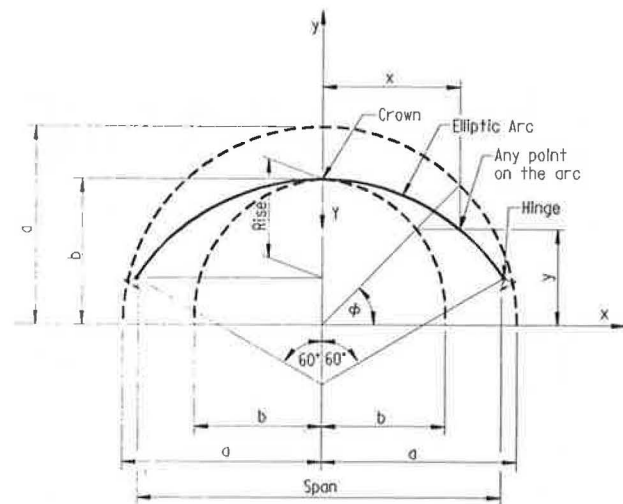
FIGURE 9   Symmetrical two-hinged elliptical arc.

Arch Analysis and Design

There are two arches spaced 54 ft (16.5 m) on center each with a span of 184 ft (56.1 m) and a rise of 49 ft (15.0 m). The depth of the cross section varies from 6.0 ft (1.83 m) at the springing to 4.0 ft (1.22 m) at the crown. The width of the top and bottom flanges are 7.0 ft (2.13 m). There are three webs that divide the box section into two equal cells (Figures 10*a* and 10*b*). High-strength steel with a yield strength of 50 ksi (344 MPa) was used throughout. All welds were made in the shop and all field splice connections were made with ⅞-in.-(22-mm)-diameter ASTM A325 high-strength bolts.

The arch was analyzed using the computer program STRUDL. The elliptical arc was modeled by a series of straight members (*9*, p. 337–338). The following load cases were used:

1. $DL + LL + I +$ differential settlement
2. $DL + LL + I +$ differential settlement + temperature
3. $DL + LL + I +$ differential settlement + wind
4. $DL +$ differential settlement + earthquake.

Load Case 4 governed because the structure is located in a seismically active region.

The arches are 7.0 ft (2.13 m) wide and are braced at the quarter points by the end crossframes and at the crown by a crown crossbeam. The arches can resist transverse forces with-
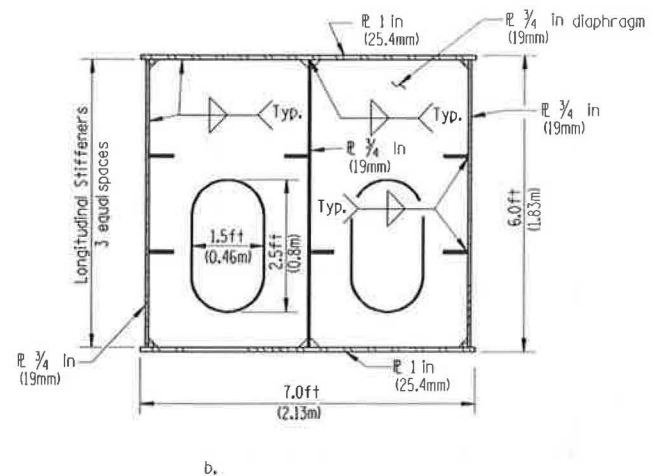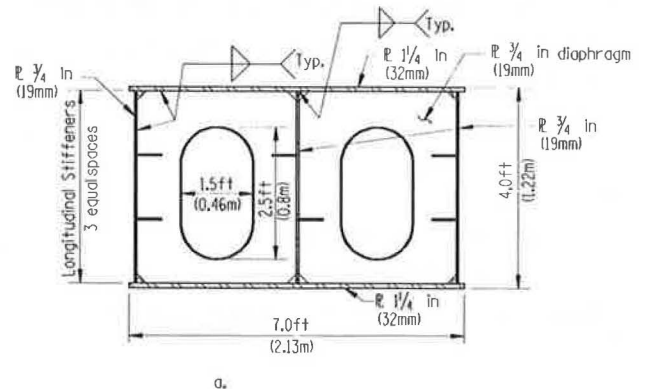
FIGURE 10   (a) Arch cross section at crown, and (b) arch cross section near springing.

out the need for cross-bracing, which gives the structure a streamlined appearance.

The flange plate thicknesses were checked for local buckling according to AASHTO specifications (10, p. 145–146) so that

$$b/t_f = 4250/(f_a + f_b)^{0.5} \leq 47 \tag{7}$$

where

b = width of flange plates between webs and
t_f = flange thickness.

Two longitudinal stiffeners were used at the third points of each arc web so that (10)

$$D/t = 10,000/f_a^{0.5} \leq 120 \tag{8}$$

$$I_s = 2.2\ Dt^3 \tag{9}$$

$$b'/t' = 1,625/(f_a + f_b/3)^{0.5} \leq 12 \tag{10}$$

where

D = web depth,
t = web thickness,
I_s = moment of inertia of the web stiffener about its base,
b' = width of outstanding stiffener element,
t' = thickness of outstanding stiffener element,
f_a = axial stress resulting from the applied loadings, and
f_b = bending stress resulting from the applied loadings.

The arch sections satisfied the following interaction equation (10, p. 145–146)

$$f_a/F_a + f_{bx}/F_{bx} + f_{by}/F_{by} \leq 1.0 \tag{11}$$

where

F_a = allowable axial stress, and
F_b = allowable bending stress.

The allowable axial stress, F_a, was determined from (10, p. 145–146)

$$F_a = (F_y/2.12)[1 - (KL/r)^2 F_y/4\pi^2 E] \tag{12}$$

where

F_y = yield stress of the steel,
2.12 = factor of safety,
K = 1.1 for a two-hinged arch with rise-to-span-ratio less than 0.3,
L = one-half the length of the arch rib for in-plane buckling,
r = radius of gyration, and
E = modulus of elasticity of steel.

Load Transfer

New girder bearing stiffeners were field-bolted to the existing girders at the end abutments, end crossframes, and crown crossbeam. Permanent steel jacking beams were placed between the existing girders, which were spaced at 14.25 ft (4.34 m)

centers and field-bolted to the bearing stiffeners. These beams were designed so that the existing superstructure could be lifted off the existing piers and the load transferred to the new arches.

Jacks were located adjacent to the girders (Figure 11) with space allowed for new bearings under the girders. Jacking was completed at the end crossframes before jacking at the crown crossbeam. This applied most of the superstructure dead load as two symmetrical concentrated loads 28 ft (8.5 m) from the arch pin bearings, which reduced the bending moment on the arch.

The contractor was permitted to jack the superstructure up 2.5 in. (6.4 cm) maximum at each end crossframe and 2 in. (5.1 cm) at the crown crossbeam so the girders would not be overstressed. During jacking, strict tolerances for differential deflection of the existing deck/girder system were established to prevent damage to the existing 7.25-in.-(18.4-cm)-thick reinforced concrete deck. A maximum differential settlement of 0.125 in. (3 mm) between adjacent girders was specified. Survey readings were taken 12 hr, 24 hr, and 15 days after load transfer to monitor foundation settlement. Minor settlement could be corrected by jacking and shimming the girder bearings, whereas excessive settlement could be corrected by jacking and shimming the four arch bearings. Fortunately, foundation settlement was less than 0.25 in. (6 mm) after the arch was erected; there was no additional settlement after load transfer.

COST

The contractor, David A. Mowat, Bellevue, Washington, bid $3,900,000 for the bridge reconstruction, which was 14.7 percent over the engineer's estimate of $3,400,000. Included in this amount was $1,600,000 for the tieback retaining walls, which were constructed by Malcolm Drilling Co., Inc., San Francisco, California. The steel was fabricated by Universal Structural, Inc., Vancouver, Washington. A total of 446 tons (404.5 metric tons) of steel was bid at $1.46/lb ($3.22/kilogram).
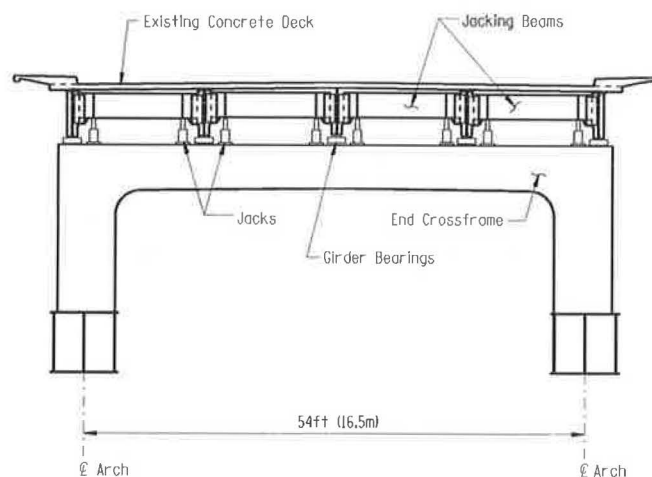
FIGURE 11 End crossframe, jacking beams, and jacks.

SUMMARY

Two steel arches replaced existing reinforced concrete piers of the Capitol Boulevard undercrossing so that I-5 below could be widened from four to eight lanes. Variable depth elliptical arches with no transverse wind bracing were designed, fabricated, and erected over I-5 with minimal interruption and hazard to highway users.

Several alternative structure types were considered, and models were used to study the aesthetics of the bridge types. An external peer review was an important aid to compare cost estimates and constructibility of the alternative bridge types.

Tieback walls were used for shoring during construction and as a final earth retaining structure. Spread footings, not normally associated with arch structures, were constructed and foundation settlement monitored continuously during construction. The transfer of load to the arches from the existing piers was accomplished by simple jacking.

Cost of the project was $3,900,000, including $1,600,000 for tieback wall construction.

ACKNOWLEDGMENTS

REFERENCES

1. F. Leonhardt. *Brucken: Asthetik und Gestaltung/Bridges: Aesthetics and Design*. Deutsche Verlags-Anstalt, Stuttgart, Germany, 1982.
2. R. S. Cheney. *Permanent Ground Anchors*. Report FHWA-DP-68-1. FHWA, U.S. Department of Transportation, Jan. 1984.
3. K. Terzaghi and R. B. Peck. *Soil Mechanics in Engineering Practice*, 2nd ed. John Wiley & Sons, Inc., New York, 1967.
4. V. Leontovich. *Frames and Arches*. McGraw-Hill Book Co., New York, 1959.
5. D. B. Steinman and S. R. Watson. *Bridges and Their Builders*. G. P. Putnam Sons, New York, 1941.
6. J. A. L. Waddell. *Bridge Engineering, Volume I*. John Wiley & Sons, Inc., New York, 1916.
7. D. A. Nettleton and J. S. Torkelson. *Arch Bridges*, Structural Engineering Series No. 2. FHWA, U.S. Department of Transportation, Sept. 1977.
8. T. M. Wang and J. A. Moore. Lowest Natural Extensional Frequency of Clamped Elliptic Arcs. *Journal of Sound and Vibration*. Vol. 30, No. 1, Jan. 1973.
9. M. D. Vanderbilt. *Matrix Structural Analysis*. Quantum Publishers, Inc., New York, 1974.
10. *Standard Specifications for Highway Bridges*, 13th ed. American Association of State Highway Officials, Washington, D.C., 1983.

Strengthening of Steel Stringer Bridges by Transverse and Longitudinal Stiffening

Terry J. Wipf, F. Wayne Klaiber, and Marcus J. Hall

Adding material to existing steel stringer bridges has been commonly used as a strengthening method. For simple-span bridges, addition of material can include coverplating, creating composite action with the deck, or increasing transverse stiffness of the existing diaphragm system. For simple-span bridges, these methods may increase live-load ratings by as much as 30 percent, depending on span length. Continuous stringer bridges behave differently when stiffened because of the way stiffening affects the distribution of stress. Because continuous bridges are indeterminate in the transverse direction as well, selective longitudinal stiffening of the stringers and its effect on the whole structural system should be carefully evaluated. In some cases, addition of material to continuous stringers may be detrimental at unstiffened locations. If properly designed, selective longitudinal stiffening can be beneficial in strengthening other locations in the bridge by changing the stress distribution throughout the bridge. Fatigue-critical details associated with stiffening an existing stringer should be checked, because of possible detrimental effects.

According to the Federal Highway Administration, nearly 40 percent of the approximately 600,000 bridges in the United States are currently classified as either geometrically or structurally deficient. When the general condition of a bridge is adequate yet structurally deficient, strengthening can often be used as an alternative to replacement or posting. The feasibility of bridge strengthening has been discussed in detail by Klaiber et al. (1); they grouped strengthening methods into four categories: (a) addition or modification of a member or support, (b) reduction of dead load, (c) application of external posttensioning, and (d) increased bridge stiffness in either the transverse or the longitudinal direction. Although the last method has been applied in the field, there has been no conclusive evaluation of its effectiveness as a strengthening method.

Increased stiffness in the longitudinal direction is achieved by the addition of coverplates, or, if composite action does not already exist, increased stiffness can be achieved by making the beam composite with the deck in desired locations. Increasing the transverse stiffness of a structure involves increasing the stiffness of existing diaphragms or crossframes or adding diaphragms or crossframes.

A previous paper by Dunker et al. (2) briefly addressed transverse and longitudinal stiffening as a means of strength-ening both determinate and indeterminate steel bridges. Dunker noted that for determinate structures, one strengthening method is the addition of material at locations of overstress. Applying this idea to indeterminate structures has the effect of stiffening the regions where material is added; however, some of the beneficial stiffening effects may be reduced because the stiffened region may also attract additional stress. This paper investigated the effects of transverse and longitudinal stiffening on distribution of strain at both the stiffened and unstiffened locations in determinate and indeterminate bridges.

ANALYTICAL MODEL

The finite element model shown in Figure 1 used in this investigation was developed on Iowa State University's version of ANSYS (3), a general-purpose program. Two types of elements were employed. Quadrilateral shell elements were used to model the deck, and three-dimensional beam elements were used to model the beams, diaphragms, and curbs.

To place the beam's element at the centroid of the beam, a connector element between the centroid of the deck and the centroid of the beam was needed. A rigid link is typically used to attach the two elements (4, 5); however, the rigid link does not account for the transverse flexibility that exists in the steel beam. Because the flexibility in the beam is important in studying the effects of diaphragms on load distribution, an alternate connector element was needed. A three-dimensional beam element, similar to one employed by Dunker (6), was used. The element was given the torsional and flexural moments of inertia of one-half the beam web, thus obtaining the desired flexibility. To ensure that this element did not contribute in carrying any longitudinal bending moment, a moment release connection was employed at the deck. A view of the finite element model for the bridge is shown in Figure 2.

Verification of the finite element model developed in this investigation was accomplished by comparing the model results with field test data and results from a previously developed finite element model (using the SAP IV program) of an existing simple-span bridge (7). The bridge was a four-stringer, steel I-beam structure on a 50-ft span with a width of 30 ft. Agreement with strain and deflection data was considered good as shown in Figures 3 and 4. It should be noted that field test data indicated that partial end restraint existed on the bridge, thus the difference between the test data and the theoretical curves that assume ideal support conditions. The

T. J. Wipf and F. W. Klaiber, Bridge Engineering Center, Department of Civil and Construction Engineering, Iowa State University, Ames, Iowa 50011. M. J. Hall, Office of Bridges, Iowa Department of Transportation, Ames, Iowa 50010.
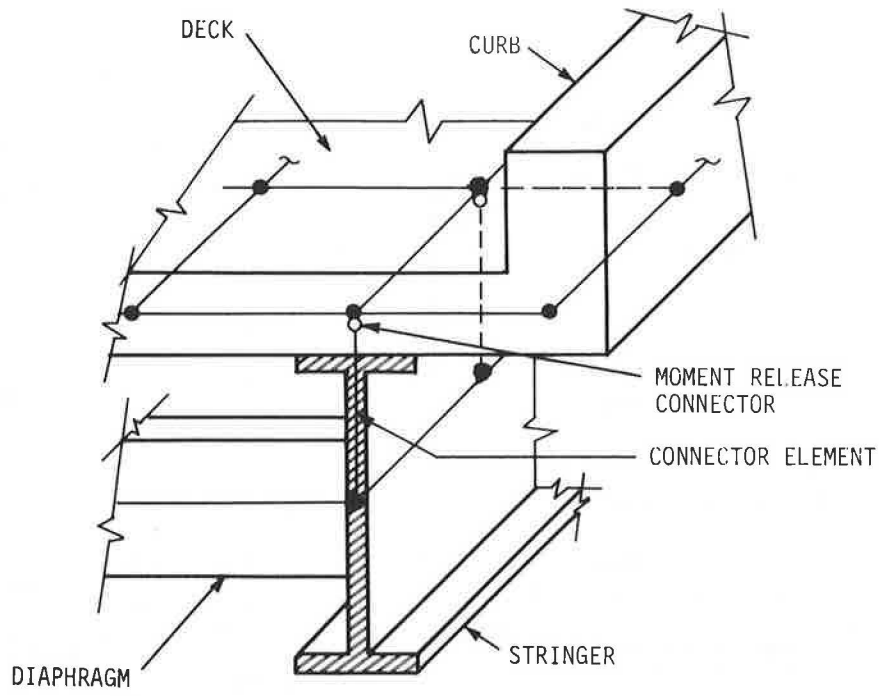
FIGURE 1   Elemental configuration using ANSYS finite element model.
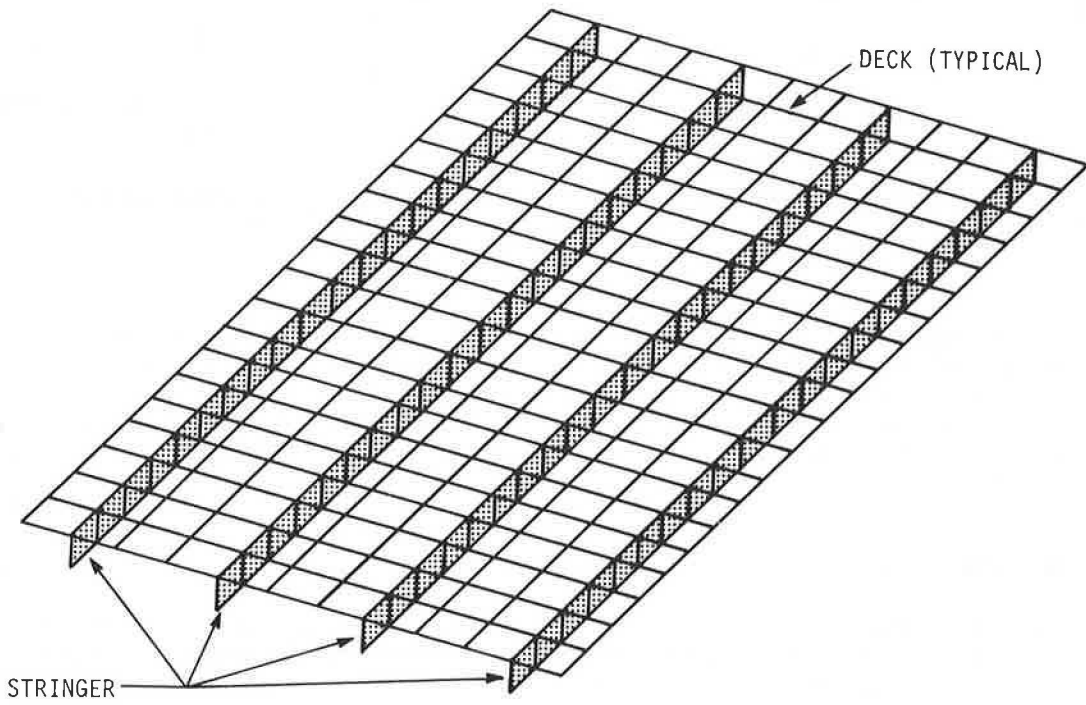
FIGURE 2   Finite element mesh of bridge model.
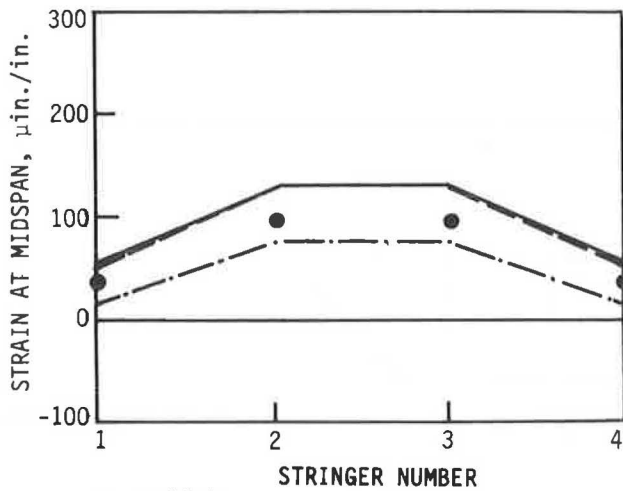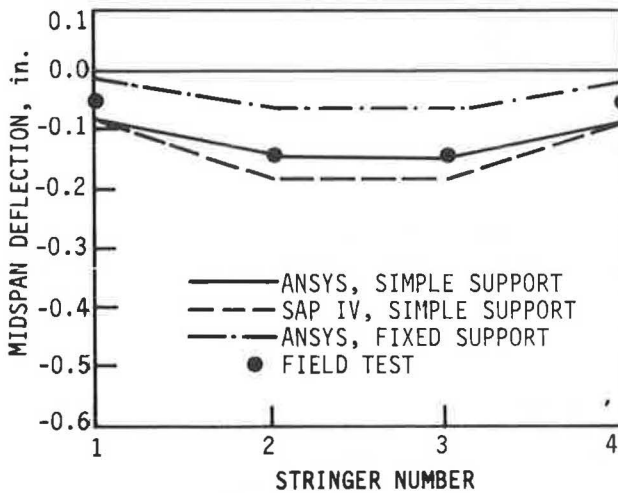
FIGURE 3 Summary of results at bridge midspan with centric truck loading.

FIGURE 4 Summary of results at bridge midspan with eccentric truck loading.

comparison of analytical results between the SAP IV model and the ANSYS model was excellent for strain data but not as good for deflection data, although the comparison was still considered good. The major reason for this difference was the inherent difference in the deck element types employed by ANSYS and SAP IV.

TRANSVERSE STIFFNESS

The effects of increased transverse stiffness on load distribution were examined by investigating a series of simply supported, I-beam bridges subjected to four loading conditions. Bridges investigated were assembled by use of the parameters presented in Table 1. Loading consisted of two 20-kip concentrated loads placed 6 ft apart. The loads were applied both centrically and eccentrically at midspan and quarter span. For eccentric loading, the external load was placed 2 ft from the curb. When a concentrated load acted between nodes in the

finite element mesh, it was distributed to the nodes by use of an equivalent area method approach.

An increase in transverse stiffness was obtained by varying the size of the diaphragms and their location. A base condition for each bridge was established by applying the four load cases to each bridge without the presence of diaphragms. Transverse stiffness added to each bridge was based on two different diaphragm sizes analogous to modifications of existing diaphragms that can be practically achieved in the field by coverplating existing diaphragms or by replacing existing diaphragms with larger diaphragms. These modifications could realistically increase diaphragm moment of inertia, I, from 50 percent to 150 percent of the moment of inertia, I, of the existing bridge stringers. The rigidity of the connection of the diaphragm to the stringer in the analytical model was varied between limits of a simple connection (nonrigid) and a fixed connection (rigid). Little sensitivity in strain results was noted between these connection rigidity limits. The results presented in this paper assume a rigid diaphragm connection.

TABLE 1   BRIDGE PARAMETERS INVESTIGATED IN TRANSVERSE STIFFNESS
MODEL

Parameters	Model Values
Bridge length (ft)	30, 60, 90
Bridge width (ft)	30, 38
Stringer spacing (ft)	6.5, 9.5
Diaphragm moment of inertia (Percent of stringer moment of inertia)	0, 50, 150
Diaphragm location (Number of diaphragms equally spaced throughout the bridge)	1, 2, 3
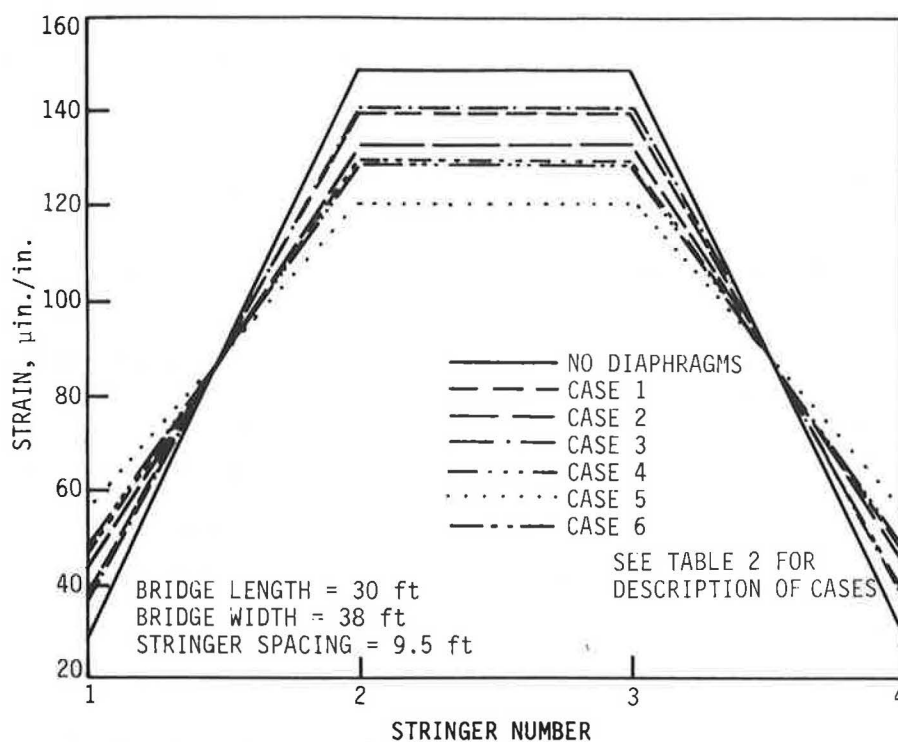
FIGURE 5   **Maximum strains at bridge centerline with centric loading.**

Position of diaphragms considered were (a) midspan only, (b) third points only, and (c) quarter points.

The distribution of strain at the midspan of each bridge was compared to that of other bridges of the same length, width, and stringer spacing. As an example, the strain distributions for a bridge 30 ft long, 38 ft wide, and with stringer spacing of 9.5 ft are shown in Figure 5 (centric loading) and Figure 6 (eccentric loading). Shown in these figures are the strains at the midspan of each stringer for seven different diaphragm configurations. The bridge with no diaphragms was used as the base condition. The diaphragm sizes and locations for the other six cases are listed in Table 2.

Noteworthy in these figures is the general flattening (a more linear change in strain across the bridge cross section) of the curves in Cases 1 through 6. This flattening, illustrated in both Figures 5 and 6, is expected with increases in transverse stiffness. In all bridges investigated, the maximum strain occurred in the exterior beam because of an eccentrically applied load at midspan. The reduction in strain for this critical loading condition for each bridge is shown in Table 3.

In all but two cases, reductions in maximum strains were achieved, with the largest reduction in strain at 29.7 percent, which occurred in the 90-ft-long, 38-ft-wide bridge with a stringer spacing of 9.5 ft. The average reduction for all bridges
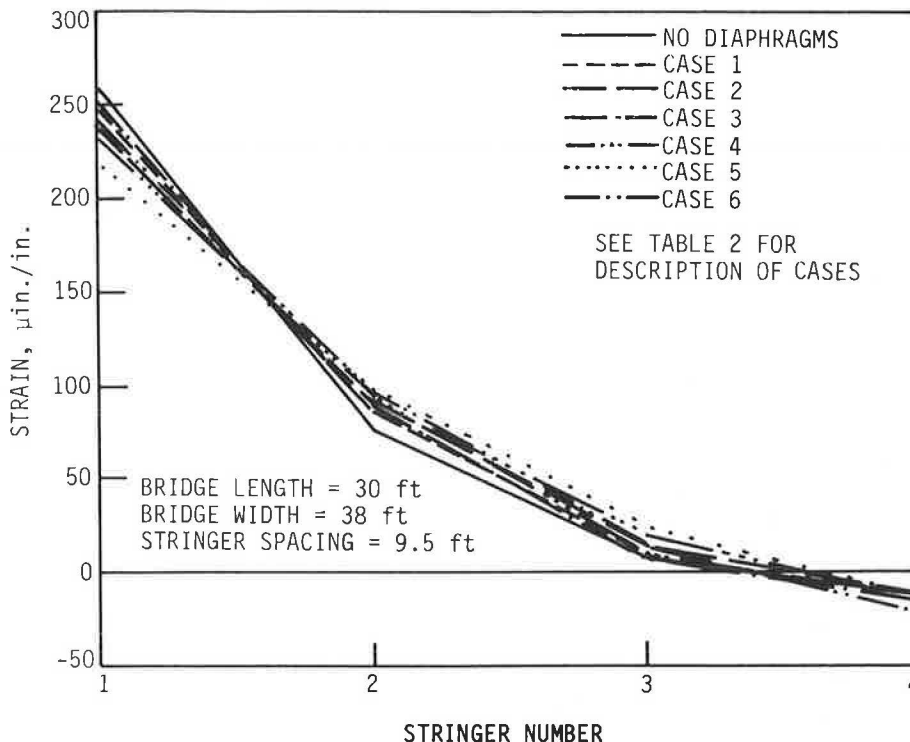
FIGURE 6   Maximum strains at bridge centerline with eccentric schemes.

TABLE 2   DIAPHRAGM SIZE AND LOCATION FOR BRIDGES ANALYZED IN FIGURES 5 AND 6

	Diaphragm Size (Percent of Stringer Moment of Inertia)	Diaphragm Location
Case 1	50%	Third points
Case 2	50%	Midspan only
Case 3	50%	Quarter points
Case 4	150%	Third points
Case 5	150%	Midspan only
Case 6	150%	Quarter points

was approximately 10 percent. The following general observations were made:

● Greater reduction in strain occurred in the longer span bridges.
● The most effective transverse strain distribution occurred when diaphragms were located at the one-quarter points. The greatest reduction in stress occurred when a larger number of smaller diaphragms were spaced throughout the bridge. Locating diaphragms at the one-third points produced stress reductions approximately one-third as large as reductions produced by diaphragms at the one-quarter points.
● With all other parameters being equal, greater stress

reductions occurred in bridges with larger stringer spacing for all configurations of added diaphragms.
● For longer span bridges, the greatest stress reduction occurred in the wider bridges. For the shorter span bridges, the stress reduction was similar for all bridge widths considered.
● The greater the diaphragm stiffness, the greater the stress reduction.

LONGITUDINAL STIFFNESS

The addition of coverplates in continuous stringer bridges affects the transverse stiffness of the whole bridge superstruc-

TABLE 3 STRAIN REDUCTION IN SIMPLE SPAN EXTERIOR STRINGERS AS A RESULT OF
INCREASED TRANSVERSE STIFFENING

Diaphragm Size (Percent of stringer moment of inertia)	Stringer Spacing (ft)	Bridge Width (ft)	Bridge Length (ft)	Reduction in Strain (%) Diaphragm Location		
				1/4 pts.	1/3 pts.	mid-span
50	6.5	30	30	3.2	1.6	0.0
			60	13.0	4.2	1.0
			90	24.8	7.1	3.5
50	9.5	30	30	8.4	4.0	3.2
			60	16.8	5.2	4.6
			90	25.1	5.8	5.8
50	9.5	38	30	7.4	3.5	2.7
			60	17.2	6.5	7.0
			90	24.6	7.2	8.7
150	6.5	30	30	4.5	4.5	0.0
			60	17.2	8.9	2.1
			90	27.7	12.8	4.3
150	9.5	30	30	14.3	8.8	6.0
			60	25.4	12.1	7.5
			90	29.5	12.1	7.2
150	9.5	30	30	14.3	9.3	5.8
			60	23.3	12.6	11.2
			90	29.7	13.2	11.3

ture system, although in analysis this effect is usually neglected. The same is true when the stringers are made composite with the deck. If longitudinal stiffening of the superstructure is considered for strengthening an existing bridge, these modifications and their effect on the transverse stiffness should be considered.

The variations in load distribution that resulted from stiffening selected longitudinal regions of a bridge were evaluated by analytically investigating a matrix of three-span, continuous, I-beam bridges. Each bridge consisted of four stringers spaced 8 ft on center with a total bridge width of 28 ft and two different configurations of span length (see Table 4). The six different stiffening schemes investigated are shown in Figure 7. The bold lines in this figure represent the stiffened locations on the beams. Combinations of longitudinal stiffening schemes and bridge lengths were examined with the diaphragm's moment of inertia at 10 percent and stiffened longitudinal moment of inertia at 200 percent that of the unstiffened stringer. This increase in the stringer moment of inertia can be obtained in the field by (a) adding coverplates or (b) creating composite action between the stringer and deck.

Loading of the model bridges consisted of 10-ft-wide lane loads of 640 lb per linear foot. The four loading conditions

that produced both maximum negative and maximum positive moments for centric and eccentric positions were investigated. Obviously the maximum negative moment occurred at the first interior support when the first two spans were loaded, and the maximum positive moment occurred when the two exterior spans were loaded.

Base conditions were established by applying the four loading conditions to a bridge containing no longitudinal stiffened sections and having standard diaphragms at the supports and midspans. Modifications to this base condition were then made by increasing the longitudinal stiffness as noted earlier.

Noting that strain reduction will obviously occur at the location where material is added, we concentrated the investigation on evaluating the reduction in the maximum strain at secondary locations in continuous-span bridges when the stiffness was increased at a primary location. The secondary location of the bridge was defined as any location in the bridge where stiffening was not applied. These regions will be affected by increased stiffness at other locations because of the indeterminacy of the whole bridge system. For example, when all positive moment regions in a bridge were stiffened, the focus of the investigation was on the reduction in strain in the negative moment regions. For such an example, the critical loading condition occurred when the bridge was loaded to cause

TABLE 4 STRAIN REDUCTION FOR THREE-SPAN CONTINUOUS STRINGERS AS A RESULT OF
INCREASED LONGITUDINAL STIFFENING

Scheme No.	Span Lengths (ft)	Strain Reduction at Pier Loaded for Max. Neg. Mom. (%)		Strain Reduction in Span 1 Loaded for Max. Pos. Mom. (%)	
		Centric Loading	Eccentric Loading	Centric Loading	Eccentric Loading
1	40-50-40	20.6	21.3	1.5	2.8[1]
	70-100-70	36.1	34.9	1.3	3.8[1]
2	40-50-40	4.5	6.5	-2.9	1.0[1]
	70-100-70	5.7	6.9	2.1[1]	6.1[1]
3	40-50-40	1.4	16.0	0.7	0.6[1]
	70-100-70	4.8	26.3	1.2	0.7
4	40-50-40	1.6	3.7	4.3	-5.5[1]
	70-100-70	4.6	2.2	10.2	-3.6[1]
5	40-50-40	2.5	3.3	-4.2	-0.6
	70-100-70	2.2	2.6	0.4[1]	4.5[1]
6	40-50-40	1.8	3.0	1.0	1.4
	70-100-70	3.4	4.1	1.1	1.3

[1] Maximum strain changed location from base condition.

Note: Stiffened section I 200 percent of stringer I; diaphragm I 10 percent
      of stringer I for all cases shown.

maximum negative moment. Schemes 1 and 3 were developed
with the primary intention of strengthening the negative moment
region. Schemes 2, 4, 5, and 6 were developed to strengthen
positive moment regions. All six schemes were analyzed so
that the effects of stiffening could be observed in both the
primary and secondary regions.

The reductions in maximum strain from the base condition
for the six stiffening schemes are illustrated in Table 4. As
expected, large reductions in strain appeared in the stiffened
regions, and smaller reductions appeared in the unstiffened
regions. The most favorable reduction in strain noted at a
secondary location was 4.5 percent. For the primary or stiff-
ened regions, reductions of approximately 20 percent were
noted. Several unexpected effects were observed from these
data. As shown for Scheme 5, when the longer bridges were
loaded centrically and eccentrically to cause maximum posi-
tive moment, the location of maximum strain in the bridge
occurred at a different position than in the base condition. In
addition, when the shorter bridge was loaded both centrically
and eccentrically to cause maximum positive moment, the
point of maximum strain changed and increased in magnitude
from that found in the base condition. Because of this unde-

sirable behavior, refinement in the method's application was
considered.

A number of additional load cases were therefore consid-
ered by modifying the length of the stiffened region in the
stringer as well as changing both the longitudinal stiffness of
the stringer and transverse stiffness of the bridge.

Positive Moment Region

Scheme 2 was reanalyzed with the stiffened section of the
positive moment region extended to cover $^8/_{10}$ of the span
length. Two cases were considered: (a) moment of inertia of
longitudinal section at 200 percent of the stringer and
(b) moment of inertia of the longitudinal section at 300 per-
cent of the stringer. The results of strain reduction in the
negative moment region are shown in Table 5. As shown, the
strain reductions are not significantly different; however, they
did show improvement when compared with the earlier con-
dition illustrated in Table 4. The most favorable condition is
shown in Table 5 where the strain reduction from base con-
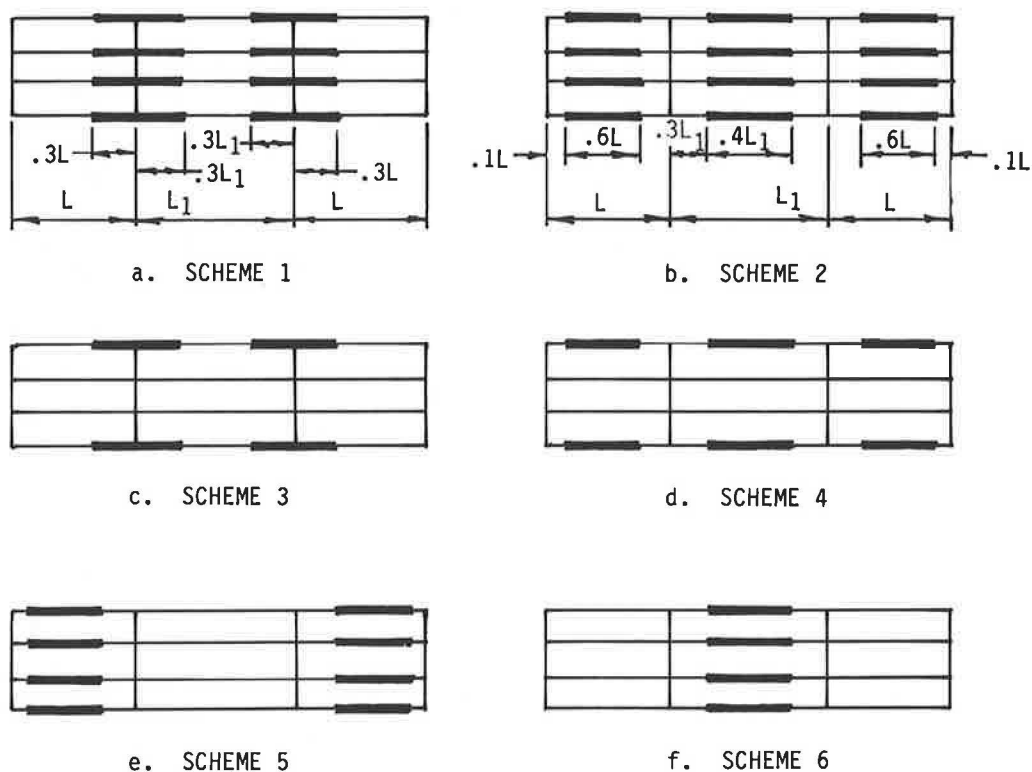dition was approximately 10 percent. It should be noted that

FIGURE 7 Longitudinal stiffening schemes.

the strain reduction in the positive region improved only slightly when the region of coverplating was extended to cover $^8/_{10}$ of the span.

Negative Moment Region

Scheme 1 was further evaluated by considering increases in moment of inertia of 150 percent and 300 percent of the existing stringer moment of inertia. The results of these cases are also shown in Table 5. The maximum reduction in strain was 2.3 percent for the case of a 300 percent increase in longitudinal inertia; results did not differ significantly from those in Table 4.

Combined Transverse and Longitudinal Stiffening

A brief study employing simultaneous transverse and longitudinal stiffening was performed on the three-span, continuous bridge used in this study. In each case, the diaphragm's moment of inertia was increased to 100 percent that of the stringer.

Table 5 also illustrates results with only the transverse stiffness increased. As shown, when the long bridge was centrically loaded to produce maximum positive moment, an increase in the maximum strain was observed. This can be attributed to the additional moment drawn by the large stiffness at midspan. To compensate for this increase in moment, we added additional longitudinal stiffness by application of two of the earlier stiffening schemes.

The first combination utilized Scheme 3 (with the existing stringer moment of inertia increased 200 percent) and was

loaded to cause maximum positive moment. The results, shown in Table 5, closely resemble the results shown in Table 4 for an increase in transverse stiffness only.

The second combination utilized Scheme 4 (with the existing stringer moment of inertia increased 200 percent) and was loaded to cause maximum negative moment. Results shown in Table 5 reveal that strain reduction greater than 10 percent can be obtained with centric loading. However, eccentric loading produced less favorable results.

Fatigue and Strength

Selectively stiffening existing stringers transversely or longitudinally may have an effect on existing live load stress ranges at critical locations. The corresponding effects on fatigue stresses therefore need to be checked when considering strengthening by these methods.

Transverse stiffening will not increase the flexural strength of a bridge, although it does improve its rating capacity, and may not be desirable if flexural strength is critical. Longitudinal stiffening will increase the flexural strength of an existing stringer if regions of strengthening are at plastic hinge locations.

SUMMARY AND CONCLUSIONS

The usual strategy of adding material at overstressed locations in determinate bridges is an obvious solution for increasing the rating of a bridge. Applying this procedure to indeterminate structures may have a detrimental effect, however. For the bridges investigated, a practical amount of transverse

TABLE 5   STRAIN REDUCTION FOR THREE-SPAN CONTINUOUS STRINGERS MODIFIED FROM CONDITIONS IN TABLE 4

Longitudinal Stiffening Scheme No.	Modification of Stiffened Section (% of Stringer I)	Modification of Diaphragm (% of Stringer I)	Span Lengths (ft)	Strain Reduction at Pier Loaded for Maximum Negative Moment (%)		Strain Reduction in Span 1 Loaded for Maximum Positive Moment (%)	
				Centric Loading	Eccentric Loading	Centric Loading	Eccentric Loading
2	200	10	40-50-40	4.3	6.7	--	--
			70-100-70	5.7	7.7	--	--
2	300	10	40-50-40	7.4	11.1	--	--
			70-100-70	9.8	12.7	--	--
1	150	10	40-50-40	--	--	0.9	1.6
			70-100-70	--	--	0.7	2.1
1	300	10	40-50-40	--	--	2.6	4.1[1]
			70-100-70	--	--	2.3	5.7[1]
-	100	10	40-50-40	7.3	0.2	9.3	1.5[1]
			70-100-70	5.4	2.4	-2.5	6.4[1]
3[2]	200	100	40-50-40	--	--	10.4	1.2[1]
			70-100-70	--	--	-4.2[1]	7.5
4[2]	200	100	40-50-40	11.1	2.3	--	--
			70-100-70	12.7	3.5	--	--

[1]Maximum strain changed location from base condition.

[2]Combined transverse and longitudinal stiffening case.

stiffening added to existing bridges can decrease the maximum strains by as much as 30 percent on longer span bridges. Adding longitudinal stiffness to indeterminate structures can decrease maximum strain by 8 to 10 percent. Combining transverse and longitudinal stiffening on continuous stringer bridges did not have a significant beneficial effect on strain reduction when compared to longitudinal stiffening only.

ACKNOWLEDGMENT

REFERENCES

1. F. W. Klaiber, K. F. Dunker, T. J. Wipf, and W. W. Sanders, Jr. *NCHRP Report 293: Methods of Strengthening Existing High-way Bridges.* TRB, National Research Council, Washington, D.C., 1987, 114 pp.
2. K. F. Dunker, F. W. Klaiber, and W. W. Sanders, Jr. Strengthening of Steel Stringer Bridges by Selective Stiffening. In *Transportation Research Record 1118*, TRB, National Research Council, Washington, D.C., 1987, pp. 43–48.
3. G. J. DeSalvo and J. A. Swanson. *ANSYS—Engineering Analysis System.* Swanson Analysis Systems, Inc., Houston, Pa., June 1985.
4. E. S. DeCastro and C. N. Kostem. *Load Distribution in Skewed Beam Slab Highway Bridges.* Report 378A.7. Fritz Engineering Laboratory, Lehigh University, Bethlehem, Pa., 1975.
5. W. C. Gustafson and R. N. Wright. Analysis of Skewed Composite Girder Bridges. *Journal of the Structural Division*, ASCE, Vol. 94, No. ST4, April 1968, pp. 919–941.
6. K. F. Dunker. *Strengthening of Simple Span Composite Bridges by Post-Tensioning.* Ph.D. dissertation. Iowa State University, Ames, 1985.
7. F. W. Klaiber, D. J. Dedic, K. F. Dunker, and W. W. Sanders, Jr. *Strengthening of Existing Single Span Steel Beam and Concrete Deck Bridges.* Part I, Final Report. Engineering Research Institute, Iowa State University, Ames, 1983.

Behavior of Composite Steel Bridge Beams Subjected to Various Posttensioning Schemes

WILLIAM E. WILEY, F. WAYNE KLAIBER, AND KENNETH F. DUNKER

An initial investigation phase of research on strengthening continuous composite bridges by posttensioning has been completed; results are summarized. The effects of various posttensioning schemes were investigated on a one-third-scale continuous three-span composite bridge model. Although various tests performed on the bridge model verified that positive and negative moment regions of continuous composite bridges could be strengthened by posttensioning, the model size prevented the testing of different tendon profile shapes and the necessary hardware. Thus, the primary objective of this research was to investigate the effectiveness of various posttensioning schemes applicable to the negative moment regions of continuous composite bridges through the testing of a full-scale laboratory model. The model was subjected to four different posttensioning tendon configurations with and without the use of strengthening angles. Data from the various tests were compared to the unstrengthened model to determine the more effective posttensioning arrangement. Data from the various tests were also used to determine the extent of composite action remaining after the concrete deck cracked.

Many bridges across the United States have deteriorated so that they are inadequate for original design loads or have been rendered inadequate because of changes in standards of design and maintenance. Approximately half of the bridges in the United States were built before 1940. Many of these bridges were designed for lower traffic volumes, smaller vehicles, slower speeds, and lighter loads than they now experience. Frequently, maintenance of these aging bridges has also been inadequate. The FHWA classifies nearly 40 percent of the bridges in the nation as deficient and in need of repair or replacement. Many of these bridges are deficient because their load-carrying capacity is inadequate for today's traffic. Strengthening of deficient bridges is in most instances more economical than posting them for reduced loads or completely replacing them.

Improving the live-load capacity of different bridge types has been accomplished by several methods. Research at Iowa State University (ISU) began with strengthening simple-span composite steel-beam and concrete-deck bridges. Posttensioning was shown to be a viable means of improving the live-load capacity of these bridges (1). Research progressed from laboratory study through field testing (2,3) and concluded with a design manual (4). Because strengthening of simple-span composite bridges by posttensioning had been successful, extension of the method to continuous composite bridges

appeared promising. Further research at ISU investigated this possibility (5,6).

To determine how posttensioning could be used to strengthen a continuous composite bridge, Daoud (7) investigated the effects of various posttensioning schemes on a one-third-scale continuous three-span composite bridge model. Provisions were made to posttension both positive and negative moment regions of the bridge model. Because the bridge model was one-third scale, it was not possible to apply posttensioning to the model in the same manner that it would be applied to a real bridge. In the positive moment regions of the model bridge, the posttensioning tendons were located below the bottom flanges of the beams. On an actual bridge, in the positive moment regions tendons would be located a few inches above the bottom flange. In the negative moment regions of the bridge model, the posttensioning tendons were located above the concrete deck, whereas on an actual bridge, negative tendons would be located a few inches below the bottom of the deck in the negative moment regions. Placement of the tendons on the bridge model was acceptable for determination of posttensioning distribution effects even though the tendons would be placed differently on an actual bridge.

OBJECTIVES

Although various tests performed on the bridge model verified that negative moment region posttensioning could be used to strengthen a continuous composite bridge, it was impossible to test the effects of different tendon profile shapes or positions and the necessary hardware. Thus, the primary objective of this research was to investigate posttensioning schemes applicable to the negative moment regions of continuous composite bridges through testing of a full-scale laboratory model. The secondary objectives were to investigate

- The extent of composite action in the negative moment region;
- The seating losses when the tendons are tensioned;
- Changes in tendon force with applied load; and
- The effects of adding strengthening angles near the bottom flange.

LITERATURE REVIEW

Klaiber et al. (8) cited over 375 articles on various techniques for strengthening and repairing various types of bridges. Their

Department of Civil and Construction Engineering, Bridge Engineering Center, Iowa State University, Ames, Iowa 50011. Current affiliation, W. E. Wiley: Burns and McDonnell, P.O. Box 419173, Kansas City, Mo. 64141.

report included 33 examples of how posttensioning could be applied to single- and multiple-span bridges of steel, concrete, and composite construction. The report discussed several effects that should be considered before a bridge is strengthened by posttensioning as well as the resulting advantages. A careful analysis should be made to ensure that posttensioning forces and moments do not introduce unwanted effects. These unwanted effects include concrete cracking, additional or new overstresses at critical locations, localized buckling of the flanges or web, longitudinal and transverse distribution effects, or a significant reduction in the overall factor of safety for the bridge. Only a brief literature review has been included in this paper. Readers who are interested in a more detailed review of the literature are referred to papers by Wiley (6) and Klaiber et al. (8).

In 1964, Tachibana et al. (9) conducted an experimental investigation by strengthening two-span composite beam models representative of a double girder bridge. One of the beams was prestressed before the concrete deck was cast, and the second beam was prestressed after the deck had been cast and cured. The magnitude of load producing a plastic hinge at the support was slightly higher for the first beam than for the second.

Strengthening and rehabilitation completed in 1979 on the Pit River Bridge and Overhead on I-5 in Shasta County, California (10,11), made use of prestressing tendons and compression bars. The 24-in.-deep wide-flange stringers were strengthened in negative moment regions by placing straight prestressing tendons near the top flanges of the beams and compression bars on top of the bottom flanges.

In 1981, Grace (12) investigated the transverse and longitudinal distribution of deflection and moment in two scale-model bridges. One of the model bridges was allowed to crack over the center support, while a portion of the second model's concrete deck at the center support was prestressed. Results of this investigation indicated that prestressing could be used to control cracking of the concrete deck at the center support.

Alternative designs for new bridge structures have made efficient use of prestressed steel and prestressed composite concrete and steel members. In 1982, this type of construction was used on the Bonners Ferry Bridge in Idaho (13). The 10-span, continuous, cable-stressed composite concrete and steel structure was presented as an alternative to prestressed concrete design. As a result, considerable savings were realized in construction costs by reducing the weight of materials in the entire structure. In the Bonners Ferry Bridge, prestressing was used in both positive and negative moment regions on the plate girder beams. In addition to longitudinal prestressing, the bridge's concrete deck was prestressed transversely along the bridge's entire length.

In 1985, Preston (14) gave three examples of prestressing techniques that have been used in New Zealand to strengthen reinforced concrete bridge superstructures. These examples included prestressing a simple span with cables deflected at midspan, prestressing a continuous bridge with straight cables located as close as practical to the neutral axis of the section, and prestressing a continuous bridge with deflected cables.

In 1986, Troitsky et al. (15) compared the effects of six different cable configurations by testing a 1/20-scale plexiglas model of a two-span plate girder bridge with an orthotropic steel deck. Experimental results were compared to an ana-lytical study. Of the cable configurations used, the authors indicated that where negative dead-load moment governs the design, the harped cable configuration exhibited relatively optimal results.

In 1988, at the University of Maryland, Ayyub (16) discussed the results of tests on full-scale, prestressed composite T-beams subjected to negative moment. The authors indicated that posttensioning beams in this manner significantly increased both the yield and ultimate load capacity of the beam. The posttensioning also placed the concrete slab in compression, which delayed cracking, reduced tensile stresses in the concrete under service loads, and reduced deflections.

LABORATORY MODEL AND INSTRUMENTATION

Proper modeling of posttensioned negative moment regions (i.e., the portion of a bridge between inflection points adjacent to an interior pier when the bridge is under uniform load) of a continuous composite bridge required construction of a full-scale model of that portion of a bridge, hereafter referred to as the mockup. The mockup simulated the negative moment region of an interior stringer of a 150-ft, three-span Iowa Department of Transportation (DOT) V12-series bridge. General dimensions of the mockup and the loading mechanism are shown in Figures 1 and 2. Overall length of the mockup was limited by laboratory space; the concrete deck width, 6 ft 3 in., was determined by using the AASHTO effective flange width requirements for an interior stringer of a prototype bridge (17).

The rolled steel beam in the mockup was a W 24 × 76, identical to that used for interior stringers in the 150-ft Iowa DOT V12-series bridges. Although coverplates on a 150-ft V12 bridge extend 9.5 ft on each side of a pier support centerline, the coverplates on the mockup were restricted to a shorter length because of posttensioning jack clearances. Coverplate thickness and width were chosen to match the depth and moment of inertia of an interior beam in the prototype bridge. Angle-plus-bar shear connectors similar to those on the prototype bridge were used for shear connection.

The deck thickness, 6.5 in., shown in Figure 1b, duplicated that of V12 bridge decks. Holes (3 in. in diameter) shown in Figure 1a were provided in the deck of the mockup to allow passage of the hold-down and loading mechanisms. Two blockouts were provided in the concrete deck for passage of the above-deck harped cables through the deck and for simplified attachment of the above-deck straight tendon anchorages. Reinforcing provided in the concrete deck, both in size and spacing, was duplicated from the V12 bridge series.

The load mechanism produced a negative moment in the mockup similar to that at an interior support within a real bridge. Strain gauges were mounted on the top and bottom flanges and coverplates at several sections along the steel beam. Two of the instrumented sections, Sections 4 and 5, are shown in Figure 2. Vertical deflections were measured at the load point and at the cantilevered end of the beam at Points A and B respectively. Strengthening angles similar to those used by the Iowa DOT to modify section properties and reduce live-load stresses were instrumented and bolted to the beam web just above the bottom flange in eight of the
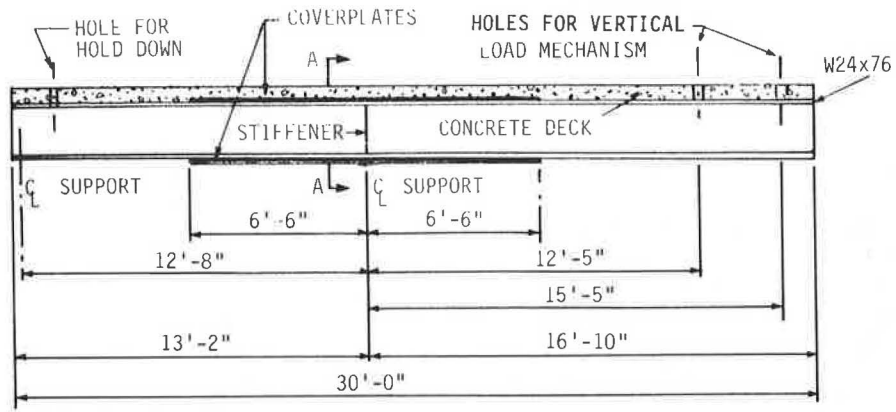
a. ELEVATION
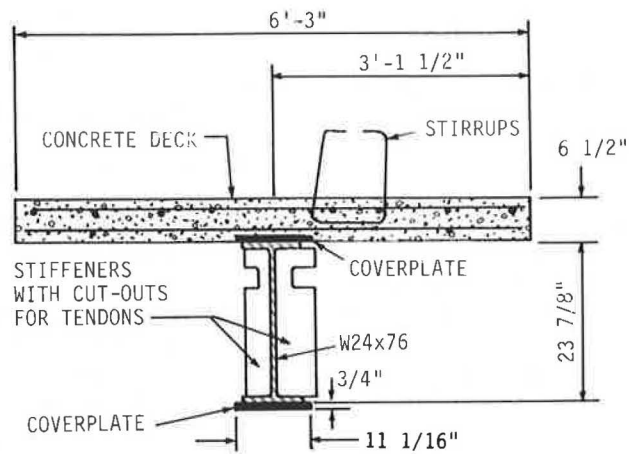
b. CROSS SECTION A-A

FIGURE 1 Full-scale mockup.

FIGURE 2 Location of loading and instrumentation.

tests. Posttensioning tendons, both the threadbars and the cables, were instrumented so that tendon forces could be accurately measured.
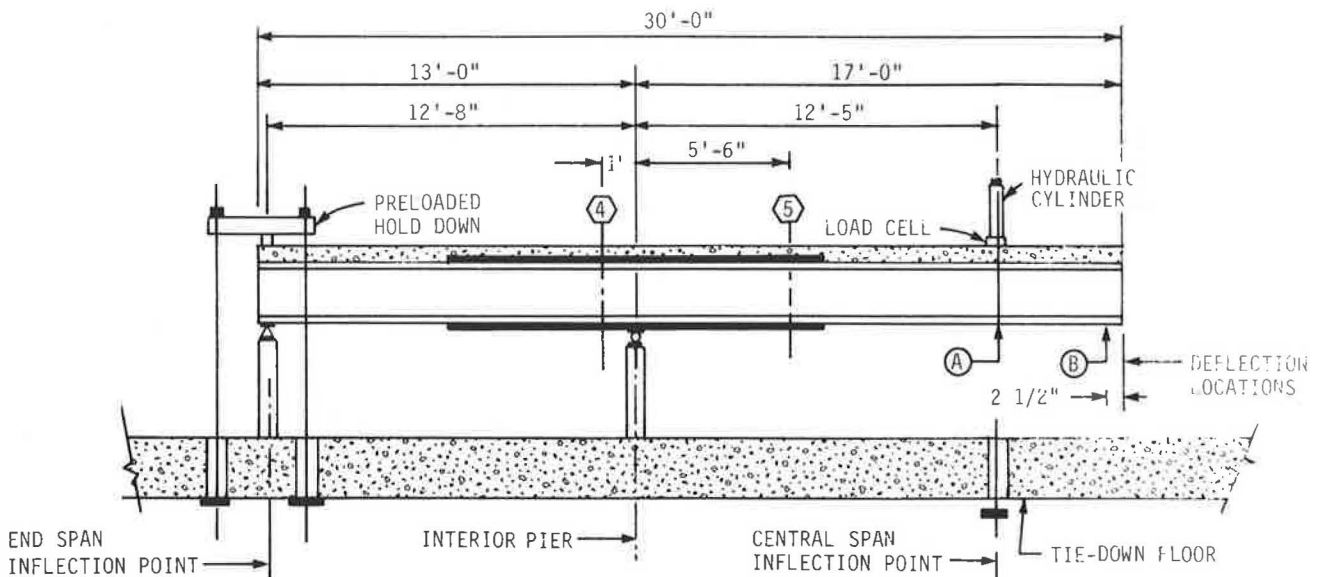
Straight tendons used were 1.25-in.-diameter Grade 150 Dywidag threadbars, whereas cables used were $\frac{7}{16}$-in.-diameter Grade 270 seven-wire stress-relieved prestressing strand. Because all testing was in the assumed elastic range of both the threadbars and the prestressing strand, and because all tendons were instrumented and calibrated, the actual strength properties of the tendons were not determined. The compressive strength of the concrete, f'_c, was 6,700 psi; the modulus of rupture, f'_r, was 477 psi.

The compressive strength of the concrete used in the mockup was considerably higher than that found in a prototype bridge, which has a normal design value of about 3,000 psi. However, the testing program employed involved elastic tests rather than ultimate strength tests, and thus this higher strength was not of great concern. The higher strength, however, would have some effect on the cracking of the concrete and thus on the degree of apparent composite action.

TESTS PERFORMED

A summary of the various tests performed on the mockup is provided in Table 1. Note that test numbers do not necessarily indicate order of completion. A target tendon force of 100 kips was applied to the mockup for the tests involving posttensioning (Tests 4 through 13).

Three tests (Tests 1, 2, and 3 in Table 1) were performed on the mockup without posttensioning applied. The initial

cracking test, Test 1, was performed to (a) determine initial behavior of the beam as a result of cracking of the concrete and (b) approximate field conditions on an actual bridge. Because the posttensioning techniques investigated were intended as rehabilitation measures, they would be applied to a bridge that has been in service for many years. As a result of the age of the bridge and concrete shrinkage and weathering, the concrete deck would likely be cracked in regions of negative moment.

After the cracking test, Test 2 was performed to determine the basic strength, degree of apparent composite action within the negative moment region, and behavior of the beam. Behavior observed in subsequent tests was compared to the results of this test. The third test, Test 3, determined the effectiveness of the strengthening angles that were used to modify section properties. Three load cycles were applied to the beam in an effort to "seat" the angles on the beam. Even though the bolts securing the angles were tightened by the turn-of-the-nut method, some slip between the beam web and the angles occurred. This method of seating the angles was intended to give a better indication of their effectiveness after repeated loading.

The next 10 tests (Tests 4 through 13) explored schemes applicable to posttensioning the negative moment region of continuous composite bridges. Straight and harped tendon profiles were tried above and below the concrete deck (see Figure 3). In addition, each of the four tendon configurations were tried with and without the strengthening angles. Tests 5 and 7 were performed to determine if posttensioning in the presence of a partial load had any effect on performance of the system. Because no adverse or unusual effects were noted,

TABLE 1 SUMMARY OF TESTS PERFORMED

Test No.	Tendon Profile[1]	Angles Used?[2]	Comments
1	--	N	Initial cracking of concrete
2	--	N	Basic beam data
3	--	Y	Basic beam plus angles
4	1	N	
5	1	N	Partial load[3]
6	1	Y	Partial load
7	1	Y	
8	2	N	
9	2	Y	
10	3	N	
11	3	Y	
12	4	N	
13	4	Y	
14	--	Y	Additional angle bolts
15	--	Y	Angles spliced together
16	--	Y	Angles shimmed

[1]See Fig. 3 for tendon profiles.

[2]Y = yes; N = no.

[3]Partial vertical load applied before tendons tensioned.

a. STRAIGHT TENDON BELOW THE DECK (TENDON PROFILE 1)

b. HARPED CABLE TENDON BELOW THE DECK (TENDON PROFILE 2)

c. STRAIGHT TENDON ABOVE THE DECK (TENDON PROFILE 3)

d. HARPED CABLE TENDONS ABOVE THE DECK (TENDON PROFILE 4)
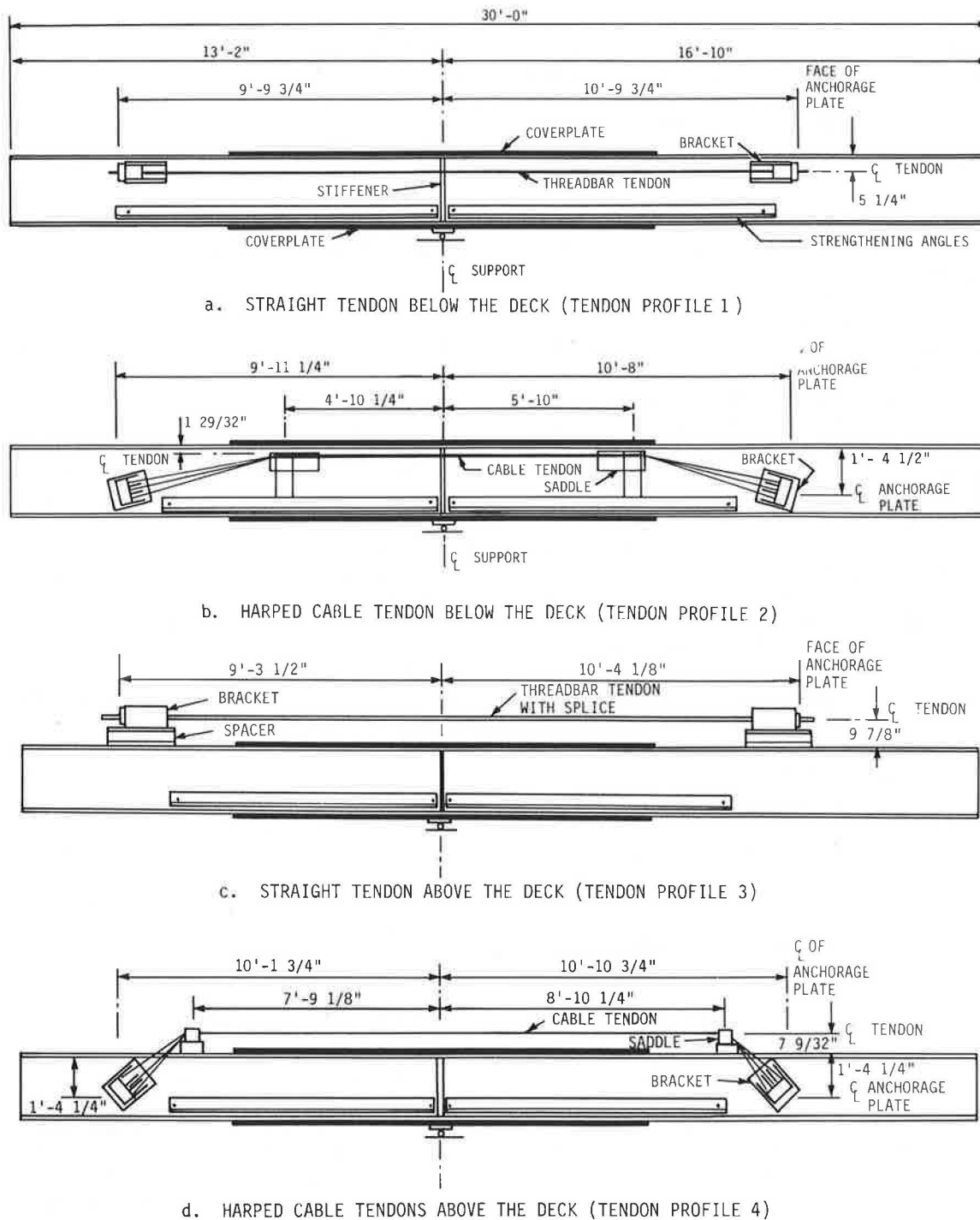
FIGURE 3 Various tendon profiles investigated.

similar tests with the other tendon configurations were not performed. For each tendon configuration, the tendons were tensioned and seated, one or two cycles of vertical load were applied to the mockup, and the tendon force was released.

Of the tendon configurations shown, the straight tendon below the deck (Tests 4 through 7; see Figure 3a) was the simplest because it required the fewest pieces of hardware and the least amount of effort to install. This tendon arrangement consisted of a pair of straight threadbar tendons mounted

a few inches below the underside of the concrete deck, below the neutral axis of the completely composite mockup but above the neutral axis of the steel beam.

The arrangement of harped cable tendons below the deck (Tests 8 and 9; see Figure 3b) was almost as complex as the arrangement of harped tendons above the deck (see Figure 3d). Harping the tendons in this manner produced beneficial vertical shears that added to the effect of the eccentric force. This configuration required the addition of harp brackets and

the use of three cables on each side of the beam web. The anchorage and the harp brackets were bolted in pairs to the web of the steel beam (one on each side). Tensioning the cables was a three-stage process because the cables were tensioned in pairs to simulate probable field procedures.

A single threadbar tendon was used above the concrete deck (Tests 10 and 11; see Figure 3c). Because the threadbar and anchorage brackets protruded above the level of the concrete, this posttensioning configuration was deemed impractical for a field application. However, placing the tendon above the concrete deck put it well above the neutral axis of the completely composite beam and yielded a useful comparison to the work by Daoud (7). If the brackets and tendons could be embedded in the concrete deck, this configuration could be used in the field.

Placing the harped cable tendons above the deck (Tests 12 and 13; see Figure 3d), was the most complex tendon configuration attempted. A pair of anchorage brackets was bolted to the beam web below the deck and the harp brackets were bolted to the top flange inside the deck blockouts. Although the cables were above the deck for this configuration, in an actual bridge, embedding the harps and cables in the deck would be easier than embedding a threadbar and anchorages. Harping the cables above the deck produced larger vertical shear and placed the axial force above the neutral axis of the composite beam. Again, because three cables were used on each side of the web, tensioning was a three-stage process.

Several schemes to reduce the observed shear lag problems in the strengthening angles, as a result of the angles' discontinuity around the bearing stiffener at the center support, were investigated. For Test 14, extra bolts were installed near the bearing stiffener. For Test 15, a splice was added around the bearing stiffener. For Test 16, shims were wedged into the space between the ends of the strengthening angles and the bearing stiffener.

ANALYTICAL MODELS AND CALCULATIONS

The Iowa DOT V12-series bridges and the mockup were constructed by using shear connectors to provide composite action between the steel beam and the concrete deck. However, the bridges and thus the mockup were designed on the assumption that only the steel beam would carry load in the negative moment regions. This assumption implies that although the bridges and the mockup were built compositely, composite action was neglected in the negative moment region.

To determine the extent of composite action remaining after the deck had cracked, experimental data were compared to analytical results from two theoretical models. The non-composite model assumed that only the W 24 × 76 beam and coverplates resisted the applied posttensioning forces and vertical load. In the completely composite model, the reinforced concrete and the steel beam were assumed to act together. Section properties of the completely composite model were based on uncracked concrete transformed into an equivalent area of steel.

In the manual calculations, it was assumed that a linear distribution of strain existed at each cross section, that superposition was valid, and that secondary posttensioning effects were negligible. Finite element modeling was also used. The simple beam, finite element model was a line of beam elements. The composite finite element model used beam elements for the steel beam, plate elements for the concrete deck, and rigid links for the shear connectors.

DATA INTERPRETATION

As previously noted, vertical load during the first test cracked the concrete deck of the mockup to simulate field conditions in a real bridge. Three cycles of vertical load, each with a larger peak load, produced several transverse cracks in the deck of the mockup and a permanent 0.28 in. deflection at the load point. Test 2 established the strain and deflection characteristics of the unstrengthened mockup after the deck had cracked. The effects of adding the strengthening angles were determined in Test 3.

Figure 4 presents the strain profiles at Section 4. Top and bottom coverplate experimental strains are plotted and connected by a straight line for those tests conducted without the presence of the strengthening angles. The straight line connecting the top and bottom flange strains was intended only to help differentiate between the results from each test, and was not intended to indicate the strain distribution. Strains measured in all the tests were bracketed by the strains predicted by the analytical models, which indicated that partial composite action still existed within the mockup after the deck cracked.

Strain profiles at Section 4 resulting from posttensioning are shown in Figure 4a. All four of the tendon profiles produced beneficial compressive strain in the top flange; however, only the above-deck schemes (Tendon Profiles 3 and 4) produced beneficial tension in the bottom flange.

Figure 4b shows strain profiles at Section 4 after vertical load was applied to the mockup. Test 2, the unstrengthened mockup, was the basic condition to which results of the other tests were compared. All of the posttensioning tendon configurations reduced the top flange tensile strains. Posttensioning below the deck slightly increased bottom flange compressive strains, whereas posttensioning above the deck reduced them.

Shown in Figures 5 and 6 are load-deflection curves for the tests without the strengthening angles. Theoretical load-deflection curves for both of the unstrengthened analytical models are also shown on each plot. The results from Test 2, shown in Figure 5, lie approximately midway between the two theoretical curves, again indicating partial composite action within the mockup after the deck had cracked. Each of the posttensioning tendon schemes produced an uplift of the cantilevered end of the mockup while it was being tensioned and before vertical load was applied. The above-deck tendon schemes produced larger uplifts than the below- deck schemes because of the larger tendon-to-mockup centroid eccentricities. Because the curves for the posttensioned tests are essentially parallel to the Test 2 curve, it can be concluded the posttensioning did not significantly change the stiffness of the mockup. Load-deflection curves for the tests with the strengthening angles in use (although not included in this paper) had steeper slopes than the corresponding tests without the angles. Thus, as one would expect, addition of the strengthening angles did stiffen the mockup.

After the beam was posttensioned, any change in deflection of the beam caused a change in the tendon force. Figure 7
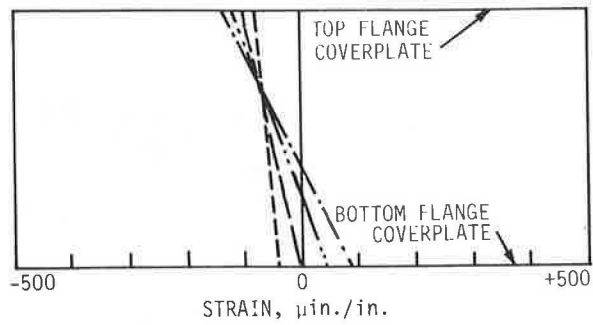
a. TENDONS TENSIONED - NO VERTICAL LOAD
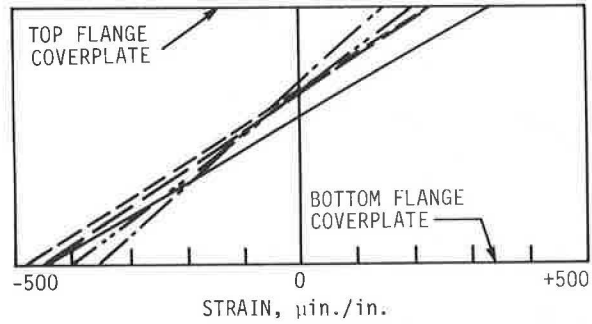
b. TENDONS TENSIONED PLUS VERTICAL LOAD APPLIED

——————— TEST 2:   NO POST-TENSIONING
—— —— TEST 4:   THREADBAR TENDONS BELOW DECK (FIG. 3a)
—— · —— TEST 8:   HARPED CABLE TENDONS BELOW DECK (FIG. 3b)
—— · —— TEST 10:   THREADBAR TENDONS ABOVE DECK (FIG. 3c)
—— ·· —— TEST 12:   HARPED CABLE TENDONS ABOVE DECK (FIG. 3d)
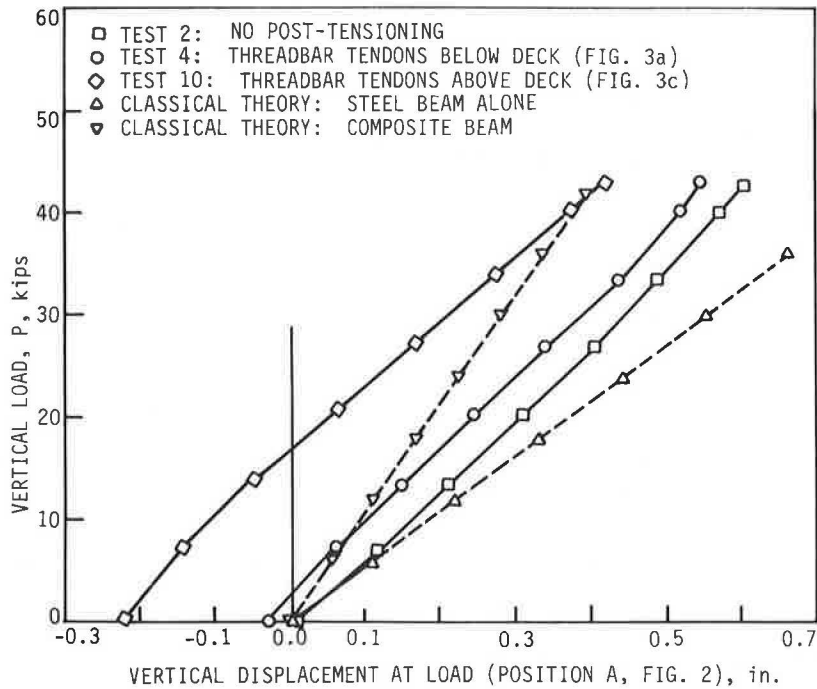
FIGURE 4   Strain profile at Section 4.

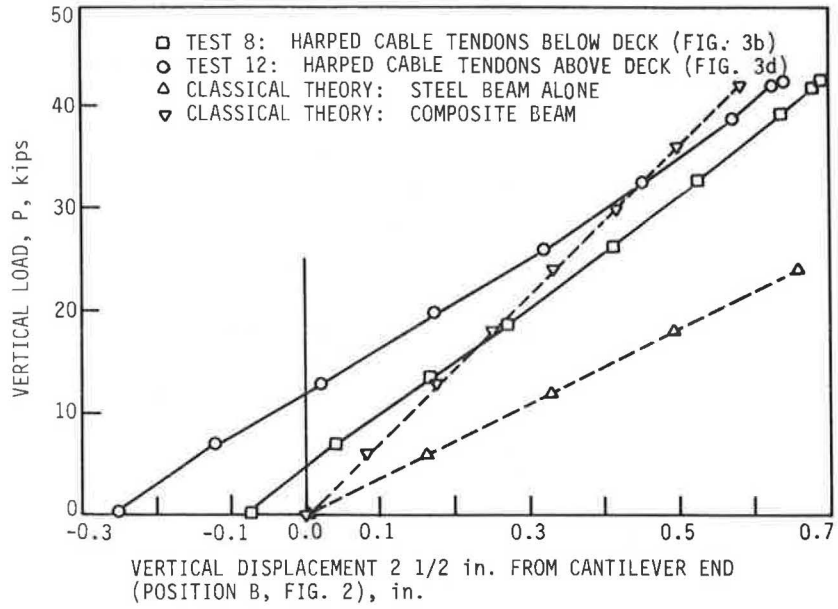**FIGURE 5   Load-deflection curves—straight tendons.**

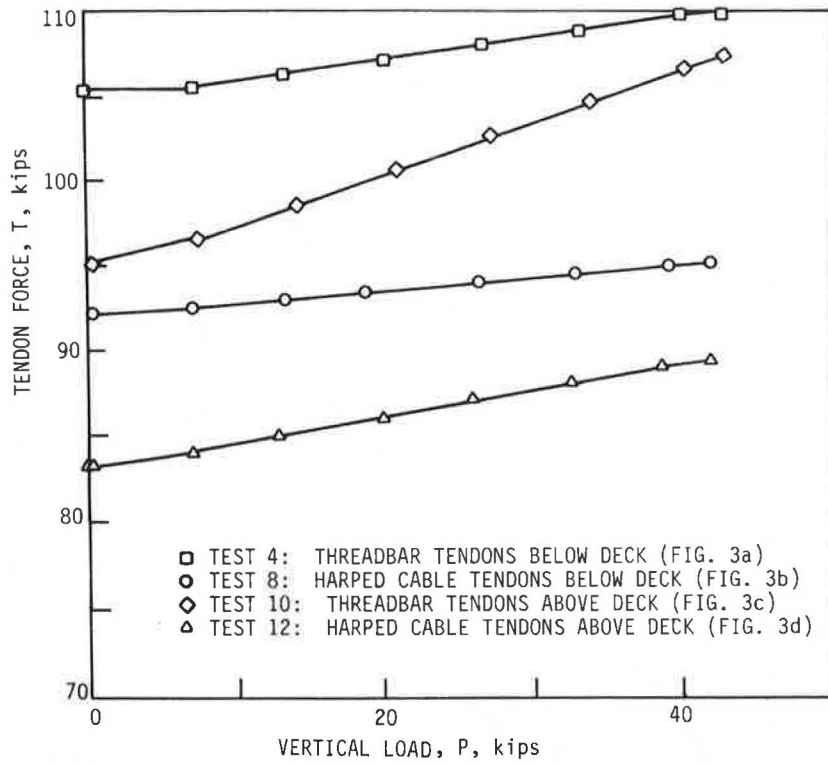**FIGURE 6** Load-deflection curves—harped tendons.

FIGURE 7 Change in tendon force due to vertical loading.

illustrates the variation in posttensioning tendon force with applied vertical load for the tests without the strengthening angles in use. Because of difficulties encountered with the cable anchoring chucks, the total force in the cable tendons was about 90 percent of the force in the threadbars below the deck. As shown in Figure 7, for all tendon configurations, tendon force increased as vertical load was applied. Tendon force increased more rapidly for the straight threadbars (Tendon Profiles 1 and 3) than for the harped cables (Tendon Profiles 2 and 4) and the tendon force increased more rapidly when the tendons were above the deck (Tendon Profiles 3 and 4) than when below (Tendon Profiles 1 and 2). The presence of the strengthening angles also caused the tendon force to increase more rapidly. Seating losses, the difference between maximum tendon force and tendon force after the tensioning jacks had been released, was less than 5 percent for the threadbars but ranged from 10 percent to 18 percent for the cable tendons. The high seating losses were primarily due to the short length of the cable tendons.

Addition of the strengthening angles shifted the neutral axis of the mockup downward and increased the moment of inertia. This resulted in a decrease in the bottom flange strains and essentially no change in the top flange strains. Because of the increase in the moment of inertia, total deflections were also slightly reduced. For those tests with posttensioning, the strengthening angles enhanced the effects of the posttensioning. Because the angles were not continuous over the center support and the flanges of the angles did not bear against the bearing stiffener, shear lag effects were evident at Section 4 near the center support. Tests 14, 15, and 16 indicated that restoring continuity around the bearing stiffener increased the effectiveness of the angles near the center support, where they were most needed.

As previously noted in an actual bridge, the concrete deck in the negative moment region over an interior support cracks because of traffic, weathering, and other time effects. When the deck cracks, the concrete becomes discontinuous, and the steel beam and deck no longer act in a completely composite sense. However, tension stress in the concrete transfers to the reinforcing bars, and some composite action theoretically still exists. Testing the mockup provided an opportunity to determine the degree of apparent composite action that remains when the concrete deck cracks. The apparent composite action was determined by comparing experimental strains and deflections to data from the simple steel and completely composite analytical models.

Table 2 summarizes the low, high, and average values of apparent composite action calculated from both strain and deflections for different groups of tests. Each group includes data common to one measurement—strain at a particular section or deflection at a particular point—and one analysis method—manual calculations or finite element analysis. Although a large amount of experimental scatter was evident from the range of high and low values for each group, the average values for all the groups fell within the range of 50 to 70 percent.

Both the manual and finite element analytical methods gave comparable predictions of strains and deflections. The finite element method has the advantage of more quickly modeling and analyzing different geometries and load cases. Neither the simple steel beam nor the completely composite analytical model was accurate at predicting strains or deflections, but

TABLE 2   RANGE AND AVERAGE PERCENT OF APPARENT COMPOSITE ACTION

| Group | Data Utilized | Analysis Method | % Apparent Composite Action | | | | Tests Included |
			Low Value	High Value	Average Value	Test 2 Value	
1	Strains at Sec. 4[a]	CTM[b]	39	81	58	62	2, 3, 4, 5, 6, 7, 8, 9, 10, 11, 12
2	Strains at Sec. 4	CTM	61	81	68	62	2, 4, 8, 10, 12
3	Strains at Sec. 4	FEM[c]	63	81	69	63	2, 4, 8, 10, 12
4	Strains at Sec. 5	CTM	40	90	65	54	2, 3, 4, 5, 6, 7, 8, 9, 12, 13
5	Strains at Sec. 5	CTM	40	58	51	54	2, 4, 8, 12
6	Strains at Sec. 5	FEM	49	53	51	53	2, 4, 8, 12
7	Deflections at Pt. A	CTM	35	48	42	48	2, 3
8	Deflections at Pt. A	FEM	35	79	60	68	2, 4, 10
9	Deflections at Pt. B	FEM	58	88	69	--	8, 10, 12

[a]See Figure 2 for location of sections and deflection points.
[b]Classical theory method.
[c]Finite element method.

they did provide definite boundaries for both strain and deflection.

SUMMARY AND CONCLUSIONS

This paper discusses the results of an experimental investigation to determine the feasibility and effectiveness of posttensioning the negative moment region of continuous composite bridges. A full-scale model of an interior stringer within a bridge was constructed. The model was load tested and four different posttensioning tendon configurations were investigated with and without the use of strengthening angles. Data from the tests with posttensioning were compared to results from a test on the unstrengthened model. Experimental data were compared to analytical calculations to determine the extent of composite action that remained after the concrete deck had cracked.

The following conclusions were drawn:

• Posttensioning, with either harped cable or straight threadbar tendon arrangements, can be used to strengthen negative moment regions.

• Even though force in the harped cable tendons was about 90 percent of that in the threadbars, the cables produced about the same changes in strains and deflections in the composite beam. Thus, the vertical shears created when the cables were harped compensated for the lower cable force.

• The threadbar tendons were simpler and easier to install than the harped cable tendons.

• Tendon force increased when vertical load (simulated live load) was applied for all the posttensioning tendon configurations. Rate of increase was dependent on tendon level, tendon profile, and the presence of the strengthening angles.

• Strengthening angles can be used along with posttensioning to reduce strain in the compression flange. The angles are subject to shear lag and should be well developed at critical stress locations. When fully developed and used with posttensioning, they enhance the posttensioning effects.

• The mockup displayed from 50 to 70 percent apparent-composite action in negative moment bending.

ACKNOWLEDGMENTS

REFERENCES

1. F. W. Klaiber, K. F. Dunker, and W. W. Sanders, Jr. *Feasibility Study of Strengthening Existing Single Span Steel Beam Concrete Deck Bridges*. ERI Project 1460, ISU-ERI-Ames-81251, Final Report. Engineering Research Institute, Iowa State University, Ames, 1981.
2. F. W. Klaiber, D. J. Dedic, K. F. Dunker, and W. W. Sanders, Jr. *Strengthening of Existing Single-Span Steel Beam and Concrete Deck Bridges, Part I*. ERI Project 1536, ISU-ERI-Ames-83185, Final Report. Engineering Research Institute, Iowa State University, Ames, 1983.
3. K. F. Dunker, F. W. Klaiber, B. L. Beck, and W. W. Sanders, Jr. *Strengthening of Existing Single-Span Steel Beam and Concrete Deck Bridges, Part II*. ERI Project 1536, ISU-ERI-Ames-85231, Final Report. Engineering Research Institute, Iowa State University, Ames, 1985.
4. K. F. Dunker, F. W. Klaiber, and W. W. Sanders, Jr. *Design Manual for Strengthening Single-Span Composite Bridges by Post-Tensioning, Part III*. ERI Project 1536, ISU-ERI-Ames-85229, Final Report. Engineering Research Institute, Iowa State University, Ames, 1985.
5. K. F. Dunker, F. W. Klaiber, F. K. Daoud, W. E. Wiley, and W. W. Sanders, Jr. *Strengthening of Existing Continuous Composite Bridges*, ERI Project 1846, ISU-ERI-Ames-88007, Final Report. Engineering Research Institute, Iowa State University, Ames, 1987.
6. W. E. Wiley. *Post-Tensioning of Composite T-Beams Subjected to Negative Moment*. M.S. thesis, Iowa State University, Ames, 1988.
7. F. K. Daoud. *Experimental Strengthening of a Three-Span Composite Model Bridge by Post-Tensioning*. M.S. thesis. Iowa State University, Ames, 1987.
8. F. W. Klaiber, K. F. Dunker, T. J. Wipf, and W. W. Sanders, Jr. *Methods of Strengthening Existing Highway Bridges*. NCHRP Report 293: TRB, National Research Council, Washington, D.C., 1987, 114 pp.
9. Y. Tachibana, K. Kondo, and K. Ito. *Experimental Study on Composite Beams Prestressed with Wire Cables*. Final Report. International Association for Bridge and Structural Engineering, 7th Congress, Rio de Janeiro, Brazil, Aug. 10–16, 1964.
10. G. D. Mancarti. Resurfacing, Restoring and Rehabilitating Bridges in California. *Proc., International Conference on Short and Medium Span Bridges*, Toronto, Ontario, Canada, Aug. 8–12, 1982.
11. G. D. Mancarti. Strengthening California's Steel Bridges by Prestressing. In *Transportation Research Record 950*, TRB, National Research Council, Washington, D.C., 1984, pp. 183–187.
12. N. F. F. Grace. *Effect of Prestressing the Deck in Continuous Bridge of Composite Construction*. M.A. Sci. thesis. University of Windsor, Windsor, Ontario, Canada, 1981.
13. C. Seim. Steel Beats Concrete for Idaho Bridge. *Civil Engineering*, Vol. 53, No. 8, Aug. 1983, pp. 28–32.
14. R. L. Preston. *Strengthening Methods for Bridge Superstructures*. National Roads Board, Wellington, New Zealand, 1985.
15. M. S. Troitsky, Z. A. Zielinski, and M. S. Pimprikar. Experimental Evaluation of Prestressed Steel and Plate Girder Bridges. *Proc., Experimental Assessment of Performances of Bridges*, ASCE, Boston, Mass., Oct. 27, 1986, pp. 1–6.
16. B. M. Ayyub, Y. G. Sohn, and H. Saadatmanesh. *Static Strength of Prestressed Composite Steel Girders*. Final Report to National Science Foundation. Department of Civil Engineering, University of Maryland, College Park, May 1988.
17. *Standard Specifications for Highway Bridges*, 13th ed. AASHTO, Washington, D.C., 1983.

Test of Continuous Prestressed Concrete Girders Without End Blocks

GIRISH HIREMATH, RAFIK ITANI, AND UMESH VASISHTH

This study investigates the feasibility of eliminating end blocks from pretensioned continuous bridge girders. The removal of end blocks is estimated to reduce girder cost by 5 to 10 percent. The girders studied are the Washington State Department of Transportation (WSDOT) Series 14 type, which are characterized by 5-in.-thick webs. Previous research has recommended the elimination of end blocks for simple span bridges. A controlled laboratory test on two 20-ft-long Series 14 girders is performed. The girders are without end blocks and continuous throughout the deck. Their joint details are similar to those normally used in the field. At the continuous end, strains induced in the stirrups are monitored during the detensioning process and during various stages of loading. The load is applied at a distance of 13 ft 10 in. from the continuous end. The limiting load at which the flexural steel yielded is 408 kips. The maximum applied load is 480 kips, which is 54 percent higher than the ultimate design shear of 325 kips. At ultimate design shear, the deflection of the free end is 1.2 in. Even though the nominal strength of the concrete in the diaphragm is less than that of the girder, the cracks have been restricted to the girders. The maximum 28-day compressive strength of the concrete in the diaphragm is 4,000 psi, as compared to the 9,880 psi of the girders. It is concluded that the modified girders perform effectively under applied loads and hence warrant the removal of end blocks.

The structural efficiency and cost effectiveness of prestressed concrete has made its use advantageous in long span bridges. For bridges with unusual layouts and long spans, the post-tensioning method of prestressing has been widely adopted. Otherwise, precast and pretensioned concrete girders have been used for spans between 40 and 140 ft.

For many years bridge girders have contained enlarged webs at their ends over the transitional lengths. These enlargements are known as end blocks. End blocks are thought to be necessary for the distribution of prestressing force. Their construction requires special formwork, which contributes as much as 5 to 10 percent to the total cost. Therefore, end blocks are both uneconomical and undesirable and, if possible, should be omitted from pretensioned girders.

End blocks have been used because of concern over the bursting stresses in the end regions. However, since the prestressing force is transferred through the bond between the concrete and the strands, end blocks may not be required for pretensioned girders. In fact, researchers have concluded that satisfactory performance can be obtained if adequate stirrup reinforcement is provided (1–3). The state of Washington has, however, retained end blocks as a measure of safety.

The reason for retaining them is that the Washington series of girders have a higher-depth-to-web thickness ratio than the comparable AASHTO girders or those used in previous research.

Precast, pretensioned girders are often used in combination with a cast-in-place (CIP) deck. The CIP deck is an efficient structural system because it produces continuity for resisting live loads. The elimination of end blocks would reduce the area of cross section available for shear transfer at the continuous support.

This article describes an experimental study in which a continuous CIP deck and Washington State Department of Transportation (WSDOT) Series 14 girders without end blocks were subjected to ultimate shear and bending moment. The performance of the end regions of the girders at the continuous joint was monitored for crack propagation and stresses.

EXPERIMENTAL SETUP

WSDOT Series 14 girders are used for spans of 120 to 140 ft. These girders are characterized by their 73.5-in. depth and 5-in. web thickness (Figure 1). They are usually designed for an ultimate shearing force of 325 kips (4). Table 1 shows the design loads at a continuous joint for a span of 132 ft 10 in.

With these loads as the basis, two 20-ft Series 14 girders without end blocks were designed and erected on a concrete pedestal to form a typical continuous joint. The experimental setup is shown in Figure 2. Details of the girders and the continuous joint are shown in Figures 3 and 4.

The stirrups within Girders A and B were instrumented with strain gauges. A #4 steel bar was placed at the center and 3 in. from the bottom so that the stresses could be monitored in the vicinity of the end regions. Figure 5 shows the locations and numbers of the gauges on the stirrups and the steel bars. Symmetric instrumentation was used for Girder B, with 200 designations for gauges; for example, gauges 101 and 201 were in identical locations of Girder A and Girder B, respectively.

The strains were measured during detensioning, immediately after the slab and the diaphragm were cast, and during the load application. Before each event strain gauges were initialized.

OBSERVATIONS AND RESULTS

This section discusses the stresses and the strains during the prestress transfer caused by the applied loads. It also presents

G. Hiremath and Rafik Itani, Department of Civil and Environmental Engineering, Washington State University, Pullman, Wash. 99164-2910. U. Vasishth, Washington State Department of Transportation, Olympia, Wash. 98504. Current address: 1858 Lakemoor Place, Olympia, Wash. 98502.
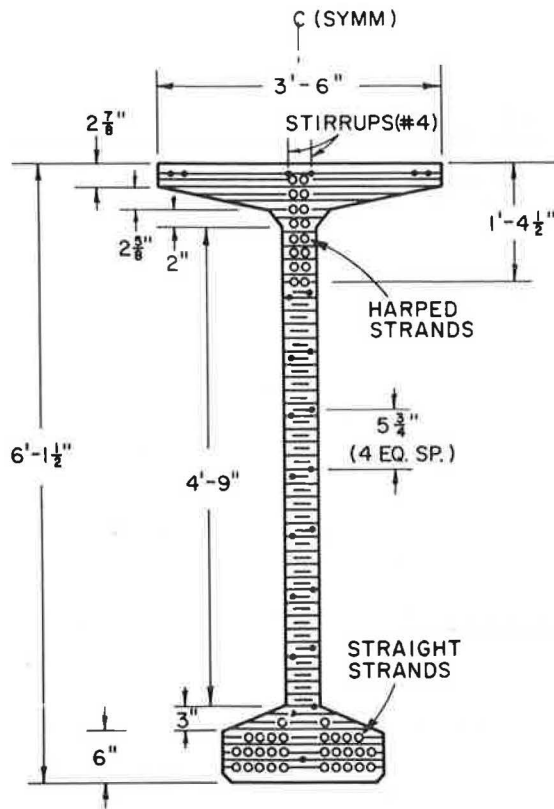
FIGURE 1 View of the continous end of a test girder.

the results of the combined effect of detensioning, casting of the slab and the diaphragm, and the applied loads.

During Prestress Transfer

The stresses in the stirrups and the longitudinal steel bar were obtained through the multiplication of the strains by the modulus of elasticity of steel ($E = 29,000$ ksi). Figures 6a–c show the variation in the stresses along the length of the girders. The following observations were made:

- The stress in the stirrups decreased with an increase in the distance from the ends of Girders A and B.
- Near the girder ends and at the levels of the centroidal axis, the stress was approximately 20 ksi (Figure 6a). At the locations of the resultant prestressing force and juncture between the web and bottom flange, the stresses were 23 ksi (Figures 6b and 6c). The stresses decreased with an increase in the distance, except at Gauges 230; 123 and 223; and 131 and 231, where the stresses varied from 20 ksi to 29 ksi.
- Stresses greater than 3.5 ksi indicated the presence of microcracks in the concrete. This was based on the assumption that the tensile strength of concrete is $7.5 \sqrt{f'c}$ and the modulus of elasticity of concrete is $33 \, w^{1.5} \sqrt{f'c}$.
- The stresses in Girders A and B agreed well except at the junction of the web and the bottom flange. The region was highly susceptible to microcracking and the subsequent nonuniform behavior of concrete.

TABLE 1   DESIGN LOADS AT A CONTINUOUS SUPPORT

Case	Maximum Moment Case (ft-kips)	Maximum Shear Case (kips)
Vdl	99.	99.
VDL cont.	35.	35.
Vll	34.	45.
Vu	250.	274.
Mdl	-952.	-952.
Mll	-1067.	-804.
Mu	-3554.	-2980.

DL (Uniform Continuous) = 0.43 K/ft.
Impact = 1.194
Distribution = .955
Span = 132.8 ft.

Where, Vdl = factored dead load, kips

Vdl cont. = factored uniform continums dead load, kips

Vll = factored live load, kips

Vu = design factored load, kips

Mdl = factored moment due to dead load, ft-kips

Mll = factored moment due to live load, ft-kips

Mu = design factored moment, ft-kips

ACTIVE END

PASSIVE END

LOAD CELL

DIAPHRAGM

GIRDER A

GIRDER B

ACTUATOR

6'-2" 13'-10" 13'-10" 6'-2"

1'-6"
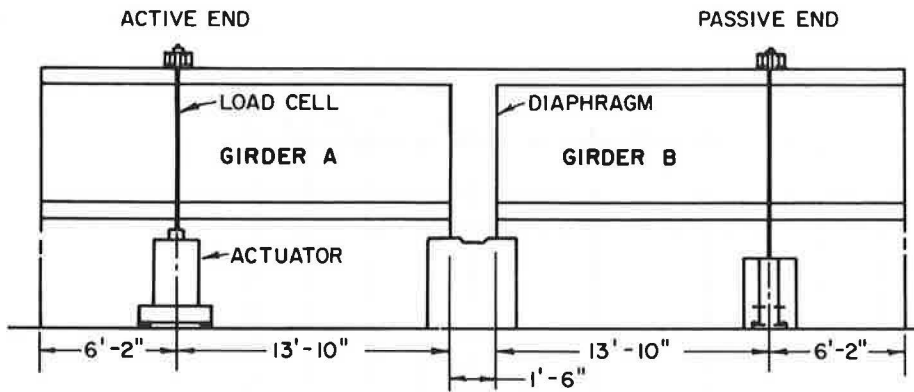
FIGURE 2 Elevation of the experimental setup.

20'-0"

SHEAR REINFORCEMENT(#4-TYP)

@ 2" @ 4" @ 10" @ 15½" @ 10" @ 4" @ 2"

2"

18"

C.G. OF HARPED STRANDS

8¼"
2"

14½"

2'-9¼"

7 @ 7"

C.G. OF
STRAIGHT
STRANDS

9" 2"

HORIZONTAL BAR WITH STRAIN GAGES (#4 x 5'-6")
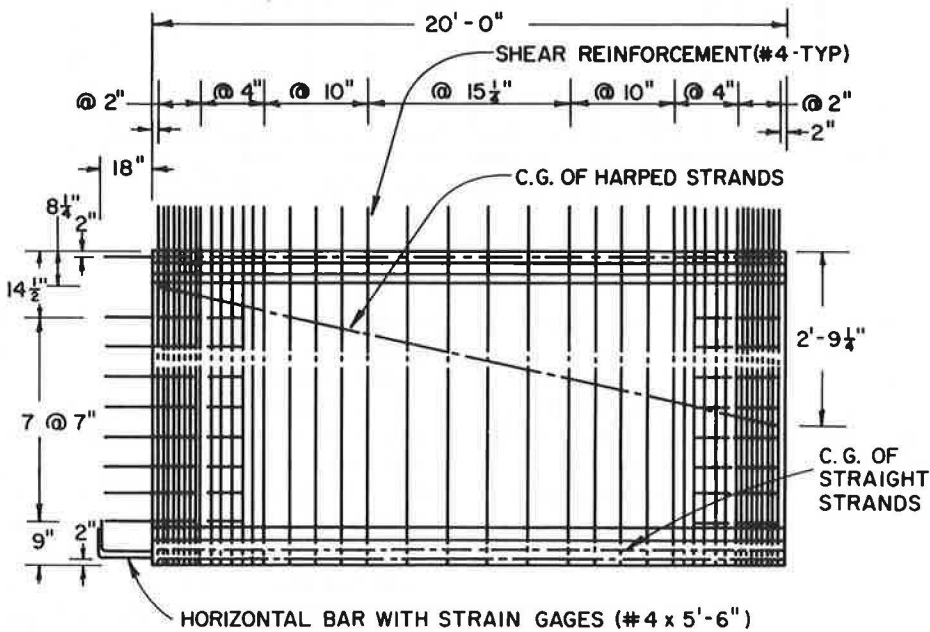
FIGURE 3 Longitudinal section of a test girder.

₵ HINGE

TOP OF
GIRDER

TOP OF SLAB
(reinforcement not shown)

END OF
GIRDER

#5 EXTENDED GIRDER
REINFORCEMENT
(continuity reinforcement)

3'-10"

HINGE BARS (#10)

4"

WOODED BLOCKS
(4"x 4"x 2'-0')

½" RUBBER PAD

1½"x 7¼"CONT. SHEAR KEY

4'-0"

1¼" A325 BOLT

STEEL PLATE
(¼"x 3'-9"x 4'-6")

FIGURE 4 Details of the continuous joint.

FIGURE 5 Configuration of strain gauges on stirrups of Girder A.

Figure 7 shows the stresses in the #4 steel bar at different locations along its length. The tensile stresses varied between 2 and 4 ksi and were considerably lower than those in the stirrups because the bar was outside the spalling and bursting zones. In addition, the bar was oriented in the direction of the cracks caused by spalling and bursting stresses. The compressive zone began at a distance of 28 in., which was beyond the transition zone of 25 in. from the end.
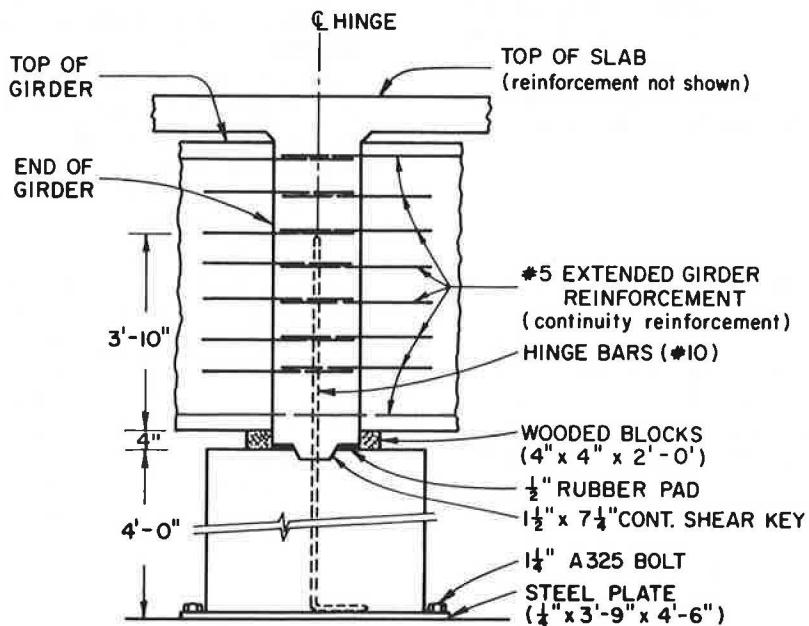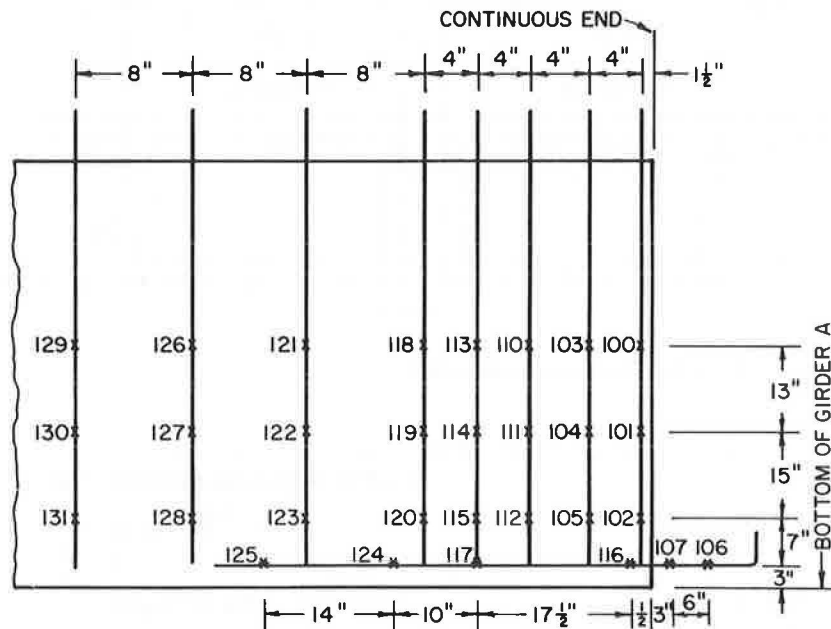
During Applied Loads

The results from the tests were independent of the strains recorded after detensioning and during the casting of the slab and diaphragm. The first applied load was 30 kips. This was followed by increments of 60 kips up to a load of 210 kips. At that level the increments were then decreased to 30 kips until a load of 510 kips was reached. At each load step the deflection at the point of loading and the strains were recorded.

Cracking Pattern

No significant cracking was observed until a load of 150 kips was reached. At that stage, cracks that had begun at detensioning propagated. The greatest increase in the length of the cracks was about 6 in. These were predominantly in the direction of the inclined prestressing strands in the webs. Vertical cracks caused by flexural stresses were noticed in the slab and the top flanges when a load of 210 kips was reached. Some of these cracks propagated into the webs as the load was increased to 270 kips. At that load lead, cracking was more prominent in the webs than in the slabs and the top flanges. These were on the tension side and within a distance of $h/4$ from the diaphragm, where h was the overall depth of the composite section. Up to this stage the flexural and the flex-

ure-shear cracks had been more dominant than those caused by web shear. The cracks were inclined at angles varying between 50 and 90 degrees.

As the load was increased, new cracks formed and earlier cracks extended. The cracks appeared to be equally spaced in the longitudinal direction and located away from the diaphragm. For loads higher than 300 kips, the cracks were mostly caused by web shear. At 300 kips, the cracks extended toward the bottom flange. Loads of 300, 330, and 360 kips created cracks that were located beyond a distance of $h/2$ from the ends and inclined at angles between 30 and 35 degrees. Similar cracking patterns were observed in both girders.

The observations made are summarized below:

● Cracks in the slab and top flange were caused by excessive flexural tensile stresses. The first visible flexural crack formed at an applied load of 210 kips.
● At an applied load of 270, the cracks were mainly caused by flexural shear. These were generally on the tension side of the web and fell within a distance of $h/4$ from the girder. The applied load of 270 kips corresponded to a maximum shear of 291 kips, which was higher than the design ultimate shear of 274 kips (Table 1).
● Cracks within a distance $h/2$ from the face of the diaphragm were inclined at varying angles, depending on their location with respect to the neutral axis. Cracks in the tension zone were inclined at an angle between 40 and 50 degrees to the horizontal. Cracks in the compression zone were inclined at an angle of 25 to 30 degrees. Thus, in the tensile region, flexural-shear cracks occurred, whereas in the compression region cracks were caused by shear stresses combined with direct and flexural-compressive stresses.
● For cracks farther away than $h/2$, the angle of inclination varied from 25 to 30 degrees. These cracks were caused by loads of more than 270 kips. Cracks caused by loads of 270, 360, 390, 420, 450, and 480 kips were located 1 ft 6 in., 3 ft, 3 ft 8 in., 6 ft 3 in., 10 ft, and 10 ft 3 in. from the face of the

(a)
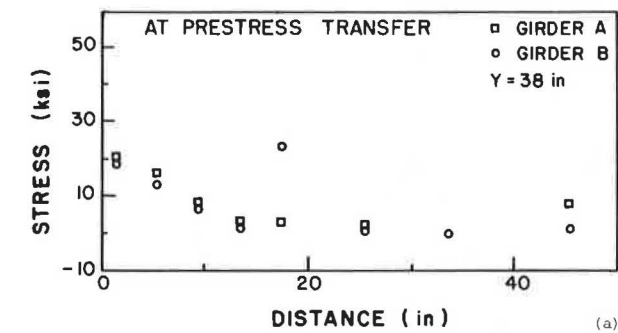
Y = DISTANCE FROM THE BOTTOM OF THE GIRDERS TO THE CENTROIDAL AXIS

(b)
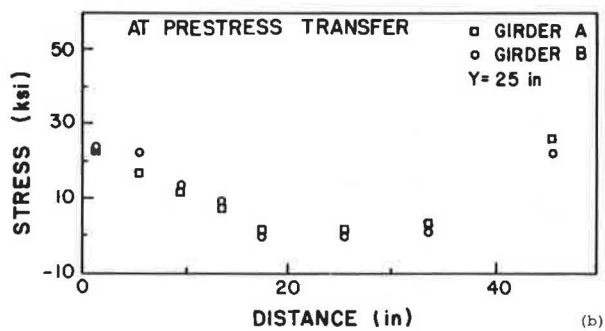
Y = DISTANCE FROM THE BOTTOM OF THE GIRDERS TO THE RESULTANT PRESTRESSING FORCE
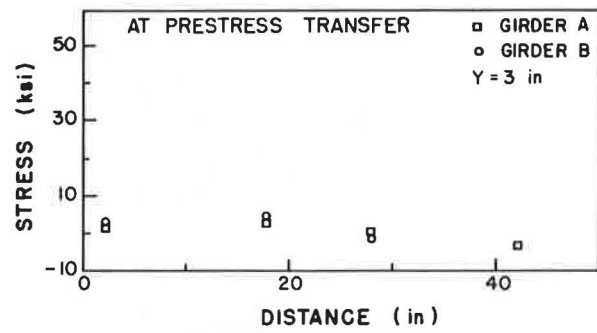

(c)
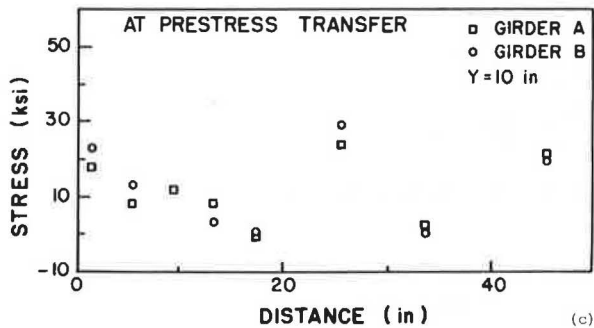
Y = DISTANCE FROM THE BOTTOM OF THE GIRDERS TO THE JUNCTION OF THE BOTTOM FLANGE AND THE WEB

FIGURE 6 Stresses in stirrups versus distance from the continuous end at the (a) centroidal axis, (b) resultant prestressing force, and (c) junction of the flange and the web.

diaphragm and along the centroidal axis. The corresponding angles of inclination at these locations were 65, 50, 35, 30, 29, and 25 degrees.

● Most of the web-shear cracks originated at the junction of the top flange and web and propagated toward the bottom flange at an angle of 30 degrees. Web-shear cracking was observed at loads higher than 300 kips.

Strains recorded during the test were caused by only the applied loads because the gauges had been initialized before loading. A sudden increase in strain in a gauge is a result of

Y = DISTANCE FROM THE BOTTOM OF THE GIRDERS TO THE HORIZONTAL BAR AT THE CENTER OF THE BOTTOM FLANGE

FIGURE 7 Stresses in the horizontal bar at the center of the bottom flange versus distance from the continuous end.

cracking in the concrete and the subsequent transfer of loads to the stirrup.

Strains Versus Applied Loads

The variation in strains in the gauges that occurred as the applied load increased from 30 to 480 kips is discussed in the following subsections.

Gauges on the Stirrups

In Figures 8 and 9, strains versus applied loads are plotted for the gauges on the stirrups located 38 in. from the bottom of the girders.

Figure 8 shows (Gauges 100 and 200) the presence of microcracks at a load of 150 kips. For loads greater than 150 kips, the strain increased. Gauge 213 indicated the formation of microcracks at a load of 270 kips, whereas for loads greater than 270 kips, Gauge 113 showed a rapid increase in strains. The gauges shown in Figure 8 were located below the centroidal axis of the composite section.

Figure 9 shows that Gauges 118 and 218 behave linearly up to a load of 300 kips, whereas Gauges 129 and 229 show a linear response up to 360 kips. At loads of more than 300 and 360 kips, respectively, concrete cracking transferred the load to the stirrups.

The response of the stirrups at the level of the resultant prestressing force, that is, 25 in. from the bottom of the girders, can be seen in Figures 10 and 11.

Figure 10 shows that deviation occurs at a load of 270 kips. In the case of Gauges 114 and 214, there was a transition from a compressive strain to a tensile strain. For Gauges 122 and 222, deviation from linearity occurred at a load of 360 kips.

For Gauges 127 and 227 (Figure 11) the cracking load was 360 kips. Gauge 130 indicated a linear increase in tensile strains of up to a load of 390 kips and then deviated from linearity. Gauge 230 did not function.

The strains in the gauges at the junction of the web and the bottom flange are plotted in Figures 12 and 13.

Gauges 105 and 205, shown in Figure 12, indicated com-

FIGURE 8　Stresses in the stirrups due to applied loads—Gauges 100, 200, 113, and 213.

FIGURE 9　Stresses in the stirrups due to applied loads—Gauges 118, 218, 129, and 229.

FIGURE 10　Stresses in the stirrups due to applied loads—Gauges 114, 214, 122, and 222.

FIGURE 11 Stresses in the stirrups due to applied loads—Gauges 127, 227, 130, and 230.
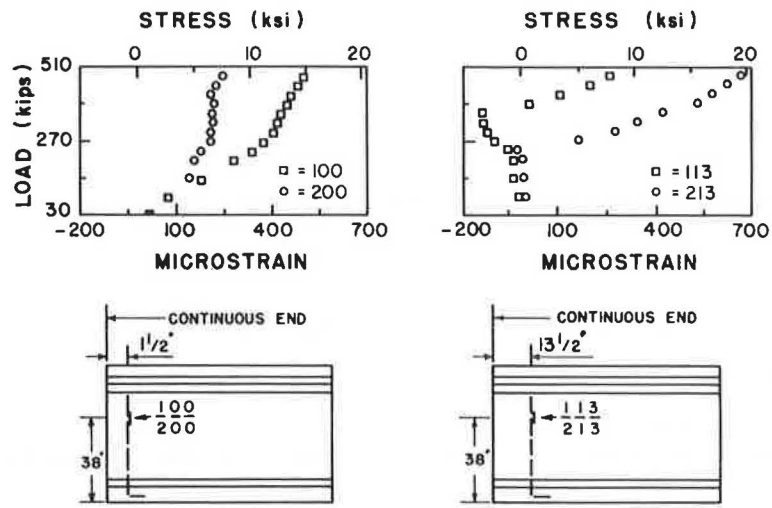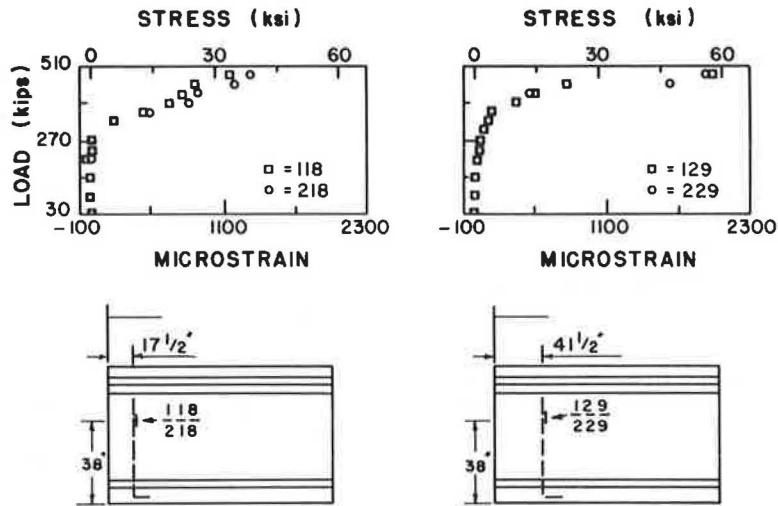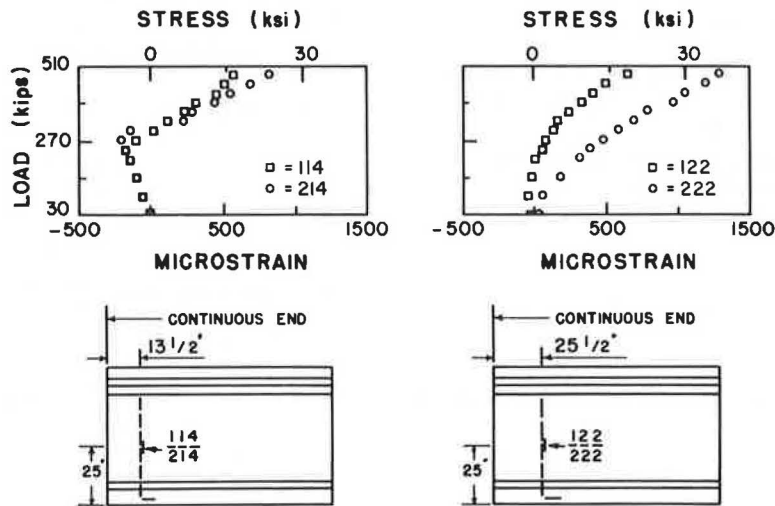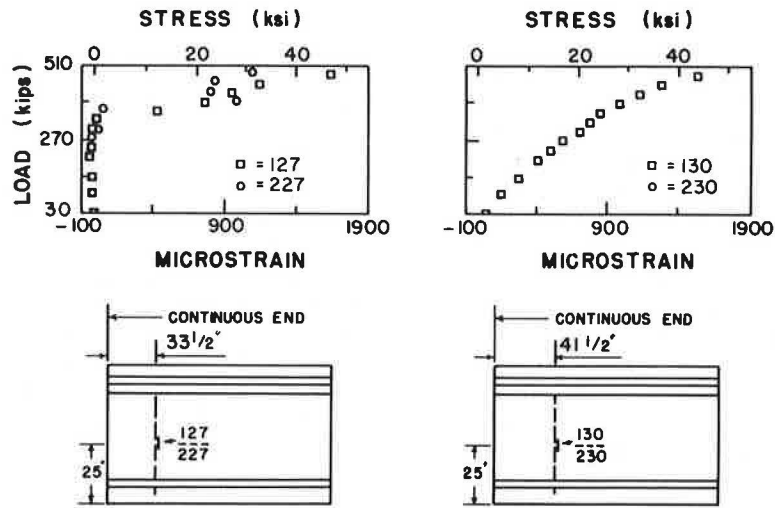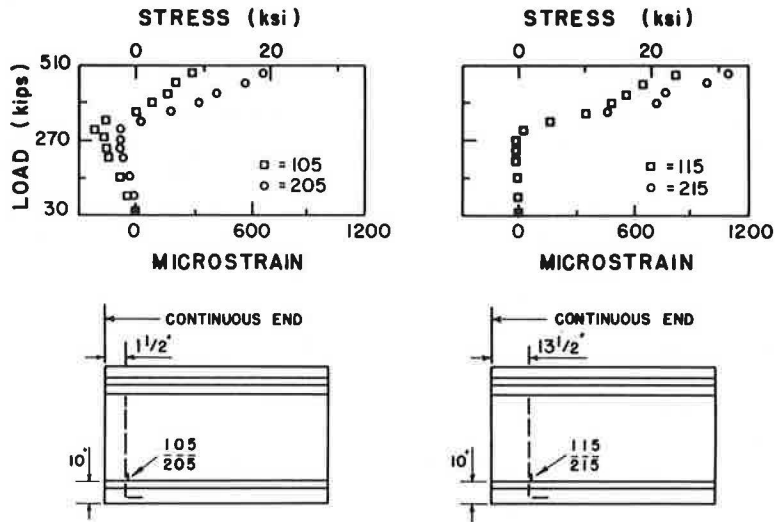

FIGURE 12 Stresses in the stirrups due to applied loads—Gauges 105, 205, 115, and 215.
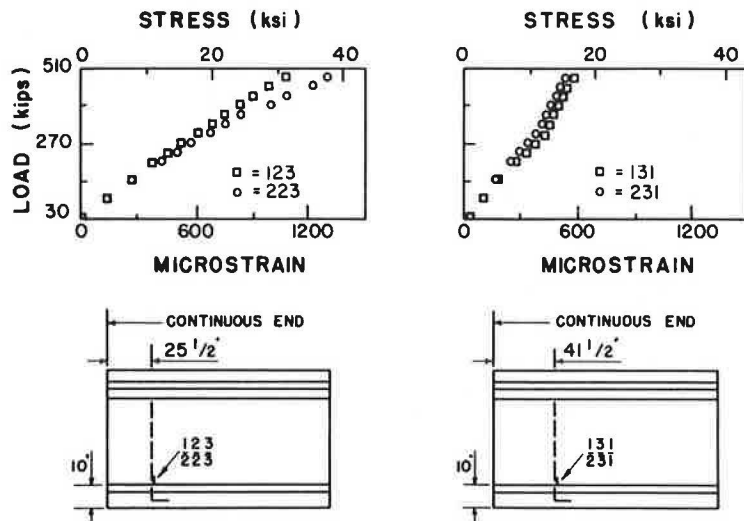

FIGURE 13 Stresses in the stirrups due to applied loads—Gauges 123, 223, 131, and 231.

pressive strain, whereas Gauges 115 and 215 showed negligible strains up to a load of 300 kips. Beyond that point, the strains became increasingly tensile. Figure 13 shows that Gauge 123 behaved linearly up to a load of 480 kips, whereas Gauge 223 deviated from linearity at 360 kips. The steady increase of tensile strains in the gauges was caused by the strutting behavior of the concrete. Strutting action caused the stirrups to be in tension. The results agreed with the cracks observed near the web and the bottom flange.

The following conclusions can be drawn from the strains in the stirrups:

● Loads at which the strain-versus-load curve deviate from linearity increased for gauges located farther away from the diaphragm.
● Generally gauges located within 13.5 in. from the diaphragm showed good agreement at loads less than 270 kips.
● In general, gauges located beyond 13.5 in. behaved linearly up to a load of 300 kips.

Strains Along the Center of the Bottom Flange

Strains in the steel bar located 3 in. above and along the centerline of the bottom flange are presented in Figures 14 to 16.

Gauges 106, 206, 107, and 207 were located within the diaphragm. Therefore, they indicated compressive strains (Figure 14). Figures 15a and 15b compare experimental and theoretical values as obtained by the flexural equation.

The theoretical values were based on the assumptions that concrete acts as a homogeneous and linearly elastic material. Tensile reinforcement in the slab was transformed into an equivalent area of concrete. The deviation of the experimental values from the theoretical results began at a load of 270 kips.

Figure 16 shows the development of cracks at Gauges 124 and 224 and at a load of 330 kips. Gauge 225 did not function,

whereas Gauge 125 deviated from linearity at a load of 270 kips.

The strains in the steel bar lead to the following conclusions:

● The maximum compressive strain at the midsection of the diaphragm was 0.0017, which was about 50 percent of the maximum compressive strain that concrete can sustain.
● The tension in Gauges 124, 224, and 125 can be explained on the basis of the compression strut theory. The formation of cracks in the web near the bottom flange resulted in a strutting action in the web. The horizontal component of the force in the strut was resisted by the bottom flange, which behaved as a tension member.

Combined Effective Strains and Stresses

In the previous subsection, the strains and stresses caused by applied loads and corresponding moments were studied. This subsection presents the combined strains resulting from the effective prestressing force and the slab. Tables 2, 3, and 4, which assume a prestressing loss of 25 percent and a linear relationship between the prestressing force and stresses, show the combined effect of prestressing force, the weight of the slab, and the applied load.

Table 2 shows the stresses from gauges that are 38 in. from the bottom of the girders. At a load of 300 kips, the greatest stress in the stirrups was 20 ksi, and it occurred 1.5 in. from the diaphragm. Up to the applied load of 360 kips, stresses in the stirrups decreased as the distance from the diaphragm increased. For loads higher than 360 kips, stresses in the stirrups farther than 17.5 in. increased. At a load of 480 kips, the first yielding occurred in the stirrup located 41.5 in. from the diaphragm.

Table 3 shows the stresses that are located 25 in. from the bottom. Within a distance of 9.5 in., stresses increased as the distance from the diaphragm increased. The greatest stress at

FIGURE 14 Stresses in the horizontal bar at the center of the bottom flange due to applied loads—Gauges 106, 206, 107, and 207.
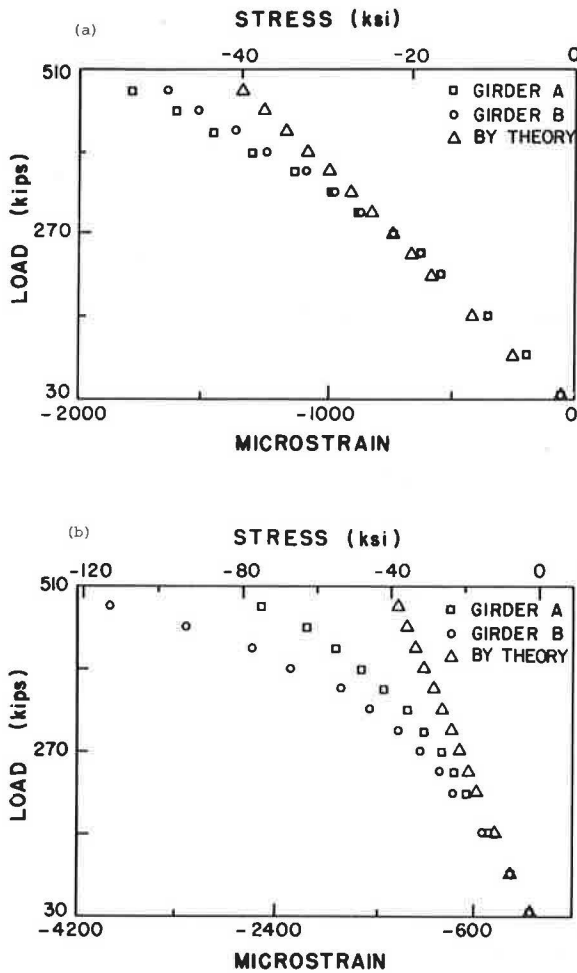
FIGURE 15 Comparison of the experimental and theoretical results—(a) Gauges 106 and 206 and (b) Gauges 107 and 207.

a load of 300 kips was 17 ksi and occurred at a distance of 25.5 in. Beyond that load and except for gauges 222 and 127, the stresses decreased. At the maximum load of 480 kips, stresses in the stirrups located within the transfer length of 25 in. were about 50 percent of the yield stress. At that load level, yielding occurred in the stirrup located 25.5 in. from the diaphragm.

At the junction of the web and the bottom flange, that is, 11 in. from the bottom, and at a load of 300 kips, the maximum stress in the stirrups was 17 ksi and occurred at 33.5 in. (Table 4). At 480 kips, the stresses within a distance of 17.5 in. were within 50 percent of the yield stress, whereas stresses at 33.5 in. were 57 ksi.

Table 5 shows the maximum stresses in the stirrups along the length of the girders. The following data can be observed from the table.

- The maximum stress at a load of 300 kips was 20 ksi and occurred at 1.5 in. from the end of the girder. That stress is 33 percent of the yield stress (60 ksi).
- Within the transfer length of 25 in., the maximum stress caused by a load of 480 kips was 36 ksi, which was about 60 percent of the yield strength. For locations beyond the transfer length, the maximum stress at 480 kips was 60 ksi.
- As the load increased from 300 kips to 480 kips, the stresses increased with an increase in the distance from the diaphragm.

Load Versus Deflection Curve

The deflection of the active side was measured at the point of load application. Figure 17 shows a curve of load versus deflection. The curve is linear up to 270 kips of applied load. Thereafter, deflection increased steadily with an increase in the applied load. The maximum deflection was 3.3 in., whereas the deflection at 270 kips was 1.2 in. The recovery after the

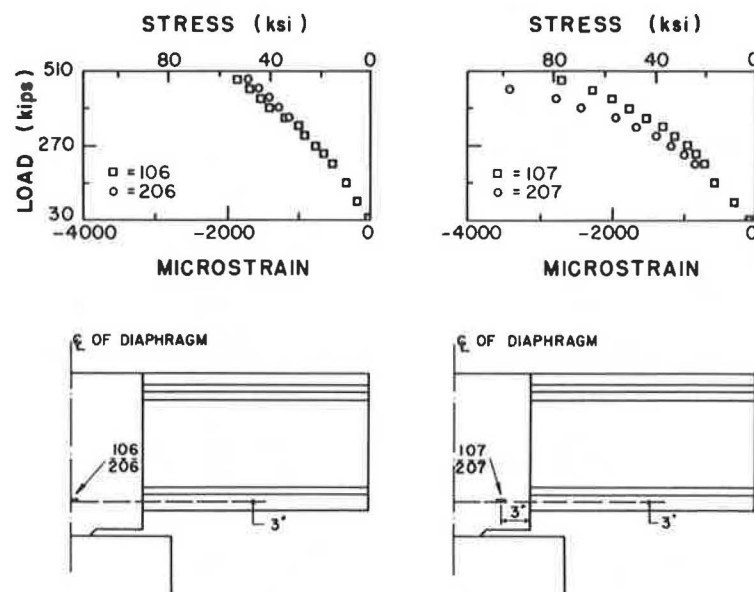FIGURE 16 Stresses in the horizontal bar at the center of the bottom flange due to applied loads—Gauges 124, 224, 125, and 225.
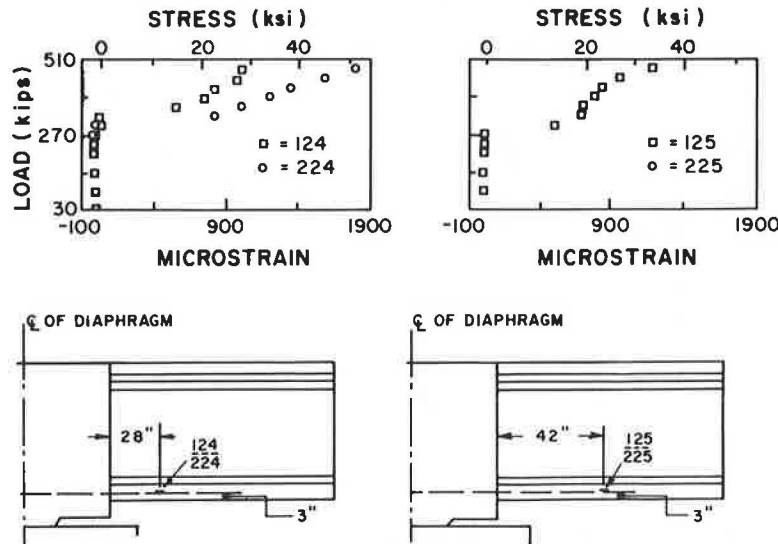
TABLE 2   STRESSES (ksi) IN STIRRUPS AT y = 38 in. LOAD COMBINATION: EFFECTIVE PRESTRESS PLUS WEIGHT OF THE SLAB PLUS THE APPLIED LOAD

	x 1.5		x 5.5		x 9.5		x 13.5		x 17.5		x 25.5		x 33.5		x 41.5	
	Girder															
	A	B	A	B	A	B	A	B	A	B	A	B	A	B	A	B
Load (kips)	Gage No.															
	100	200	103	203	110	210	113	213	118	218	121	221	125	226	129	229
30	10	10	9	7		5		1	2		1	-1			6	
90	14	13	1	3		2		1	2		1	-1			6	
150	14	13	1	3		2		1	2		2	0			7	
210	17	14	0	-1		2		1	2		3	0			7	
240	18	14	-2	-2		3		1	3		3	1			8	
270	19	15	-3	-4	NG	2	NG	6	3	NG	4	1	NG	NG	8	NG
300	20	15	-3	-4		3		9	7		8	3			9	
330	20	15	-3	-5		4		11	8		12	8			11	
360	21	15	-2	-4		7		13	15		19	9			11	
390	21	15	-2	-2		10		16	21		27	18			16	
420	21	15	-1	-3		11		17	23		29	29			20	
450	22	15	-1	-5		13		18	26		33	37			27	
480	23	16	-2	-5		15		19	34		44	43			60	

x = distance of a stirrup from the face of the diaphragm in inches

y = distance of the gases from the bottom of girder A and girder B

NG = Not Good

TABLE 3   STRESSES (ksi) IN STIRRUPS AT y = 25 in. LOAD COMBINATION: EFFECTIVE PRESTRESS PLUS WEIGHT OF THE SLAB PLUS THE APPLIED LOAD

	x 1.5		x 5.5		x 9.5		x 13.5		x 17.5		x 25.5		x 33.5		x 41.5	
	Girder															
	A	B	A	B	A	B	A	B	A	B	A	B	A	B	A	B
Load (kips)	Gage No.															
	101	201	104	204	111	211	114	213	119	219	122	222	127	227	130	230
30	7		11	11	10	8	6	6	-1	-1	-6	1	-2			
90	5		9	10	8	7	4	5	-1	-2	-6	3	-2			
150	2		7	7	6	6	4	4	-1	-3	-5	6	-3			
210	1		5	6	4	5	2	2	-2	-5	-5	10	-3			
240	1		4	5	2	4	1	2	-2	-5	-3	12	-3			
270	2	NG	4	4	3	10	3	0	-2	-8	-3	14	-3			
300	2		5	4	7	14	7	2	0	1	-1	17	-2			
330	3		6	5	9	16	9	12	8	5	-1	20	-1			
360	5		6	5	9	17	13	13	13	5	1	23	10			
390	7		7	9	10	20	15	18	15	8	4	27	19			
420	8		8	11	10	21	19	21	17	13	6	30	24			
450	9		8	13	11	23	20	25	18	17	8	33	29			
480	10		9	15	13	25	22	28	20	19	12	60	42			

x = distance of a stirrup from the face of the diaphragm in inches

y = distance of the gases from the bottom of girder A and girder B
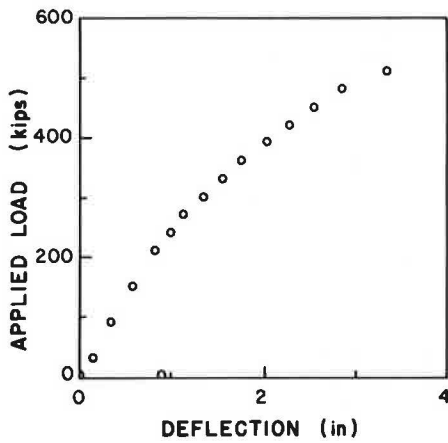
NG = Not Good

FIGURE 17   Applied loads versus deflection.

the first yielding of the stirrups occurred at an applied load of 480 kips, which corresponded to a total shear of 500 kips. The girders showed an excess capacity of 54 percent beyond the ultimate shear.

The first yielding of the longitudinal steel occurred at a moment of 5,407 ft-kips. The maximum ultimate design moment was 3,554 ft-kips, so the composite section had 52 percent excess moment capacity over the maximum design moment.

Therefore, the logical conclusion is that Series 14 girders without end blocks can perform effectively as continuous girders as long as (a) they are placed normal to the support and (b) the construction sequence presented in this paper is followed. Even though no impact or fatigue loadings were used, the conclusions should hold considering the high levels of factor of safety for ultimate moment and shear force.

REFERENCES

1. W. T. Marshall, and A. H. Mattock. Control of Horizontal Cracking in the Ends of Pretensioned Concrete Girders. *PCI Journal*, Vol. 7, No. 5, Oct. 1962, pp. 56–74.
2. P. Gergely, M. A. Sozen and C. P. Siess. *The Effect of Reinforcement on Anchorage Zone Cracks in Prestressed Concrete Members.* Structural Research Series 271. University of Illinois, Urbana, 1963.
3. N. M. Hawkins. Behavior and Design of End Blocks for Prestressed Concrete Beams. *Civil Engineering Transactions*, Institute of Engineers, Barton, Australia, Vol. CE8, No. 2, Oct. 1966.
4. *Bridge Design Manual Volume 1—Criteria.* Washington State Department of Transportation, Olympia, July 1982.
5. Precast-Prestressed Concrete Bridges (6 parts). *PCA Journal*, May 1960, Sept. 1960, Jan. 1961, May 1961, Sept. 1961.

TABLE 4   STRESSES (ksi) IN STIRRUPS AT y = 11 in. LOAD COMBINATION: EFFECTIVE PRESTRESS PLUS WEIGHT OF THE SLAB PLUS THE APPLIED LOAD

	: x															
	1.5		5.5		9.5		13.5		17.5		25.5		33.5		41.5	
	Girder															
	A	B	A	B	A	B	A	B	A	B	A	B	A	B	A	B
Load (kips)	Gage No.															
	102	202	105	205	112	212	115	215	120	220	123	223	128	228	131	231
30	11	14	5	9	8		6	1	0	-13			2	-1		
90	10	14	5	9	8		6	1	0	-13			2	-1		
150	8	13	3	8	7		5	1	-1	-14			2	-1		
210	5	11	2	7	7		5	1	-1	-14			2	-1		
240	4	10	2	7	6		5	1	-1	-14			1	-1		
270	3	9	1	7	6	NG	5	1	-1	-14	NG	NG	1	-1	NG	NG
300	3	9	0	7	5		6	2	-1	-15			17	-1		
330	4	9	2	10	8		10	6	-1	2			40	18		
360	5	11	6	14	12		15	14	1	3			38	38		
390	6	12	8	18	13		19	21	18	11			41	41		
420	7	13	10	21	15		21	22	20	14			44	45		
450	6	14	11	25	16		24	28	24	22			49	52		
480	6	15	14	27	20	28	31	30	27	57			57	57		

x = distance of a stirrup from the face of the diaphragm in inches

y = distance of the gages from the bottom of girder A and girder B

NG = Not Good

TABLE 5   MAXIMUM STRESSES (ksi) IN THE STIRRUPS

X	1.5	5.5	9.5	13.5	17.5	25.5	33.5	41.5
Load (kips)								
30	14	11	10	6	2	1	2	6
90	14	10	8	6	2	3	2	6
150	14	8	7	5	2	6	2	7
210	17	7	7	5	2	10	2	7
240	18	7	7	5	2	10	2	7
270	19	7	10	6	3	14	1	8
300	20	7	14	9	7	17	17	9
330	20	10	16	11	8	20	40	11
360	21	14	17	15	15	23	38	11
390	21	18	20	19	21	27	41	16
420	21	21	21	21	23	30	44	20
450	22	25	23	24	26	33	49	27
480	23	27	25	28	31	36	52	60

x = Distance from the face of the diaphragm

removal of the load was 2.4 in., that is, the net plastic deformation was 0.9 in.

SUMMARY AND CONCLUSIONS

The Series 14 girders have been statically tested and designed for a maximum factored shear, V_u, of 274 kips and a moment, M_u, of 3,552 ft-kips. The maximum ultimate shear, V_u, for Series 14 girders is equal to 325 kips. This is approximately equal to an applied test load of 300 kips, in addition to the maximum manufactured dead load shear of 21 kips. At that shear force, the maximum effective stress in the stirrups was 20 ksi, which was 33 percent of yield stress. That load corresponded to the initiation of web cracking.

At higher loads, web cracking increased, and the stirrups located beyond the transfer length of 25 in. indicated higher stresses than those located within the transfer length. Finally,

Dynamic Analysis of Girder Bridges

Eui-Seung Hwang and Andrzej S. Nowak

This paper deals with the calculation of dynamic loads in girder bridges. Three major elements are considered: vehicle dynamics, road roughness, and bridge dynamics. The parameters representing the road profile and axle weights are treated as random variables. The statistical models are established on the basis of the available test, measurement, and analytical data. The mathematical equations relating forces and deformations are formulated, with the system of equations solved by a numerical integration method. Using the Monte Carlo technique, a procedure is developed for simulation of the dynamic load spectra. The approach is demonstrated on a typical steel girder bridge. The resulting distribution functions of the dynamic load are presented on a normal probability scale.

The dynamic load is an important parameter in bridge design and evaluation. In the current AASHTO standards (1), dynamic load (impact), I, is treated as an equivalent additional static load:

$$I = \left(\frac{50}{L + 125}\right) LL \tag{1}$$

where

L = span length in ft and
LL = live load.

In Ontario, the dynamic load allowance (fraction of live load) is specified as a function of the natural frequency of vibration of the bridge (2), as shown in Figure 1. A similar approach is used in the revised Swiss code (SIA 160) (3).

On the other hand, observations and measurements indicate that the dynamic behavior of the bridge is a function of three major factors (4–9):

• Dynamic properties of the vehicle (mass, suspension, axle configuration, tires, speed);
• Road roughness (approach, roadway, cracks, potholes, waves); and
• Dynamic properties of the bridge structure (span, mass, support types, material, geometry).

In this study a procedure is developed to quantify the dynamic load effect. The three factors just listed are considered. The analysis is performed for the syperstructure of a simply supported girder bridge. The dynamic load effect in a bridge is measured in terms of a dynamic load factor (DLF). DLF is defined as the ratio of the maximum deflection experienced by the bridge (including dynamic effects) and the maximum

static deflection at midspan. Mathematical equations relating forces and deformations are formulated and solved using a numerical integration method. A simulation procedure, based on Monte Carlo technique, is developed to calculate the bridge dynamic load spectra.

The proposed procedure can be used for the development of more efficient design and evaluation criteria.

VEHICLE DYNAMICS

From the dynamic analysis point of view, the truck is composed of the body, wheels with tires, and the suspension system. There is a variety of configurations, including tractor with or without trailer(s) and different axle loads and axle spacings. In this study the four most common vehicles are used: two single trucks (S2 and S3) and two semi tractor-trailers (T4 and T5) as shown in Figure 2.

It is assumed that trucks are equipped with multileaf spring type suspensions. Leaf springs can be treated as nonlinear devices that dissipate energy during each cycle of oscillation. Their characteristics were measured by Fancher et al. (10). The results show that the force-deflection relationship does not depend on the frequency of oscillations occuring in the 0 to 15 Hz range, but it depends on the motion amplitude and the nominal load. Fancher et al. (10) derived nonlinear (logarithmic) equations relating forces and deflections of the truck suspension system. These equations are used in simulation of the DLF.

Tires can be treated as linear elastic spring components. The spring constants were measured by Fancher and Ervin (11). A typical value of 10,000 lb per in. per tire is used in this study.

A truck body is represented by a distributed mass subjected to rigid body motions. Vertical displacements and pitching rotations are considered. A trapezoid mass distribution is assumed with a constant mass density ρ (Figure 3). The mass moment of inertia about the mass central axis is

$$I = \frac{\rho h^3}{36} \frac{p^2 + 4pq + q^2}{p + q} \tag{2}$$

where p, q, and h are shown in Figure 3. Let $r = c/(a + b)$ and W = total mass; then

$$I = W/6 \left[4(r^2 + r + 1)ab + (2r^2 + 2r - 1)(a^2 + b^2)\right] \tag{3}$$

where a, b, and c are dimensions also shown in Figure 3. A model of a single truck and the corresponding free body diagram are shown in Figure 4. Four equations can be obtained,
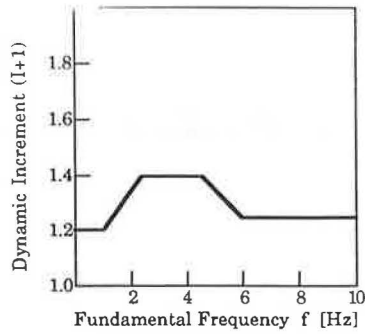
Department of Civil Engineering, The University of Michigan, Ann Arbor, Mich. 48109.

FIGURE 1   Dynamic load allowance in Ontario (2).

(a) Two Axle Single Truck (S2)   (b) Three Axle Single Truck (S3)

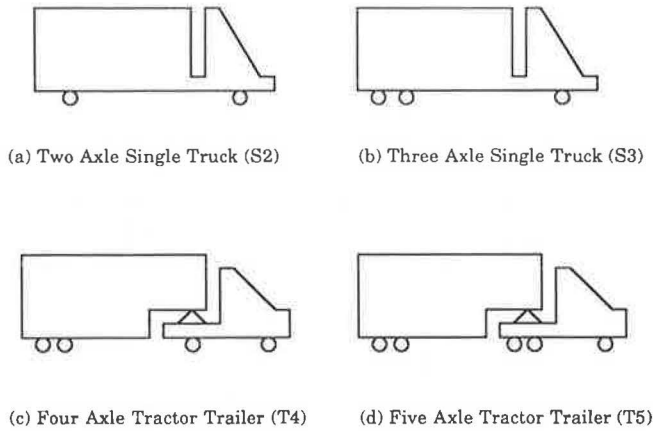(c) Four Axle Tractor Trailer (T4)   (d) Five Axle Tractor Trailer (T5)
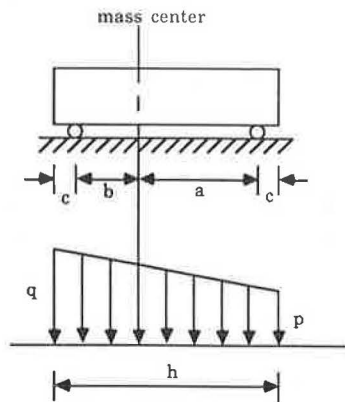
FIGURE 2   Trucks used in the study.

FIGURE 3   Truck body model.

three for the vertical equilibrium and one for the rotation equilibrium, as follows:

$$m_1(a_2\ddot{y}_1 + a_1\ddot{y}_2) + SF_1 + SF_2 = 0$$

$$m_2\ddot{y}_3 + TF_1 - SF_1 = 0$$

$$m_3\ddot{y}_4 + TF_2 - SF_2 = 0 \tag{4}$$

$$I_y(\ddot{y}_1 - \ddot{y}_2)/s + SF_1a_1s - SF_2a_2s = 0$$

where

y_i = vertical displacements,
m_i = masses,
SF_i = suspension forces,
TF_i = tire forces,
s = distance between axles,
a_i = distances between mass center and axles, and
I_y = pitching rotation moment of inertia.

A model of a tractor-trailer and the corresponding free body diagram is shown in Figure 5. Seven equations can be obtained from the vertical and rotation equilibrium,

$$m_1\ddot{y}_{c1} + SF_1 + SF_2 + P_j = 0$$

$$m_2\ddot{y}_{c2} + SF_3 - P_j = 0$$

$$m_3\ddot{y}_4 + TF_1 - SF_1 = 0$$

$$m_4\ddot{y}_5 + TF_2 - SF_2 = 0 \tag{5}$$

$$m_5\ddot{y}_6 + TF_3 - SF_3 = 0$$

$$I_1\ddot{\theta}_1 + a_1s_1SF_1 - a_2s_1SF_2 - (a_3 - a_1)s_1P_j = 0$$

$$I_2\ddot{\theta}_2 - a_6s_2SF_3 - a_5s_2P_j = 0$$

where

s_i = distances between axles,
P_j = tractor-trailer interaction force,
y_{ci} = deflections at mass center,
θ_i = rotations at mass center,
I_i = pitching rotation moments of inertia, and other notations as in Equation 4.

From the truck geometry,

$$y_{c1} = a_1y_2 + a_2y_1$$

$$y_{c2} = a_5y_3 + a_6(a_4y_1 + a_3y_2)$$

$$\theta_1 = (y_1 - y_2)/s_1 \tag{6}$$

$$\theta_2 = (a_4y_1 + a_3y_2 - y_3)/s_2$$

Substituting these geometric equations into equilibrium equations, the following six equations of motion are obtained for a tractor-trailer:

$$m_3\ddot{y}_4 + TF_1 - SF_1 = 0$$

$$m_4\ddot{y}_5 + TF_2 - SF_2 = 0 \tag{7}$$

$$m_5\ddot{y}_6 + TF_3 - SF_3 = 0$$

$$\begin{bmatrix} c_1 & c_2 & c_3 \\ c_2 & c_4 & c_5 \\ c_3 & c_5 & c_6 \end{bmatrix} \begin{Bmatrix} \ddot{y}_1 \\ \ddot{y}_2 \\ \ddot{y}_3 \end{Bmatrix} = - \begin{Bmatrix} SF_1 \\ SF_2 \\ SF_3 \end{Bmatrix}$$

where

$c_1 = I_2a_4^2/s_2^2 + I_1/s_1^2 + a_2^2m_1 + a_4^2a_6^2m_2,$
$c_2 = I_2a_3a_4/s_2^2 - I_1/s_1^2 + a_1a_2m_1 + a_3a_4a_6^2m_2,$
$c_3 = a_4a_5a_6m_2 - I_2a_4/s_2^2,$

(a) truck model

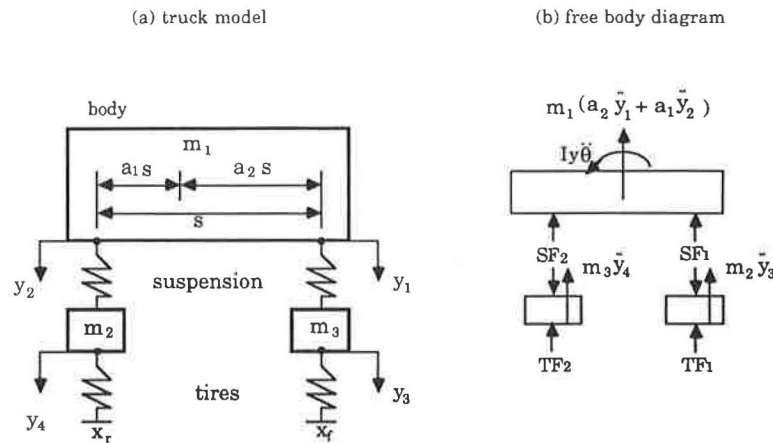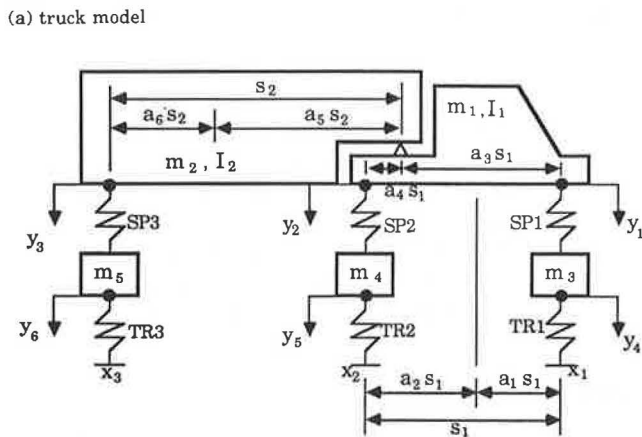(b) free body diagram

FIGURE 4   Model of a single truck.

(a) truck model

(b) free body diagram

FIGURE 5   Model of a semi tractor-trailer.

$c_4 = I_2 a_3^2 / s_2^2 + I_1 / s_1^2 + a_1^2 m_1 + a_3^2 a_6^2 m_2,$
$c_5 = a_3 a_5 a_6 m_2 - I_2 a_3 / s_2^2,$ and
$c_6 = a_5^2 m_2 + I_2 / s_2^2.$

Table 1 gives the probability of occurrence for each truck type (12). It clearly indicates that the dominant type is a five-axle semi tractor-trailer. For each truck type, the calculations were based on truck weight measurement data (12), with the statistical parameters of the total weight given in Table 2. The weight distribution over axles and axle distances are assumed

TABLE 1   FREQUENCY OF OCCURRENCE FOR VARIOUS TRUCK TYPES

Truck Types	Frequency of Occurrence (%)
2-axle single (S2)	9
3-axle single (S3)	5
4-axle semi (T4)	19
5-axle semi* (T5)	67

* 5-axle semi tractor-trailer includes 6 or more axle semi tractor-trailers and 5-axle splits.

TABLE 2   STATISTICS OF TOTAL WEIGHT

Truck Type	Total Weight , W (kips)				
	Mean Value	Standard Deviation	Distribution Type	Minimum Value	Maximum Value
S2	15.26	4.42	Normal	10.0	30.0
S3	26.35	8.32	Normal	11.5	70.0
T4	27.99	8.06	Normal	13.7	70.0
T5	44.41	17.11	Normal	15.2	90.0

to be constant as shown in Table 3. The axles' own weights are assumed as constants with values taken from Francher and Ervin (11): 1,200 lb per front axle, 2,500 lb per mid axle, and 1,500 lb per rear axle.

ROAD ROUGHNESS

The road profile must be generated to analyze the effect of road surface roughness. The road profile is the realization of a random process and the surface roughness can be described by a spectral density function. The statistical model can be established using recent developments in profile measuring and spectral analysis.

TABLE 3   WEIGHT DISTRIBUTION AND
AXLE DISTANCES

Truck Type	Weight Distribution (%)			Axle Distances
	Front	Middle	Rear	(ft)
S2	40	-	60	16.0
S3	31	-	69	18.2
T4	24	39	37	12.0, 29.7
T5	18	47	35	14.0, 33.1

In this study, the road surface is modeled as a stationary
Gaussian random process (13). A stationary Gaussian random
process, $X(t)$, can be generated using a simple periodic cosine
function of time with amplitude α, circular frequency ω, and
phase angle θ,

$$X(t) = \alpha \cos (\omega t - \theta) \tag{8}$$

A finite sum of N discrete functions can also be considered

$$X(t) = \sum_{n=1}^{N} \alpha_n \cos (\omega_n t - \theta_n) \tag{9}$$

Assume the phase angle θ_n is an independent random var-
iable distributed uniformly in the range of 0 to 2π. Then

$$E[\cos \theta_n] = \int_0^{2\pi} (\cos \theta_n)[1/(2\pi)] \, d\theta_n = 0 \tag{10}$$

Thus, the ensemble first two moments are

$$E[X(t)] = \sum_{n=1}^{N} \alpha_n E[\cos (\omega_n t - \theta_n)] = 0 \tag{11}$$

$$E[X^2(t)] = E\left[\sum_{n=1}^{N} \alpha_n \cos (\omega_n t - \theta_n) \sum_{m=1}^{M} \alpha_m \cos (\omega_m t - \theta_m) \right]$$

$$= \sum_{n=1}^{N} \frac{1}{2} \alpha_n^2 \tag{12}$$

Both $E[X(t)]$ and $E[X^2(t)]$ do not depend on t; hence the
process $X(t)$ is stationary.

For a stationary Gaussian random process the following
equation must be satisfied for the mean, m, variance, σ^2, and
spectral density function, $S(\omega)$:

$$\sigma^2 = \int_{-\infty}^{\infty} S(\omega) \, d\omega - m^2 \tag{13}$$

By substituting $m = 0$ and by discretizing the integral, the
following equation is obtained:

$$\sigma^2 = 2 \sum_{n=1}^{N} S(\omega_n) \, \Delta\omega = E[X^2(t)] \tag{14}$$

Combining Equation 12 and Equation 14 yields

$$\alpha_n = \sqrt{4S(\omega_n) \, \Delta\omega} \tag{15}$$

Therefore, the random process $X(t)$ can be expressed as fol-
lows:

$$X(t) = \sum_{n=1}^{N} \sqrt{4S(\omega_n) \, \Delta\omega} \cos (\omega_n t - \theta_n) \tag{16}$$

Honda et al. (14) showed that the spectral density of the
bridge surface roughness can be approximated by an expo-
nential function. The spectral density $S(\gamma)$ can be represented
by

$$S(\gamma) = a \cdot \gamma^{-n} \qquad \gamma_a \leq \gamma \leq \gamma_b \tag{17}$$

where a is the roughness coefficient, n is the spectral shape
index, γ is the spacial frequency, and γ_a and γ_b are the lower
and upper limit. The statistics of a and n are shown in Table
4. From Equation 16 and Equation 17, the road profile can
be generated by randomly selecting the phase angle θ. The
roughness model does not include bumps or discontinuities.

BRIDGE DYNAMICS

It is assumed that the static and dynamic load distribution
factors are the same. Consequently, the whole bridge is con-
sidered as a prismatic beam with flexural stiffness, EI. The
equation of motion is

$$EI \frac{\partial^4 y}{\partial x^4} + \frac{\partial^2 y}{\partial t^2} = p(x, t) \tag{18}$$

where $p(x, t)$ = applied distributed force. This fourth order
partial differential equation can be solved by the method of
separation of variables. The general solution is

$$y(x, t) = \sum_{n=1}^{\infty} \phi_n(x) z_n(t) \tag{19}$$

In case of the simply supported beam, the shape function
$\phi_n(x)$ is

$$\phi_n(x) = \sin (n\pi x/L) \tag{20}$$

TABLE 4   STATISTICS OF PARAMETERS IN SPECTRAL
DENSITY FUNCTION

Parameter	Mean Value	Standard Deviation	Distribution Type	Minimum Value	Maximum Value
a	$0.0098 \; cm^2/c/m$		exponential	0.0	0.06
n	1.92	0.283	normal	1.3	2.5

Substituting Equation 19 and 20 into Equation 18 and including the damping effect, z_n, yields the following equation relating modal mass, $M_n = \int_\phi^L \phi_n^2(x)m\,dx = mL/2$, modal force, $F_n(t) = \int_0^L \phi_n(x)p(x, t)\,dx$, and natural frequency, $\omega_n = n^2\pi^2\sqrt{EI/mL^4}$, flexural stiffness of the cross section, EI, and distributed applied force, $p(x, t)$:

$$\ddot{z}_n(t) + 2\xi_n\omega_n\dot{z}_n(t) + \omega_n^2 z_n(t) = F_n(t)/M_n \qquad (21)$$

The flexural stiffness is the most important parameter. However, it is difficult to evaluate EI because it depends on flexural stiffnesses of girders as well as transverse flexibility of the slab and diaphragms. EI can be calculated from the first flexural natural frequency of the bridge, f. The frequency, f(Hz), can be calculated for a given span length, $L(m)$, using the formula established by Cantieni (15):

$$f = 95.4 \cdot L^{-0.933} \qquad (22)$$

The stiffness can be calculated from the first natural frequency.

DYNAMIC LOAD FACTOR

A computer procedure was developed by the authors at The University of Michigan to calculate the maximum deflection (static and dynamic) and the DLF, following the flowchart shown in Figure 6. The program incorporates the equations describing dynamics of the vehicle, road roughness, and dynamics of the bridge. The Monte Carlo technique is used to generate basic parameters, including the road profile and the truck weight. The approach is demonstrated on a typical simply supported steel girder bridge with a 100-ft span. The first flexural frequency is 3.935 Hz (calculated using Equation 22). The nth order frequency is $n^2 \times 3.935$ Hz. The flexural stiffness can be calculated using continuous beam theory, $EI = 4.867 \times 10^{12}$ lb-in.^{2}. The damping of the bridge is assumed as 2 percent of the critical damping for each mode. In computations the time step used is 0.001 sec and the relative tolerance for convergence of each time step is 0.001. A typical example of a bridge response is shown in Figure 7.

The spectral density function is calculated for each road profile. However, an infinite number of road profiles can have the same spectral density. To examine the effect of different
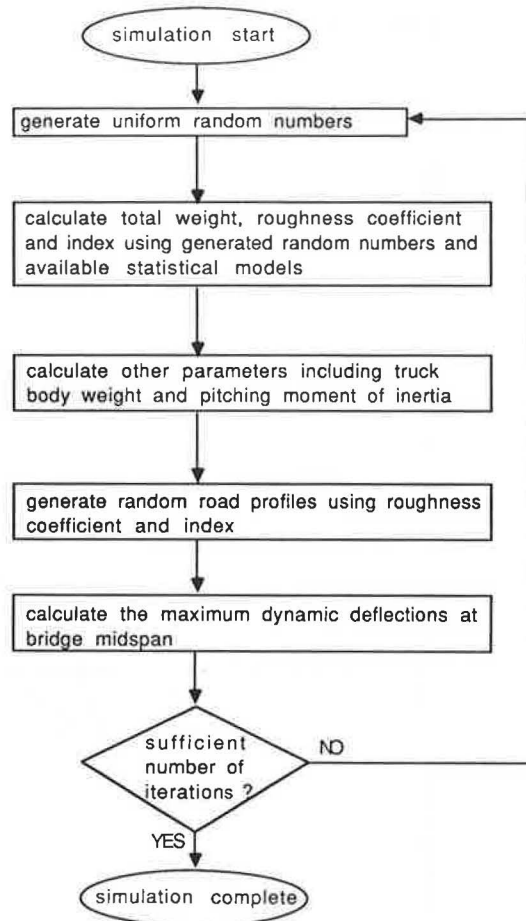

FIGURE 6 Flowchart of a computer simulation procedure.

profiles on the DLF, the calculations are carried out for randomly selected 10, 20, and 40 profiles. The resulting DLF values for a five-axle truck are plotted on the normal probability graph (13) in Figure 8. The vertical scale on the right is the cumulative probability (percentage). The vertical scale on the left is the inverse standard normal distribution. Normal and only normal distributions are represented by straight lines on this graph. The distributions plotted in Figure 8 indicate
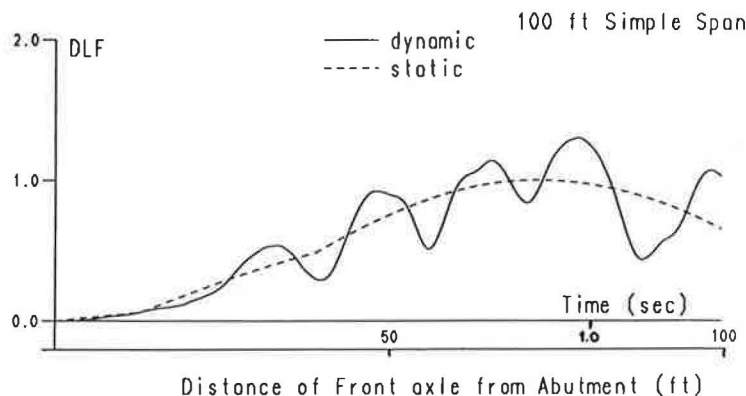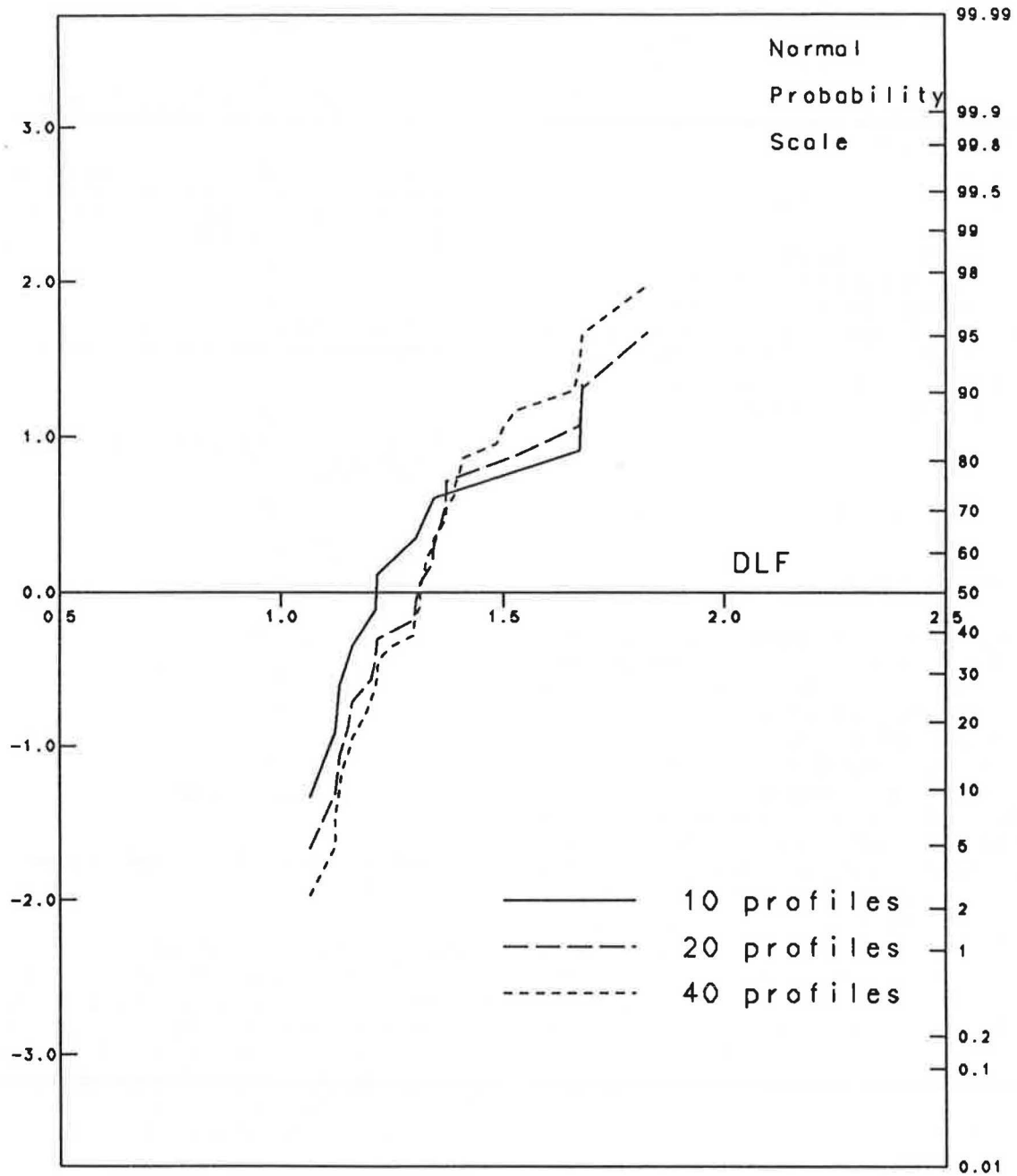

FIGURE 7 Typical example of bridge reponse for T5 truck.

FIGURE 8   Dynamic load factor for various numbers of road profiles.

that 20 profiles provide a sufficient accuracy, and therefore it is used in further calculations.

Values of DLF are calculated separately for each truck type. For each type, 50 weights are generated, and for each weight, 20 road profiles are generated. This results in 1,000 DLF values per truck type. The DLF spectra for the considered truck types are plotted in Figure 9 on normal probability scale. The largest values of DLF were obtained for the single truck S2, and the lowest values for semi tractor-trailer T4. For each truck type, the mean and standard deviation of DLF are calculated and presented in Table 5. The large values are determined by bad surface conditions of existing bridges (*14*), and they are too high for design.

CONCLUSIONS

A procedure has been developed for calculation of the DLF. Three main factors are considered in the analysis: vehicle dynamics, road roughness, and bridge dynamics. The available test, measurement, and analytical data are reviewed and incorporated in computations. The developed method is demonstrated on a typical steel girder bridge. DLF values are generated using the Monte Carlo technique. It has been observed that simulation of 20 road profiles provided sufficiently accurate results. Spectra of DLF values have been calculated for the four most common truck types. The results are plotted on the normal probability graph.
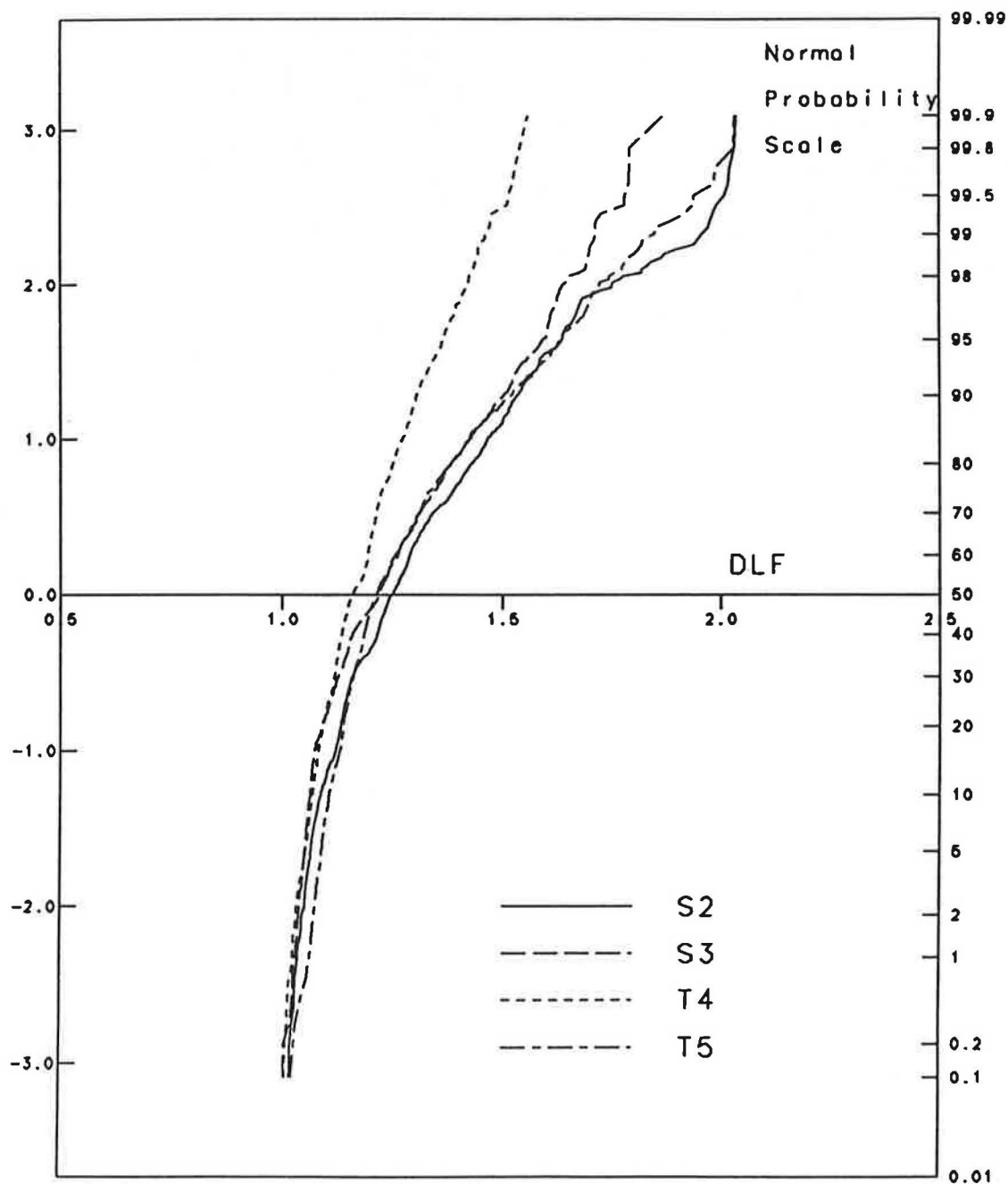
FIGURE 9 Dynamic load factor for various truck types.

TABLE 5 STATISTICS OF DYNAMIC LOAD FACTOR

Truck Type	Mean	Standard Deviation
S2	1.288	0.184
S3	1.249	0.168
T4	1.179	0.096
T5	1.271	0.171

The developed procedure provides an analytical tool for quantification of the dynamic load. The important application is in the development of efficient design and evaluation criteria. However, there is a need for more measurement data including vehicle characteristics and bridge response parameters.

ACKNOWLEDGMENTS

REFERENCES

1. *Standard Specifications for Highway Bridges*. AASHTO, Washington, D.C., 1983.
2. *Ontario Highway Bridge Design Code*. Ministry of Transportation and Communications, Downsview, Ontario, Canada, 1983.
3. *Schweizer Norm*. Schweizer Ingenieur und Architekt, Nov. 1985.
4. J. R. Billing. *Dynamic Tests of Bridges in Ontario, 1980*. Research and Development Reports, Vol. 26. Ministry of Transportation and Communications, Downsview, Canada, 1982.
5. R. K. Gupta. Dynamic Loading of Highway Bridges. *Journal of the Engineering Mechanics Division*, ASCE, Vol. 106, No. EM2, April 1980, pp. 377–393.
6. D. J. Harman. *Survey of Commercial Vehicles Weights 1978 to 1982*. Report RR236. Ministry of Transportation and Communications, Downsview, Canada, Nov. 1985.
7. H. Honda, T. Kobori, and Y. Yamada. Dynamic Factor of Highway Steel Girder Bridges. *Proc., International Association of Bridge and Structural Engineering*, P-98/86, Zurich, Switzerland, May 1986, pp. 57–75.
8. T. Huang. Vibration of Bridges. *Shock and Vibration Digest*, Vol. 8, No. 3, 1976, pp. 61–76.
9. C. O'Connor and R. W. Pritchard. Impact Studies on Small Composite Girder Bridge. *Journal of the Structural Engineering Division* ASCE, Vol. 111, No. 3, March 1985, pp. 641–653.
10. P. S. Fancher, R. D. Ervin, C. C. MacAdam and C. B. Winkler. *Measurement and Representation of the Mechanical Properties of Truck Leaf Springs*. Technical Paper Series 800905. Society of Automotive Engineers, Warrendale, Pa., 1980.
11. P. S. Fancher and R. D. Ervin. *A Component Factbook for Straight and Articulated Heavy Trucks*. Report UMTRI-86-12. University of Michigan Transportation Institute, 1986.
12. F. Moses and M. Ghosn. *Instrumentation for Weighing Trucks-in-Motion for Highway Bridge Loads*. FHWA-OH-83-001, Final Report. FHWA, U.S. Department of Transportation, March 1983.
13. J. R. Benjamin and C. A. Cornell. *Probability, Statistics, and Decision for Civil Engineers*. McGraw-Hill Book Co., New York, 1970.
14. H. Honda, Y. Kajikawa and T. Kobori. Spectra of Road Surface Roughness on Bridges. *Journal of the Structural Engineering Division*, ASCE, Vol. 108, No. ST9, Sept. 1982, pp. 1956–1966.
15. R. Cantieni. *Dynamic Load Tests on Highway Bridges in Switzerland*. Report 211. Swiss Federal Laboratories of Materials Testing and Research, Dübendorf, 1983.

Dynamic Testing of Highway Bridges— A Review

B. BAKHT AND S. G. PINJARKAR

A review is presented of the recent technical literature in the English language dealing with bridge dynamics in general and dynamic testing of highway bridges in particular. It is shown that several definitions have been used for the impact factor and thus the same set of field test data may lead to widely varying estimates of the impact factor. In nearly all the reviewed references, there is little or no justification for using a particular definition, suggesting that each of the various definitions was regarded as axiomatic, requiring no justification. It is also shown that there are additional factors that may be responsible for misleading conclusions from the test data; these factors include vehicle type, vehicle weight, transverse position of the vehicle with respect to the reference point, differences in dynamic increment of strains and deflections, presence of bearing restraint forces, and roughness of the riding surface. A preferred method of interpreting the field test data for obtaining a representative value of the impact factor is suggested. It is shown that the impact factor is not a tangible entity susceptible to deterministic validation.

Vehicles that are expected to cross a highway bridge during its lifetime are accounted for in the design of the bridge through a statistically applied design load and a certain prescribed fraction of it, which is traditionally referred to as the impact factor, and lately as the dynamic load allowance. The static design load is a tangible entity that can be derived from the static weights of actual and foreseen vehicles in such a way that the load effects induced by it in any bridge are representative, with a certain degree of reliability, of the load effects induced by these actual and foreseen vehicles. The impact factor, on the other hand, is an abstract entity that is supposed to account for the magnification of load effects in a bridge caused by the interaction of the vehicle and the bridge.

Despite its abstract nature, the impact factor has been used in the design of bridges for several decades. There have been numerous attempts to measure this elusive quantity in bridges through dynamic field testing. The purpose of this paper is to review, and draw some general conclusions from, the technical literature dealing with bridge dynamics in general and dynamic testing of highway bridges in particular. It is noted that this paper is a summary of a more detailed report (1).

DEFINITION OF IMPACT FACTOR

As long ago as 1931, it was suggested that the *impact increment of dynamic force* be defined as the amount of force, expressed

B. Bakht, Structures Research Office, Research and Development Branch, Ministry of Transportation, 1201 Wilson Avenue, Central Building, Downsview, Ontario, Canada M3M 1J8. S. G. Pinjarkar, Raths, Raths and Johnson, Inc., 835 Midway Drive, Willowbrook, Illinois 60521.

as a fraction of the static force, by which the dynamic force exceeds the static force (2). Recognizing that the impact increment of dynamic force is not necessarily the same as the *impact increment of stress*, the latter was defined as the amount of stress, expressed as a fraction of static stress, by which the actual stress as a result of moving loads exceeds the static stress.

Researchers interpreting test data from dynamic load tests have often used the term *dynamic increment* for the same quantity that has been defined by Fuller et al. (2) as the impact increment of stress or that could have been defined as the impact increment of deflection. However, there is no uniformity in the manner by which this increment is calculated from test data. The different ways of calculating the dynamic increment can be explained conveniently with the help of Figure 1, which has been constructed from data of an actual dynamic test with a two-axle vehicle on a right simply supported plate girder bridge (3). This figure shows the variation of both the dynamic and static deflections at midspan of a girder with respect to time. The dynamic deflections were obtained when the test vehicle traveled on the bridge at normal speed, and the static deflections were obtained when the vehicle traveled at crawling speed so as not to induce dynamic magnification of deflections. Figure 1 also shows the median deflections that were obtained by averaging consecutive peaks of dynamic deflections. As can be seen in this figure, the median deflections are not the same as the static deflections; however, a numerical procedure for filtering out the dynamic portion of the response can give the median responses that are fairly close to the static responses.

It may be noted that a fictitious scale of deflections has been introduced in Figure 1 in order to facilitate the explanation regarding the interpolation of the test data. Regarding this figure, a notation is now introduced, as follows:

δ_{stat} = maximum deflection under the vehicle traveling at crawling speed.

δ_{dyn} = maximum deflection under the vehicle traveling at normal speed. This deflection is also denoted as δ_{max}.

δ'_{stat} = maximum deflection obtained from the curve of median deflections. Note that δ_{stat} and δ'_{stat} do not necessarily take place at the same load location.

δ_{min} = minimum dynamic deflection in the vibration cycle containing δ_{max}.

δ_1 = static deflection corresponding to δ_{max}. As may be seen in Figure 1, δ_1 is not necessarily the maximum static deflection.

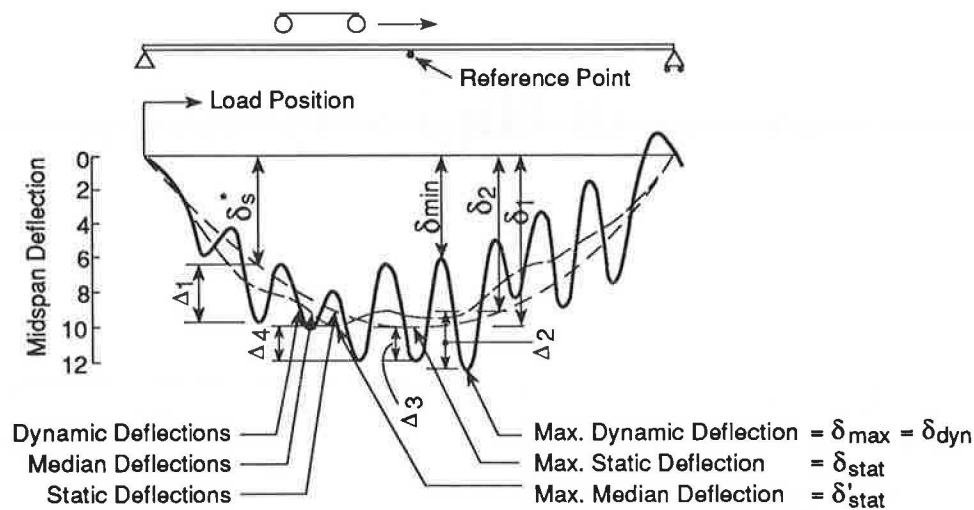δ_2 = median deflection corresponding to δ_{max}.

FIGURE 1 Midspan deflections under a moving vehicle load.

δ_s^* = static deflection at the same location where Δ_1 is recorded.

Δ_1 = maximum difference between dynamic and static deflections; as shown in Figure 1, Δ_1 does not necessarily take place at the same load position that causes either δ_{stat} or δ_{dyn}.

Δ_2 = maximum difference between dynamic and median deflections.

Δ_3 = difference between dynamic and static deflections at the same load location that causes δ_{stat}.

Δ_4 = difference between dynamic and median deflection at the same load location that causes δ'_{stat}.

These definitions can be more general if the word *deflection* is replaced by *response*.

From the data plotted in Figure 1, the various deflection parameters are found to have the following values according to the fictitious scale from which units are deliberately omitted to maintain generality: δ_{stat} = 10.0; δ_{dyn} = δ_{max} = 12.3; δ'_{stat} = 9.9; δ_{min} = 6.2; δ_1 = 9.1; δ_2 = 9.8; δ_s^* = 6.4; Δ_1 = 3.2; Δ_2 = 3.1; Δ_3 = 2.0; and Δ_4 = 2.0.

The various definitions are now described, many of which have been used in the past to obtain from the test data the dynamic increments, or similar parameters given different names. For the sake of convenience, all these different parameters will henceforth be referred to generically as dynamic amplification factors and will be denoted by the symbol I.

Definition 1

According to the definition of impact increment of dynamic response by Fuller et al. (2), the largest of I would be given by

$$I = \Delta_1/\delta_s^* \tag{1}$$

Using this expression, the deflection data of Figure 1 would lead to I = 0.500. It should be noted, however, that this method is the result of a hypothetical and impractical extrapolation of a definition, which, perhaps, was not intended for

this purpose. This method has not been used to interpret test data in any of the references that were studied for this state-of-the-art report.

Definition 2

A commonly used variation of Definition 1 is that I is taken as the ratio of the measured instantaneous dynamic response to the maximum static response. Thus,

$$I = \Delta_3/\delta_{stat} \tag{2}$$

This definition of I has been used in the interpretation of data from several dynamic tests (e.g., 3–5) and in nearly all analytical studies (e.g., 6–9). According to Definition 2, the value of the impact factor obtained from the data given in Figure 1 is 0.200.

Definition 3

When the static deflections are assumed to be the same as median deflections, Definition 2 of I changes to

$$I = \Delta_4/\delta'_{stat} \tag{3}$$

This definition gives I the value of 0.202. It is noted that this definition does not seem to have been used by any of the references cited in this paper.

Definition 4

Definition 4 was used in Switzerland to interpret test data from the dynamic bridge tests conducted during 1949 to 1965 (10). According to this definition, the dynamic increment I is given by

$$I = \frac{\delta_{max} - \delta_{min}}{\delta_{max} + \delta_{min}} \tag{4}$$

It is noted that this definition of the dynamic increment was abandoned in Switzerland after 1965 in favor of Definition 5 which follows. However, this definition has been used in New Zealand until fairly recently (*11,12*).

Definition 5

According to the fifth definition, which has been used in Switzerland for tests conducted before 1945 and after 1965 (*10*), the dynamic increment I is given by

$$I = \frac{\delta_{dyn} - \delta_2}{\delta_2} \tag{5}$$

Using this definition, the data in Figure 1 give $I = 0.255$.

Definition 6

A variation of Definition 5 would be when the static response corresponding to the maximum dynamic response is taken as the same as the median response obtained from the dynamic test data. In this case, I is given by

$$I = \frac{\delta_{dyn} - \delta_1}{\delta_1} \tag{6}$$

leading to a value for I of 0.352. This definition has been extensively used to interpret the results of many dynamic tests on bridges in Ontario (e.g., *13–16*).

Definition 7

For interpreting the data from some dynamic tests conducted in Ontario (*17,18*), the following expression was used for obtaining I:

$$I = \frac{\delta_{dyn} - \delta'_{stat}}{\delta'_{stat}} \tag{7}$$

For the specific case under consideration, the value of I is then found to be 0.242.

Definition 8

If the actual static responses are used instead of median responses, the following variation of Equation 7 is obtained:

$$I = \frac{\delta_{dyn} - \delta_{stat}}{\delta_{stat}} \tag{8}$$

This definition gives I a value of 0.230 for the data in Figure 1.

COMPARISON OF VARIOUS DEFINITIONS

Table 1 contains the values of I obtained by the various definitions from the same set of data. It can be seen in this table that the values of I are all different and range from 0.2 to 0.5.

In nearly all of the references studied for this paper, there is little or no discussion or justification for using a particular definition of the dynamic amplification factor. This seems to suggest that each of the various definitions was regarded as being axiomatic and requiring no justification. Yet the variety of results given in Table 1 confirm that the definition of I is far from axiomatic. What can be regarded as axiomatic, however, is the definition of the amplification factor for the response at a given instant. According to this definition, $I = \Delta/\delta_s$, where Δ is the difference between the static and dynamic responses at the instant under consideration, and δ_s is the corresponding static response.

The axiomatic definition of amplification factor is used, justifiably, in all of the analytical studies; it is, however, of little use in bridge design because its value changes with time and load position. What is required for design purposes is a single value of the amplification factor with which maximum dynamic response can be computed from the maximum static response, so that

$$\delta_{dyn} = \delta_{stat} (1 + I) \tag{9}$$

The values of δ_{dyn} obtained by using δ_{stat} of 10.00 and the values of I given by the various definitions are also given in Table 1. Ideally, the use of the amplification factor according to Equation 9 should have returned the same value of δ_{dyn}

TABLE 1   VALUES OF DYNAMIC AMPLIFICATION FACTOR *I* AND COMPUTED MAXIMUM DYNAMIC DEFLECTION

Definition No.	1	2	3	4	5	6	7	8
Value of I	0.500	0.200	0.202	0.330	0.255	0.352	0.242	0.230
Value of δ_{dyn} from Eq. (9)	15.00	12.00	12.02	13.33	12.55	13.52	12.42	12.30

Note: Maximum value of measured dynamic deflection is 12.30.

that was measured in the field, that is, 12.30. It can be seen in Table 1 that none of the definitions has given the correct value of δ_{dyn}, except Definition 8, the equation for which (Equation 8) is, in fact, the same as Equation 9, which gives the correct value of δ_{dyn}. It is interesting to note that the apparently logical Definition 8 has not been used in any of the references studied for this state-of-the-art study, a complete list of which is given in a previous paper by Bakht and Pinjarkar (1).

At a cursory glance, it may seem strange that such a variety of definitions emerges from the process of selecting a single governing value from the values of I that are obtained by an axiomatic definition. A careful scrutiny of the problem will readily reveal that the diversity in the definitions of I from measured responses is the consequence of the fact that (a) the static response of a bridge is not necessarily the same as the median response obtained from the dynamic test data and (b) the maximum static and dynamic responses do not always take place under the same load position (e.g., 3). If the static and median responses were identical and the maximum static and dynamic responses took place simultaneously, the diversity of definitions of I would disappear and Definitions 2 through 8 would all give the same value of I for a given set of data.

FACTORS RESPONSIBLE FOR MISLEADING CONCLUSIONS

The technical literature reports a fairly large scatter in the values of the dynamic amplification factor of a given response, even when the bridge and the vehicle are the same. From these observations it can readily be concluded that the dynamic amplification factor is not a deterministic quantity. To obtain a single value of this factor for design purposes, it is necessary, as is shown later in the paper, to know the statistical properties of the scatter of data, in particular the mean and variance of the amplification factor. The various parameters that can influence the statistical properties of the amplification factors computed from the test data are discussed in the following subsections. If not accounted for carefully, these parameters can influence misleadingly the way in which the measured data are interpreted.

Vehicle Type

It is already known that the dynamic amplification factor for a bridge is influenced significantly by the dynamic characteristics of the vehicle with respect to those of the bridge. Despite this fact, most dynamic tests on bridges have been conducted with specific test vehicles. The data from such tests cannot, for obvious reasons, be regarded as representative of actual conditions. The amplification factors obtained from tests with only specific test vehicles can provide only a qualitative insight into the problem of bridge dynamics. They should not be used to obtain the final single value of the impact factor that is to be used in calculations for design or evaluation. A representative value of the impact factor can be calculated realistically only when data are gathered under normal traffic and over relatively long periods of time.

Vehicle Weight

Several researchers have concluded from observed data that the dynamic amplification factor resulting from a vehicle decreases with the increase of vehicle weight (e.g., 2, 11, 12, 17). It can be appreciated, in light of this information, that the amplification factors corresponding to lightly loaded vehicles, which are irrelevant to the design load effects, are likely to weigh the data unduly on the higher side. The data corresponding to lightly loaded vehicles should not be used at all in the calculation of the impact factor, unless, of course, the impact factor is sought specifically for lighter vehicles, as it may be for the evaluation of the load carrying capacity of existing substandard bridges.

Vehicle Position with Respect to Reference Point

The cross section of a three-lane slab-on-girder bridge is shown in Figure 2. The bridge has five girders, all of which are instrumented for dynamic response measurement; it carries a vehicle in the far right-hand lane so that Girders 4 and 5 carry the vehicle load directly. In this case, Girders 1 and 2, being remote from the applied load, will carry a very small portion of the static load. Yet the dynamic amplification of the small portion of the static load carried by these two girders is likely to be fairly large. It has been observed by several researchers that the dynamic amplification factor at a reference point well away from the load can be larger than that for a reference point directly under the load. Clearly, the former amplification factor has no relevance as far as the maximum static load effects are concerned at the cross section of a bridge.

A parameter, α, is used by Cantieni (10) to define the relative position of the vehicle with respect to that of the reference point; this parameter is defined by

$$\alpha = \frac{D}{H + 1.25} \tag{10}$$

where D is the distance (in meters) in the transverse direction between the reference point and the nearest line of wheels, H is the depth of construction of the bridge (also in meters) at the instrumented cross section, and the number 1.25 in the denominator is the half-width of the vehicle in meters. When α is less than 1.0, the reference point is assumed to lie within the direct influence zone, in which case the dynamic test data are considered to be relevant. In a case when α is greater than 1.0, the data are ignored, being of no consequence.
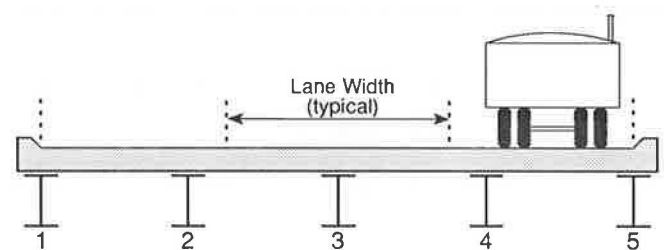

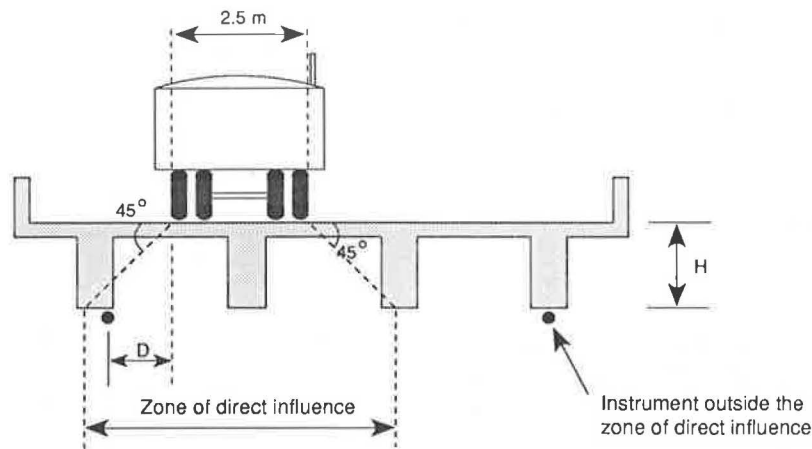**FIGURE 2   Cross section of a three-lane bridge.**

FIGURE 3   Definition of the zone of direct influence (*10*).

Figure 3 identifies the zone of direct influence defined by Cantieni (*10*). It can be seen that this zone is obtained simply by drawing 45 degree lines on the bridge cross section from the outer line of wheels of the test vehicle. This limit on the zone of influence cannot be regarded as being applicable to all bridges because it does not take into account the transverse load distribution characteristics of the bridge. It may be more appropriate to take into consideration only the data from that reference point at which the static load response is the maximum across the cross section.

The statistical properties of the dynamic amplification factor, computed from the test data, can be regarded as realistic only if the extraneous data from outside the zone of influence are excluded from consideration. It is surprising that the attempt to exclude such extraneous data has been explicitly mentioned in only a few of the references reviewed for the study at hand.

Deflection Versus Strain Measurements

The response of a bridge in dynamic tests is conventionally measured by means of vertical deflections. The measurement of strains is resorted to only when the measurement of deflections is found to be difficult (e.g., *19, 20*). The dynamic amplification factors obtained by both approaches are assumed to be applicable with equal validity to all responses including deflections, bending moments, and shear forces. Strictly speaking, the practice of regarding the amplification factors as being applicable for other responses is not correct. It has been demonstrated convincingly by the AASHO test (*4*) that, under similar conditions, the dynamic amplification factors computed from measured deflections are always greater than the corresponding factors computed from measured strains. The same conclusion has also been reached by others (e.g., *18*).

Bearing Restraint Effects

With the exception of AASHO tests (*4*), the measured frequencies of tested bridges were nearly always found to be much greater than the calculated frequencies. This observation leads to the conclusion that the flexural stiffness of bridges is nearly always greater than the calculated stiffness. The reason for this apparent discrepancy has been attributed, wrongly, in many of the references to (a) a very high modulus of elasticity of concrete; (b) interaction with the main components of secondary components such as horizontal bracings and barrier walls; and (c) the presence of a high degree of composite action between the girders and deck slab, even when they do not have any mechanical shear connection between them.

Unintentional composite action in an apparently non-composite bridge can also not always be regarded as a major factor to stiffen the bridge. This is so because even those slab-on-girder bridges, which have mechanical shear connectors between the deck slabs and girders and in which full composite action has been considered in the calculations, have been found stiffer than shown by calculations.

The effective flexural rigidity of the tested bridges by using both the measured midspan static load deflections and the measured frequencies were calculated by Biggs and Suer (*3*). When it was found that the two procedures gave different flexural rigidities, it was concluded that, "although this cannot be completely explained, it is possible that the causes are a greater participation of secondary elements and a greater degree of frictional restraint at the ends of the span." This is, perhaps, the first time in recent literature that attention has been paid to the presence of bearing restraint effects as being the possible cause of bridges being stiffer than shown by calculations. Recent tests have confirmed that fairly large bearing restraint forces develop in slab-on-girder bridges at the interfaces of girders and the surfaces they rest on (*21–23*). These large bearing restraint forces have been found to stiffen the bridges appreciably.

The observed frequencies of composite steel and pre-stressed concrete bridges tested in the AASHO study (*4*) were in good agreement with the calculated values that were obtained by using the measured cross sections and other properties of the actual bridges. It is noted that, in these bridges, the girders were supported by rocker-type bearings, which prevented the development of substantial bearing restraint forces.

The presence of bearing restraint forces induces compressive strains in the bottom flanges of the girders; consequently, the girder strains do not remain directly proportional to the girder moments. In such cases it is doubtful whether dynamic

amplification factors obtained from girder strains can apply exactly to girder moments. The inclusion of bearing restraint forces in the interpretation of measured dynamic strains is still not a practical proposition. This problem, however, still needs a careful study.

MISCELLANEOUS OBSERVATIONS

Quality of the Riding Surface

It is mentioned in nearly every reference dealing with bridge dynamics that the roughness of the riding surface of a bridge and its approaches has a significant influence on the dynamic magnification of load effects in the bridge. It is usual in dynamic bridge tests to account for the riding surface irregularities by placing a wooden plank of appropriate thickness in the path of the test vehicle. As might be expected, the dynamic amplification factors corresponding to such tests are always larger than those that correspond to similar tests without the wooden plank.

The practice of performing dynamic tests by creating a temporary irregularity in the riding surface of even well-maintained bridges has been defended on the basis that even a well-maintained bridge can have a sudden irregularity introduced in the riding surface, for example, as a result of an object being dropped accidentally from a vehicle or the accumulation of packed snow. It should be noted, however, that in bridges with more than one lane, the design loading for failure almost invariably corresponds to the rare event of exceptionally heavy vehicles being simultaneously present in two or more lanes of the bridge. The probability of such a rare event happening, at the same time as the formation of an accidental irregularity in the riding surface of an otherwise well-maintained bridge, is indeed so small as to be negligible.

The commentary to the second edition of the Ontario Code (24) suggests that a high value of the dynamic load allowance should be used if the approach is likely to remain unpaved for extended periods of time, or if the expansion joints between the superstructure and approach pavements are not expected to be flush with the roadway. Taking a cue from this suggestion, it may be appropriate to test such bridges by placing a plank in the path of the test vehicle. For well-maintained bridges, on the other hand, there does not seem to be any justification for adopting this approach.

Multilane Loading

It has been observed in many references that the dynamic amplification factor for more than one vehicle is always less than that for a single vehicle, and the out-of-phase dynamic actions of the various vehicles are usually cited as the reason for this phenomenon. It seems appropriate that the value of the impact factor should decrease with the increase in the number of loaded lanes. The commentary to the Ontario Code in its first edition (25) specified a separate set of multipresence reduction factors for the dynamic load allowance (DLA). These factors were much smaller than the corresponding factors for static loading. The separate reduction factors for DLA were abandoned in favor of the same factors for both the static loading and DLA in the second edition of the Code. It has

been shown by Jaeger and Bakht (26) that the multipresence factor for combined static and dynamic loading, m_f, is approximately given by

$$m_f = \frac{m_{fs} + m_{fd} \, DLA}{1 + DLA} \tag{11}$$

where m_{fs} and m_{fd} are the multipresence reduction factors for static and dynamic loadings, respectively.

RECOMMENDED PROCEDURE

From a survey of the technical literature dealing with dynamic testing of highway bridges, a preferred procedure emerges naturally for obtaining, through a test, a representative value of the impact factor for single vehicles that can be used realistically in the load capacity evaluation of an existing bridge. The various steps involved in this preferred and recommended procedure are given in the following subsections.

Instrumentation

For obtaining the dynamic amplification factors for longitudinal moments, it is preferable to measure strains rather than deflections. In slab-on-girder bridges, strains can be measured conveniently at the bottom flanges of the girders, even if the girders are of concrete, in which case special strain gauges or strain transducers may have to be used. Care should be exercised in selecting a crack-free zone for instrumentation of concrete components.

Calibration Test

It is desirable to perform both static and dynamic tests on the bridge with vehicles of known weights and configurations. The static test can be performed either under a stationary vehicle positioned at preselected locations or under a vehicle moving at crawling speed of less than about 10 km/hr. If the latter procedure is adopted, it may still be necessary to filter out the dynamic responses in order to obtain the static load responses. However, in this case the filtered responses can be expected to be very close indeed to the actual static load responses.

Elimination of Extraneous Data

At a given instrumented cross section, the data corresponding to only a single reference point should be considered when computing the dynamic magnification factor resulting from a vehicle pass on the bridge. This reference point should be the one at which the maximum static, or median, value of the response is recorded for the vehicle pass under consideration.

As discussed earlier, the dynamic amplification factors corresponding to light vehicles, being relatively on the high side, tend to bias the data. It is, therefore, necessary that the data considered for developing the statistics of the dynamic amplification factor correspond to the weight class of the design or evaluation vehicle. This can be achieved as follows.

The maximum response at a reference point resulting from the design or evaluation vehicle can be readily obtained by extrapolation of the data obtained from the calibration tests. Let this maximum response be denoted as ε. As shown in Figure 4, the observed maximum static load response can be divided into a number of strata, with each stratum representing the vehicles of a certain class of weight that relates to the load effects in the bridge rather than the gross vehicle weight. It is recommended that the observed data from the dynamic test should be divided into various groups, depending upon the division of the maximum static load effects, of the kind shown in Figure 4. For example, the dynamic amplification factors corresponding to the design or evaluation vehicle should be obtained only from that data for which δ'_{stat} lies within 0.9ε and 1.1ε.

Method for Obtaining Dynamic Amplification Factor

From a purely logical standpoint, the appropriate definition for computing the dynamic amplification factor from measured responses would appear to be Definition 5, described earlier. However, this definition requires that a bridge be tested under the same vehicle separately for both dynamic and static effects. Such a requirement is obviously not realistic
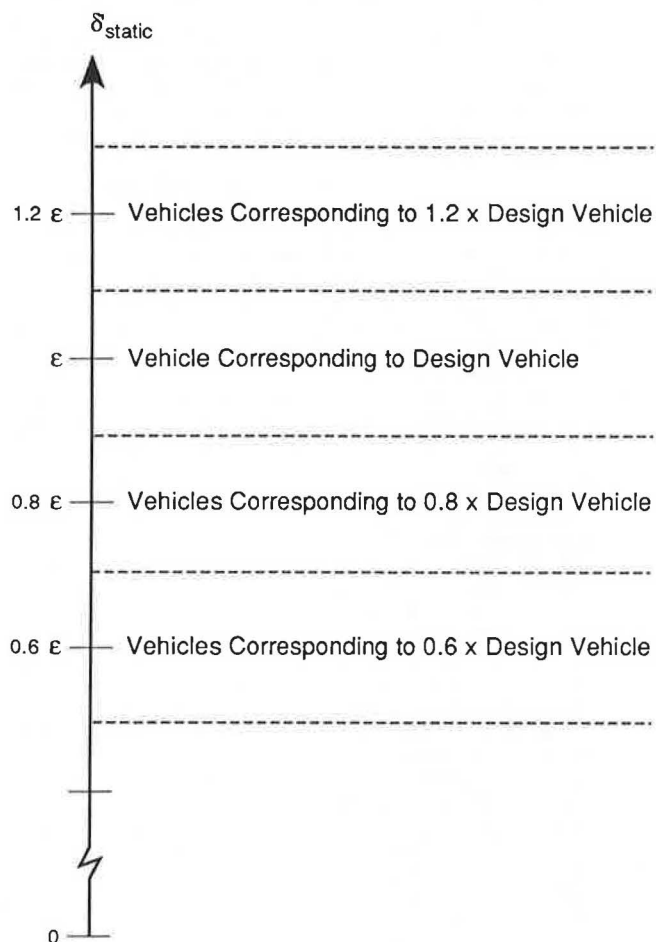

FIGURE 4   Scheme for classifying vehicles.

when data are being collected under normal traffic. In such a case, it is suggested that the next best definition is Definition 7. This definition can give fairly reliable results, especially if it is found from the calibration test that the maximum static load response δ_{stat} is close in magnitude to the corresponding maximum median response δ'_{stat}. The case in which the two maximum responses are significantly different from each other is rather rare. For such bridges, Definition 7 can still be used but only after making appropriate adjustments for the difference between δ_{stat} and δ'_{stat}.

It is noted that when a vehicle is longer than the length of the influence line of the instrumented component, the static response at a reference point resulting from the moving vehicle may not be smooth, that is, it may have "static oscillations." For such cases, the obtaining of the median responses by automatic filtering is made especially difficult when the period of static oscillations matches with the period of dynamic oscillations.

Calculation of Impact Factor

The term *impact factor* is used here to denote that single value of the dynamic amplification that is used in the calculations for the design or evaluation of the bridge. It is noted that, as mentioned earlier, the impact factor is also referred to as the *dynamic load allowance*.

Simply because of the scatter in their values, the dynamic amplification factors computed from the dynamic test data cannot be used directly as the impact factor. Neither should an upper-bound value of the amplification factor be used as the impact factor, because this is likely to prove overly conservative. A logical approach to computing a representative value of the impact factor from the test data would be to cater for the variability of the amplification factor in the same way as is done for the variability of the static loads. One procedure proposed in the commentary to the second edition of the Ontario Code (*24*) and reported by Billing (*17*) can be used to achieve this goal. According to this procedure, the specified value of the impact factor, I_s, depends not only on the statistics of the amplification factor but also on the live load factor specified in the Code and the safety margin to which the Code is calibrated. The expression for obtaining I_s is as follows:

$$I_s = \frac{\bar{I}\,(1 + \nu s\beta)}{\alpha_L} \tag{13}$$

where

$\bar{I}$ = mean value of the dynamic amplification factor,

ν = coefficient of variation of the dynamic amplification factor, that is, the ratio of standard deviation and mean,

s = the separation factor for dynamic loading, which has been found to have a value of 0.57,

β = the safety index, which typically has a value of about 3.5 for highway bridges, and

α_L = the live load factor.

It is noted that when the distribution of mean largest vehicle weights is log normal, it may be more appropriate to use the following expression for obtaining the specified value of this

impact factor:

$$I_s = \frac{\bar{I}}{\alpha_L} e^{v s \beta} \qquad (14)$$

The use of the live load factor in Equations 13 and 14 requires some discussion. The use of the live load factor in determining the specified value of the impact factor is open to question, as the live load factor alone does not define the variability of the static loads. This variability is accounted for by both the live load factor and the specified static loads. For example, it is possible to get the same live load effects by simultaneously doubling the live load factor and halving the specified static loads. In this case, the specified value of the impact factor would be reduced incorrectly if Equations 13 and 14 were used.

Ideally, α_L, in Equations 13 and 14, should account for the variability of static loads, rather than being equal to the live load factor. It is recommended that, in the absence of more rigorous analysis, the value of α_L should be taken as 1.4, which is also the live load factor as specified in the Ontario Code (24). Using the numerical values of the various variables, Equations 13 and 14 can be written as

$$I_s = 0.71 \, \bar{I} \, (1 + 2.0v) \qquad (15)$$

$$I_s = 0.71 \, \bar{I} \, e^{2.0v} \qquad (16)$$

It should be noted that for $\bar{I}$ and v to be representative of actual conditions, there should be a sufficient number of values of the amplification factor obtained from the test data.

CONCLUSIONS

From a survey of the technical literature dealing with the dynamic testing of highway bridges, it has been found that there is a general lack of consistency in the manner in which the test data are interpreted to obtain the values of the dynamic amplification factor. A preferred method of calculating these factors has been proposed. It has been shown that the impact factor is not a tangible entity susceptible to deterministic evaluation; it can be accounted for in the design and evaluation of bridges only by a probabilistic approach. Despite being obtained from field data by a preferred procedure, the impact factor still remains an abstract entity that should, in general, be treated only as a design convenience. A recommended procedure for obtaining a design value of the impact factor by testing a highway bridge under dynamic loads has been developed.

REFERENCES

1. B. Bakht and S. A. Pinjarkar. *Review of Dynamic Testing of Highway Bridges*. Structures Research Report SRR-89-01. Ontario Ministry of Transportation, Downsview, Canada, 1989.
2. A. H. Fuller, A. R. Eitzen, and E. F. Kelly. Impact on Highway Bridges. *Transactions*, ASCE, Vol. 95, Paper 1786, 1931, pp. 1089–1117.
3. J. M. Biggs and H. S. Suer. Vibration Measurements on Simple-Span Bridges. *Bulletin 124*, HRB, National Research Council, Washington, D.C., 1956, pp. 1–15.
4. *Special Report 61D: AASHO Road Test: Report 4—Bridge Research*. HRB, National Research Council, Washington, D.C., 1962.
5. R. C. Edgerton and G. W. Beecroft. Dynamic Studies of Two Continuous-Plate Girder Bridges. *Bulletin 124*, HRB, National Research Council, Washington, D.C., 1956, pp. 33–46.
6. S. J. Fenves, A. S. Veletsos and C. P. Siess. Dynamic Studies of the AASHO Road Test Bridges. In *Highway Research Record 73*, HRB, National Research Council, Washington, D.C., 1962, pp. 83–96.
7. J. F. Fleming and J. P. Romualdi. Dynamic Response of Highway Bridges. *Journal of the Structural Division*, ASCE, Vol. 87, No. ST7, 1961, pp. 31–61.
8. C. F. Scheffey. Dynamic Load Analysis and Design of Highway Bridges. *Bulletin 124*, HRB, National Research Council, Washington, D.C., 1956, pp. 16–32.
9. A. Wiriyachai, K. Chu, and V. K. Garg. Bridge Impact Due to Wheel and Track Irregularities. *Journal of the Engineering Mechanics Division*, ASCE, Vol. 108, No. EM4, 1982, pp. 648–662.
10. R. Cantieni. *Dynamic Load Tests on Highway Bridges in Switzerland: 60 Years Experience of EMPA*. Report 271. Swiss Federal Laboratories for Materials and Testing Research, Dübendorf, 1983.
11. R. Shepherd and R. J. Aves. Impact Factors for Simple Concrete Bridges. *Proc., ICE, Part 2, Research and Theory, Volume 55*. March 1973, pp. 191–210.
12. S. J. Thurston. *Impact Factors Measured on Two Bridges*. Central Laboratories Report 5-83/4. Ministry of Works and Development, Lower Hutt, New Zealand, 1983.
13. B. Bakht. *Live Load Testing of Soil-Steel Structures*. Structures Research Report SRR-80-4. Ontario Ministry of Transportation, Downsview, Canada, 1980.
14. B. Bakht. Soil-Steel Structure Response to Live Loads. *Journal of the Geotechnical Engineering Division*, ASCE, Vol. 107, No. GT6, 1981, pp. 779–798.
15. T. I. Campbell, P. F. Csagoly, and A. C. Agarwal. Frequency Matching in Continuous Post-Tensioned Concrete Highway Bridges. In *Vibrations of Concrete Structures*, Publication SP-60. American Concrete Institute, Detroit, Mich., 1979, pp. 139–154.
16. J. P. C. King, M. Holowka, R. A. Dorton, and A. C. Agarwal. Test Results from the Conestogo River Bridge. In *Transportation Research Record 665*, TRB, National Research Council, Washington, D.C., 1978, pp. 90–98.
17. J. R. Billing. Dynamic Loading and Testing of Bridges in Ontario, 1980. *Proc., International Conference on Short and Medium Span Bridges*, Toronto, Canada, Vol. I, 1982, pp. 125–139.
18. D. T. Wright and R. Green. *Highway Bridge Vibrations, Part II, Ontario Test Program*. Department of Civil Engineering, Queen's University; Ontario Ministry of Transportation, Downsview, Canada, 1962.
19. J. R. Billing. *Dynamic Test of Bridges in Ontario, 1980: Data Capture, Test Procedure and Data Processing*. Structures Research Report SRR-88-02. Ontario Ministry of Transportation, Downsview, Canada, 1982.
20. R. Cantieni. *Dynamic Tests on Bridges*. Section Concrete Structures Report. Swiss Federal Laboratories for Materials and Testing Research, Dübendorf, 1981.
21. B. Bakht. *Testing of an Old Short-Span Slab-on-Girder Bridge*. Structures Research Report SRR-88-01. Ontario Ministry of Transportation, Downsview, Canada, 1988.
22. B. Bakht. *Observed Behaviour of a New Medium-Span Slab-on-Girder Bridge*. Structures Research Report SRR-88-02. Ontario Ministry of Transportation, Downsview, Canada, 1988.
23. B. Bakht. *Ultimate Load Test on a Slab-on-Girder Bridge*. Structures Research Report SRR-88-03. Ontario Ministry of Transportation, Downsview, Canada, 1988.
24. *Ontario Highway Bridge Design Code*, 2nd ed. Ontario Ministry of Transportation, Downsview, Canada, 1983.
25. *Ontario Highway Bridge Design Code*, 1st ed. Ontario Ministry of Transportation, Downsview, Canada, 1979.
26. L. G. Jaeger and B. Bakht. Multiple Presence Reduction Factors for Bridges. *Proc. Structures Congress, Structural Division*, ASCE, 1987, pp. 47–59.

Evaluation of Bridge Vibration Through Field Measurement of Strains

Ben T. Yen and Leon L. Y. Lai

The dynamic characteristics of girder bridges can be evaluated from measured live load strains in girders resulting from regular truck traffic. The evaluation includes the determination of the dominant vibrational modes and the corresponding damping ratios. Results from a single-span and a three-span skewed bridge show that both are dominated by a flexure mode of vibration with a damping ratio of about 2 percent. A beam model is used to simulate the dynamic response of the single-span bridge to a test truck. The results compared well with the measured stresses.

Bridges are subjected to vehicular loads that generate dynamic forces and corresponding deflection and stresses in the bridge components. These dynamic effects are incorporated in bridge design through using the well-known impact factor (1). An increase of static live load stresses by the impact factor provides a simple method of estimating maximum stresses resulting from moving vehicles traversing the bridges.

In recent years a large number of bridges have been found to have incurred damages that are attributed to impact and fatigue. Obviously, the increase of vehicular weights and traffic volumes in the last 2 to 3 decades has contributed to these damages. On the other hand, the advance in technique of design resulting in more "efficient" bridge structures could have also introduced relatively more serious vibrations of the bridges and caused the damages.

Vibration of bridges causes cyclic stresses in bridge components and connections. The cyclic stress is one of the governing factors of fatigue damage (2,3). Current design rules for highway bridges imply that each vehicle generates one maximum stress cycle and specify the design cycles according to traffic volume (1,3). These assumptions provide simple rules for design of bridges. For the evaluation of actual bridge response to truck loads and of possible fatigue damages, the examination of vibration of bridges in question is necessary.

Evaluation of bridge dynamic characteristics has been pursued by many bridge engineers and researchers. The study reported herein attempts to derive an approach for estimating from measured strains the essential characteristics of vibration as one step for evaluation of fatigue damages.

B. T. Yen, Department of Civil Engineering, Fritz Engineering Laboratory #13, Lehigh University, Bethlehem, Pa. 18015. L. L. Y. Lai, Alfred Benesch & Company, 474 North Centre Street, Pottsville, Pa. 17901.

EVALUATION OF DYNAMIC CHARACTERISTICS

Vibrational Frequencies, Modes, and Damping

A bridge deflects under load and sustains strains at all of its components. The "static" strain at a point of the bridge as a function of time can be estimated by using influence lines. Trucks traverse a bridge at high speed generating vibration of the bridge and cyclic stresses at all points. Figure 1 is a schematic of stress-time relationship for the bottom flange of a girder. The cyclic stresses occur at a specific frequency corresponding to the nature of the bridge and truck condition. An example of measured strain-time record is shown in Figure 2. After departure of the truck, vibration gradually damped out.

For a given position of a truck on a bridge, the static deflection shape of the bridge can be computed by analyzing the total bridge structure. With moving trucks, the deflection shape changes with time. Classical dynamic analysis employs the technique that the dynamic deflection shape at any time is the summation of a number of characteristic shapes with different amplitudes at that time (4,5). The characteristic shapes correspond to vibrational modes, each of which has a frequency of repeated vibration and a damping characteristic. Figures 3 and 4 show schematically "flexure" and "torsional" modal shapes of vibration.
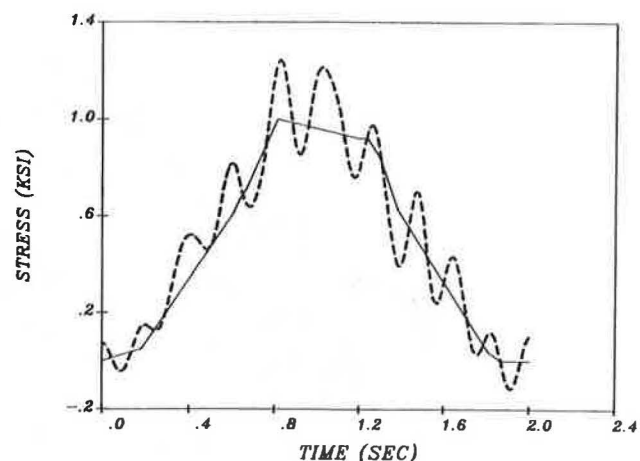

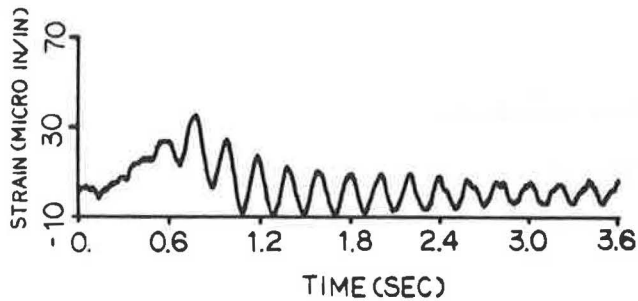FIGURE 1 Static and dynamic variation of stresses.

FIGURE 2   Example of strain-time record.

The prevalent methods of evaluating bridge vibration include the application of bridge vibrational forces to determine the modal frequencies and damping ratios, measurement of variation of acceleration with time and determination of dominant frequencies through modern computational techniques, and finite element analysis of the bridge to compute the modal deflection shapes and corresponding frequencies. The primary application appears to be for the assurance that the characteristic frequencies do not correspond to dominant speed of the vehicles on the bridge; thus, no resonance would be induced.

Strains and Displacements

For the purpose of evaluation of bridge behavior and fatigue damages, a comprehensive evaluation of bridge vibration is necessary. Because measurement of strains and displacements is more familiar and provides more direct information to bridge engineers for analysis than the measurement of acceleration at bridge components, either displacements or strains will be chosen as the basic data for analysis. In actual cases, measurement of deflection is usually more difficult than measurement of strains. Furthermore, the measurement of strains at specific locations of bridges has been more widely used in recent years. Strain data are chosen for this study.

Within the common load ranges of bridges, the relationship between displacement at a point and the corresponding strain at that point is linear (4–6). This linear relationship is evidently illustrated by the strain-time and deflection-time data shown in Figure 5, obtained from a strain gauge and a deflection gauge on the bottom flange at midspan of a girder bridge. Consequently, the classical method of modal superposition of displacements can be directly applied to strains. In other words, computational techniques of data analysis can be applied to displacement as well as to strains.

Use of FFT

A widely used technique for the determination of frequencies and corresponding damping ratios of random vibrations is the use of Fast Fourier Transformation (FFT) (4,5). By representing the measured strain-time data as the sum of contributions from all the vibrational modes and analyzing the data through time intervals, the dominant frequencies are determined. The output of this analysis is commonly presented in the form of a power spectrum, which is a diagram depicting the dominant frequencies.

As an example, a portion of the strain-time record of Figure 5 is analyzed. The portion of record chosen is that of "free" or "residual" vibration after the passage of the truck. The results of analysis are shown in Figure 6. For this case, the dominant vibrational frequency was 4.92 cycles per second (4.92 Hz) with a damping ratio of 1.92 percent. There were also minor contributions from frequencies of 10.94 Hz and 15.86 Hz. To confirm these results, the corresponding displacement data of Figure 5 are also analyzed using the same procedure. The resulting power spectrum is also shown in Figure 6. The results are practically identical to those from the strain records.

Having demonstrated that evaluation of dynamic characteristics can be made through the analysis of strain data, the application of the procedure to two bridges is described in the following sections.
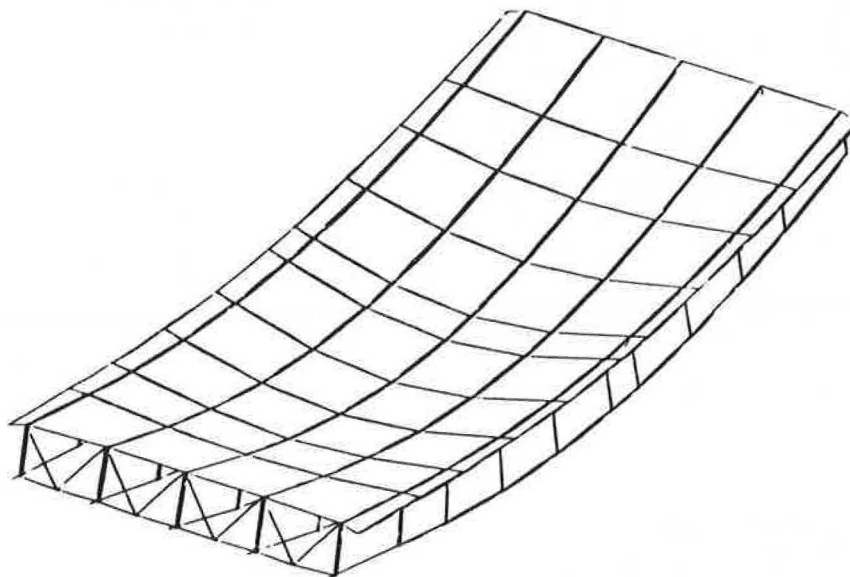

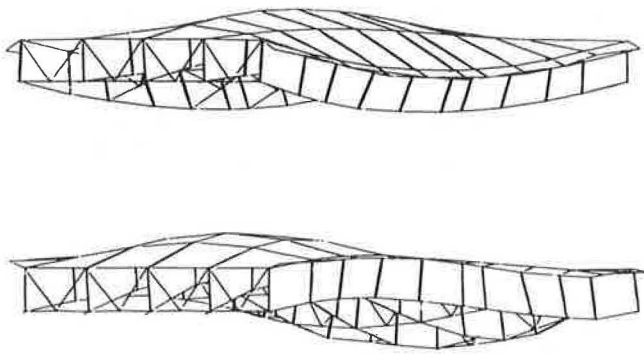FIGURE 3   Deflection shape of fundamental flexural mode.

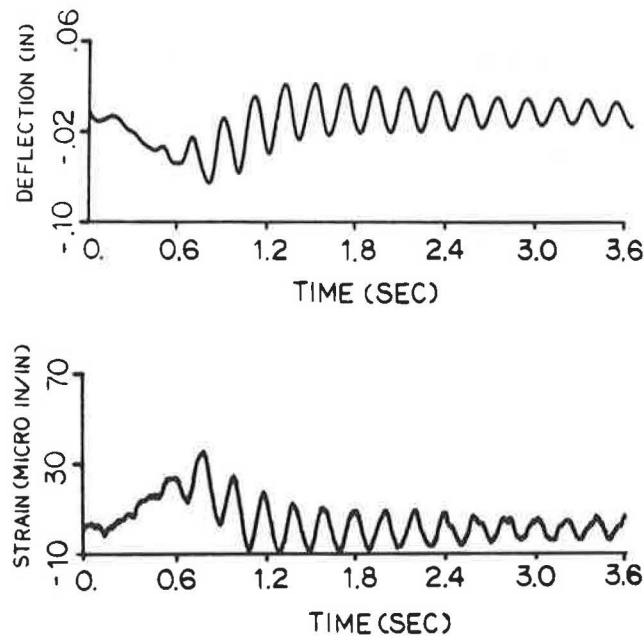FIGURE 4　Deflection shapes of higher vibrational modes.

FIGURE 5　Typical deflection and strain data of girder.

FIGURE 6　Power spectrum of deflection and strain.

VIBRATION OF TWO BRIDGES

Simple-Span Multigirder Bridge

A simple-span, five-girder right-angle (no skew) steel highway bridge was monitored for strains at the bottom flange of a girder and for vertical deflection of the same girder. The span length is 84 ft 10 in., the riveted girders are 8 ft apart, and the deck width is 32.5 ft curb to curb for two traffic lanes. The 8.5-in. deck is composite with the riveted girders.

An example of the measured strain-time data and the corresponding deflection-time records are those shown in Figure 5. The results of analyzing these data using the FFT approach are given in Figure 6, as power spectra from deflections and strains. The dominant vibrational frequency was 4.92 Hz. These results were presented in the last section as the basis for the approach.

The strain and deflection data were analyzed at the same point on a bottom flange from 21 random trucks which traveled over the bridge. Again, only the free vibration portion, when the trucks have moved away from the bridge, were used.

The resulting power spectra are placed in a line in Figure 7. For all cases, the dominant vibrational frequency was about 4.92 Hz, either from the strain data or the deflection record.

This condition that the simple-span bridge vibrates only in one mode provides strong possibility for the evaluation of bridge behavior. (An earlier examination of measured data from a simple-span prestressed concrete bridge also showed that the bridge vibrates predominantly in one mode.) To explore this condition further, the bridge was analyzed using the finite element method for modal shapes and frequencies. The computed natural frequencies of the first 10 modes are listed in Table 1. Also listed in the table are the results of analyzing the recorded strain data of Figure 5. The computed fundamental (lowest) natural frequency is 5.32 Hz compared to the value of 4.92 Hz from strain data. The detectable contributing frequencies of 10.94 Hz and 15.86 Hz correspond to the fourth and fifth natural mode. The contribution of these two higher modes is so small, as indicated by the power spectra of Figures 6 and 7, that the bridge practically vibrates only in the lowest natural mode.

For visual impression, the computed vibrational shape of the lowest mode is shown in Figure 3, and those of fourth and fifth modes are sketched in Figure 4. It is the shape of the lowest natural mode that is corresponding to the customary static deflection shape of the bridge, the shape that engineers envision during design.
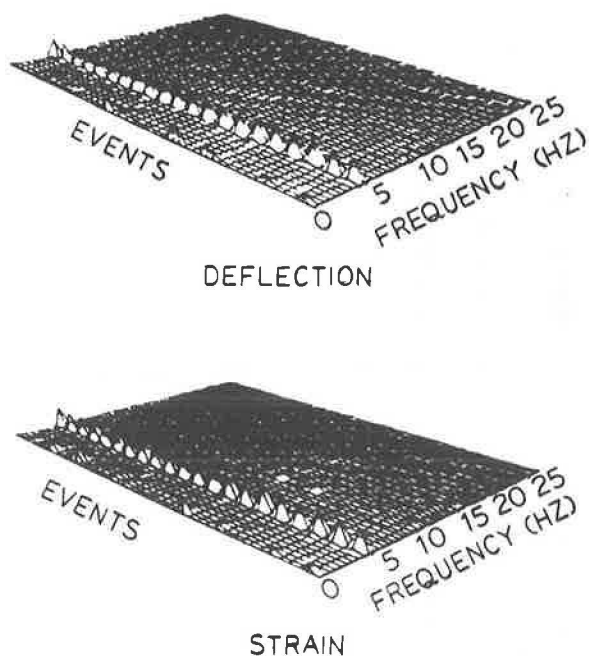
DEFLECTION

STRAIN

FIGURE 7   Power spectra from data of 21 trucks.

TABLE 1   COMPUTED AND MEASURED NATURAL FREQUENCIES

Finite Element Method Natural Frequency (Hz)	Natural Frequency From Strain Data (Hz)
5.3244	4.922
7.0033	
9.4497	
11.1330	10.9375
16.3426	15.8594
17.4229	
18.6485	
21.6410	
22.2794	
24.2604	
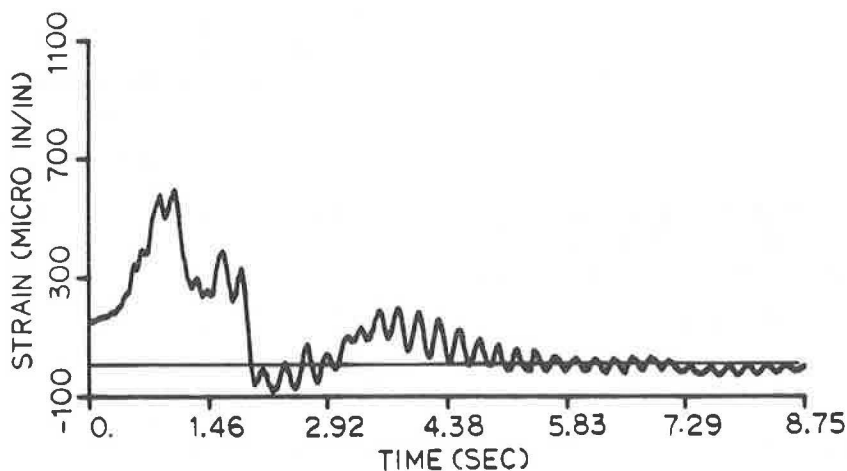
FIGURE 8   Strain record of a truck.

The use of this condition of vibration in a single mode will be made later.

Three-Span, Skewed, Continuous Bridge

The second bridge studied is a three-span continuous bridge with six steel girders. The spans are 48.75 ft, 175.0 ft, and 48.75 ft long. The rolled girders are equally spaced at a distance of 5 ft 10.5 in. The deck has a width of 30 ft, curb to curb, and is not constructed compositely with the girders. There are two traffic lanes. The bridge is skewed, at 77 degrees. Transducers for strain measurement were mounted on a girder in one of the side spans. No deflection measurement was made.

Figure 8 shows an example of strain-time records from the transducer. Live load stress reversal is evident, in full agree-

ment with the condition of continuous spans. The vibrational characteristics of this and three other records were analyzed by the FFT approach. The resulting power spectra are shown in Figure 9.

Examination of the spectra reveals that, similar to the simple-span bridge, this three-span bridge also vibrates predominantly in one mode. The frequency of vibration is 5.47 Hz. The corresponding damping ratio is 2.3 percent.

Finite element analysis was conducted on this three-span bridge with a skew. A model assuming full composite action was analyzed, which provided a lowest natural frequency of 5.96 Hz. That the frequency of vibration by strain data is slightly lower than that by computation is in agreement with the results of the simple-span bridge analyzed earlier. This condition strengthens the belief that the procedure of this study for determining vibrational characteristics can be applied to most bridges, simple or continuous span.
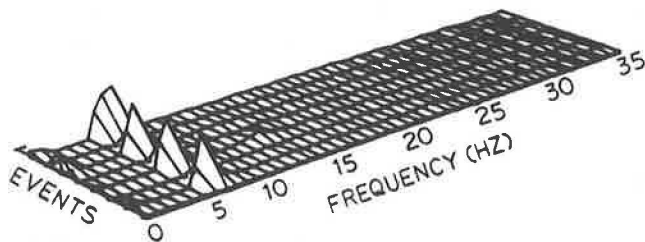
FIGURE 9   Power spectra corresponding to four trucks.
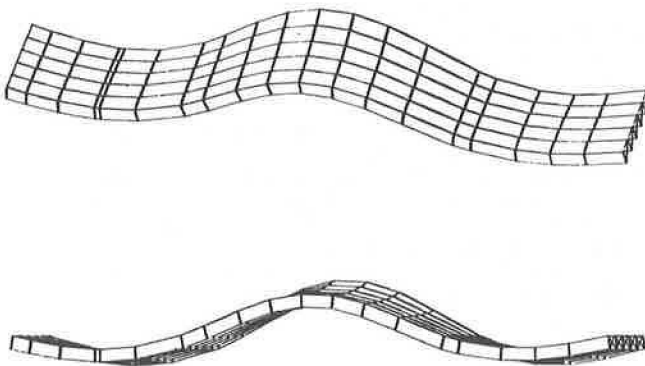

FIGURE 10   Vibrational shape of a three-span bridge, lowest mode.

The computed vibrational shape of the bridge without skew and corresponding to the lowest mode is shown in Figure 10, in two views. Again, for this bridge, bending appears to dominate.

EVALUATION OF BRIDGE BEHAVIOR

With the vibrational characteristics of a bridge determined from measured strains, the dominant vibrational modes and the corresponding damping ratios are known. For the two bridges studied, each vibrates in a flexural, fundamental mode. This condition suggests that each bridge can be modeled as an equivalent beam with a known frequency and damping.

The dynamic behavior of a beam subjected to moving truck loads and vibrating in known modes can be evaluated using traditional methods of dynamic analysis (4–6). The governing factors include the configuration, speed, and vibrational characteristics of the trucks; the headway between trucks; and the condition of the approach to the bridge. Except for the last, all factors are related to the traffic. These factors can be classified and grouped, in fact standardized as HS20 or lane loading (1), for the purpose of designing the bridges. These factors, however, must be examined case by case in order to evaluate the behavior of each bridge. For the simple-span bridge studied, strain measurements were made in conjunction with an earlier research on weigh-in-motion technology (7). The vehicular properties and the speed of a truck that generated the strain-time data were measured fairly accurately. A procedure is being developed to compute the stress variation at a point on a girder as the truck traverses the

bridge, as a case study (8). In this computation, the truck is considered as rigid body masses with known vibrational characteristics. A schematic of the truck is shown in Figure 11. The bridge is considered as a beam with its frequency of vibration and damping ratio determined from the measured strain data. After the stress-time relationship of the equivalent beam is computed, the stress-time variation at the girder of consideration is estimated through proportioning the responses among the girders. The results are given in Figure 12.

In Figure 12, the solid line represents the computed variation of stress as the truck traveled on the bridge. The dashed line is from actual measurement of strains. The agreement between the computed and measured stresses is good both in magnitude and in fluctuation of stress.

This good agreement, of course, is because the characteristics of both the bridge and the truck are obtained by measurement. The important points, however, are that the bridge vibrational characteristics can be evaluated from measured strains and that the stress-time variation at a point of the bridge can be computed quite accurately. Extension of this approach is being attempted to estimate the number of stress range cycles resulting from average daily truck traffic for the purpose of fatigue life evaluation.
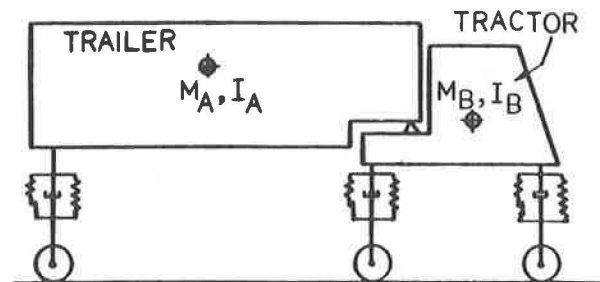
M : MASS
I : PITCHING INERTIA

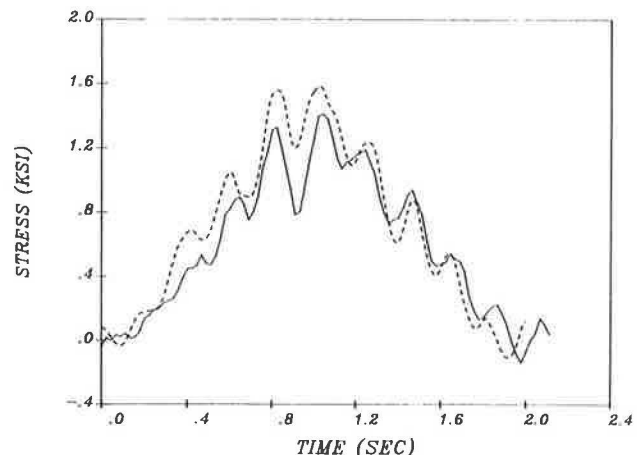FIGURE 11   Schematic of a truck for analysis of bridge.

FIGURE 12   Computed and measured stress variation.

SUMMARY AND CONCLUSIONS

The following summary and conclusions can be drawn from the results of this study.

- Vibrational characteristics of bridges, that is, frequencies and damping ratios, can be derived from measured strain-time data of the bridges. Strains are relatively easier to measure than deflection and are more familiar than acceleration to engineers.
- Strain data from trucks of regular traffic can be used for evaluation.
- Results from a single-span bridge and a three-span continuous bridge show that bridges appear to vibrate predominantly in one frequency.
- Analysis of these bridges indicates that the dominant frequency corresponds to the fundamental mode of vibration. The fundamental mode shape is analogous to the static deflection shape envisioned in bridge design.
- When the axle spacing, weight, and speed of the truck that generates the measured strain data are known, the stress-time variation at points of the bridge can be computed with good accuracy.
- Extension of this work is recommended for the purpose of estimating the number of stress cycles resulting from trucks on bridges.

ACKNOWLEDGMENTS

REFERENCES

1. *Standard Specification for Highway Bridges*, 13th ed. AASHTO 1983.
2. J. W. Fisher and B. T. Yen. Design, Structural Details, and Discontinuities in Steel. *Proc., Specialty Conference on the Safety and Reliability of Metal Structures*, Vol. 217, ASCE, Nov. 1972.
3. J. W. Fisher. *Bridge Fatigue Guide*. American Institute of Steel Construction, Chicago, Ill., 1977.
4. R. W. Clough and J. Penzien. *Dynamics of Structures*. McGraw-Hill Publishing Co., New York, 1975.
5. M. Paz. *Structural Dynamics*. Van Nostrand Reinhold, New York, 1985.
6. J. M. Biggs. *Introduction To Structural Dynamics*. McGraw-Hill Publishing Co., New York, 1964.
7. J. H. Daniels, J. L. Wilson, L. Y. Lai, B. T. Yen, and R. Abbaszadeh. *Weigh-in-Motion and Response Study of Four In-Service Bridges*. FHWA-RD-86-045. FHWA, U.S. Department of Transportation, Washington, D.C., 1987.
8. L. Y. Lai. *Traffic Induced Stress Range Cycles in Bridge Main Members*. Ph.D. dissertation. Lehigh University, Bethlehem, Pa., Oct. 1988.

Structural Applications of Composite Materials to Highway Tunnels

CHARLES E. KAEMPEN

Highway tunnels constructed of concrete enclosed by a double-wall tubular composite structure are shown to be economically feasible and merit serious attention by planners of advanced transportation methods that must contend with water crossings. Modern techniques for mechanically coupling and sealing tubular composite structures are shown to now enable composite materials to compete with welded steel joints in strength and long-term service. Engineering properties and commercial applications of the new class of twined-strand unidirected composite materials are presented along with cost and performance comparisons between composites and identical pipe and tank structures made of steel. A detailed engineering solution to the problem of providing an affordable fixed transportation link between Europe and Africa across the Strait of Gibraltar is presented. This example shows how structural composites can be used with concrete to fabricate the type of highway tunnel envisioned as an inevitable adjunct to conventional approaches used to solve current and future transportation problems.

Unidirected twined-strand composites comprise a new class of composite materials that are less expensive to fabricate into highway tunnel structures than equivalent strength structures made of carbon steel. Modern techniques for mechanically coupling and sealing tubular composite structures now enable composite materials to compete with welded steel joints in strength and long-term service. Tubular double-wall composite structures now provide an alternate method of forming and reinforcing concrete highway tunnels and culverts. Combining the exceptional tensile strength and corrosion resistance of unidirected composite material with the compressive strength and formability of concrete provides a new approach to the construction and installation of future highway tunnels.

CHARACTERISTICS OF COMMERCIAL COMPOSITES

There is a continuing trend among engineers, architects, and developers to replace steel structures with structures made from commercial composite material. One of the principal reasons is that structures made from commercial composite material do not deteriorate from weathering or corrosion and thus require less maintenance. Another reason is that they are safer and less expensive to transport and install because of their lower weight. Unlike steel, commercial composite materials will not experience failure because of structural fatigue caused by repeated flexure under stress.

Commercial composite materials are fracture resistant and have incredible energy-absorbing characteristics. Commercial

Kaempen & Associates, Consulting Engineers, 3202 Larkstone Drive, Orange, Calif. 92669.

composites are 100 times more thermally insulative than steel and thus are a safer structural material because they do not weaken as rapidly when exposed to fire. Today, special inexpensive inorganic polymers can be employed as the glass-filament impregnating matrix to provide noncombustible commercial composites that can remain structurally competent when exposed for extended durations to temperatures as high as 2,000°F. These new noncombustible high-temperature structural composites do not produce toxic smoke or gases when exposed to fire. Commercial composites are also electrically insulative and can be made to be either translucent or opaque. Commercial composites are the most versatile structural material available.

The term *commercial composites* is used to refer to unidirected high-strength composites made from continuous strands of glass fiber and to distinguish them from *aerospace composites*, which are unidirected composites made from carbon or aramid fibers. Aerospace composites, such as those used by Burt Rutan to build the Voyager aircraft, which flew nonstop around the world, cost at least 10 times more than commercial composites having the same weight. Aerospace composites can be as stiff as steel while having a density lower than magnesium. Both aerospace composites and commercial composites are several times stronger than steel.

The recent development of *twined-strand composites* has now made it possible to make composite couplers that can mechanically join commercial composites so that the joint strength at least equals the maximum tensile strength of the composite laminar structure being connected. Figure 1 summarizes the result of ASTM Procedure A cyclic pressure tests (ASTM D2992) performed on specimens of reinforced thermosetting resin pipe (RTRP) made from twined-strand composite material. These tests demonstrate that the hydrostatic design basis strength (HDBS) of the twined strand composite material exceeds 60,000 lb/sq in., a value approximately three times higher than the maximum allowable design strength of steels used to make pipe conforming to the ASME B31.3 code for pressure piping.

CHARACTERISTICS OF TWINED-STRAND COMPOSITES

Twined-strand composites are a new class of unidirected composites that comprise helically twisted strands of continuous filament reinforcement. Figure 2 illustrates the composite twine structure disclosed in recent U.S. and world patents awarded to the author (U.S. Patent Nos. 4,680,923 and 4,740,422). Figure 3 illustrates the construction of a high-strength mechanical coupler made from twined-strand composites.
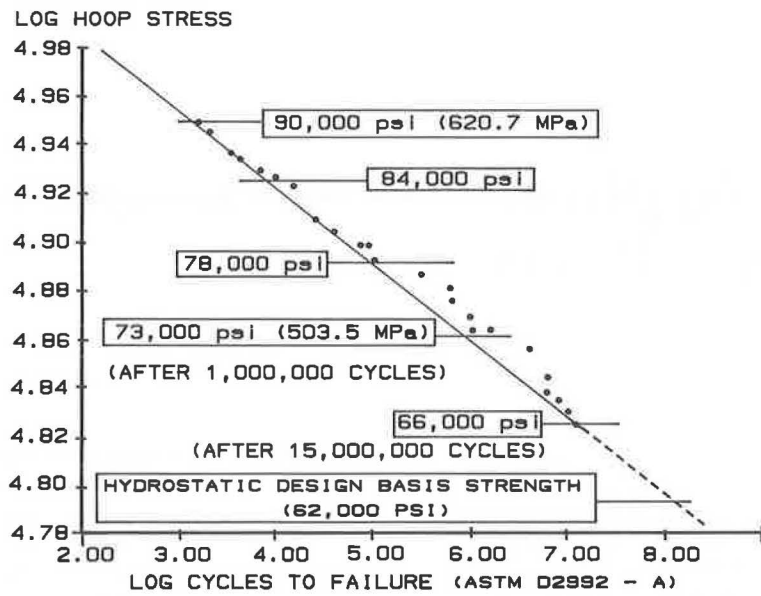
FIGURE 1   Plot of stress versus cycles resulting from ASTM D2992 cyclic tests of composite pipe made from twined strands of glass fiber.
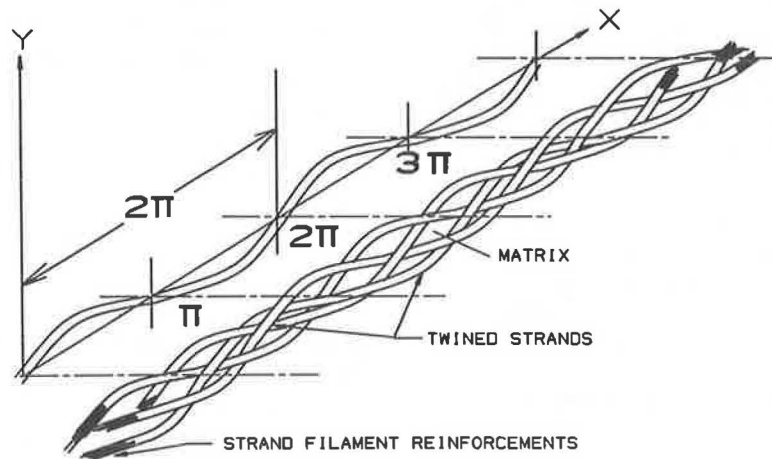

FIGURE 2   Enlarged view of unidirected twined-strand composite structure defined by sine wave frequency of strand twining.
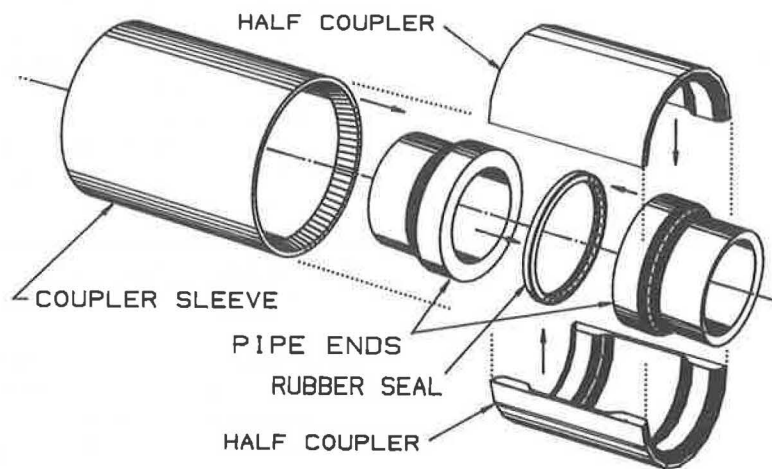

FIGURE 3   Exploded view of a high-strength composite coupler and seal assembly.

Tubular-shaped twined-strand composite structures take less time to manufacture than tubular composite structures made by conventional filament winding processes. This is one reason twined-strand composite structures are less expensive to manufacture than other composite structures. In addition to providing a superior method of being structurally connected, twined-strand composites are also stiffer than conventional multi-ply composite laminates.

Tubular structures made from twined composite material may comprise as few as two plies: an inner ply of circumferentially oriented twines (CIRC) surmounted by an outer ply of longitudinally oriented twines (LONGO). The inner ply of CIRC twines is primarily employed to resist the radially directed hoop stresses produced by pressure or compressive loads. The outer ply of LONGO twines is primarily employed to resist longitudinally directed tensile and compressive stresses such as those produced by bending or pulling. The outer ply composite twine structure is configured as a flared-end laminate that comprises the flanged-end portion of a tubular composite structure, which can be mechanically connected by a composite coupler assembly.

Figure 4 illustrates composite pressure pipe connected by this unique high-strength coupling. Figures 5 and 6 illustrate a cross section view of the structural configuration and of a typical tubular twined composite structure connected and sealed with a high-strength composite coupling. Figure 7 shows a typical installation of a high-pressure petroleum pipeline mechanically connected by a two-piece composite coupler and coupler retaining sleeve. Such mechanically connected composite pressure pipe with removable end plugs have been hydrostatically tested repeatedly at pressures as great as 10,000 psi without leakage or structural failure. Such pipe has been thoroughly tested to meet the structural requirements established for fiberglass pressure vessels by ASME Section X of the boiler and pressure vessel code and for nonmetallic pipe established by the ASME B31.3 and B31.4 pipe codes. The high-pressure mechanically coupled composite pressure pipe illustrated in Figure 8 has been made and sold by U.S. and Canadian licensees since April 1982.

Table 1 presents the physical properties of a single composite ply made of unidirected twines of continuous strands of glass filaments.

COST AND CONNECTABILITY COMPARISONS: COMPOSITES VERSUS STEEL

Primary load-bearing structures made from commercial composites can today be designed to be competitive in cost with equivalent structures made of steel or reinforced concrete. Commercial composites made from glass roving and polyester resin today sell for approximately $3.00/lb and cost approximately $2.00/lb. Glass roving and polyester resin cost less than $0.90/lb when purchased in quantity. Commercial composites made from twined strands of glass roving impregnated with polyester resin possess the physical properties shown in Table 1.

To illustrate the fact that, as a primary load-bearing structural material, commercial composites now compete in cost with steel, a comparison of pipe material costs is presented. The maximum allowable design strength of steel used to make pipe that meets the ASME B-31 pipe code requirements is 20,000 psi (138 MPa). This is only one-third the allowable design strength of commercial composites, which, as can be seen from Table 1, possess an HDBS of 60,000 psi as determined from cyclic test results (ASTM D2992A).

The current sale price of steel pipe is not less than $0.40/lb when purchased in multiton shipments. Because 1 lb of commercial composite material equals the structural performance of 12 lb of steel, at least $4.80 worth of steel will be required to perform as well as 1 lb of commercial composite material selling for $3.00/lb. Of course, cost versus strength comparisons reflect only part of the picture. Reliability as an end use structure also depends on the ease and reliability of joining and sealing the structural materials. Until the recent advent of high-strength composite mechanical couplers, one of the principal advantages of using steel instead of composite material as a structural material was that steel could be structurally connected without any sacrifice in structural strength. Conventional composite structures comprising a multitude of overlapping laminate plies cannot be connected without a substantial sacrifice in structural strength. This is because when conventional composites are connected the joint strength is no greater than the strength of the matrix or bonding adhesive. Composite matrix materials possess only one-tenth of the strength of the composite filament reinforcements.
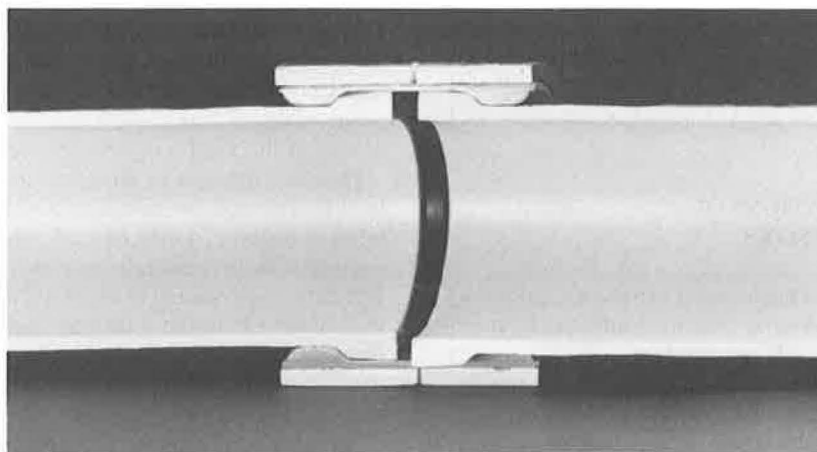

FIGURE 4 **Photographic section detail of sealed and coupled composite pipe.**
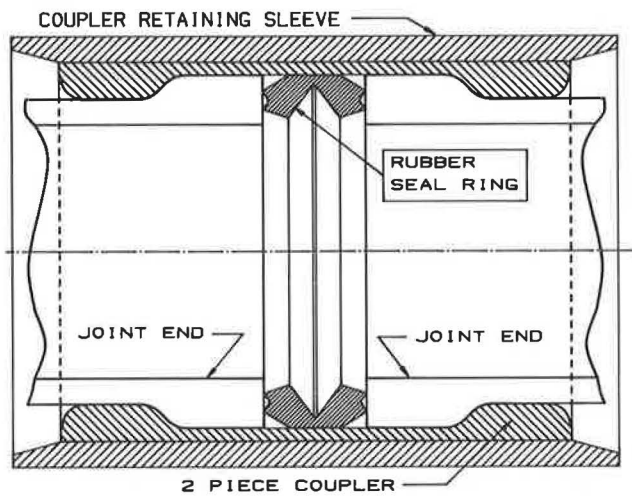
FIGURE 5 Section detail of a high-tensile-strength composite coupler and seal assembly.
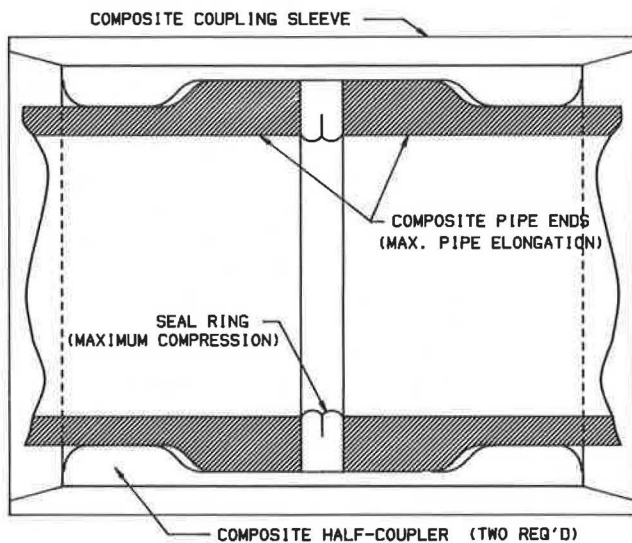

FIGURE 6 Section view showing how coupled pipe thermal expansion can be accommodated by composite coupler assembly.

By using the new high-strength twined-strand composite couplers, tubular composite structures can now be connected quickly and reliably to exhibit the same joint strength and sealing integrity as a welded steel structure of the same wall thickness.

STRUCTURAL APPLICATIONS OF COMMERCIAL COMPOSITES

Because of the widespread engineering experience gained by using commercial composites as primary load-bearing structures, the time has come to begin planning and constructing highway tunnels, bridges, and underroad culverts that use this amazingly versatile and cost-effective structural material.

The reliability and effectiveness of glass-reinforced polymeric resin composite material has been demonstrated in numerous applications. For example, the U.S. Navy selected this material for use in constructing the forward portion of
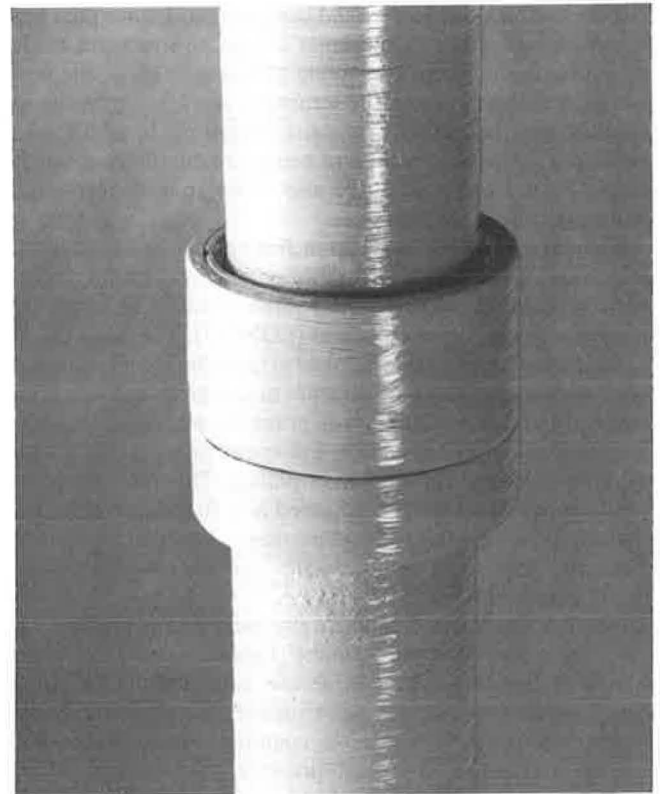

FIGURE 7 Photograph of a 6-in.-diameter mechanically coupled 3,000 psi pressure pipe.

the 30-ft-diameter Trident submarine. Minesweepers and other ships made of this material have been in service for over 10 years. Bridges in China and Germany made of glass-polyester composites are already in service. Large-diameter chimney liners and free-standing chimneys that resist corrosion have been in service for many years.

In 1982 a 40-ft-diameter, 45-ft-high fuel storage tank that met the National Fire Protection Association requirements for aboveground storage of flammable liquids (NFPA 30) was constructed entirely of commercial composites at Aransas Pass, Texas. This structure was constructed on the job site despite high winds, frequent rainstorms, blistering heat, and high humidity. The structure was thoroughly tested before being placed into service.

This tank was constructed as a double-wall tank. The inner tank composite material was selected on the basis of strength and compatibility with water or petroleum products. The outer tank and rib structure was made of a noncombustible composite material that could resist long-term exposure to fire, as well as the wind and weather present in the area.

Figures 9 through 11 illustrate how this tank was built and how it appeared on completion. The tank incorporated an internal floating roof to control vapor emission, as well as a fixed roof to prevent rain and dust from entering the tank. The tank was designed to meet the dimensional requirements of American Petroleum Institute tanks and included a 30-in.-diameter removable manway and inlet and drain fittings near the bottom. Roof vents were provided to allow rapid filling and discharge.

A major advantage of composite fuel storage tanks is that they are less vulnerable to lightning strikes, which are the major source of fuel tank fires. The double-wall all-composite tank shown in Figure 11 was designed to enable fire extin-
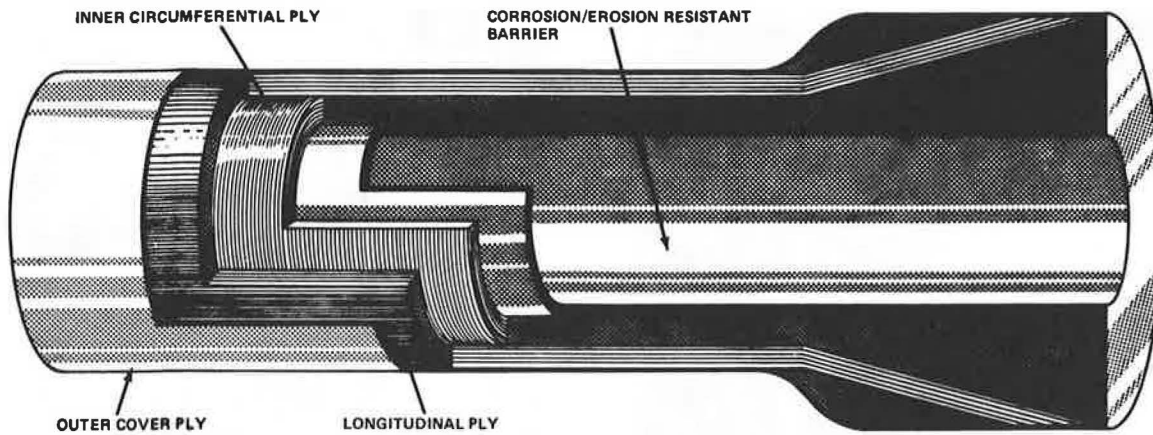
FIGURE 8 Perspective section view of twined composite pipe joint laminate construction.

Labels: INNER CIRCUMFERENTIAL PLY; CORROSION/EROSION RESISTANT BARRIER; OUTER COVER PLY; LONGITUDINAL PLY

TABLE 1 PHYSICAL PROPERTIES OF A SINGLE
COMPOSITE PLY OF UNIDIRECTED TWINES

Physical Property	Value (Metric Value)
Maximum longitudinal tensile strength (ASTM D638)	125,200 PSI (0.863 GN/m²)
Hydrostatic design basis strength (ASTM D-2992-A) (Maximum allowable design tensile strength)	60,000 PSI (0.414 GN/m²)
Longitudinal compressive strength	50,000 PSI (0.345 GN/m²)
Longitudinal tensile modulus (ASTM D638)	3.51×10^6 PSI (24.2 GN/m²)
Longitudinal interlaminar shear strength (ASTM D2344)	5,000 PSI (34.5 MN/m²)
Transverse shear strength (ASTM D732)	33,000 PSI (0.227 GN/m²)
Longitudinal Poisson's ratio (ASTM D638)	0.25
Longitudinal coefficient of thermal expansion (ASTM D696)	11×10^{-6} in./in./ft
Density (ASTM D1505)	0.064 lb/in.³ (1771 kg/m³)

NOTE: Twines consist of 3 to 25 strands of helically configured E-glass filament reinforcements impregnated with thermosetting polyester matrix, a filament volume fraction equal to 46 percent, and a twined strand frequency from 10 to 100 cycles per meter.

FIGURE 9 Fabricating a 42-ft-diameter composite structure on the job site by process of twine winding.
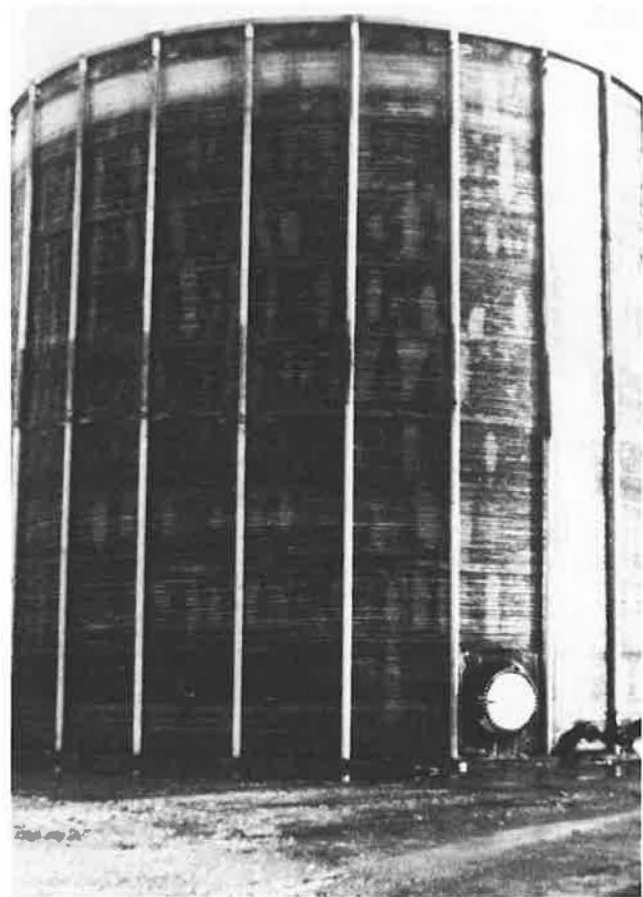

FIGURE 10 View of the inner wall of a 42-ft-diameter double-wall composite structure.

guishing foam to be pumped through the tank wall vertical tube support columns in the unlikely event the contents did ignite. Another key feature characterizing composite fuel storage tanks is they are less likely to ignite flammable vapors resulting from static electric spark discharge. Such events are common hazards with steel tanks during filling operations.

Composite materials also do not rust or corrode. Thus, they require minimal maintenance.
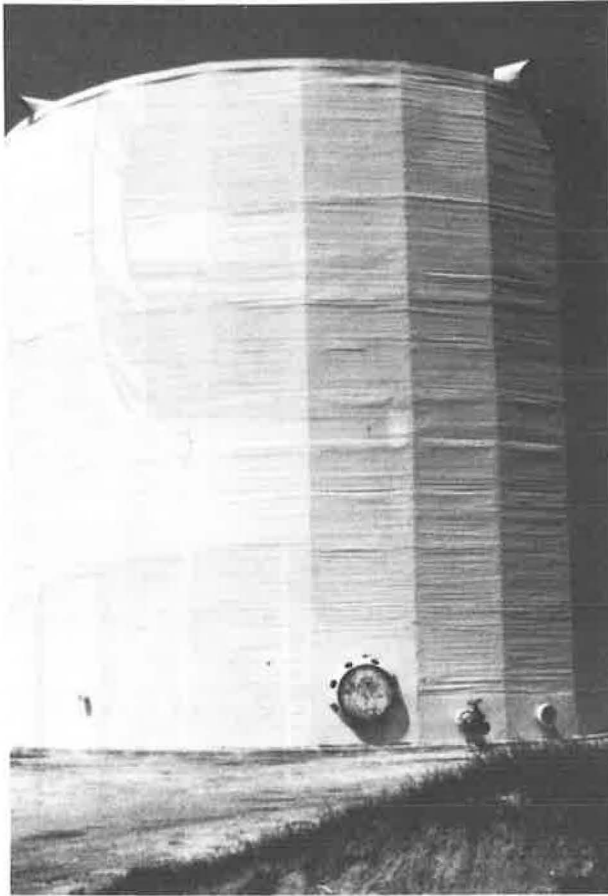
FIGURE 11   View of a 42-ft-diameter double-wall composite fuel storage tank.

FIGURE 12   Illustration of a submersible composite-reinforced concrete four-track railway tunnel.

HOW COMPOSITE STRUCTURES CAN BE USED TO FORM AND REINFORCE CONCRETE

The Aransas Pass, Texas, project demonstrated the feasibility of making large high-performance structures of commercial composites at a cost that is competitive with the same structures made of steel or steel-reinforced concrete. Furthermore, now that the problem of reliable and high-strength connectability has been solved, the innate performance and installation advantages provided by commercial composite structures currently recommend their replacement for steel in future concrete highway projects involving bridges or tunnels.

Figure 12 illustrates a submerged composite-concrete transport tube structure that can serve as a submerged highway tunnel for automotive or railroad traffic. The double-wall composite transport tube provides a convenient pour form by which the concrete is configured into an appropriate structural member able to resist the substantial compression forces imposed by water submersion at significant depths. An inner composite shell provides a second concrete forming structure to shape the tunnel transport space interior. The new class of twined-strand composite material is used to make the outer and inner walls of the transport tube structure, as well as the mechanical coupler assemblies that enable the tube sections to be connected to provide the desired length of highway tunnel. The corrosion resistance provided by the composite
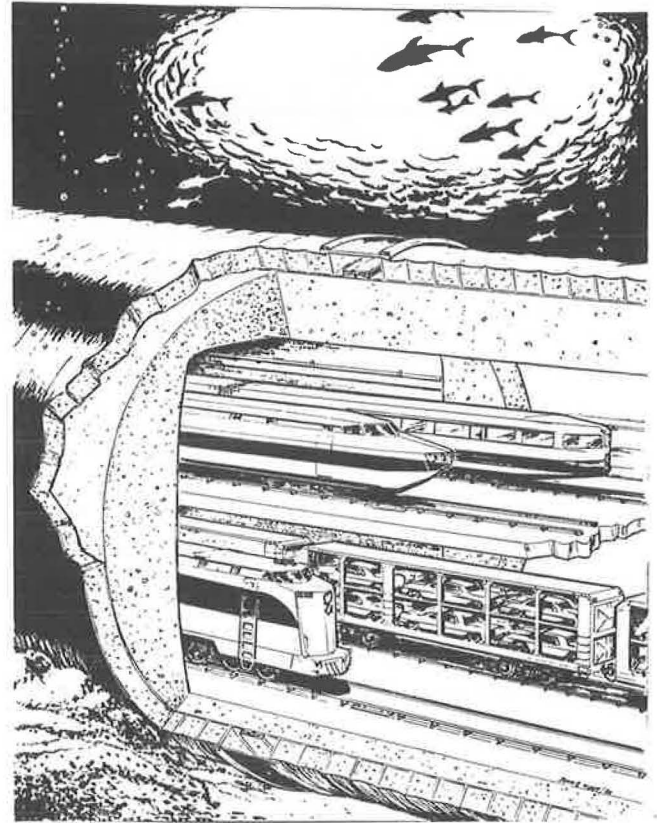
structure makes it an ideal material with which to enclose and reinforce concrete that is required to remain serviceable when the structure is exposed to the corrosive effects of seawater.

APPLICATIONS OF COMMERCIAL COMPOSITES TO SUBMERGED RAILWAY TUNNELS

Metropolitan subways and waterway crossings are two specific rail transport projects that can benefit from the use of mechanically connected tubular structures made of commercial composite materials. Both types of rail transport employ tunnels that must be designed to resist a variety of tensile, bending, and compressive loads, including shock loads imposed by earthquakes. Because tubular composite tunnel structures can be easily fabricated by using modern filament processing techniques, they are ideal structural candidates for making use of the unique properties attainable with mechanically coupled tubular structures made of commercial composites.

An example of how commercial composites can be used effectively to solve a modern transportation problem is described in the following paragraphs.

In 1982 a colloquium was held in Madrid to discuss the feasibility of linking Europe with Africa by a fixed transportation link across the Strait of Gibraltar. Although most of the engineering approaches suggested at the colloquium were feasible from an engineering point of view, the primary problem turned out to be one of cost rather than engineering know-

how. It was quickly recognized that such a transport link would not be economically feasible if it were based on the income that would be derived from either freight or passenger traffic diverted from existing ferry and air transport services. The primary justification for such a link would hinge upon its value both to tourism and as a means to provide more rapid transport of certain perishables.

If the link could also encourage future commercial and industrial investment in Spain and Morocco by being associated with advanced technology and engineering, the transport link might also be justified by the prestige associated with such an engineering accomplishment. Furthermore, if the link could also promote fiber optic communications as well as pipeline transport of fuel and potable water, there might be additional commercial justification for such a project.

As the Madrid colloquium made clear, the cost of either a bridge or a tunnel would range from $2 to $6 billion, or perhaps more. The problem with using a bridge as the transport link is twofold: a bridge would impede sea traffic, and the bridge piers would be exposed to collision damage from ships. The problem with using a bored tunnel as the transport link is even more complicated. Earthquakes in the region could affect the tunnel during and after construction. Furthermore, digging the tunnel would be dangerous and would require going to depths greater than had been dug before for such tunnels. At its shallowest part, the strait is 300 m deep. The engineering approaches suggested at the Madrid colloquium did not consider the possibility of using commercial composites as an engineering material that might solve both the engineering problems and the cost problems. Perhaps one reason was simply that a method of connecting and sealing composite structures so that they have the same strength and sealing integrity as a welded steel structure of the same thickness had not yet been developed and proven in service.

Figures 13 through 18 illustrate a submerged composite-concrete railroad transport tunnel that can provide a fixed link across the Strait of Gibraltar at a fraction of the cost of either a bored tunnel or bridge. It has been determined that a two-track electric railroad tunnel, similar in size to that of the famous 32-mi-long Seikan tunnel in Japan, connecting the
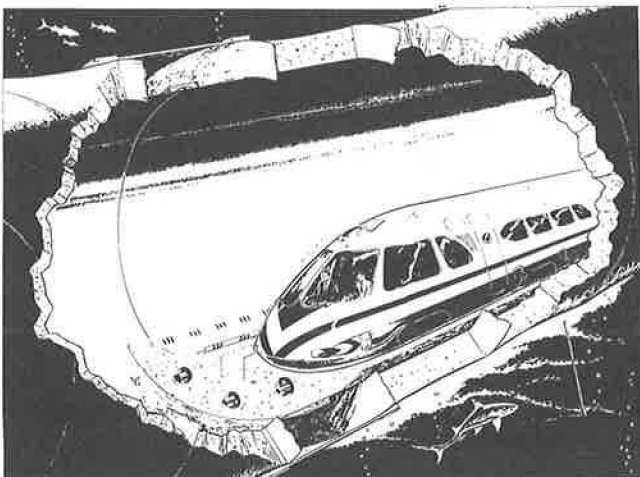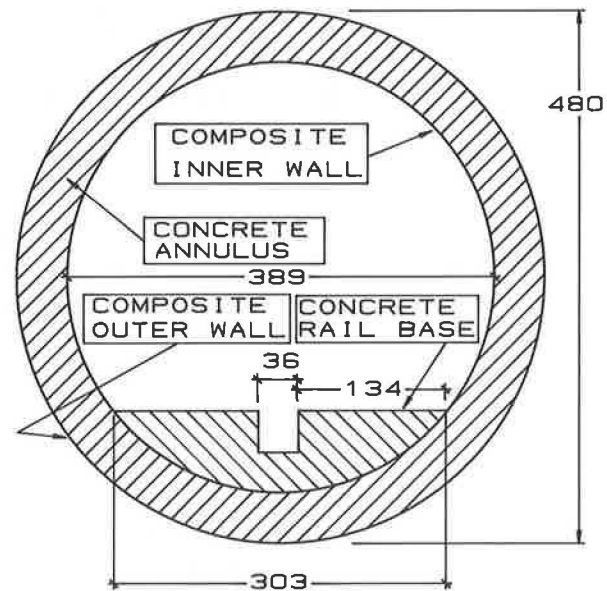

FIGURE 14 Cross section of the proposed two-track submersible tunnel.

coast of Spain with the coast of Morocco, can be constructed in less than 4 years at a cost of approximately $500 million.

The submerged transport tube would traverse the "sill" region of the Strait between Malabata near Tangier, Morocco, and Punta Paloma near Tarifa, Spain. This route is approximately 28 km in length and does not exceed a depth of 300 m anywhere along the route. Route geographic details are shown in Figure 19. As currently envisioned, the proposed transport tube would be cylindrical in cross section with an outer diameter of 40 ft (12.18 m) and an interior railroad passage area of 749 sq ft (69.5 sq m). The transport tube would consist of 348 cylindrical double-wall tube sections made entirely of glass-reinforced polyester resin designed to be mechanically connected by a pair of composite mechanical coupling structures, each of which is able to resist a tensile end load of 25,000 lb (4,473 kg) per circumferential in.

The inner wall of the double-wall composite transport tube has a diameter of 32.4 ft (9.87 m). The inner wall is separated from the outer wall by annular composite ribs approximately 1.16 m in height spaced 20 ft (6.14 m) apart.

The annulus of the double-wall composite transport tube is filled with concrete to provide a compression strength capable of resisting submersion to a depth of 1,200 ft (368 m). The weight of the concrete in the annulus plus the weight of concrete forming the rail base structure on which the tracks are laid is sufficient to provide the neccessary stability and negative bouyancy needed to offset a flotation force of approximately 81,000 lb per lineal foot. The transport tube is designed to handle the combined concentrated load of two freight trains each having a length of 1,478 ft (450 m) and a combined weight of 1,100 metric tons.

The transport tube is designed to be anchored to the ocean floor wherever it must be suspended to ensure that the railroad grade does not exceed 2 degrees. Special couplers are used to provide sufficient angular displacement between adjacent coupled tube structures so that the tube structure is sufficiently flexible to accommodate installation variations caused by the irregular ocean floor contour.
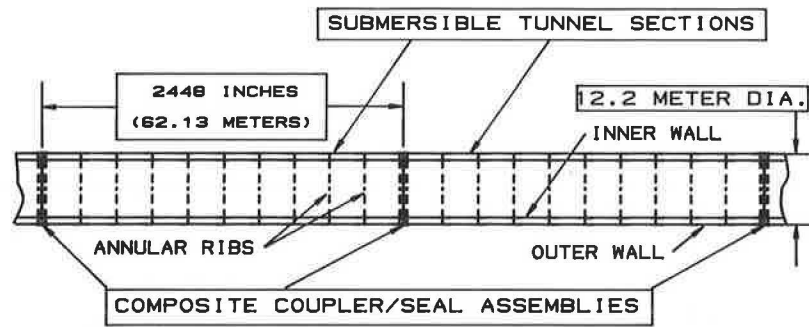

FIGURE 13 Illustration of the proposed Gibraltar Highway submersible tunnel.

FIGURE 15 Side elevation section view of composite transport tubes joined by high-tensile-strength composite couplers.
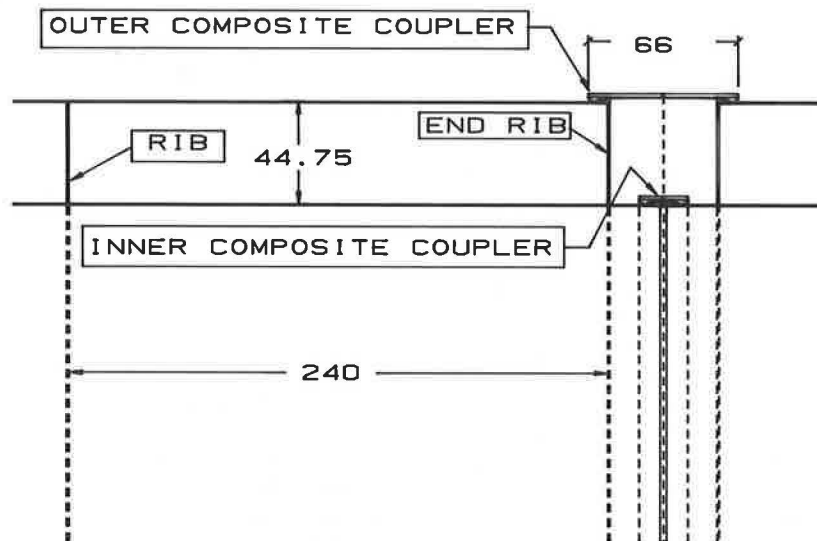

FIGURE 16 Detail of coupler and rib structure of a composite submersible tunnel structure.
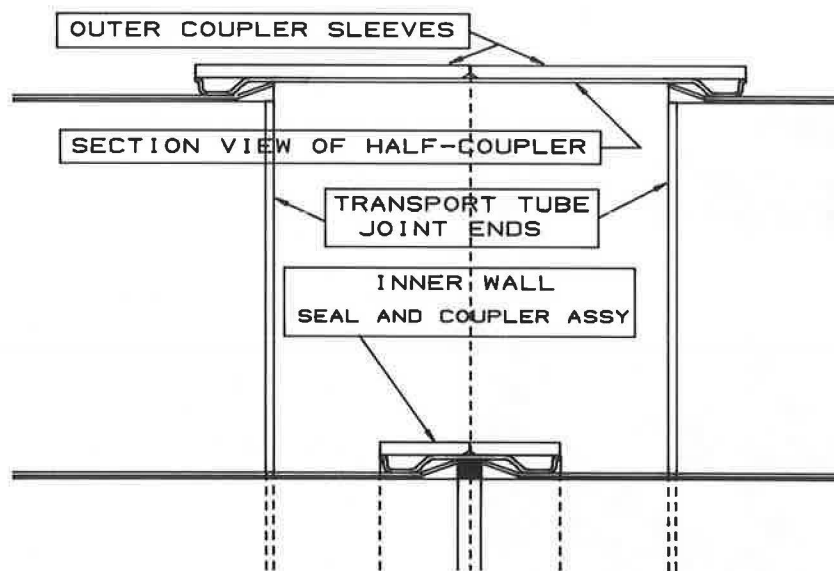

FIGURE 17 Side elevation section detail of composite coupler assemblies used to join composite tunnel structures.
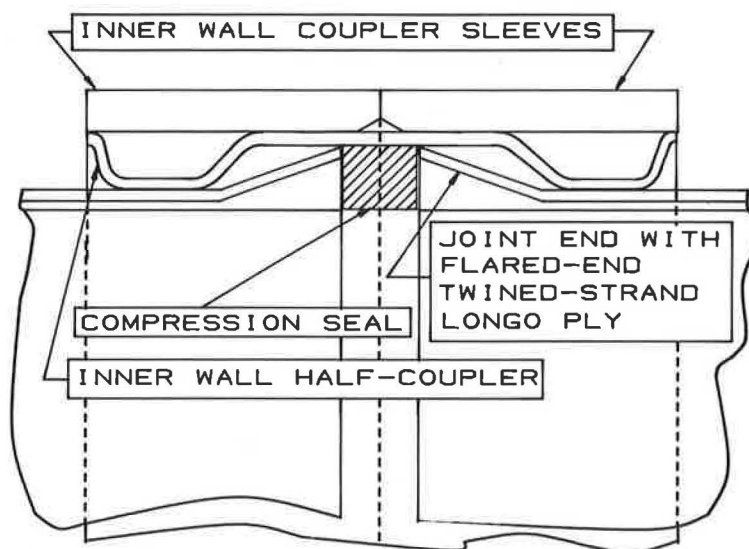
FIGURE 18 Enlargement of section view of tunnel joint seal and coupler.

Each section of the prefabricated double-wall composite tube structure is 240 ft (73.1 m) long and weighs approximately 400,000 lb (181,000 kg). The coupler assembly used to connect the outer wall structure consists of a two-piece semicylindrical flanged composite coupler member that is held together by two cylindrical composite sleeve members. Each of the coupler halves weighs approximately 3,155 lb (1431 kg); each of the cylindrical coupler sleeve members is 30 in. wide and 41 ft in diameter and weighs 4,500 lb (2,042 kg). The coupler assembly used to connect and seal the inner wall structure comprises a two-piece composite flanged semicylindrical coupler member held together by two cylindrical sleeve members. The inner wall of the transport tube section is sealed by a 3-in.-wide compressed rubber seal ring. The weight of the inner wall composite coupler and sleeve structure assembly is approximately 6,000 lb (2722 kg). The rubber seal that withholds an external pressure of at least 600 psi (4.14 MPa) is estimated to weigh less than 400 lb (181.4 kg).

Each section of the proposed composite transport tube would be fabricated on shore in a 600-ft-long shop adjacent to the seashore. The shop would have a concrete floor extending into the sea. The shop floor would provide a 600-ft canal located 4 ft below the sea level at low tide and sealed at the seaward end by a removable dam. After the tube structure has been fabricated, the water would enter into the canal and the tube structure floated out to where it would be anchored offshore a safe distance. Half of the tube structure would be made in Morocco, the other half in Spain. A special barge, designed to serve as a floating dry dock, would be positioned under two floating tube structures and emptied so that the assembly of the couplers and seals could be performed safely above water in the open air. After the tube structures have been connected, they would be sealed at their opposite ends and air tested to check the integrity of the seals. As the line of tubes are assembled along the shores of Spain and Morocco, the sealed ends of each length would be towed together and connected. The floating tube string would be anchored at each shore and then filled with only enough seawater to provide the negative bouyancy to allow it to slowly sink into place. After the transport tube has been properly positioned on the

sea floor, it would be permanently anchored by composite cables attached to the annular ribs comprising each tube section.

The final portion of the construction would begin after the transport tube had been checked out and the structure confirmed to be competent and perfectly sealed. The concrete rail bases would be poured in place and the ballast pumped out. Ventilation would be provided to crews working from either end to lay the railroad tracks and install the electric lights and other utilities. When completed, the tube would be subjected to a rigorous series of tests to ensure its safety and performance while subjected to the tidal action of the water moving into and out of the Mediterranean Sea.

It is estimated that approximately 98 million lb of glass roving and 65 million lb of polyester resin would be required to fabricate the 384 sections of composite transport tube. Those materials are currently available at a cost of approximately $0.90/lb ($2.00/kg). The cost of the concrete would not exceed the cost of the transport tube into which it would be poured. The costs involved in constructing the equipment and training the crews to make and install the tubes is not expected to exceed the total material cost. Because the cost of materials required to make the 28-km-length of transport tube will not exceed $250 million, it is reasonable to expect that the total cost to complete the submerged tunnel railroad link between Europe and Africa would not exceed $500 billion and that it would require no more than 4 years to make and 1 year to test and check out before being placed into service. By removing the concern associated with corrosion of steel or deterioration of concrete exposed to seawater, the proposed submerged composite-concrete transport tube and railroad will probably remain serviceable at least to the year 2200.

OTHER USES OF COMPOSITE TRANSPORT TUBE STRUCTURES

Because prefabricated composite transport tubes of sizes suitable for highway and railroad transport can be individually tested under a variety of service and installation environments before being placed into service, they offer a new approach
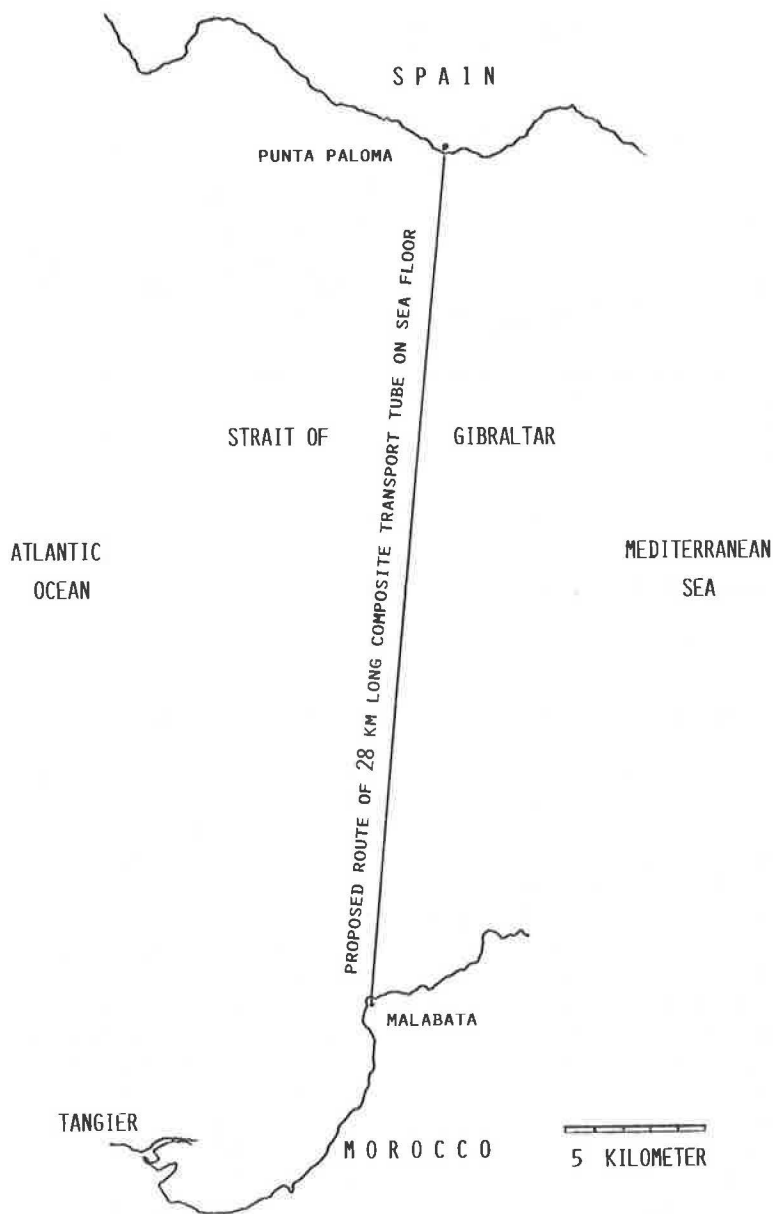
FIGURE 19 The route recommended for installation of a submerged composite railway tunnel.

for solving future transportation problems. They are uniquely suited for constructing temporary or emergency roadways. They can provide the armed forces with traffic or shelter structures that can be deployed by ship to remote areas for rapid installation. They are envisioned as a means by which supersonic surface transport will become attainable because such double-wall transport tubes can be cryogenically evacuated of air while concomitantly employing superconductive materials that make magnetically levitated high-speed trains practical.

CONCLUSION

Use of composites to fabricate tubular double-wall transport tube structures is now economically feasible. The country that becomes a leader in this field of technology will inevitably benefit from the continuing worldwide growth in passenger and freight traffic. The construction and transport of large structures, such as off-shore platforms and floating hotels, has demonstrated that large-diameter composite transport tubes can be towed and installed virtually anywhere. Where such transport is impractical, the transport tubes can be fabricated on or near their installation site. Shipboard fabrication is even possible by using the equipment, processes, and materials now employed in the fabrication of similar-size composite structures. It is envisioned that composite transport tubes will eventually become a major item of export trade for those nations that pursue this promising new field of transportation technology.

Properties of Pultruded Fiber Reinforced Plastic Structural Members

LAWRENCE C. BANK

Fiber reinforced plastic (FRP) beam sections, produced by the pultrusion process for load-bearing structural engineering applications, are manufactured by a number of U.S. companies. For design purposes both stiffness and strength properties of these structural members are required. The shear stiffness of pultruded FRP beams is considered in this paper. A new material/structural stiffness property, called the beam section shear modulus, is proposed. Using the beam section shear modulus, a procedure is presented to account for the effects of shear deformation on the response of FRP beams. Results of an experimental program conducted to obtain the section shear modulus for a variety of commercially produced FRP beams are reported. Values of the section flexural modulus for FRP beams are also given. The analysis of a rigid portal frame structure is presented to demonstrate the influence of the beam section stiffness properties on frame deflections and forces.

Fiber reinforced plastic (FRP) thin-walled beams are beginning to see application in a variety of civil engineering structures. Further use of these attractive construction materials depends to a large part on structural designers gaining a familiarity with FRP materials, their properties, and their design requirements (1). As noted by Green (1), "Standard codes of practice for design and application of plastic composites are urgently needed. . . ." and "Relevant data must be scientifically gathered and presented in a usable form so that the information can be readily interpreted by structural engineers." It is the purpose of this paper to provide some of this information for a particular class of FRP structural members, specifically, pultruded FRP beams. Pultruded FRP structural beams are produced in standardized profile shapes such as, I-beams, wide-flange (WF) beams, channels, and angles. The work described in this paper concentrates on commercially produced standard shapes because it is felt that the widespread use of FRP structural members will depend, to a large extent, on the standardization of the pultrusion industry. As noted by Wigotsky (2), "Tailorability at the expense of standardization compounds confusion in the architect's material selection process, not confidence."

Although FRP beam sections are geometrically similar to steel beam sections, their mechanical (stiffness) and structural (strength) properties are very different. These differences influence both the behavior of FRP structures and the procedures that need to be used in their analysis and design. When designing a structure, the ultimate strength as well as the ability to behave as desired under service-load conditions must be considered. This paper concentrates on the stiffness properties of FRP beams and is, therefore, concerned primarily with the serviceability of FRP structures. Investigations of the strength and failure mechanisms of FRP beams have been considered by Sims et al. (3), and studies of the stability of FRP thin-walled sections have been reported by Lee and Hewson (4). The ASCE *Structural Plastics Design Manual* (5) gives an overview of the issues associated with the design of FRP structures.

In previous work on the subject of the stiffness and deflections of FRP beams (3,4,6) it has been demonstrated, both theoretically and experimentally, that shear deformation effects can have a significant influence on the response of FRP beams. This is because of the anisotropic stiffness properties of the walls of thin-walled FRP beams and, in particular, in pultruded FRP beams, the low in-plane shear stiffness of the material relative to its longitudinal stiffness. This paper presents a methodology to account for the shear deformation in terms of an experimentally determined beam section shear modulus. In typical pultruded FRP beams, serviceability requirements often govern beam design (1), making accurate calculation of deflections critical. In addition, because FRP beams will have shorter spans than conventional steel beams, shear deformation effects, which are usually neglected in steel beams, must be accounted for in FRP beams.

The paper is divided into three sections. First, shear deformation beam theory is reviewed and the motivation for introducing a section shear modulus is discussed. The significance of shear deformation on the response of short-span FRP beams is demonstrated. Second, results of an experimental investigation, in which section shear and flexural moduli were obtained for a variety of pultruded FRP beams, are presented. Third, results from the analysis of a rigid portal frame are presented to demonstrate numerically the effects of shear deformation by comparing the response of a frame consisting of isotropic material beams to one consisting of anisotropic pultruded FRP beams.

SECTION SHEAR MODULUS OF PULTRUDED FRP BEAMS

The theory for the deflection of beams accounting for the effects of shear deformation is discussed in such texts as *Mechanics of Materials* by Gere and Timoshenko (7). The theory presented in this paper follows from Timoshenko's original work in this area (8) and is the one commonly used in the analysis of sandwich beams (9) in which significant shear deformations occur because of the shear flexibility of the beam core. In the shear deformation beam theory used here, two variables are used to describe the deformation of the beam subjected to transverse loading; the total deflection and the

Department of Civil Engineering, The Catholic University of America, Washington, D.C. 20064.

slope resulting from bending deformation only. Two first-order equations for the static response of the beam are solved together with appropriate boundary conditions relating to the total deflection and the bending slope. The details of the equations are not repeated because they can be found elsewhere (6–9).

The solution to the two equations for the case of beams of isotropic materials is given in the following general form:

$$w(x) = f_1(x)/EI + f_2(x)/kAG \tag{1}$$

where $w(x)$ is the beam deflection function, $f_1(x)$ and $f_2(x)$ are functions that depend on the loading and boundary conditions, E is the isotropic Young's modulus of the material, I is the second moment of area, k is the shear coefficient, A is the cross-sectional area, and G is the isotropic shear modulus of the material. The shear coefficient, k, accounts for the fact that the distribution of shear strain is not uniform over the cross section. For thin-walled isotropic sections the shear coefficient can be found by a method developed by Cowper (10). Cowper shows that the shear coefficient for thin-walled beam sections is a function of both the material properties and the geometrical properties of the cross section, even for isotropic beams. Cowper also shows that for common thin-walled beam sections (e.g., I-beams and T-beams) the properties of both the webs and the flanges enter into the formula for k.

In structural engineering applications the term kAG is often replaced by the term A_sG, where A_s is called the *effective shear area*. The effective shear area is usually approximated by the area of the web (or webs) in thin-walled sections (i.e., $A_s = A_w$).

Equation 1 can be applied to the analysis of thin-walled beams composed of anisotropic composite materials, such as pultruded FRP beams, as discussed by Bank and Bednarczyk (6). To use Equation 1 for the thin-walled composite beam, the "appropriate" mechanical and geometrical properties of the composite beam must be used for E, I, k, A, and G. This paper proposes a set of "appropriate" mechanical and geometrical properties to be used for thin-walled pultruded FRP beams.

Consider, first, the first term in Equation 1. The second moment of area I is a geometrical property of the cross section, which can be calculated by known methods. Because it is only a function of the cross-section geometry, it is retained for the pultruded FRP beam. The appropriate stiffness property proposed for the pultruded FRP beam that replaces E in the isotropic formulation, is the *beam section flexural modulus*, designated as E_b (where the subscript b stands for "beam") in what follows. In pultruded FRP beams the beam section flexural modulus is generally different from the coupon flexural modulus, which is different from the coupon longitudinal modulus. These differences exist because of the nature of the laminated structure of the pultruded composite material and the variation in properties in parts of the beam cross section. For this reason manufacturers of pultruded beams give full-size flexural moduli for design purposes, as well as coupon tensile and flexural moduli (11,12). The section flexural modulus is obtained from tests on full-size pultruded FRP beams.

Consider, now, the second term in Equation 1. The cross-sectional area A is a geometric property (like I) that can be precisely calculated. It is proposed, therefore, to retain it

in this formulation as an appropriate property for the pultruded FRP beam. The appropriate properties of the pultruded FRP beam required to replace the terms k and G in the isotropic formulation are the most difficult to determine. The isotropic shear modulus must be replaced by an appropriate anisotropic shear modulus. Because of differences in reinforcement in the flanges and the webs of pultruded beams, the shear moduli of these different parts of the cross section will be different. Consequently, a unique value of G for the pultruded FRP beam cannot be found, as in the isotropic case. The shear coefficient, k, depends on the geometrical and the material properties of the beams. Because the properties can vary around the cross section, the shear coefficient for the pultruded FRP beams will be a function of the different shear and longitudinal moduli of the webs and the flanges.

A procedure to find the appropriate k and G for thin-walled composite beams that incorporates all the different anisotropic stiffness properties has been proposed for characterizing advanced composite material beam structures (13) but is felt to be unsuitable for pultruded composite beams for a number of reasons. First, because of the irregular internal structure of pultruded composite parts, micromechanical models cannot be used to accurately characterize the stiffness properties. Consequently, coupon tests must be relied on to obtain material properties. Because of the variability in properties around the cross section of pultruded FRP beams, numerous coupon tests are required. Second, coupon tests are both time-consuming and expensive. Because pultruded FRP beams, of the types discussed in this paper, are considered primarily for civil engineering purposes, expensive characterization impedes widespread use of the material. In addition, because the shear modulus cannot be calculated from E and ν as in isotropic materials, independent shear coupon tests are required. These tests are difficult to perform. Finally, even with coupon material properties available, the resulting theory (13) is felt to be too complex for pultruded FRP beams for use in civil engineering applications.

For these reasons a new material/structural property is proposed to characterize thin-walled pultruded FRP beams. Analogous to the beam section flexural modulus, a *beam section shear modulus* is proposed for the pultruded FRP beam. The section shear modulus is identified as G_b in which the subscript stands for "beam" (as in the beam section flexural modulus). G_b replaces the term kG in the isotropic formulation. G_b is not equal to the material shear modulus G. As in the case of the beam section flexural modulus, the beam section shear modulus is found from direct experiment on full-size pultruded FRP beams. Coupon tests are therefore avoided. The beam section shear modulus G_b is a function of the material properties and the geometrical properties of the beam. The form of Equation 1 proposed for the analysis of pultruded FRP beams is

$$w(x) = f_1(x)/E_bI + f_2(x)/G_bA \tag{2}$$

All the terms in Equation 2 have been defined previously. In what follows, an experimental program is described in which E_b and G_b were measured for a variety of commercially produced pultruded FRP beams.

The approximate approach of using an effective shear area A_s, as in the case of isotropic beams, can be used for composite beams. If the effective shear area is taken as the web area,

then the shear modulus of the web material G_w needs to be obtained from a coupon test (or by micromechanical calculation). The term kAG in Equation 1 now becomes $A_w G_w$. In this approximate approach the effect of shear deformation in the beam flanges, which has been shown to be significant in thin-walled composite beams (*6*), is neglected. A comparison between the two approaches is presented in what follows.

The significance of shear deflection in pultruded FRP beams, given by the second term in Equation 2, can be investigated analytically by considering the response of a simply supported center-loaded beam of span L. For this case the maximum deflection, w, under the load, P, is written in the form of Equation 2 with appropriate loading and boundary conditions as

$$w = PL^3/48E_b I + PL/4G_b A \tag{3}$$

Neglecting shear deflection, the deflection w can be written in terms of an apparent beam section flexural modulus E_a as

$$w = PL^3/48E_a I \tag{4}$$

Equating Equations 3 and 4 gives the apparent beam section flexural modulus in terms of the section anisotropy ratio (E_b/G_b) and the slenderness ratio (L/r), where r is the radius of gyration, as

$$E_a = \frac{E_b}{1 + 12[(E_b/G_b)/(L/r)^2]} \tag{5}$$

In Figure 1 the ratio E_a/E_b is plotted against the slenderness ratio for values of E_b/G_b, which are appropriate for pultruded FRP beams. As the influence of shear deflection increases, the ratio E_a/E_b decreases from its maximum value of 1.0. It can be seen that the effects of shear deflection increase as (a) the section anisotropy ratio increases and (b) the slenderness ratio decreases. The effects of shear deflection are most severe for L/r ratios less than 60. It is therefore strongly recommended that the contribution of shear deflection be included in deflection calculations when L/r is less than 60.
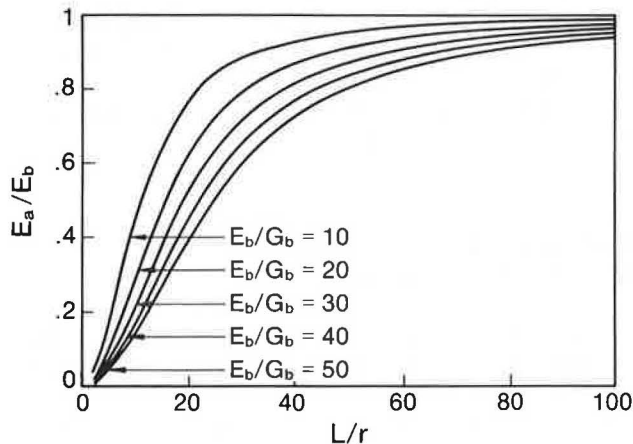

FIGURE 1 **Apparent flexural modulus as a function of anisotropy and slenderness ratios.**

FULL-SIZE TESTS ON PULTRUDED FRP BEAMS

The beam section flexural modulus and the beam section shear modulus were obtained for a number of "off-the-shelf" pultruded FRP beams produced by Creative Pultrusions, Inc. The experimental methodology used to obtain the section moduli is based on a variation of the three-point bend flexure test (ASTM D790) and is described in detail by Bank (*14*). In this variation, the three-point bend test is applied to full-size pultruded beams at slenderness ratio (L/r) values of less than 30 so as to fall into the steep slope region shown in Figure 1. This procedure has the advantage of yielding measurable values of the section flexural and shear moduli from tests on relatively short-span beams. To obtain comparable values of the apparent beam section flexural modulus that are negligibly influenced by shear deformation (and therefore approach the beam section flexural modulus described in this work) L/r values need to be in the 100 range as can be seen from Figure 1.

The test requires loading a simply supported beam at its midspan and measuring the deflection under the load. The relationship between the midspan deflection w, the load P, and the section elastic moduli, given by Equation 3, can be rewritten in the following form:

$$\frac{4Aw}{PL} = \frac{(L/r)^2}{12E_b} + \frac{1}{G_b} \tag{6}$$

Equation 6 is the equation of a straight line in the $4Aw/PL$ versus $(L/r)^2$ plane in which the slope of the line is $1/12E_b$ and the intercept is $1/G_b$. The experimental data points are obtained by measuring w for a constant load P at different values of $(L/r)^2$. The slope and intercept are obtained by performing a linear regression through the experimental data points. The section moduli are then obtained by simple calculation. Alternatively, Equation 3 can be rewritten as

$$\frac{4Iw}{PL^3} = \frac{1}{(L/r)^2 G_b} + \frac{1}{12E_b} \tag{7}$$

In this form, G_b is obtained from the slope and E_b from the intercept of the line in the $4Iw/PL^3$ versus $1/(L/r)^2$ plane. Both calculation methods were used to find the section moduli in this investigation. In the opinion of Sims et al. (*3*), it is more accurate to use values for the moduli obtained from the regression line slope than from the intercept.

In this investigation all the beams were tested at $(L/r)^2$ values ranging from 150 to 500 in increments of 50 (i.e., L/r values of 12.2 to 22.4). A total of seven different beams having different sizes, shapes, and material properties were tested. At each slenderness ratio, the beam was loaded to two different loads and the midpoint deflection recorded for each load. The average value of w/P was then used in the subsequent calculations. The larger of the two loads was that which gave a maximum deflection of approximately $L/300$ for the longest span (i.e., $(L/r)^2 = 500$). The smaller load was two-thirds of the larger load. Under these loads the deflections were measured with a dial indicator having a 0.0001-in. sensitivity. The linear regressions had correlation coefficients above 0.995 in all the tests, which indicated consistent data. The

TABLE 1 PROPERTIES OF I AND WF BEAMS IN TEST PROGRAM

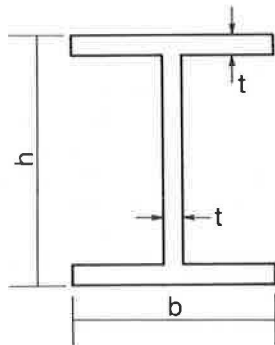| Beam	I (in⁴)	A (in²)	r (in)	L_{max} (in)
WF 4 × 4 × 1/4 Vinylester	7.94	2.888	1.66	37.12
WF 6 × 6 × 3/8 Vinylester	40.17	6.480	2.50	55.90
WF 8 × 8 × 3/8 Vinylester	99.18	8.730	3.38	75.58
WF 4 × 4 × 1/4 Polyester	7.94	2.888	1.66	37.12
WF 8 × 8 × 3/8 Polyester	99.18	8.730	3.38	75.58
I 4 × 2 × 1/4 Polyester	4.40	1.890	1.54	34.44
I 8 × 4 × 3/8 Polyester	70.62	5.725	3.12	69.77

FIGURE 2 Geometrical properties of pultruded FRP beams.

beams tested are given in Table 1 together with some pertinent geometrical properties (11). In Table 1, L_{max} refers to the maximum length of the beam required for testing at $(L/r)^2 = 500$. As can be seen these are all manageable lengths and did not require a particularly large testing area. The beams are described by three numbers: height by flange width by constant wall thickness (in inches) as shown in Figure 2. All data are reported in standard U.S. units because these units are overwhelmingly used in the pultrusion industry and by designers in the United States. Figure 3 shows, as a typical example, the experimental data points and the linear regression lines for the WF 6 × 6 × 3/8 vinylester beam.

The values of E_b and G_b obtained from the experiments are given in Table 2. From Table 2 it can be seen that there is some difference in values predicted by Equations 6 and 7. This difference is not particularly significant. The two sets of

values are best thought of as defining bounds for the experimental values, and an average value is suggested for design purposes. The results show clearly the higher values of the section anisotropy ratio for the wide flange beams (E_b/G_b around 30) as compared with the I-beams (E_b/G_b around 20) indicating greater shear deformation effects in the WF beams. These values correlate with the lower values of G_b for the WF beams. The vinylester beams have higher values of E_b and G_b than the polyester beams for the same cross-sectional geometry. A variation in section properties for different sized beams of the same material system is observed. In the WF series the section properties all decrease as the size of the section is increased. The I-beams show a slight increase as the section size is increased. This variation is probably attributable to the manufacturing process in which the fiber content and layout change to some degree from beam to beam.

As is seen from Table 2, E_b is not constant and shows a dependence on beam shape and material. The range of values for E_b is, however, consistent with the full-size flexural moduli recommended by the manufacturer (11). These are 2.5 Msi for polyester beams and 2.8 Msi for vinylester beams. (These values of the section flexural moduli are suggested, by the manufacturer, for use with all beam section shapes.)

Values of G_b are not given by the manufacturer. Based on the results of the limited tests performed, minimum section shear moduli G_b are suggested for use with the manufacturer suggested E_b values. (In the absence of experimental values for vinylester I-beams, the recommended G_b values are based on the polyester I-beam values scaled with respect to the I-beam/WF beam ratio.) The values of G_b suggested are

- Polyester WF beams: $G_b = 0.075$ Msi
- Polyester I-beams: $G_b = 0.125$ Msi
- Vinylester WF beams: $G_b = 0.085$ Msi
- Vinylester I-beams: $G_b = 0.140$ Msi

It is of interest to compare the experimental results, using the beam section shear modulus approach, with the approximate approach using the effective shear area (i.e., web area) and the web shear modulus G_w. Values for the web shear modulus were found for four of the beams in a separate investigation (15) and are given in Table 3. For these four beams the values of AG_b and A_wG_w are compared in Table 3. (G_b is taken from Table 2, Equation 6.) Results of Table 3 indicate that the approximate approach is less conservative than the beam section modulus approach. This implies that the beam web is not the only part of the section that is subjected to shear deformation. The approximate approach should, therefore, be used with caution. The two approaches show the same overall trends.

ANALYSIS OF A FRAME WITH FRP STRUCTURAL MEMBERS

The analysis of a rigid portal frame constructed of pultruded FRP is described to demonstrate the influence of shear deformations on the deflections and on the redistribution of bending moments and shear forces in a statically indeterminate structure. The response of an isotropic material frame is compared with the response of a highly anisotropic FRP frame. Because a range of beam section modulus values was found
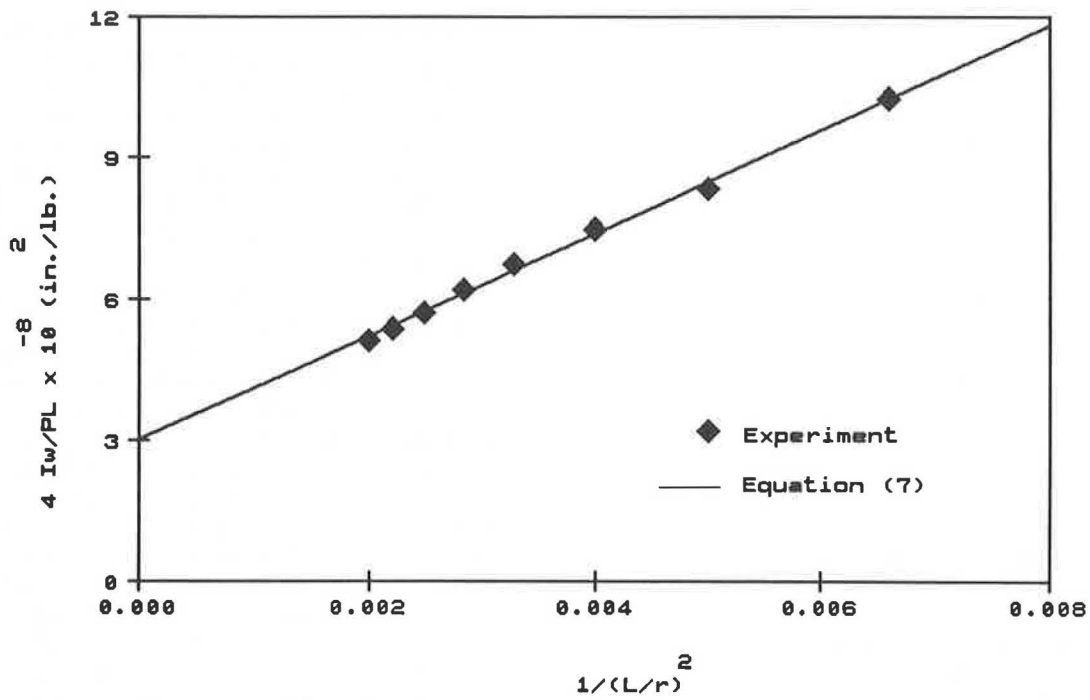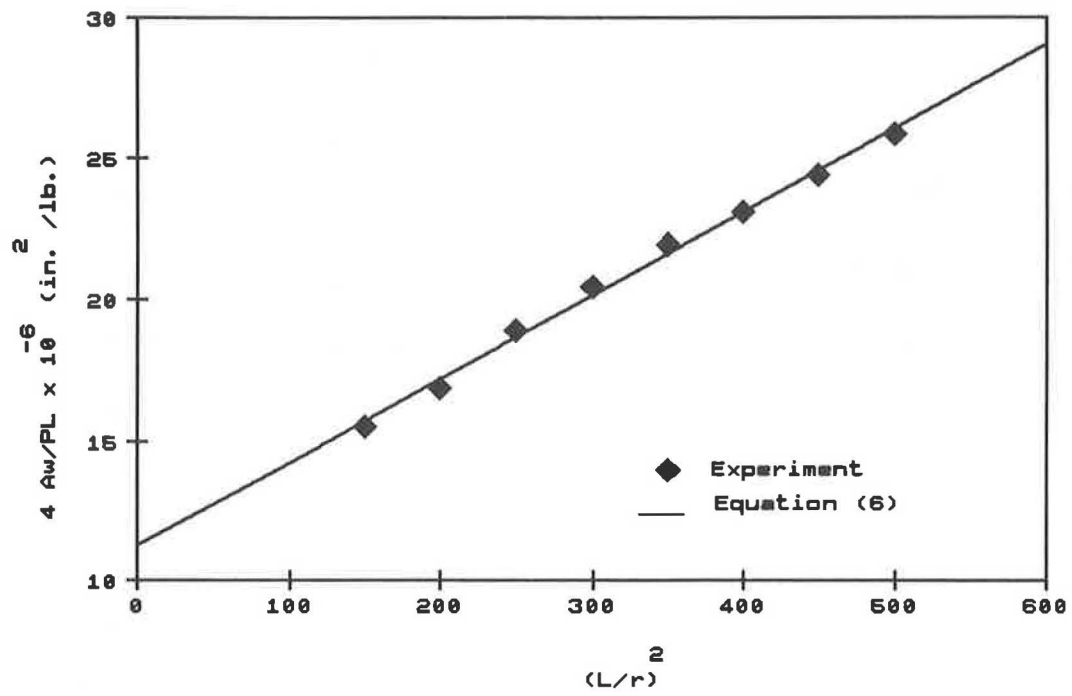
FIGURE 3   Typical test results for a pultruded FRP beam.

TABLE 2 RESULTS OF TESTS ON I AND WF BEAMS IN
TEST PROGRAM

Beam	[from eq. (6)]			[from eq. (7)]		
	E_b	G_b	E_b/G_b	E_b	G_b	E_b/G_b
	(Msi)	(Msi)		(Msi)	(Msi)	
WF 4 × 4 × 1/4 Vinylester	3.28	0.112	29.3	3.19	0.115	27.7
WF 6 × 6 × 3/8 Vinylester	2.82	0.089	31.7	2.74	0.092	29.8
WF 8 × 8 × 3/8 Vinylester	2.78	0.084	32.8	2.79	0.085	32.9
WF 4 × 4 × 1/4 Polyester	3.05	0.089	34.2	3.14	0.087	36.0
WF 8 × 8 × 3/8 Polyester	2.48	0.076	32.7	2.45	0.077	31.9
I 4 × 2 × 1/4 Polyester	2.67	0.134	20.1	2.85	0.130	22.0
I 8 × 4 × 3/8 Polyester	2.91	0.132	22.1	3.12	0.124	23.5

TABLE 3 COMPARISON OF SECTION SHEAR MODULUS
AND APPROXIMATE APPROACHES

Beam	$G_w^{\ddagger}$	AG_b	$A_w G_w$
	(Msi)	(× 10^6 lbs)	(× 10^6 lbs)
WF 4 × 4 × 1/4 Vinylester	0.391	0.323	0.391
WF 4 × 4 × 1/4 Polyester	0.291	0.257	0.291
WF 8 × 8 × 3/8 Vinylester	0.330	0.733	0.990
WF 8 × 8 × 3/8 Polyester	0.281	0.663	0.844

‡ : taken from Ref. 15

in the experimental program, representative values are used
for the beam section flexural and shear moduli in this part of
the paper.

The frame has a height of 120 in. and a span of 144 in. and
has moment resisting connections at the base of the columns
and the top corners as shown in Figure 4. The columns and
girder are WF 8 × 8 × 3/8 in. pultruded FRP beams with
geometric properties of $I = 99.18$ in.⁴ and $A = 8.73$ in.². For
comparison purposes two section anisotropy ratios are con-
sidered: $E_b/G_b = 5$ and $E_b/G_b = 40$. The first represents an

TABLE 4 NUMERICAL DATA FOR PORTAL FRAME
EXAMPLE

	$E_b/G_b = 5$	$E_b/G_b = 40$
$\delta_{max(girder)}$	-0.3859	-0.5566
$\delta_{B\ horizontal}$	-0.3819	-0.4839
$\delta_{B\ vertical}$	-0.0123	-0.0123
$M_{max(girder)}$	59660	62657
M_A	-10960	-18663
M_B	-25778	-23600
M_C	-75415	-71418
M_D	59402	53521
$V_A = V_B$	-123.5	-41.2
$V_C = V_D$	1123.5	1041.2

δ:deflection (in); M:bending moment (lb-in); V:shear force (lbs)

isotropic beam section, whereas the second represents a highly
anisotropic FRP beam section. As can be seen from Table 2,
actual values of E_b/G_b range from 20.1 to 36.0. E_b is taken
as 3.0 Msi and G_b is taken as 0.6 Msi (isotropic with E/kG
= 5.0) and 0.075 Msi (anisotropic). As can be seen from
Table 2, these values fall into the range obtained for FRP
beams. The frame is loaded with a uniform line load of 500
lb/ft on the girder and a horizontal load of 1,000 lb at the top
left corner of the frame as shown in Figure 4.

The static response of the two frames, including shear and
axial effects, was analyzed by a computer code using the stiff-
ness method of matrix structural analysis. The stiffness method
can be readily adapted to account for shear deformations
and effects of axial loads as described in texts such as Ghali
and Neville (16). Shear deformation effects are often included
in the analysis of shear wall structures and should always be
included in the analysis of FRP structures.

Plots of the deflected shapes are shown in Figure 5, and
distributions of bending moments are shown in Figure 6.
Numerical data for significant points on the frames are given
in Table 4. The loading was fairly light yielding girder max-
imum deflection ratios from $L/375$ to $L/323$. Shear defor-
mation increased maximum deflection by approximately 45
percent. Redistribution of the bending moments is seen to be
especially significant in the columns where changes of 70 per-
cent at Support A occur when shear deformation effects are
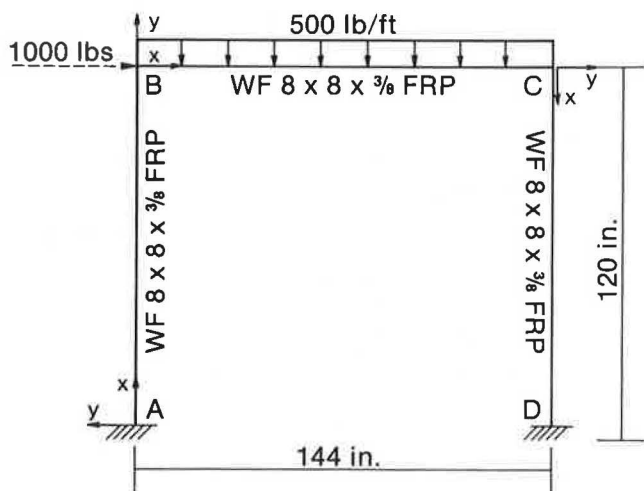included. Redistribution of shear forces in the columns is also
seen.
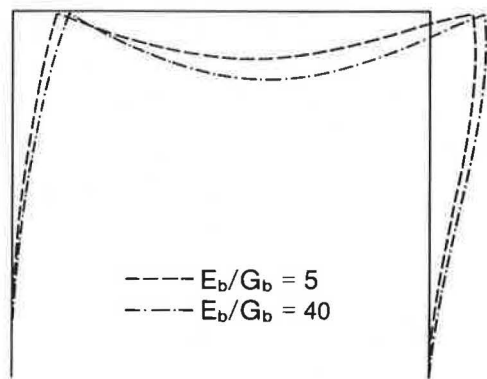
FIGURE 4   FRP portal frame dimensions and loading.

FIGURE 5   Deflection of portal frame.

DISCUSSION OF RESULTS

The experimentally determined values presented here for the section flexural modulus and the section shear modulus are valid only for the pultruded FRP beams considered in this investigation. It is felt, however, that these moduli should be obtained for all standard pultruded FRP beams by the methodology described and should be reported by manufacturers in their technical data. As in the case of currently reported section flexural moduli, it is likely that average or minimum values of the section shear modulus will be reported for whole classes of structural elements. The experimental methodology is especially easy to implement and does not require particularly sophisticated loading or measuring devices. If the beams are tested in the L/r range of 10 to 30, the methodology produces reliable data (confirmed by the linear regression correlation coefficients). The proposed procedure for characterizing the stiffness properties of pultruded FRP beams enables designers to use a shear deformation beam theory without having to resort to costly characterization of the anisotropic material. The theory is felt to be appropriate for structural engineers and can easily be incorporated into existing stiffness matrix analysis computer codes as demonstrated in the rigid frame example.
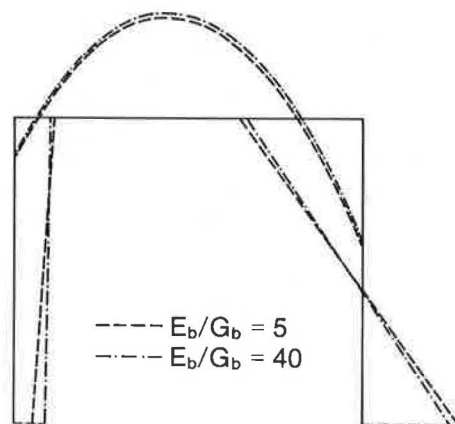

FIGURE 6   Bending moments in portal frame.

The design of pultruded FRP beams for strength considerations is a separate topic and has not been addressed in this paper. Basic research is needed to gain a fundamental understanding of local buckling and crippling failure mechanisms in pultruded FRP beams. For local buckling analysis of the flanges and the webs of pultruded FRP beams, stiffness and strength properties of the FRP material in these parts of the cross section need to be obtained from coupon tests. Although the section shear modulus characterization proposed in this paper is useful for beam deflection calculations, in-plane material shear modulus values are still needed for local buckling calculations (5). An experimental program, using the Iosipescu shear test fixture, was conducted to obtain in-plane shear modulus values for the same beams that were tested in full-size bending in this paper. Results of this investigation are reported by Bank (15). The response of pultruded FRP beams to long-term loads, cyclic loads, and thermal and chemical environments all need to be further investigated to gain a level of understanding that will give structural engineers confidence in the material. The subject of connections in pultruded FRP structures has not been addressed in this paper. In the frame example, the rigid column/girder connection will need to be designed to provide the necessary moment carrying capacity. Currently, pultruded FRP nuts and threaded rods are available for this purpose. Connection details usually follow those used in steel construction. Research is needed on the performance of mechanical connections in full-scale FRP structures.

As mentioned in the introduction, this paper has focused on standard pultruded FRP beams, in particular, on the I- and wide flange beams. These beams have a symmetrical cross section. It may well be that for strength and stability considerations pultruded FRP beams should have unsymmetrical cross sections, that is, thicker compression flanges to resist local buckling. In this case the trade-off between enhanced performance and designer confusion will have to be evaluated.

CONCLUSION

The analysis and design of pultruded FRP beams, including the effects of shear deformation, can be accomplished for civil engineering design purposes with the aid of a new material/

structural stiffness property called the beam section shear modulus. This stiffness property can be obtained for standard pultruded beams using a test methodology that simultaneously gives the beam section flexural modulus. Results of tests using the methodology have been presented. Using these stiffness properties designers can realistically account for the effects of shear deformation in FRP beam structures. Because a large majority of pultruded FRP beams will be designed for serviceability requirements and will have short spans because of the relatively low stiffness of pultruded FRP beams, the need to account for shear effects is all the more critical if effective use of the material is to be accomplished.

ACKNOWLEDGMENTS

REFERENCES

1. A. Green. Glass-Fiber-Reinforced Composites in Building Construction. In *Transportation Research Record 1118*, TRB, National Research Council, Washington, D.C., 1987, pp. 73–76.
2. V. Wigotsky. Plastics in Construction—Busy Bee but Dozing Giant. *Plastics Engineering*, Oct. 1984, pp. 17–23.
3. G. D. Sims, A. F. Johnson, and R. D. Hill. Mechanical and Structural Properties of a GRP Pultruded Section. *Composite Structures*, Vol. 8, 1987, pp. 173–187.
4. D. J. Lee and P. J. Hewson. The Use of Fiber-Reinforced Plastics in Thin-Walled Structures. In *Stability Problems in Engineering Structures and Components* (T. H. Richards and P. Stanley, eds.), Applied Science Publishers, London, 1979, pp. 23–55.
5. *Structural Plastics Design Manual*. Manuals and Reports on Engineering Practice No. 63. ASCE, New York, 1984.
6. L. C. Bank and P. J. Bednarczyk. A Beam Theory for Thin-Walled Composite Beams. *Composites Science and Technology*, Vol. 32, 1988, pp. 265–277.
7. J. M. Gere and S. P. Timoshenko. *Mechanics of Materials*, 2nd ed. PWS Engineering, Boston, Mass., 1984, pp. 407–414.
8. S. P. Timoshenko. On the Correction for Shear of the Differential Equation for the Transverse Vibration of Prismatic Bars. *Philosophical Magazine*, Vol. 41, 1921, pp. 744–746.
9. A. G. Allen. *Analysis and Design of Structural Sandwich Panels*. Pergamon Press, London, England, 1969.
10. G. R. Cowper. The Shear Coefficient in Timoshenko's Beam Theory. *Journal of Applied Mechanics*, ASME, Vol. 33, 1966, pp. 335–340.
11. *Creative Pultrusions Design Guide*. Creative Pultrusions, Inc., Alum Bank, Pa., undated.
12. *Extren Fiberglass Structural Shapes Engineering Manual*. Morrison Molded Fiber Glass Co., Bristol, Va., undated.
13. L. C. Bank. Shear Coefficients for Thin-Walled Composite Beams. *Composite Structures*, Vol. 8, 1987, pp. 47–61.
14. L. C. Bank. Flexural and Shear Moduli of Full-Section Fiber Reinforced Plastic (FRP) Pultruded Beams. *Journal of Testing and Evaluation*, ASTM, Vol. 17, 1989, pp. 40–45.
15. L. C. Bank. Shear Properties of Pultruded Glass FRP Materials. *Journal of Materials in Civil Engineering*, ASCE, 1990 (in press).
16. A. Ghali and A. M. Neville. Chapter 16. In *Structural Analysis—A Unified Classical and Matrix Approach*, 2nd ed. Chapman and Hall, London, 1978.